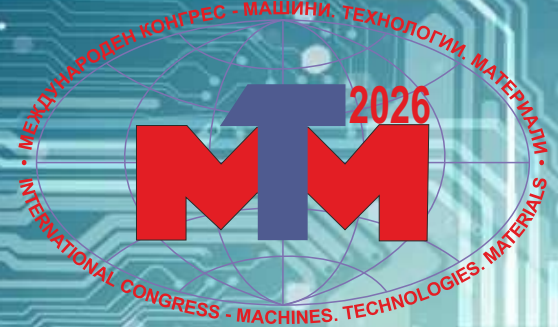
XXIII INTERNATIONAL SCIENTIFIC CONGRESS

WINTER SESSION

25 - 28.03.2026, BOROVETS, BULGARIA



MACHINES. TECHNOLOGIES. MATERIALS 2026

PROCEEDINGS

ISSN 2535-0021 (PRINT)
ISSN 2535-003X (ONLINE)

SCIENTIFIC-TECHNICAL UNION OF MECHANICAL ENGINEERING - INDUSTRY 4.0
BULGARIA

XXIII INTERNATIONAL CONGRESS
WINTER SESSION
"MACHINES.TECHNOLOGIES.MATERIALS"
25-28.03.2026 BOROVETS, BULGARIA

PROCEEDINGS

YEAR IX, ISSUE 1 (33), BOROVETS, BULGARIA 2026

VOLUME I
MACHINES. TECHNOLOGIES. MATERIALS.

ISSN 2535-0021 (PRINT)
ISSN 2535-003X (ONLINE)

ALL ARTICLES ARE PUBLISHED AFTER PEER REVIEW BY TWO INDEPENDENT REVIEWERS.

PUBLISHER:

SCIENTIFIC TECHNICAL UNION OF MECHANICAL ENGINEERING INDUSTRY-4.0

108, Rakovski Str., 1000 Sofia, Bulgaria
tel. (+359 2) 987 72 90,
tel./fax (+359 2) 986 22 40**,**
office@mtmcongress.com
www.mtmcongress.com

INTERNATIONAL EDITORIAL BOARD

Chairman: Prof. DHC Georgi Popov

Members:

Prof. Ahmet Ertas	TR	Prof. Milan Vukcevic	ME
Prof. Andrzej Golabczak	PL	Prof. Mihail Aurel Titu	RO
Prof. Gennady Bagluk	UA	Prof. Mohamed El Mansori	FR
Prof. Detlef Redlich	DE	Prof. Movlazade Vagif Zahid	AZ
Prof. Dipten Misra	IN	Prof. Nadežda Jankelová	SK
Prof. Dmitry Dmitriev	UA	Assoc. Prof. Nikola Šibalić	ME
Prof. Dmitry Kaputkin	RU	Prof. Oana Dodun	RO
Prof. Dobre Runchev	NM	Prof. Peter Kostal	SK
Prof. Esam Husein	KW	Prof. Raul Turmanidze	GE
Prof. Eugene Eremin	RU	Prof. Roumen Petrov	BE
Prof. Idilia Bachkova	BG	Prof. Seiji Katayama	JP
Assoc. Prof. Iryna Charniak	BY	Prof. Sergej Dobatkin	RU
Acad. Ivan Vedyakov	RU	Prof. Sergej Nikulin	RU
Prof. Ilir Doci	KO	Prof. Svetlana Gubenko	UA
Prof. Iurie Melnic	MD	Prof. Sveto Cvetkovski	NM
Prof. Janette Brezinová	SK	Prof. Vadim Kovtun	BY
Prof. Jaroslaw Piatkowski	PL	Prof. Viacheslav Prokhorov	RU
Prof. Juan Alberto Montano	MX	Prof. Wu Kaiming	CN
		Acad. Yurij Kuznetsov	UA

INTERNATIONAL ORGANIZING COMMITTEE

Chairman:
Prof. Galina Nikolcheva

Vice Chairmen:
Dr. Eng. Raycho Georgiev

Members:

Assoc. Prof. Georgi Pandev (BG)
Assoc. Prof. Dimitar Karaivanov (BG)
Assoc. Prof. Hasan Erdem Camurlu (TR)
Assoc. Prof. Hristo Karamishev (BG)
PhD Pencho Sirakov (BG)
Eng. Marko Mumović (ME)

Members:

Eng. Askin Mutlu (TR)
Eng. Oleg Mihaylov (BG)
Eng. Radoslav Daskalov (BG)
Eng. Ivan Opacak (HR)
Eng. Uldis Zaimis (LV)

CONTENTS

MACHINES

Wear Performance of Agricultural Harrow Discs Coated by Plasma-Jet Thermal Deposition
Corneliu Munteanu, Iurie Melnic, Vlad Nicolae Arsenoaia, Bogdan Istrate, Fabian Cezar Lupu, Vitali Vișanu, Constantin Zîrnescu, Vladimir Badiul 5

Analysis of risk in the development of device for field testing of anchor bolts
Nikola Šibalić, Marko Mumović 9

Segmental exergy analysis of a complex 210 mw three cylinder steam turbine
Mrzljak Vedran, Poljak Igor, Glučina Matko, Anđelić Nikola 13

Thermodynamic analysis of steam turbine and condenser from combined cycle power plant
Mrzljak Vedran, Prpić-Oršić Jasna, Baressi Šegota Sandi, Lorencin Ivan 17

Theoretical investigation into the influence of a teeth fault to gear train vibrations
Svetlin Stoyanov 21

Bio-electrochemical system based electro-generative pipeline element
Rosen Ivanov 23

Active damping in cable-stayed-bridge structures using hydraulic actuators
Enkeleda Kokona, Helidon Kokona, Klodian Dhoska 27

Two-stroke low-speed engines and maritime transition to net-zero
Ozren Bukovac, Jelena Kolundžija 30

TECHNOLOGIES

Investigation of Cutting Edge Radius Influence on Tool Wear Using FEM Simulation in DEFORM 3D
Martin Necpal, Marek Vozár 33

Kinetic investigation of copper ions adsorption onto corn stalks
Milan Gorgievski, Miljan Marković, Nada Štrbac, Vesna Grekulović, Milica Zdravković, Marina Marković, Kristina Božinović 36

Implementation of slow stress rating test method (SSRT) in determination susceptability to hydrogen embritlement of P460NL1 steel
Sveto Cvetkovski, Dr Rudolf Vallant, Fabian Bobner, Tobias Walder, Thomas Staubman, Fernando Warchomicka 39

Machine Learning Prediction of Mechanical Properties for Al-Cu Alloys Using Monte Carlo Data Augmentation
Mihail Kolev, Tatiana Simeonova, Ivo Lozanov, Vilyana Kazanlaklieva, Viktoria Gerdzhikova 44

Analytical-numerical approach for computation of welding residual stresses in large shell structures
Nikolay Doynov, Vesselin Michailov, Hartmut Pasternak 47

Fiberglass casing string cementation operations in wellbore
Igor Medved, Borivoje Pašić 51

Analysis of workover operations over a ten-year period in an oil and gas field with sucker rod pump production
Borivoje Pašić, Igor Medved, Antonio Knežević 55

Forecast-oriented optimization of production plans: closed-loop decision-making and model risk management
Belozyorov M., Kalashnikov E. 59

Rolling element bearing fault detection using accelerometer and laser displacement measurements
Mihaela Vještica, Braut Sanjin, Goranka Štimac Rončević 63

Finite Element Modeling of a Flat Reinforced Expanded Polytetrafluoroethylene Gasket
Evlogi Mladenov, Ivo Draganov 67

Preparation of biocompatible hydrogels incorporating sensing nanoparticles
Nadya Nikolova, Stanislav Baluschev, Ivanka Nikolova 71

Possibilities for accelerating chemical-thermal treatment
Valery M. Konstantinov, Vladislav A Leshok 74

Analytical solutions for boundary value problems of transport phenomena in the design of multilayer structures
Renat Sadykov, Airat Osipov, Artem Akhmerov 76

Cathodic Protection Modeling of Steels in Corrosive Chemical Environments Using COMSOL Multiphysics
Julieta Daniela Chelaru 80

Photoluminescence properties of Sm3+-doped ZrO2–TiO2–Al2O3 coatings
Stancho Yordanov, Bojidar Jivov, Vladimir Petkov, Shaban Uzun, Mihaela Aleksandrova 83

Modeling of Densification Kinetics during Electro-Pulse Consolidation of Titanium Powder
Olha Syzonenko, Mykola Prystash, Andrii Torpakov, Tetiana Makrukha 87

Preparation and Optical Properties of Gelatin-SiO2 Hybrid Coatings on Glasses for Photovoltaic Applications
Stancho Yordanov, Tatyana Ivanova, Shaban Uzun, Vladimir Petkov, Ina Gospodinova 92

Investigation of leak rate through a profile expanded polytetrafluoroethylene gasket
Евлоги Младенов 95

Applications of DNA Complexes to Sensor Technology and Molecular Probes for Early Diagnosis of Neurodegenerative Disease
Hristina Sbirkova-Dimitrova, Hristo Gerginov, Boris L. Shivachev 99

Secondary neutron monitoring at Rozhen Observatory (MNMS-ROZH) data
H. Nichev, T. Arsov, Ch. Angelov, N. Serafimov, N. Tyutyundzhiev, M. Petrov 100

MATERIALS

Development of an All-Optical Platform for Real-Time Monitoring of Hypoxia Dynamics
Stanislav Baluschev, Maria Micheva, Ivanka Nikolova, Katharina Landfester 101

Fermented grape pomace ash – by-product of rakia (brandy) production
Aleksandar Nikolov, Liliya Tsvetanova, Borislav Barbov, Ivan Tsanev, Yana Tzvetanova 105

Influence of femtosecond laser processing parameters on the surface morphology of titanium alloy
Ljerka Slokar Benić, Hrvoje Skenderović, Franjo Kozina, Matej Barać 112

Effect of non-metallic inclusions on the grain structure of low-carbon steels under severe plastic deformation
Svetlana Gubenko 116

Comparative Analysis of Natural Ruby and Synthetic Corundum Ceramics by UV–Vis and Raman Spectroscopy
Ivan Tsanev*1, Tsvetan Dimitrov2, Liliya Tsvetanova1, Rositsa Titorenkova 120

Observed Damage Patterns and Material Strength Deficiencies in URM Dwellings After the 2019 Albania Earthquake
Marjo Hysenlliu 124

Structure and properties of AlB12-Al detonation coatings on Steel 45
Aleksandr Umanskyi, Valery Muratov, Vladimir Sheludko, Konstantin Haltsov, Aleksey Bondarenko, Tatiana Mosina, Vyacheslav Syrovatka, Irina Martsenyuk, Victor Varchenko, Valery Kremenitsky, Anatolii Minitskyi , Aleksey Kushchev 128

Wear Performance of Agricultural Harrow Discs Coated by Plasma-Jet Thermal Deposition

Corneliu Munteanu[1], Iurie Melnic[2*], Vlad Nicolae Arsenoaia[3], Bogdan Istrate[1], Fabian Cezar Lupu, Vitali Vișanu[2], Constantin Zîrnescu[2], Vladimir Badiul[2]
[1] "Gheorghe Asachi" Technical University of Iasi, 700050 Iasi, Romania
[2] Technical University of Moldova, 168, Ștefan cel Mare Blvd., Chișinău, Republic of Moldova
[3]Agriculture Faculty, "Ion Ionescu de la Brad" Iasi University of Life Sciences, 700490 Iasi, Romania
[*] iurie.melnic@im.utm.md

Abstract: *A comparative analysis of wear performance of coated harrow discs by plasma-jet thermal deposition was evaluated under agricultural conditions to assess the performance of atmospheric plasma spraying systems. This paper presents a long-term comparative field evaluation under identical operating conditions on a quartz-rich argic luvisol soil. Disc wear was quantified by periodic measurements of mass loss and diameter of the studied discs.*

The uncoated disc showed the most severe degradation, with a total mass loss of approximately 700 g and a rapid acceleration of wear after the first 5-10 ha of harrowing. The results obtained under field conditions demonstrate that the microstructural integrity of the coating is more critical than the nominal hardness and highlight the superior effectiveness of APS ceramic coatings for extending disc life in abrasive agricultural soils.

KEY WORDS: *WEAR PERFORMANCE, HARROW, DISCS, PLASMA-JET THERMAL DEPOSITION, PLASMA SPRAYING SYSTEMS.*

Introduction

Agricultural machinery components that interact with the soil, such as disc harrows, plowshares, tines, and other soil-cultivating elements, operate under conditions characterized by high abrasion and impact loads. During soil cultivation, the harrow disc blades are also subject to significant wear due to abrasive soil particles such as sand, small and big stones, and other hard materials that accidentally get into the soil.

Modern agricultural production relies on mechanized soil cultivation tools, such as plowshares, cultivators, disc harrows, cultivator blades, seed drill disc coulters, etc. These soil-engaging tools loosen, aerate, and mix the soil, and are essential for preparing the seedbed and ensuring crop emergence. Constant exposure to abrasive soil, rocks and agricultural residues inevitably leads to wear, which has a direct impact on operational efficiency and costs. Research shows that wear and tear is responsible for over 50% of agricultural machinery failures and can usually only function optimally after replacement.

Analysis of recent research and publications

All soil-working machines wear out faster with increasing sand content in the soil. This requires improving the mechanical properties of the working surfaces of the working parts of the machines mentioned above [1]. So, their constant exposure to soil, mineral particles, crop residue, and stones leads to progressive material degradation, affecting cutting efficiency and increasing fuel consumption to maintain consistent tillage quality [2].

Disc harrows require frequent replacement of heavily worn discs, which increases both downtime and maintenance costs, factors that are particularly important on large farms [3]. Increasing the wear resistance and service life of discs is essential for economically and environmentally sustainable agricultural production.

Insufficient wear resistance reduces the reliability and productivity of mechanized agriculture, potentially jeopardizing the efficiency of field work and even crop yields. Excessive wear of tillage machines changes the geometry, rounding the cutting edge or reducing their functional dimensions with an impact on the efficiency of soil work, increasing traction, and fuel consumption.

Extending the service life of agricultural machinery components is directly related to increasing energy saving, agricultural efficiency, and ultimately, economic sustainability. Therefore, the wear resistance of tillage tools is a priority for modern agriculture. It can be concluded that the best solutions should aim to increase surface hardness and structural strength to resist abrasion, while maintaining sufficient impact resistance [4].

Roșu et al. point out that the reduction in thickness and the loss of diameter of disc coulters of seed drills strongly depend on the physical, mechanical and technological properties of the soil, including the presence of hard mineral inclusions (stones) [5].

Despite numerous studies on the wear of agricultural discs and soil tillage tools, most published work focuses on laboratory tests, short-term field studies or evaluations of a single coating system. However, comparative studies conducted under identical field conditions over the long term, including both coated and uncoated reference discs, remain limited.

The novelty of this study lies in the simultaneous long-term comparison of coating systems and an uncoated reference disc, operating under identical working conditions such as mechanical loads, soil profiles, working depths and speeds. Unlike previous studies, the discs were evaluated on an area of over 50 hectares per disc in quartz-rich argitic luvisol soil, which allowed to identify nonlinear wear behavior and degradation mechanisms in advanced stages.

The most common solution for protecting tillage implements from wear used in practice remains hardening with Fe-Cr-C alloys, ussualy referred to as sormite or white high-chromium cast iron coatings. These coatings, usually applied by arc welding or plasma arc welding, extend the service life of workpieces several times compared to uncoated steel components. This is due to the presence of hard chromium carbides Cr_7C_3 or $(Cr,Fe)_7C_3$ embedded in a martensitic or austenitic matrix. Compared to sormite coatings, atmospheric plasma spraying (APS) allows for the application of thinner, more uniform, and more controlled coatings with minimal thermal impact on the substrate.

In this context, the present study investigates the wear performance of coated harrow discs by plasma-jet thermal deposition with three powders: Metco 71NS, Metco 136F and Metco 45C-NS, applied using a Sulzer Metco 9MCE atmospheric plasma spraying system [4].

The aim of the research is to conduct a comparative analysis of the wear performance of coated harrow discs by plasma-jet thermal deposition by plasma-jet thermal deposition method in field conditions, followed by an assessment of the effectiveness of atmospheric plasma spraying systems.

Materials and Methods

At the beginning of the study, the elemental composition of a new, uncoated harrow disc was determined using a spark optical emission spectrometer Spark-OES equipped with the SparkTiffe analytical software package [5].

Three 610 mm diameter disc specimens were prepared for coating. The method of preparing and coating the discs has already been described in several works [4, 6, 7].

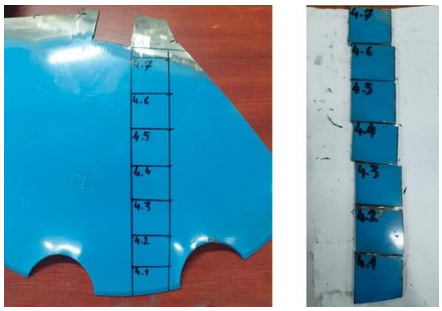
Seven radial specimens were cut from the cutting edge towards the central area of the new harrow disc (Figure 1). The resulting chemical composition values were used as initial data for

correlating the substrate material with coating adhesion, microstructural behavior, and field wear performance.

Uniform melting of the powders produces dense, well-bonded deposits:

- Metco 71NS (W_2C/WC–12Co) supply a hard carbide surface suitable for use in highly abrasive soils;
- Metco 136F (Cr_2O_3–SiO_2–TiO_2) provides a ceramic coating with high hardness, good impact absorption due to its silicon dioxide content, and excellent corrosion resistance;
- Metco 45C-NS (Co–Cr–Ni–W–C) produces a metallic coating called Stellite with balanced strength and wear resistance, suitable for surfaces subject to combined abrasive and impact loads.

These powders cover a broad functional spectrum of ceramic, carbide and cobalt metal systems, allowing for comparative evaluation of different harrow disc wear protection strategies in the field.



a) b)

Figure 1. Studied radial samples:
a) radial marking and segmentation of the disk surface before cutting; b) extracted radial samples.

The coatings were applied to both sides of each harrow disc, forming a continuous ring-shaped coating around the entire working perimeter [6].

The coatings were applied to both sides of each harrow disc, forming a continuous ring-shaped coating around the entire working perimeter. Microstructural characterization of coated and uncoated disc samples was performed by scanning electron microscopy (SEM), which can provide detailed information about surface morphology, coating microstructure, wear patterns, and particle distribution [7].

An OTMA heavy disc harrow with a 4.0 m working width was used for field testing. These harrows are equipped with four groups of 10 concave discs (two groups in front and two in the rear). The test discs, both coated and uncoated, were mounted on the harrow's front axle at an attack angle of 15° relative to the direction of travel. This configuration improves soil penetration, crop residue removal, and lateral soil movement, as well as ensuring effective stubble incorporation and uniform soil cultivation across the entire working width. The disc harrow under study was coupled with a medium-sized John Deere 7230 tractor with a power of 230 hp.

The test disc harrow was coupled to a mid-size John Deere 7230 tractor with 230 hp and a powershift transmission with high hydraulic capacity, providing consistent traction and allowing precise control of working speed and tillage depth.



Figure 2. Installed testing discs on the harrow before field testing:
1) three coted discs; 2) uncoted discs.

During field trials, stubble disking was performed after grain harvesting (Figure 3). The disc harrow under study cultivated 1,000 hectares of land, meaning each disc on the two front axles cultivated 50 hectares.

According to agronomic recommendations, the main operating parameters were:

- working depth of 0.15 m;
- forward speed of 7-8 km/h.



Figure 3. Tractor and 4-metre OTMA disc harrow during stubble field work

Since all discs were exposed to the same soil profile and operating parameters during the discing operation, differences in wear can be attributed primarily to surface characteristics rather than positional influences.

According to the methodology, disk weight measurements were taken regularly, every 20 hectares of the total treated area, corresponding to 1 hectare per disk. Before weighing, the disks were thoroughly cleaned of soil residue and dried. The weight of each disk was measured using a calibrated digital scale with an accuracy of ±1 g. For each weighing, three consecutive measurements were taken, and the average value was determined. The measurement error for the disk mass was less than ±2 g, which is negligible compared to the observed mass loss.

Diameter measurements were taken using a digital caliper with an accuracy of ±0.02 mm. The diameter of each disk was determined by measuring it in two sections and calculating the average value. This procedure allowed to identify uneven edge wear and reduce measurement variability.

To assess disk wear, four test disks (three coated and one uncoated) were weighed every 20 hectares of total cultivated area (i.e., 1 hectare per disk). This allowed us to accurately determine mass loss and increase in disk wear with increasing cultivated area.

Thus, all tested discs were subjected to identical the same operating parameters (field soil profile, operating travel speed, working depth, uniform residue load and disc attack angle), which ensured that any differences in wear could be attributed solely to the material and coating characteristics of the samples.

Rezults and discussions

Measurements of the disc masses taken before and after the coating process reveal differences in the amount of material deposited on each disc tested (Table 1).

Table 1. Mass of the disks before and after coating application

No	Disc	Coating Type	Initial Mass (kg)	Coating Mass (kg)	Final Mass (kg)
1	Sample 1	Cr_2O_3-SiO_2-TiO_2 Ceramic	10.483	0.105	10.588
2	Sample 2	WC/W_2C-Co Carbide	10.492	0.127	10.619
3	Sample 3	Co-Cr-Ni-W-C alloy	10.481	0.116	10.597
4	Uncoated Sample	No coating	10.486	0	10.486

The dynamics of disc wear, expressed as mass loss in the range of 0–50 ha/disc, reveals significant differences between the three coated discs and the uncoated disc (control). All four curves shown

in the graph demonstrate nonlinear behavior, namely, low wear rates in the early stages of operation, followed by a gradual acceleration of mass loss as the total worked surface area increases (Figure 4). This trend reflects the typical behavior of tillage tools, which before the start of work (testing) had sharp edges and smoother working surfaces, but gradually with an increase in the processed field area, wear increases, since, being subjected to increasingly intense abrasion, the edges become rounded and the contact area of the soil with the metal of the disks increases. The uncoated (control) disc exhibits the steepest wear curve.

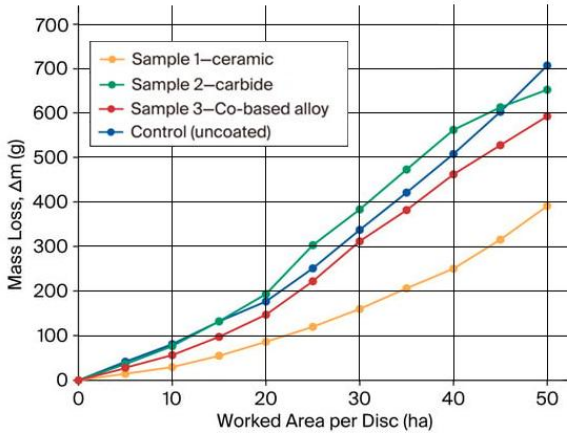


Figure 4. Mass loss of coated and control (uncoated) discs as a finction of worked area of the treated surface per disc

Compared to all the samples tested, Sample 1 demonstrates the best results. The wear curve remains virtually flat over the first few hectares (10 hectares), and even over an area of 25 hectares, the weight loss is limited (0.15 kg). After this point, wear accelerates somewhat, but the total weight loss over an area of 50 hectares remains minimal at 0.39 kg. This behavior indicates the excellent long-term stability of the ceramic coating, especially in abrasive soils rich in quartz.

The wear curves, plotted against disc diameter and constructed for an effective operating range of 0–50 ha/disc, provide information on the degradation of the disc samples studied during field work. As expected for components in contact with the ground, all four discs show a non-linear reduction in diameter, with relatively low wear in the initial stage of operation, followed by gradually accelerating degradation towards the end of the the operating range.

This type of wear is typical of abrasive wear, where the disc edges initially retain a sharp geometry, but as the blade becomes dull (rounded), contact with the soil intensifies and material removal accelerates. The control (uncoated) disc exhibits the steepest wear trajectory, resulting in an overall diameter reduction of about 26 mm after 50 hectars of worked area per disc (Figure 5).

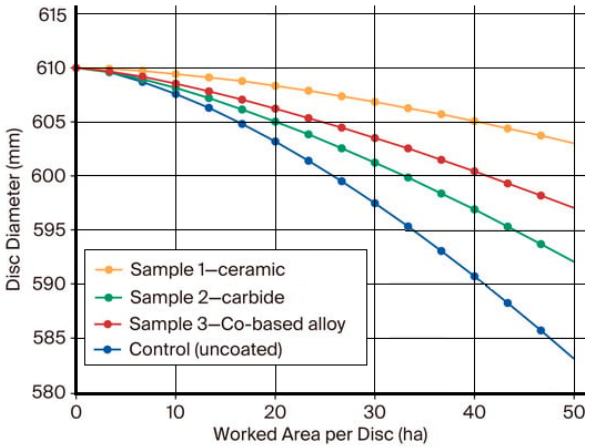


Figure 5. Variation of disc diameter as a function of the worked area per disc

The curve shows the most pronounced acceleration, confirming the susceptibility of untreated carbon steel to abrasive action in quartz-rich soils. This rapid wear in the later stages is consistent with previous studies reporting that unprotected agricultural harrow disc blades lose their geometry more quickly after the cutting edge becomes dull.

Sample 1 exhibits the smallest disc diameter loss after 50 hectares of work per disc and maintains the largest diameter throughout the entire test period. Sample 1 demonstrates the best results, with a final diameter loss of 7 mm. Its curve has the flattest slope, indicating that the ceramic coating effectively slows edge rounding and maintains the harrow disc's geometry significantly longer than discs with other processing methods.

Sample 3 demonstrates intermediate results, with a final diameter loss of 14 mm. The curve lies between the values for the ceramic and carbide coatings, reflecting the balance between strength and moderate hardness characteristic of cobalt alloys.

The results of Sample 2 were better than those of the uncoated disc, but worse than those of the ceramic-coated (Sample 1) and alloy-coated (Sample 3) discs.

Compared to the uncoated (control) disc, the tested coated variants demonstrated significantly different wear reductions. The ceramic-coated disc (Sample 1) reduced overall weight loss from approximately 700 g to 390 g after 50 ha, representing a weight loss reduction of approximately 44%. The cobalt-based alloy coating (Sample 3) provided a more modest reduction of approximately 16%, while the carbide-coated disc (Sample 2) showed only a slight improvement of approximately 7%.

Similar trends were observed for disc diameter wear. The uncoated disc (Sample 1) lost about 26 mm in diameter, while the ceramic coating limited the diameter loss to approximately 10 mm (a 62% reduction). The Co-based alloy (Sample 3) and carbide coatings of Sample 2 reduced diameter loss by 46% and 31%, respectively.

Based on these trends, the ceramic coating provides approximately 1.8 times the wear life of an uncoated disc in field testing conditions ranging from 0 to 50 hectares per disc, while the cobalt-based alloy and carbide coatings increase wear life by approximately 1.2 and 1.1 times, respectively.

The minimum working diameter of a worn harrow disc depends on its initial size, but typically discs with a diameter of 620 -660 mm should be replaced when they wear down to 500-520 mm. If the diameter is critically reduced more than 100-150 mm from the initial diameter, the disc no longer penetrates effectively and processes the soil efficiently.

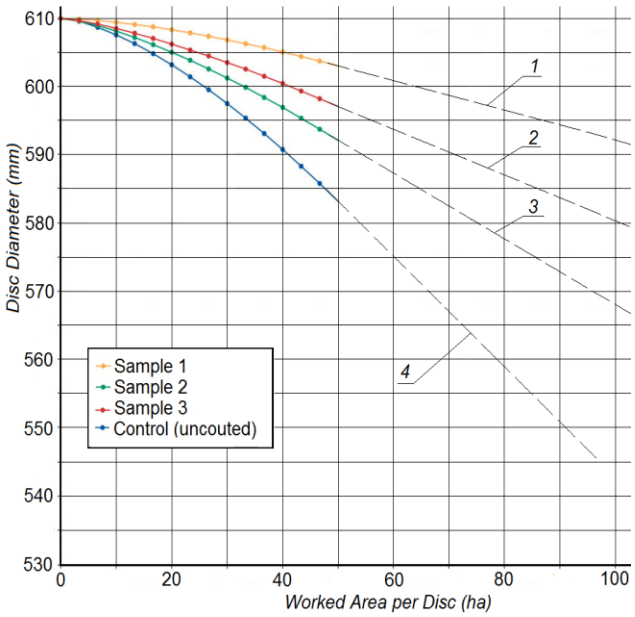


Figure 6. Experimental and theoretical method for expanding the variation of disc diameter as a function of the worked area per disc: *1 - Sample 1; 2 - Sample 3; 3 - Sample 2; 4 - uncouted disc.*

A disc is considered worn out when its diameter decreases by 15-20% of the original, which critically affects the angle of attack and the depth of soil cultivation [8, 9].

The use of heavily worn discs leads to a decrease in the quality of stubble processing and increased fuel consumption.

If we continue the curves shown in Figure 5, we see that the minimum operating period of uncouted harrow disc is 0-150 hectares of processed area per disc or more precisely less than 110 ha/disc (Figure 6, curve 4). The uncouted disc will reach its maximum permissible wear at a minimum diameter of 530 mm. In Figure 6, we see that the minimum operating period of a ceramic-coated disc (Sample 1) is more than 0-150 ha/disc (Figure 6, curve 1) and it will also reach the maximum permissible wear at a minimum diameter of 530 mm.

However, it remains unclear how ceramic-coated discs Sample 1 and other Samples will perform in the future due to blade rounding as a result of wear, and changing of disc diameter (Figure 5, curve 1, 2, 3).

In this study, the APS ceramic coating provided an estimated increase in service life of approximately 1.8 times based on the mass loss factor and approximately 2.6 times based on the diameter retention factor, indicating that, depending on the functional failure criterion, thin APS ceramic coatings can approach the lower and mid-range performance reported for conventional hardfacings while providing improved thickness control and reduced geometric variations.

The wear assessment in this study was based primarily on quantitative measurements of mass and diameter loss, supplemented by previously performed microstructural analysis of the applied coatings using a scanning electron microscope.

Further research could be expanded to include field experiments until the discs coated by plasma-jet thermal deposition method are completely worn out.

Conclusions

1. This study examined the wear performance and behaviour of harrow discs coated by plasma-jet thermal deposition method with three different thermal spray systems:

1) Sample 1 - Cr_2O_3-SiO_2-TiO_2 ceramic;
2) Sample 2 - WC/W_2C-Co carbide;
3) Sample 3 - Co-Cr-Ni-W-C alloy.

Their performance was compared with an uncoated (control) disc under field operating conditions.

2. Compared to the uncoated (control) disc, the tested coated variants demonstrated significantly different wear reductions. The ceramic-coated disc (Sample 1) reduced the overall weight loss by approximately 44%, the cobalt-based alloy-coated disc (Sample 3) had a reduction of approximately 16%, and the carbide-coated disc (Sample 2) only showed an improvement of approximately 7%. The results obtained in the field confirm that the microstructural stability of the coating determines the long-term wear resistance of harrow discs, and not only its density or nominal hardness.

3. Based on these trends, the ceramic harrow disc coating provides approximately 1.8 times longer disc life than the uncoated disc in field trials covering 0 to 50 hectares per disc, while cobalt-based alloy and carbide coatings increase disc life by approximately 1.2 and 1.1 times, respectively.

4. The research results clearly show that applying coatings to the surface of harrow discs can significantly reduce mass loss and extend their service life, and the degree of improvement largely depends on the coating materials.

5. The research results show that Cr_2O_3-SiO_2-TiO_2 ceramic coatings (Sample 1) represent a very perspective solution for increasing the durability of disc harrows operating in abrasive soil environments and significantly reducing wear of the discs coated by plasma-jet thermal deposition.

6. This study highlights the value of combining laboratory research with long-term field trials. The integration of scanning electron microscopy analysis, chemical profiling, and long-term performance data allows for more accurate predictions of coating performance than any laboratory test alone.

7. Further research could be expanded to include field experiments until the discs coated by plasma-jet thermal deposition method are completely worn out. Future research should expand field tests to study how ceramic-coated discs Sample 1 and other Samples will perform in the future due to blade rounding as a result of wear, and changing of disc diameter (Figure 5, curve 1, 2, 3).

Acknowledgments

This work and research were supported by a grant from the Romanian Ministry of Education and Research, CNCS-UEFISCDI, project number PN-IV-P8-8.3-ROMD-2023-0108, within the PNCDI IV.

References

1. A. Natsis, G. Petropoulos, C. Pandazaras. Influence of local soil conditions on mouldboard ploughshare abrasive wear. Tribol. Int., Vol. 41, 2008. pp. 151-157.
https://doi.org/10.1016/j.triboint.2007.06.002

2. Annu Rani, T.P. Singh, Jayant Singh, Vishal Patel, Mukesh Kumar Choudhary. Abrasive wear behavior of EN42 steel used in agricultural discs in field conditions. Eng. Fail. Anal. 2022, 142, 106789.
https://doi.org/10.1016/j.engfailanal.2022.106789

3. Corneliu Munteanu, Iurie Melnic, Bogdan Istrate, Mark Hardiman, Lidia Gaiginschi, Fabian Cezar Lupu, Vlad Nicolae Arsenoaia, Daniela Lucia Chicet, Constantin Zîrnescu, Vladimir Badiul. A Comprehensive Review of Improving the Durability Properties of Agricultural Harrow Discs by Atmospheric Plasma Spraying (APS). In: Coatings 2025, 15(6), 632;
https://doi.org/10.3390/coatings15060632

4. Vlad Nicolae Arsenoaia, Corneliu Munteanu, Fabian Cezar Lupu, Bogdan Istrate, Marcelin Benchea, Iurie Melnic. Field Performance and Wear Behavior of Atmospheric Plasma Spraying (APS) Coated Discs Used in Agricultural Disc Harrows. In: Agriculture 2026, 16(1), 114;
https://doi.org/10.3390/agriculture16010114

5. Roșu Bogdan Rosu, Gheorghe Voicu, Gabriel-Alexandru Constantin, Paula Tudor, Elena-Madalina Stefan. Aspects regarding the physical parameters and wear in the work process of the disc openers for seeding machines. In: Agriculture 2024, 14, 1066;
https://www.mdpi.com/2077-0472/14/7/1066

6. Corneliu Munteanu, Iurie Melnic, Bogdan Istrate, Fabian Cezar Lupu, Vitali Vișanu, Vladimir Badiul, Constantin Zîrnescu. Study of harrow discs coated by plasma-thermal method. In: *International Scientific Journal "Mechanization in agriculture & Conserving of the resources", Issue 2, 2025. pp.46-48.* ISSN print 2603-3704, ISSN web 2603-3712.
https://stumejournals.com/journals/am/2025/2/46

7. Corneliu Munteanu, Bogdan Istrate, Fabian Cezar Lupu, Marcelin Benchea, Iurie Melnic, Vitali Vișanu. Increasing the Mechanical Characteristics of the Disc Harrow Component by APS Thermal Coatings. In: Thermal Spray 2025: Proceedings from the International Thermal Spray Conference May 6–8, 2025; Vancouver, Canada. Vancouver: Published Online: May 05 2025, Paper No: itsc2025fm01, pp. iii-v; 3 pages. - PP. 508-514.
https://doi.org/10.31399/asm.cp.itsc2025p0508

8. When should i change the discs in a disc harrow?
https://www.bellotaagrisolutions.com/fr/node/851

9. SOKHT, K., TRUBILIN, E., KONOVALOV, V. Disc harrows and cultivaters. Design of Technological Parameters. Krasnodar: KubSAU, 2014, 164 p.
https://www.kubsau.ru/upload/iblock/3ed/3ed5134865100667522daf24a5faacaf.pdf

Analysis of risk in the development of device for field testing of anchor bolts

Nikola Šibalić[1*], Marko Mumović[1]
Faculty of Mechanical Engineering, University of Montenegro, Podgorica, Montenegro[1]
nikola@ucg.ac.me

Abstract: *The subject of this paper is the analysis of technological risk by the combined application of the "Cause-Effect" method and the FMEA (Failure Mode and Effects Analysis) method, in the development of a device for technical testing of anchor bolts in field conditions. These methods are essential tools when it comes to risk analysis and management. In this research, an original solution of the testing device was given, which enables the testing of anchor bolts in a wide range. With this device, the most important parameters are monitored, which testify not only to the quality of the installation, but also to the quality of the base in which they are installed, as well as the anchor bolt itself. As the use of anchor bolts in responsible structures is increasing day by day, the need for research in the direction of testing these mechanical elements placed in the base, as critical components in many applications, naturally arises. The development of the initial prototype solution begins with the adoption of input parameters (type of anchor bolt, dimensions, geometric shape, expected load and tested spatial position), as well as output parameters that provide a reliable image of the behavior of the tested anchor bolt (displacement and actual axial force). Based on the adopted parameters, dimensioning, construction and production of technical drawings are carried out. Modern CAD CAE CAM systems that include 3D modeling and reproduction of prototypes from model materials will be used for rapid prototyping, and eco-friendly materials, processed using modern CNC technologies, will be used for the operational prototype of the device. The model's functionality was tested in laboratory conditions. Applying methods for risk analysis and management allows us to improve design, increase safety and reliability, as well as measurement accuracy.*
Keywords*: RISK MANAGEMENT, "CAUSE-EFFECT", FMEA, PROTOTYPE MAKING, ANCHOR BOLT, FIELD TESTING*

1. Introduction

Anchor bolts are mechanical elements that provide a solid and reliable connection between the installation object and its foundations, and they function on the mechanical principle of expansion using a taper ie. wedge effect [1]. Anchor bolts are often used in building and mechanical structures and are used to fasten them to the base, which is usually made of reinforced concrete, stone or some other building material. they are used in conditions where there are high loads, for example in structural connections when connecting metal structures to the foundation, as in the case of bridges, towers and buildings, as well as for the installation of heavy equipment such as various machines, traffic signals, ventilation, cooling and heating systems, etc. In these conditions, in addition to normal working loads, they must withstand wind blows and seismic forces. They are also used in lightly loaded conditions such as fences, handrails and light objects. They are also used in factories to prevent machines from moving during their operation. For testing anchor bolts, the most interest exists when installing horizontal fans on tunnel ceilings. For this type of construction work, due to the high risk, it is mandatory to carry out this type of examination in order to obtain a use permit. With already existing devices for this type of testing, there are a number of obstacles that must be overcomed. If working on the ceiling of the tunnel, the height at which the device must be placed is high. Support is also needed, as well as a larger number of operators for setting up and positioning the device, as well as connecting the information measurment system and performing data acquisition. These tests are difficult due to working in a tunnel where adequate lighting does not exist, with extreme ambient conditions, so the application of this device will be mostly used in tunnels.

The basic factor that ensures the correct selection and use of an anchor bolt is the working load, that is, the anchor bolt must be dimensioned to respond to the forces that will act on it in working conditions. In addition, the influence of the environment is a very important factor, so in some cases, screws made of corrosion-resistant materials must be chosen. The most important factor is the installation itself, that is, the mounting of the anchor bolts, because it ensures that the structure we attach is adequately positioned and that the anchor bolts perform their function. That is why it is very important to perform an adequate test of the anchor bolts after their installation, because this is the only way we can be sure that they will perform their critical role [2-3].

For the safe and proper functioning of the anchor bolt testing device during prototype development, it is extremely important to know the technological risk, which includes the assessment of several types of risk such as: problems with management, with the technology used, defined safety measures, the use of environmentally friendly materials, and that the new innovative product is compatible with existing systems and processes, as well as with European safety and communication protocols. As for the testing of anchor bolts, there is no standardized method according to the ISO standard, there is a Recommendation of the European Organization for technical approvals, so that the specific innovative product, through risk analysis, will be in compliance with this document on technological risk.

2. Device development

Our initial research is related to the needs of the market and the analysis of existing solutions in terms of user satisfaction, according to the criteria of functionality, efficiency of testing, as well as the required financial investment. Existing recommendations from relevant regulatory organizations were also taken into account. Guided by these criteria, an original solution was given, which also takes into account the latest technological innovations implemented in the information measurement system.

It is necessary that the material to be used meets ecological standards, and due to the very specificity of the testing process where the device needs to be placed at a great height by the operator, the lower weight of the device, as well as corrosion resistance, are of extreme importance. For these reasons, a specific alloy will be used that meets the required mechanical properties for all the mentioned criteria. Aluminum alloy AA7075 was adopted, which is widely used in the aviation industry.

When it comes to the physical principles according to which the device functions, hydraulic principles are applied for loading and measurement, and the specificity of the system is reflected in the existence of a positive feedback loop. The initial geometry was optimized using numerical simulations based on the principle of the finite element method, with the application of advanced approaches such as topology optimization and the Box Wilson method. During construction, care was taken to ensure that the process takes place with a low coefficient of friction, which affected ease of use and measurement accuracy. The product is also ergonomically adapted to the operator. The acceptance and positioning components are designed to provide uniaxial tension as well as an extremely important part of the test to ensure the distribution of the reaction force outside the domain of the stress state in the base on which the anchor bolt is placed. This is especially difficult to do when installing on concave and convex surfaces.

This conceptual solution includes three supports for adhering to the base without the influence of other force components on the axial force, which was tested in laboratory conditions, where calibration and test measurements were performed for a controlled group of anchor bolts. In this way, feedback is obtained with

information that allows us to improve the product, which will make it easier for the product to meet our set requirements.

3. Prototype manufacturing and validation

After idea validation and prototype optimization, the product moves into a more formal design and engineering phase. This includes detailed technical drawings, technical documentation and the creation of a final prototype that is closer to the design and function of the operating device. It includes all the insights gained in the earlier stages.

Prototyping of the device from model materials was carried out through three iterations of geometry optimization, where Fig. 1 shows the CAD model of the first iteration [4].

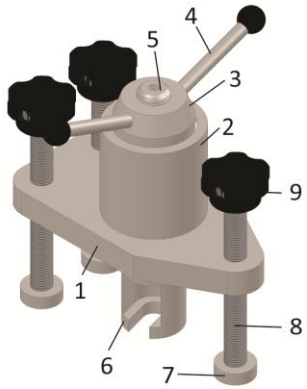


Fig. 1 *Initial model of the device for testing anchor bolts (1 - Support plate; 2 - Hydraulic cylinder; 3 - Nut; 4 - Lever; 5 - Threaded spindle; 6 - Claw; 7 - Pad; 8 - Support; 9 - Knob)*

Based on the adopted solution, an operational prototype was made from metal using AA7075-T651 alloy, 20CrMo5 steel, stainless steel 304, stainless steel 316 and ABS thermoplastic. The device consists of 43 components (Fig. 2).



Fig. 2 *Manufactured components of the device prototype*

The final prototype was tested in laboratory conditions. Functionality testing of all components of the manufactured device was performed, as well as informational measurement systems for measuring axial force and displacement. A demonstration of technical feasibility, parameterization and calibration of the measurement system was performed.

An M8 anchor bolt, which was placed in a concrete slab with a thickness of 55 mm, was tested. The test results of the installed anchor bolt are shown in Fig. 3.

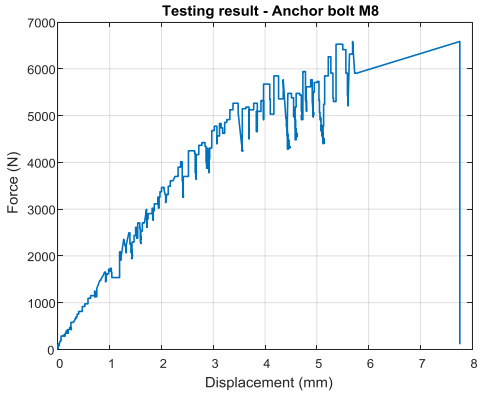


Fig. 3 *Measurement results diagram Axial force - Displacement*

4. Standards

On-site field testing is an important element of the inspection of the fastening of structures using anchor bolts.

For this type of on-site field testing, it is extremely important that the testing is done correctly, as otherwise this assessment could threaten the stability of the mechanichal structure, and therefore human lives and lead to significant economic losses.

There is no universal standard for on-site field testing in Europe. Existing international and national standards that are current have been investigated. The standards ETAG 029 Annex B.3.2 [5], ETAG 020 Annex B [6], ETAG 014 Annex D [7], BS 8539:2012 Annex B.2.3.2 [8] are used for field testing. and ASTM E488M [9]. During the development of the prototype, these standards represented the starting point from which the initial solution was formed. Also, standards concerning the general principles of designing safe machines ISO 12100:2010 [10] and safety requirements for electrical equipment and machines EN 60204-1:2018 [11] were considered. In addition to them, the standards concerning the information measurement system and the process variables that it monitors were also considered. They are represented by the standard ISO7500-1:2018 [12], which refers to the verification of force measuring systems in test machines, and ISO 376:2011 [13], which defines the calibration and accuracy classes of force sensors. Standard ISO 9513:2012 [14], in this case, refers to the measurement of displacement and it defines the calibration and classification of devices for measuring displacement or deformation in uniaxial tests. The diagram of interconnected standards is shown in Fig. 4.

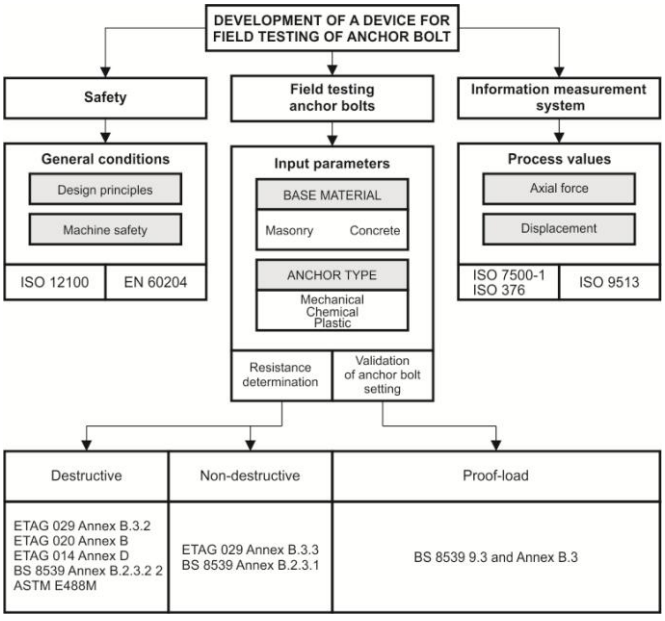


Fig. 4 *Prototype development in a standards environment*

5. Risk management

Risk assessment includes the basic elements of the risk management process that are defined in ISO 31000:2018 [15]. Risk assessment is a key element of the risk management process and gives decision makers and responsible parties a better understanding of the risks that may affect the achievement of objectives. Risk identification is the process of finding, recognizing and recording risks. Risk analysis refers to developing an understanding of risk, while risk assessment involves comparing estimated risk levels with risk criteria.

The risk assessment of the process approach of the innovative development of a prototype device for testing anchor bolts includes the above actions, through a Cause-Effect analysis. A Cause-Effect diagram can be drawn when there is a need to: identify possible causes of a problem, structure a brainstorming session, and sort ideas into useful categories. This analysis was used to identify the risks to the successful realization of the prototype development, which were identified as possible causes and are shown in Fig. 5.

- The construction of the device is a very influential category, which was analyzed using a number of interrelated factors: stiffness of the construction; mass of the device; ergonomics; functionality; device geometry optimizations; maintenance etc.
- The choice of manufacturing technology significantly affects the possibility of obtaining complex geometric shapes and the quality of processed surfaces. Among the large number of influential factors, the application of machining using modern CNC machines stands out.
- The material is a category where, on the basis of mechanical properties, chemical composition, specific weight, ergonomics, ecological footprint, alloy AA7075-T651 is adopted as the basic material.
- Since the improvement of the system was carried out through the application of ergonomics and non-contact data transmission, with the aim of measuring axial force and displacement, the influence of the human factor is relatively smaller. The response is inadequate positioning and inadequate measurement.
- The information measurement system uses sensors with an acceptable measurement range, which are easily calibrated and have high measurement reliability.

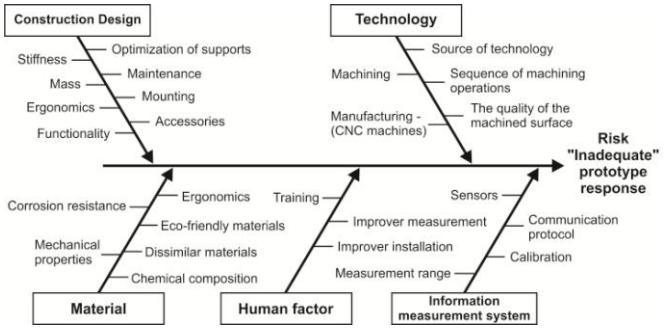


Fig. 5 *"Cause-Effect" diagram in the development of the device for the field testing of anchor bolts*

Analysis of errors and their consequences through the application of the FMEA method is a technique used to identify ways in which components, systems or processes can fail to fulfill their intended purpose. FMEA identifies all possible errors of different parts of the system, the effects that these errors can have on the system, failure mechanisms and how to avoid errors, and/or mitigate the effects of errors (failures) in the system, taking into account the ISO 31000:2018 family of standards, which defines a set of principles and guidelines for the design, implementation of the risk management framework and provides recommendations for the application of the risk management process.

For the remaining factors of the risk assessment of the development of the device for field testing of anchor bolts, the risk analysis that includes: Consequences, Probability and Level of risk as well as Risk of evaluation the used FMEA method is normally recommended for these activities. With this method, appropriate risk factors are determined, based on which the risk priority index is obtained and compared with the determined intervention limit. The optimal choice of the topology of geometric and technological parameters ensures that the risk priority index is lower than the intervention limit. In order to reduce the risk in the development of a prototype device for field testing of anchor bolts, the cycle of steps given in Fig. 6 is proposed.

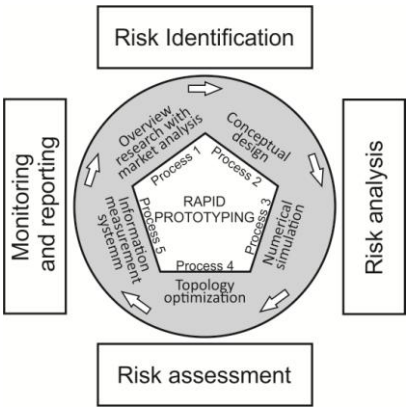


Fig. 6 *The cycle of risk in the development of a device prototype*

6. Conclusion

The process of developing a prototype device for field testing of anchor bolts is accompanied by risk due to the complex influence of several successive parameters on the form, functionality, ergonomics, measurement uncertainty and applicability in various test positions of the installed anchor bolts.

A model is proposed to consider prototype development across two levels of environment. The first level of the environment defines the specific requirements of designing, constructing and 3D prototyping from model materials (Rapid Prototyping). The second level of the environment defines the necessary quality management standards that ensure a quality and manufactured device, with an implemented measuring system and validation of the concept through laboratory testing and confirmation of the obtained results.

By analyzing the standards and applying the "Cause-Effect" and FMEA methods, which include a large number of influential parameters, potential failure mechanisms were identified, which enabled the iterative development of the device prototype. The result is the successful development of the device through improved design, increased safety and reliability, as well as greater measurement accuracy and easier data acquisition.

Acknowledgement

This paper is the result of project POC-013-24 received from the Innovation Fund of Montenegro and the University of Montenegro - Faculty of Mechanical Engineering as part of the Proof of Concept Program.

Literature

[1] R. Mallee, W. Fuchs, R. Eligehausen, Design of Fastenings for Use in Concrete - the CEN/TS 1992-4 Provisions. Fifth Edition, ISBN: 978-3-433-03044-8, (2013)

[2] F. Delhomme, G. Debicki, Z. Chaib, Experimental behaviour of anchor bolts under pullout and relaxation tests. Constr Build Mater, doi:10.1016/j.conbuildmat.2009.08.038, (2009)

[3] Hariyadi, S. Munemoto, Y. Sonoda, Experimental analysis of anchor bolt in concrete under the pull-out loading. Vol. 171, pp.

926-933, doi.org/10.1016/j.proeng.2017.01.391, (2017)

[4] N. Šibalić, M. Mumović, Rapid Prototyping of a Device for Testing the Connection of Reinforced Concrete and Anchor Bolt. ICPES 2025, Nis, Serbia, 18-19th September, doi: 10.46793/ICP
ES25.325S, (2025)

[5] ETAG 029 Annex B.3.2, Guideline for european technical approval of metal injection anchors for use in masonry, Edition April (2013)

[6] ETAG 020 Annex B, Guideline for european technical approval of plastic anchors for multiple use in concrete and masonry for non-structural applications, amended version March (2012)

[7] ETAG 014 Annex D, Guideline for european technical approval of plastic anchors for fixing of external thermal insulation composite systems with rendering, amended February (2011)

[8] BS 8539:2012 Annex B.2.3.2, Code of practice for the selection and installation of post-installed anchors in concrete and masonry (2012)

[9] ASTM E488/E488M-22, Standard Test Methods for Strength of Anchors in Concrete Elements (2022)

[10]ISO 12100:2010, Safety of machinery - General principles for design - Risk assessment and risk reduction (2010)

[11]EN 60204-1:2018, Safety of machinery - Electrical equipment of machines - Part 1: General requirements (2018)

[12]ISO 7500:2018, Metallic materials - Calibration and verification of static uniaxial testing machines - Part 1: Tension/compression testing machines - Calibration and verification of the force-measuring system (2018)

[13]ISO 376:2011, Metallic materials - Calibration of force-proving instruments used for the verification of uniaxial testing machines (2011)

[14]ISO 9513:2012, Metallic materials - Calibration of extensometer systems used in uniaxial testing (2012)

[15]ISO 31000:2018, Risk management - Guidelines (2018)

Segmental exergy analysis of a complex 210 MW three cylinder steam turbine

Mrzljak Vedran[1], Poljak Igor[2], Glučina Matko[1], Anđelić Nikola[1]
[1]Faculty of Engineering, University of Rijeka, Vukovarska 58, 51000 Rijeka, Croatia
[2]Department of maritime sciences, University of Zadar, Mihovila Pavlinovića 1, 23000 Zadar, Croatia
E-mail: vedran.mrzljak@riteh.uniri.hr, ipoljak1@unizd.hr, mglucina@riteh.uniri.hr, nikola.andjelic@riteh.uniri.hr

Abstract: *This paper presents exergy analysis results of a complex three cylinder steam turbine with nominal power 210 MW. The analysis is performed for each cylinder, cylinder part and whole turbine as well as for each segment of each turbine cylinder. In the observed turbine, Low Pressure Cylinder (LPC) has the highest exergy destruction (8668.15 kW) and the lowest exergy efficiency (87.19%), while Intermediate Pressure Cylinder (IPC) has the highest exergy efficiency (92.15%) of all cylinders. Exergy efficiency is the highest for each segment at each cylinder entrance and continuously decreases for all segments during steam expansion through each cylinder. In each cylinder, a segment which is the lowest influenced by the ambient temperature change is inlet segment - as steam expands through each cylinder, further segments became more and more influenced by the ambient temperature change. Steam re-heating process has a very beneficial influence on the exergy efficiency of the first two IPC segments (Seg. 3 and Seg. 4) which have the highest exergy efficiency in comparison to all other segments.*

KEYWORDS: EXERGY ANALYSIS, STEAM TURBINE, TURBINE CYLINDERS, CYLINDER SEGMENTS, THE AMBIENT TEMPERATURE CHANGE

1. Introduction

In the world electricity production at the moment, steam turbines take the dominant share [1, 2]. Steam turbines are inevitable components of many power plants and systems and they can also be used for various other purposes, not for the electricity production only [3, 4].

In relation to produced mechanical power, steam turbines can be generally divided to high power, medium power and low power turbines. High power steam turbines are composed of several cylinders, while medium and low power steam turbines can be composed of several cylinders or of one cylinder only [5]. Each turbine cylinder is usually composed of many turbine stages, while in the exploitation can also be found low power auxiliary steam turbines composed of just one Curtis stage [6].

Steam turbine cylinders can be single flow or dual flow cylinders, while dual flow cylinders can be symmetrical and dissymmetrical. In single flow turbine cylinder operating fluid expands in one direction only, while in the dual flow cylinder (regardless of the fact is it symmetrical or dissymmetrical) operating fluid simultaneously expands in two directions [7].

In this paper is performed exergy analysis of a complex three cylinder steam turbine which nominal power is 210 MW. Observed turbine is composed of two single flow and one dual flow symmetrical cylinder. Exergy analysis is performed not only for each cylinder, cylinder part and whole turbine, it is also performed for each segment of each turbine cylinder. It is interesting that exergy analysis results related to all segments of each cylinder show various additional information which cannot be obtained if the cylinders are observed as individual components, without their further division.

2. Description and characteristics of the analyzed steam turbine, turbine cylinders and segments

Steam turbine analyzed in this paper from the exergy viewpoint is composed of three cylinders connected to the same shaft: High Pressure Cylinder (HPC), Intermediate Pressure Cylinder (IPC) and Low Pressure Cylinder (LPC), Fig. 1. It should be highlighted that LPC is composed of two parts –left part (LPC-L) and right part (LPC-R). LPC is a dual flow symmetrical cylinder what means that both LPC parts (left and right) have the same operating parameters and performance (what will clearly be seen in the obtained exergy analysis results). HPC and IPC are single flow cylinders, Fig. 1. All cylinders are used for the Electric Generator (EG) drive.

Exergy analysis performed in this paper also contains a calculation of destruction and efficiency related to each segment of each turbine cylinder. Cylinder segments are defined between the cylinder inlet (input), outlet (output) and steam extractions.

HPC has two steam extractions – both of them are used for delivering certain steam mass flow rate to the components of high pressure feedwater heating system. HPC has two segments (Seg. 1 and Seg. 2) defined between HPC inlet and first HPC extraction (operating point 2, Fig. 1) and between the first HPC extraction and HPC outlet. Second HPC extraction is placed at the HPC outlet therefore, second HPC extraction (operating point 3, Fig. 1) did not define one more segment.

IPC has four steam extractions. The first IPC extraction (operating point 6, Fig. 1) delivers certain steam mass flow rate to the components of the high pressure feedwater heating system, second IPC extraction (operating point 7, Fig. 1) delivers certain steam mass flow rate to the deaerator, while third and fourth IPC extractions (operating points 8 and 9, Fig. 1) deliver a certain steam mass flow rate to the components of low pressure condensate heating system. IPC has four segments defined between IPC inlet and first IPC extraction (Seg. 3), between first and second IPC extraction (Seg. 4), between second and third IPC extraction (Seg. 5) and between third IPC extraction and IPC outlet (Seg. 6). As in the case of HPC, the last IPC extraction (operating point 9, Fig. 1) is placed at the IPC outlet and did not define one more segment.

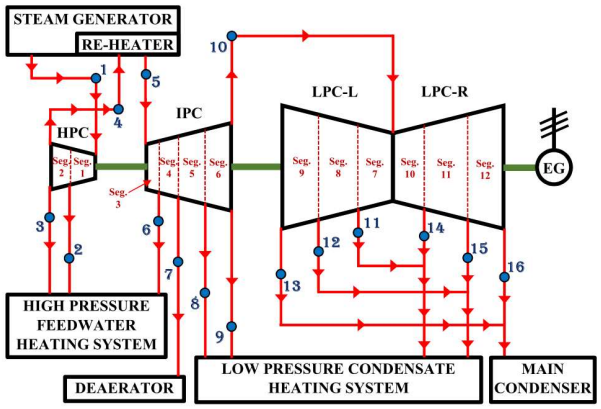


Fig. 1. *General scheme of the analyzed 210 MW steam turbine with marked segments and operating points required for the segmental exergy analysis*

LPC is a dual flow cylinder which means that steam enters in the middle of the cylinder (operating point 10, Fig. 1) and simultaneously expands through both LPC parts (one half of the steam mass flow rate at the LPC inlet expands through LPC-L and other half expands through LPC-R). Each LPC part has two steam extractions – all LPC extractions deliver a certain steam mass flow rate to the components of low pressure condensate heating system. LPC is also a symmetrical cylinder because LPC-L and LPC-R have identical steam operating parameters at the inlet, in the extractions and at the outlet (steam temperature, pressure and mass flow rate are identical in operating points 11 and 14, in operating points 12 and 15 and in operating points 13 and 16, Fig. 1). Each LPC part has three segments defined between LPC inlet and the first extraction, between first and

second extraction and between second extraction and LPC part outlet. These segments are marked from Seg. 7 to Seg. 9 for the LPC-L and from Seg. 10 to Seg. 12 for the LPC-R. Steam which expands until the outlet of each LPC part (operating points 13 and 16, Fig. 1) is delivered to the main condenser for condensation.

Steam expansion process through all the cylinders of the observed steam turbine in Specific enthalpy/Specific entropy diagram is presented in Fig. 2.

In any kind of exergy analysis (related to the turbine cylinders, cylinder parts, segments and whole turbine) are used data of the real (polytropic) steam expansion process which are measured in the plant during the exploitation and which involves all the losses. Losses which occur during the expansion process are defined with an increase in steam specific entropy, Fig. 2.

In Fig. 2 is clearly seen steam re-heating process (between operating points 4 and 5) which increases steam temperature before its expansion in the IPC. Steam re-heater in the observed plant is mounted inside steam generator and it has a very beneficial influence on segments exergy parameters, what will be shown in this analysis. It should be highlighted that operating points presented in Fig. 2 are in relation to the operating points marking from Fig. 1.

As the LPC is a symmetrical dual flow cylinder, the steam expansion process is identical in both LPC parts (LPC-L and LPC-R), what is clearly seen in Fig. 2. Only the last operating points of the observed turbine (operating points 13 and 16, Fig. 1 and Fig. 2) are under the saturation line (wet steam) which ensure that such steam can be transferred to the condensate in main steam condenser. All other operating points consist superheated steam.

Fig. 2 is obtained from known steam operating parameters, presented in Table 4 by using NIST-Refprop 9.0 software [8].

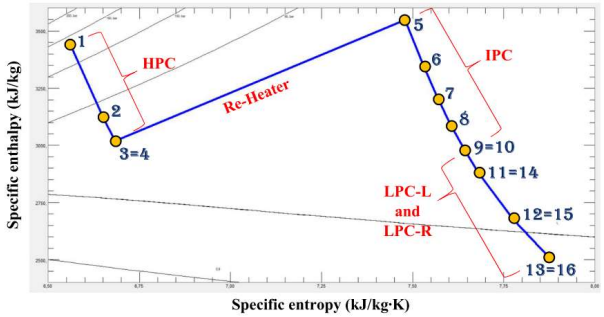


Fig. 2. *Specific enthalpy/Specific entropy (h/s) diagram of the steam expansion process throughout steam turbine and each cylinder*

3. Exergy analysis equations

Exergy analysis of any system or a component is based on the second law of thermodynamics which considers the ambient conditions in which observed system or a component operates [9].

3.1. General equations and balances

In the exergy analysis of any system or a component, general equations and balances must always be satisfied. The general exergy balance equation at steady state is defined as [10]:

$$\dot{X}_{\mathrm{H}} - P = \sum \dot{E}x_{\mathrm{OUT}} - \sum \dot{E}x_{\mathrm{IN}} + \dot{E}x_{\mathrm{D}}, \quad (1)$$

where P is mechanical power, index IN denotes input (inlet), index OUT denotes output (outlet) and index D denotes exergy destruction. $\dot{E}x$ is a fluid total exergy flow defined by the equation [11]:

$$\dot{E}x = \dot{m} \cdot \varepsilon, \quad (2)$$

where $\dot{m}$ is a fluid mass flow rate and ε is fluid specific exergy which can be defined by an equation [12, 13]:

$$\varepsilon = (h - h_0) - T_0 \cdot (s - s_0), \quad (3)$$

where h is fluid specific enthalpy, s is fluid specific entropy, T is a temperature and index 0 is related to the ambient state. The last undefined variable from Eq. 1 is an exergy transfer by heat at the temperature T ($\dot{X}_{\mathrm{H}}$) which is defined as [14]:

$$\dot{X}_{\mathrm{H}} = \sum (1 - \frac{T_0}{T}) \cdot \dot{Q}, \quad (4)$$

where $\dot{Q}$ is an energy transfer by heat.

3.2. Equations for the exergy analysis of turbine cylinders, cylinder parts, segments and whole turbine

All equations required for the exergy analysis of turbine cylinders, cylinder parts, segments and whole turbine are defined according to the recommendations and guidelines from the literature [15, 16]. Indexes in all equations presented in this subsection are related to the operating points marked in Fig. 1 and Fig. 2. In Table 1 are presented equations for the mechanical power calculation, while in Table 2 and Table 3 are presented equations for exergy input (inlet) and exergy output (outlet) calculation of each observed turbine cylinder, cylinder part, segment and whole turbine.

Table 1. *Equations for the mechanical power calculation*

Component	Mechanical power	Eq.
HPC	$P_{\mathrm{HPC}} = \dot{m}_1 \cdot (h_1 - h_2) + (\dot{m}_1 - \dot{m}_2) \cdot (h_2 - h_3)$	(5)
IPC	$P_{\mathrm{IPC}} = \dot{m}_5 \cdot (h_5 - h_6) + (\dot{m}_5 - \dot{m}_6) \cdot (h_6 - h_7) + (\dot{m}_5 - \dot{m}_6 - \dot{m}_7) \cdot (h_7 - h_8) + (\dot{m}_5 - \dot{m}_6 - \dot{m}_7 - \dot{m}_8) \cdot (h_8 - h_9)$	(6)
LPC-L	$P_{\mathrm{LPC-L}} = \frac{\dot{m}_{10}}{2} \cdot (h_{10} - h_{11}) + (\frac{\dot{m}_{10}}{2} - \dot{m}_{11}) \cdot (h_{11} - h_{12}) + (\frac{\dot{m}_{10}}{2} - \dot{m}_{11} - \dot{m}_{12}) \cdot (h_{12} - h_{13})$	(7)
LPC-R	$P_{\mathrm{LPC-R}} = \frac{\dot{m}_{10}}{2} \cdot (h_{10} - h_{14}) + (\frac{\dot{m}_{10}}{2} - \dot{m}_{14}) \cdot (h_{14} - h_{15}) + (\frac{\dot{m}_{10}}{2} - \dot{m}_{14} - \dot{m}_{15}) \cdot (h_{15} - h_{16})$	(8)
whole LPC	$P_{\mathrm{LPC}} = P_{\mathrm{LPC-L}} + P_{\mathrm{LPC-R}}$	(9)
WT	$P_{\mathrm{WT}} = P_{\mathrm{HPC}} + P_{\mathrm{IPC}} + P_{\mathrm{LPC}}$	(10)
Seg. 1	$P_{\mathrm{Seg.1}} = \dot{m}_1 \cdot (h_1 - h_2)$	(11)
Seg. 2	$P_{\mathrm{Seg.2}} = (\dot{m}_1 - \dot{m}_2) \cdot (h_2 - h_3)$	(12)
Seg. 3	$P_{\mathrm{Seg.3}} = \dot{m}_5 \cdot (h_5 - h_6)$	(13)
Seg. 4	$P_{\mathrm{Seg.4}} = (\dot{m}_5 - \dot{m}_6) \cdot (h_6 - h_7)$	(14)
Seg. 5	$P_{\mathrm{Seg.5}} = (\dot{m}_5 - \dot{m}_6 - \dot{m}_7) \cdot (h_7 - h_8)$	(15)
Seg. 6	$P_{\mathrm{Seg.6}} = (\dot{m}_5 - \dot{m}_6 - \dot{m}_7 - \dot{m}_8) \cdot (h_8 - h_9)$	(16)
Seg. 7	$P_{\mathrm{Seg.7}} = \frac{\dot{m}_{10}}{2} \cdot (h_{10} - h_{11})$	(17)
Seg. 8	$P_{\mathrm{Seg.8}} = (\frac{\dot{m}_{10}}{2} - \dot{m}_{11}) \cdot (h_{11} - h_{12})$	(18)
Seg. 9	$P_{\mathrm{Seg.9}} = (\frac{\dot{m}_{10}}{2} - \dot{m}_{11} - \dot{m}_{12}) \cdot (h_{12} - h_{13})$	(19)
Seg. 10	$P_{\mathrm{Seg.10}} = \frac{\dot{m}_{10}}{2} \cdot (h_{10} - h_{14})$	(20)
Seg. 11	$P_{\mathrm{Seg.11}} = (\frac{\dot{m}_{10}}{2} - \dot{m}_{14}) \cdot (h_{14} - h_{15})$	(21)
Seg. 12	$P_{\mathrm{Seg.12}} = (\frac{\dot{m}_{10}}{2} - \dot{m}_{14} - \dot{m}_{15}) \cdot (h_{15} - h_{16})$	(22)

Table 2. *Equations for the exergy input (inlet) calculation*

Component	Exergy input (inlet)	Eq.
HPC	$\dot{E}x_{\mathrm{HPC,IN}} = \dot{m}_1 \cdot \varepsilon_1$	(23)
IPC	$\dot{E}x_{\mathrm{IPC,IN}} = \dot{m}_5 \cdot \varepsilon_5$	(24)
LPC-L	$\dot{E}x_{\mathrm{LPC-L,IN}} = \frac{\dot{m}_{10}}{2} \cdot \varepsilon_{10}$	(25)
LPC-R	$\dot{E}x_{\mathrm{LPC-R,IN}} = \frac{\dot{m}_{10}}{2} \cdot \varepsilon_{10}$	(26)
whole LPC	$\dot{E}x_{\mathrm{LPC,IN}} = \dot{m}_{10} \cdot \varepsilon_{10}$	(27)
WT	$\dot{E}x_{\mathrm{WT,IN}} = \dot{E}x_{\mathrm{HPC,IN}} + \dot{E}x_{\mathrm{IPC,IN}} + \dot{E}x_{\mathrm{LPC,IN}}$	(28)
Seg. 1	$\dot{E}x_{\mathrm{Seg.1,IN}} = \dot{m}_1 \cdot \varepsilon_1$	(29)
Seg. 2	$\dot{E}x_{\mathrm{Seg.2,IN}} = (\dot{m}_1 - \dot{m}_2) \cdot \varepsilon_2$	(30)
Seg. 3	$\dot{E}x_{\mathrm{Seg.3,IN}} = \dot{m}_5 \cdot \varepsilon_5$	(31)
Seg. 4	$\dot{E}x_{\mathrm{Seg.4,IN}} = (\dot{m}_5 - \dot{m}_6) \cdot \varepsilon_6$	(32)
Seg. 5	$\dot{E}x_{\mathrm{Seg.5,IN}} = (\dot{m}_5 - \dot{m}_6 - \dot{m}_7) \cdot \varepsilon_7$	(33)
Seg. 6	$\dot{E}x_{\mathrm{Seg.6,IN}} = (\dot{m}_5 - \dot{m}_6 - \dot{m}_7 - \dot{m}_8) \cdot \varepsilon_8$	(34)
Seg. 7	$\dot{E}x_{\mathrm{Seg.7,IN}} = \frac{\dot{m}_{10}}{2} \cdot \varepsilon_{10}$	(35)
Seg. 8	$\dot{E}x_{\mathrm{Seg.8,IN}} = (\frac{\dot{m}_{10}}{2} - \dot{m}_{11}) \cdot \varepsilon_{11}$	(36)
Seg. 9	$\dot{E}x_{\mathrm{Seg.9,IN}} = (\frac{\dot{m}_{10}}{2} - \dot{m}_{11} - \dot{m}_{12}) \cdot \varepsilon_{12}$	(37)
Seg. 10	$\dot{E}x_{\mathrm{Seg.10,IN}} = \frac{\dot{m}_{10}}{2} \cdot \varepsilon_{10}$	(38)
Seg. 11	$\dot{E}x_{\mathrm{Seg.11,IN}} = (\frac{\dot{m}_{10}}{2} - \dot{m}_{14}) \cdot \varepsilon_{14}$	(39)
Seg. 12	$\dot{E}x_{\mathrm{Seg.12,IN}} = (\frac{\dot{m}_{10}}{2} - \dot{m}_{14} - \dot{m}_{15}) \cdot \varepsilon_{15}$	(40)

Table 3. Equations for the exergy output (outlet) calculation

Component	Exergy output (outlet)	Eq.
HPC	$\dot{E}x_{\mathrm{HPC,OUT}} = \dot{m}_2 \cdot \varepsilon_2 + \dot{m}_3 \cdot \varepsilon_3 + \dot{m}_4 \cdot \varepsilon_4 + P_{\mathrm{HPC}}$	(41)
IPC	$\dot{E}x_{\mathrm{IPC,OUT}} = \dot{m}_6 \cdot \varepsilon_6 + \dot{m}_7 \cdot \varepsilon_7 + \dot{m}_8 \cdot \varepsilon_8 + \dot{m}_9 \cdot \varepsilon_9 + +\dot{m}_{10} \cdot \varepsilon_{10} + P_{\mathrm{IPC}}$	(42)
LPC-L	$\dot{E}x_{\mathrm{LPC-L,OUT}} = \dot{m}_{11} \cdot \varepsilon_{11} + \dot{m}_{12} \cdot \varepsilon_{12} + \dot{m}_{13} \cdot \varepsilon_{13} + P_{\mathrm{LPC-L}}$	(43)
LPC-R	$\dot{E}x_{\mathrm{LPC-R,OUT}} = \dot{m}_{14} \cdot \varepsilon_{14} + \dot{m}_{15} \cdot \varepsilon_{15} + \dot{m}_{16} \cdot \varepsilon_{16} + P_{\mathrm{LPC-R}}$	(44)
whole LPC	$\dot{E}x_{\mathrm{LPC,OUT}} = \dot{E}x_{\mathrm{LPC-L,OUT}} + \dot{E}x_{\mathrm{LPC-R,OUT}}$	(45)
WT	$\dot{E}x_{\mathrm{WT,OUT}} = \dot{E}x_{\mathrm{HPC,OUT}} + \dot{E}x_{\mathrm{IPC,OUT}} + \dot{E}x_{\mathrm{LPC,OUT}}$	(46)
Seg. 1	$\dot{E}x_{\mathrm{Seg.1,OUT}} = \dot{m}_2 \cdot \varepsilon_2 + (\dot{m}_1 - \dot{m}_2) \cdot \varepsilon_2 + P_{\mathrm{Seg.1}}$	(47)
Seg. 2	$\dot{E}x_{\mathrm{Seg.2,OUT}} = \dot{m}_3 \cdot \varepsilon_3 + \dot{m}_4 \cdot \varepsilon_4 + P_{\mathrm{Seg.2}}$	(48)
Seg. 3	$\dot{E}x_{\mathrm{Seg.3,OUT}} = \dot{m}_6 \cdot \varepsilon_6 + (\dot{m}_5 - \dot{m}_6) \cdot \varepsilon_6 + P_{\mathrm{Seg.3}}$	(49)
Seg. 4	$\dot{E}x_{\mathrm{Seg.4,OUT}} = \dot{m}_7 \cdot \varepsilon_7 + (\dot{m}_5 - \dot{m}_6 - \dot{m}_7) \cdot \varepsilon_7 + P_{\mathrm{Seg.4}}$	(50)
Seg. 5	$\dot{E}x_{\mathrm{Seg.5,OUT}} = \dot{m}_8 \cdot \varepsilon_8 + (\dot{m}_5 - \dot{m}_6 - \dot{m}_7 - \dot{m}_8) \cdot \varepsilon_8 + P_{\mathrm{Seg.5}}$	(51)
Seg. 6	$\dot{E}x_{\mathrm{Seg.6,OUT}} = \dot{m}_9 \cdot \varepsilon_9 + \dot{m}_{10} \cdot \varepsilon_{10} + P_{\mathrm{Seg.6}}$	(52)
Seg. 7	$\dot{E}x_{\mathrm{Seg.7,OUT}} = \dot{m}_{11} \cdot \varepsilon_{11} + (\frac{\dot{m}_{10}}{2} - \dot{m}_{11}) \cdot \varepsilon_{11} + P_{\mathrm{Seg.7}}$	(53)
Seg. 8	$\dot{E}x_{\mathrm{Seg.8,OUT}} = \dot{m}_{12} \cdot \varepsilon_{12} + (\frac{\dot{m}_{10}}{2} - \dot{m}_{11} - \dot{m}_{12}) \cdot \varepsilon_{12} + P_{\mathrm{Seg.8}}$	(54)
Seg. 9	$\dot{E}x_{\mathrm{Seg.9,OUT}} = \dot{m}_{13} \cdot \varepsilon_{13} + P_{\mathrm{Seg.9}}$	(55)
Seg. 10	$\dot{E}x_{\mathrm{Seg.10,OUT}} = \dot{m}_{14} \cdot \varepsilon_{14} + (\frac{\dot{m}_{10}}{2} - \dot{m}_{14}) \cdot \varepsilon_{14} + P_{\mathrm{Seg.10}}$	(56)
Seg. 11	$\dot{E}x_{\mathrm{Seg.11,OUT}} = \dot{m}_{15} \cdot \varepsilon_{15} + (\frac{\dot{m}_{10}}{2} - \dot{m}_{14} - \dot{m}_{15}) \cdot \varepsilon_{15} + P_{\mathrm{Seg.11}}$	(57)
Seg. 12	$\dot{E}x_{\mathrm{Seg.12,OUT}} = \dot{m}_{16} \cdot \varepsilon_{16} + P_{\mathrm{Seg.12}}$	(58)

Exergy destruction is calculated by using an equation:

$$\dot{E}x_{\mathrm{(i),D}} = \dot{E}x_{\mathrm{(i),IN}} - \dot{E}x_{\mathrm{(i),OUT}}, \tag{59}$$

while exergy efficiency is calculated as:

$$\eta_{\mathrm{(i),EX}} = \frac{P_{\mathrm{(i)}}}{\dot{E}x_{\mathrm{(i),IN}} - \dot{E}x_{\mathrm{(i),OUT}} + P_{\mathrm{(i)}}}. \tag{60}$$

In Eq. 59 and Eq. 60 index i is related to each turbine cylinder, cylinder part, segment and whole turbine (all components which equations are presented in Table 1, Table 2 and Table 3).

4. Steam parameters required for the exergy analysis

Table 4. Steam operating parameters for the exergy analysis

O. P. *	Temp. (°C)	Pressure (bar)	Mass flow rate (kg/s)	Specific enthalpy (kJ/kg)	Specific entropy (kJ/kg·K)	Quality **	Specific exergy (kJ/kg) ***
1	537.95	132.00	172.22	3437.4	6.5608	Sh.	1485.90
2	360.44	38.28	7.92	3122.9	6.6503	Sh.	1144.70
3	302.72	23.89	11.37	3019.4	6.6826	Sh.	1031.50
4	302.72	23.89	152.93	3019.4	6.6826	Sh.	1031.50
5	537.95	22.69	152.93	3549.6	7.4791	Sh.	1324.30
6	440.44	11.39	5.94	3348.9	7.5295	Sh.	1108.60
7	368.66	6.53	4.65	3204.1	7.5696	Sh.	951.83
8	309.25	3.96	5.17	3086.2	7.6053	Sh.	823.20
9	253.53	2.37	3.79	2977.1	7.6434	Sh.	702.78
10	253.53	2.37	133.38	2977.1	7.6434	Sh.	702.78
11	202.48	1.42	3.27	2878.4	7.6810	Sh.	592.90
12	95.46	0.40	2.67	2674.8	7.7771	Sh.	360.64
13	47.68	0.11	60.75	2510.0	7.8748	0.9677	166.69
14	202.48	1.42	3.27	2878.4	7.6810	Sh.	592.90
15	95.46	0.40	2.67	2674.8	7.7771	Sh.	360.64
16	47.68	0.11	60.75	2510.0	7.8748	0.9677	166.69

* O. P. = Operating Point (in accordance to Fig. 1 and Fig. 2)
** Sh. = Superheated; 0 = water; 1 = dry saturated steam
*** At the base ambient state

Exergy analysis of the turbine cylinders, cylinder parts, whole turbine as well as each segment of each cylinder is performed by using steam operating parameters from the plant exploitation which are found in [17]. Other steam operating parameters which are not found in the literature but are required in the performed analysis are calculated using NIST-Refprop 9.0 software [8]. All steam operating parameters required in the exergy analysis are presented in Table 4. In this analysis, the base ambient state is defined by the ambient temperature of 25 °C and the ambient pressure of 1 bar.

5. Exergy analysis results and discussion

5.1. Exergy analysis results at the base ambient state

Exergy destruction and exergy efficiency of each cylinder, cylinder part and whole turbine (WT) are presented in Fig. 3.

When considering exergy destruction and exergy efficiency of each observed turbine cylinder, it is clear that LPC has the highest exergy destruction (equal to 8668.15 kW) and the lowest exergy efficiency (equal to 87.19%) of all cylinders. Both LPC parts (LPC-L and LPC-R) have the same exergy destruction and exergy efficiency, what confirms that LPC is a symmetrical dual flow cylinder. IPC has the highest exergy efficiency of all cylinders (equal to 92.15%), regardless of higher exergy destruction in comparison to HPC. Whole steam turbine analyzed in this paper has exergy destruction of 21993.62 kW and exergy efficiency of 90.68%, what is in the range of similar comparable steam turbines [18].

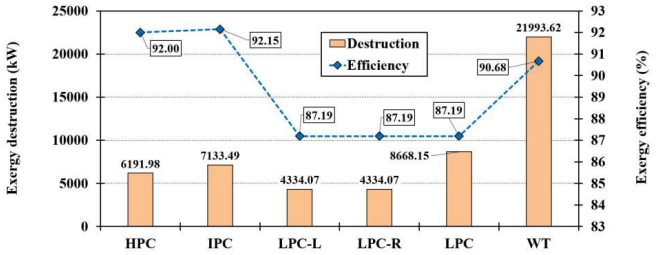


Fig. 3. *Exergy destruction and exergy efficiency of each cylinder, cylinder part and whole observed steam turbine*

Exergy destructions and exergy efficiencies of each observed steam turbine segment are presented in Fig. 4.

The highest exergy destruction, notably higher in comparison to all other segments, can be seen in Seg. 1 at the steam entrance to HPC. Such high exergy destruction of the Seg. 1 can be explained with the highest temperature and pressure of steam at the steam generator outlet (HPC inlet) – these steam parameters are the highest in the entire power plant. However, both HPC segments (Seg. 1 and Seg. 2) have very high exergy efficiencies, higher than 91%, Fig. 4.

Steam re-heating process has a very beneficial influence on the exergy efficiency of the first two IPC segments (Seg. 3 and Seg. 4) which have the highest exergy efficiency in comparison to all other segments. The disadvantage of the steam re-heating process is an increase in the exergy destruction of the first two IPC segments (Seg. 3 and Seg. 4). The exergy efficiency of segments related to each LPC part (LPC-L and LPC-R) decreases from each LPC part inlet until the outlet, Fig. 4. From Fig. 4 for all segments throughout the observed turbine is clearly visible one interesting fact related to their exergy efficiency – exergy efficiency is the highest for each segment at each cylinder entrance (Seg. 1 for the HPC, Seg. 3 for the IPC and Seg. 7 and Seg. 10 for the LPC) and continuously decreases for all segments during steam expansion through each cylinder.

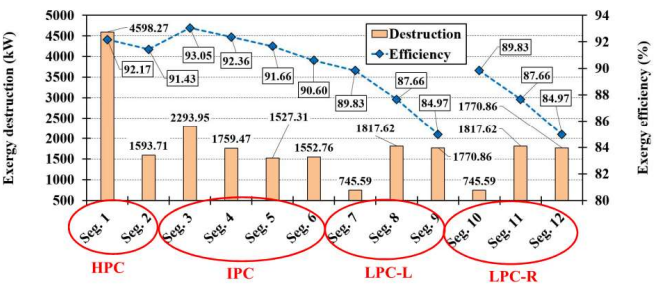


Fig. 4. *Exergy destruction and exergy efficiency of each observed steam turbine segment*

5.2. Exergy analysis results - the ambient temperature change

Due to the limited space, exergy analysis results during the ambient temperature increase from 5 °C to 45 °C are presented for the turbine segments only, Fig. 5.

It should be highlighted that during the ambient temperature increase exergy destruction continuously increases and exergy efficiency continuously decreases for all cylinders, cylinder parts, all segments and whole observed turbine. However, the intensities are not the same for each observed component and segment [19, 20].

According to Fig. 5, segments of the LPC are more influenced by the ambient temperature change in comparison to HPC and IPC segments. It is also interesting that in each cylinder, a segment which is the lowest influenced by the ambient temperature change is inlet segment - as steam expands through each cylinder, further segments became more and more influenced by the ambient temperature change. Steam re-heating process has beneficial impact also on the segments sensitivity to the ambient temperature change – if all the segments are considered, exergy efficiencies of two segments after steam re-heater (Seg. 3 and Seg. 4) are the lowest influenced by the ambient temperature change, Fig. 5.

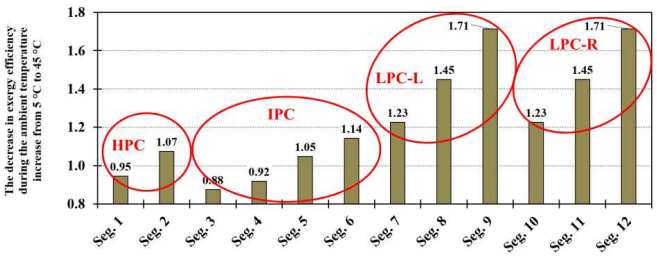


Fig. 5. *Exergy efficiency decrease of each turbine segment during the ambient temperature increase from 5 °C to 45 °C*

6. Conclusions

In this paper is performed exergy analysis of a complex three cylinder steam turbine. Exergy analysis is performed not for each cylinder, cylinder part and whole turbine only, it is also performed for each segment of each turbine cylinder. The most interesting conclusions obtained in the performed analysis are:

- In the observed turbine, LPC has the highest exergy destruction (8668.15 kW) and the lowest exergy efficiency (87.19%), while IPC has the highest exergy efficiency (92.15%) of all cylinders.
- The whole steam turbine has exergy destruction of 21993.62 kW and exergy efficiency of 90.68%, what is in the range of similar comparable steam turbines.
- Exergy efficiency is the highest for each segment at each cylinder entrance and continuously decreases for all segments during steam expansion through each cylinder.
- Segments of the LPC are more influenced by the ambient temperature change in comparison to HPC and IPC segments.
- In each cylinder, a segment which is the lowest influenced by the ambient temperature change is inlet segment - as steam expands through each cylinder, further segments became more and more influenced by the ambient temperature change.
- Steam re-heating process has a very beneficial influence on the exergy efficiency of the first two IPC segments (Seg. 3 and Seg. 4) which have the highest exergy efficiency in comparison to all other segments. Steam re-heating process also has a beneficial impact on the segments sensitivity to the ambient temperature change.

7. Acknowledgment

This work was supported by the University of Rijeka scientific grants uniri-iz-25-6 and uniri-iz-25-220 (Funded by the European Union – NextGenerationEU).

8. References

[1] Leyzerovich, A. S. (2021). Steam turbines for modern fossil-fuel power plants. River Publishers.

[2] Mrzljak, V., Anđelić, N., Lorencin, I., & Sandi Baressi Šegota, S. (2021). The influence of various optimization algorithms on nuclear power plant steam turbine exergy efficiency and destruction. Pomorstvo, 35(1), 69-86. (doi:10.31217/p.35.1.8)

[3] Lorencin, I., Anđelić, N., Mrzljak, V., & Car, Z. (2019). Genetic algorithm approach to design of multi-layer perceptron for combined cycle power plant electrical power output estimation. Energies, 12(22), 4352. (doi:10.3390/en12224352)

[4] Mrzljak, V., Poljak, I., & Prpić-Oršić, J. (2019). Exergy analysis of the main propulsion steam turbine from marine propulsion plant. Brodogradnja: Teorija i praksa brodogradnje i pomorske tehnike, 70(1), 59-77. (doi:10.21278/brod70105)

[5] Kostyuk, A., & Frolov, V. (1988). Steam and gas turbines. Mir Publishers.

[6] Mrzljak, V., Prpić-Oršić, J., & Poljak, I. (2018). Energy power losses and efficiency of low power steam turbine for the main feed water pump drive in the marine steam propulsion system. Pomorski zbornik, 54(1), 37-51. (doi:10.18048/2018.54.03)

[7] Tanuma, T. (Ed.). (2017). Advances in steam turbines for modern power plants. Woodhead Publishing.

[8] Lemmon, E. W., Huber, M. L., & McLinden, M. O. (2010). NIST Standard Reference Database 23, Reference Fluid Thermodynamic and Transport Properties (REFPROP), version 9.0, National Institute of Standards and Technology. R1234yf. fld file dated December, 22, 2010.

[9] Kanoğlu, M., Çengel, Y. A. & Dincer, I. (2012). Efficiency Evaluation of Energy Systems. Springer Briefs in Energy. (doi:10.1007/978-1-4614-2242-6)

[10] Poljak, I., & Mrzljak, V. (2023). Thermodynamic Analysis and Comparison of Two Marine Steam Propulsion Turbines. NAŠE MORE: znanstveni časopis za more i pomorstvo, 70(2), 0-0. (doi:10.17818/NM/2023/2.2)

[11] Mrzljak, V., Poljak, I., Jelić, M., & Prpić-Oršić, J. (2023). Thermodynamic Analysis and Improvement Potential of Helium Closed Cycle Gas Turbine Power Plant at Four Loads. Energies, 16(15), 5589. (doi:10.3390/en16155589)

[12] Koroglu, T., & Sogut, O. S. (2018). Conventional and advanced exergy analyses of a marine steam power plant. Energy, 163, 392-403. (doi:10.1016/j.energy.2018.08.119)

[13] Mrzljak, V., Kudláček, J., Baressi Šegota, S., & Medica-Viola, V. (2021). Energy and Exergy Analysis of Waste Heat Recovery Closed-Cycle Gas Turbine System while Operating with Different Medium. Pomorski zbornik, 60(1), 21-48. (doi:10.18048/2021.60.02)

[14] Mrzljak, V., Jelić, M., Poljak, I., & Medica-Viola, V. (2023). Exergy analysis of supercritical CO2 system for marine diesel engine waste heat recovery application. Pomorski zbornik, 63, 39-62.

[15] Aljundi, I. H. (2009). Energy and exergy analysis of a steam power plant in Jordan. Applied thermal engineering, 29(2-3), 324-328. (doi:10.1016/j.applthermaleng.2008.02.029)

[16] Erdem, H. H., Akkaya, A. V., Cetin, B., Dagdas, A., Sevilgen, S. H., Sahin, B., ... & Atas, S. (2009). Comparative energetic and exergetic performance analyses for coal-fired thermal power plants in Turkey. International Journal of Thermal Sciences, 48(11), 2179-2186. (doi:10.1016/j.ijthermalsci.2009.03.007)

[17] Rajper, M. A., Memon, A. G., & Harijan, K. (2016). Energy and exergy analysis of 210 MW Jamshoro thermal power plant. Mehran University Research Journal of Engineering & Technology, 35(2), 265-274.

[18] Mrzljak, V., Jelić, M., Poljak, I., & Prpić-Oršić, J. (2023). Analysis and Comparison of Main Steam Turbines from Four Different Thermal Power Plants. Pomorstvo, 37(1), 58-74. (doi:10.31217/p.37.1.6)

[19] Kopac, M., & Hilalci, A. (2007). Effect of ambient temperature on the efficiency of the regenerative and reheat Çatalağzı power plant in Turkey. Applied Thermal Engineering, 27(8-9), 1377-1385. (doi:10.1016/j.applthermaleng.2006.10.029)

[20] Mrzljak, V., Prpić-Oršić, J., Poljak, I., & Šegota, S. B. (2020). Exergy analysis of steam condenser at various loads during the ambient temperature change. Machines. Technologies. Materials., 14(1), 12-15.

Thermodynamic analysis of steam turbine and condenser from combined cycle power plant

Mrzljak Vedran[1], Prpić-Oršić Jasna[1], Baressi Šegota Sandi[2], Lorencin Ivan[2]
[1]Faculty of Engineering, University of Rijeka, Vukovarska 58, 51000 Rijeka, Croatia
[2]Faculty of Informatics, Juraj Dobrila University of Pula, 52100 Pula, Croatia
E-mail: vedran.mrzljak@riteh.uniri.hr, jasna.prpic.orsic@riteh.uniri.hr, sandi.baressi.segota@unipu.hr, ivan.lorencin@unipu.hr

Abstract: *Energy and exergy analyses results of steam turbine and steam condenser, which operate in commercial combined cycle power plant are presented in this paper. Energy analysis shows that steam turbine has high energy (isentropic) loss equal to 71.71 MW, and very low energy (isentropic) efficiency of 58.79% only. Simultaneously, steam condenser is an almost perfect component from the energy viewpoint. At the base ambient state, steam turbine has high exergy destruction of 61.80 MW and low exergy efficiency of 62.34%, so both used analyses show that steam turbine operation can and should be notably improved. Steam condenser has an exergy destruction of 17.12 MW and exergy efficiency of 55.17% at the base ambient state, what are acceptable results. Observed steam condenser is much more sensitive to the ambient temperature change than steam turbine. Increase in the ambient temperature from 5 °C to 35 °C decreases steam condenser exergy efficiency for 35.90%, while the same increase in the ambient temperature decreases steam turbine exergy efficiency for 2.39% only.*

KEYWORDS: ENERGY ANALYSIS, EXERGY ANALYSIS, STEAM TURBINE, STEAM CONDENSER, THE AMBIENT TEMPERATURE CHANGE

1. Introduction

Due to the high efficiency, combined cycle power plants are standard and often used power systems in the entire energy sector [1, 2]. These plants offer many benefits, however, its shortcomings must always be considered and cannot be neglected [3].

Combined cycle power plants are composed of two parts – the first part is related to the gas turbine (or more of them) and the second part is related to the steam turbine (or more of them) [4]. Combustion gases from the gas turbine are not released to the atmosphere, they are used in HRSG (Heat Recovery Steam Generator) which produces steam for the steam turbine. Therefore, HRSG represents a connection between gas turbine and steam turbine parts of the combined cycle power plant [5]. As the heat from gas turbine exhaust is effectively used in HRSG (heat utilization for the steam production), efficiency of combined cycle power plant is notably higher in comparison to the individual gas turbine or steam turbine power plant [6, 7].

Steam turbines in combined cycle power plants can be composed of only one or several cylinders, they can be arranged in various configurations, but they always drive an electric generator for the electricity production [8, 9]. Steam after steam turbines in combined cycle power plants have low pressure and temperature and must be delivered to steam condenser for condensation [10, 11].

In this paper are performed energy and exergy analyses of the steam turbine and its corresponding steam condenser from the commercial combined cycle power plant. It is presented did both components show the expected performance. A statement from the available literature that energy analysis should be avoided for any heat exchanger is confirmed in the observed steam condenser. It is investigated and presented which component is more influenced by the ambient temperature change (from the exergy viewpoint).

2. Description and operating characteristics of the analyzed steam turbine and steam condenser

Simplified scheme of the analyzed steam turbine and steam condenser is presented in Fig. 1. Observed steam turbine and steam condenser are constituent components of the combined cycle power plant [12]. However, in this paper both steam turbine and steam condenser will be observed as independent components.

Steam turbine analyzed in this paper gets steam of the highest possible pressure and temperature inside combined cycle power plant from HRSG, operating point 1, Fig. 1. Steam turbine did not possess any steam extraction, so the entire steam mass flow rate delivered to the turbine inlet expands through the turbine until the outlet, operating point 2, Fig. 1. Mechanical power produced in the steam turbine stages is used for the electric generator drive and electricity production.

From the turbine outlet, entire steam mass flow rate is delivered to the steam condenser, Fig. 1. It should be highlighted that at the turbine outlet steam is still superheated (operating point 2, Fig. 1), so the observed steam condenser has two functions: first function is steam cooling and after cooling when the steam is in the two-phase zone (wet steam) the second condenser function is steam condensing. Analyzed steam condenser is counter flow heat exchanger in which steam from the steam turbine transfer heat to the cooling water through the pipe wall (two convections and conduction through the pipe wall). After heat transfer, obtained condensate (operating point 3, Fig. 1) is delivered to the condensate pump. Steam condenser cooling is performed by using cooling water – colder cooling water is delivered to the condenser (operating point 4, Fig. 1) and warmer cooling water, after the heat transfer (operating point 5, Fig. 1) exits steam condenser. Analyzed steam condenser is similar to marine steam condensers which, in some operating regimes (at low plant loads), along with condensation must ensure steam cooling [13].

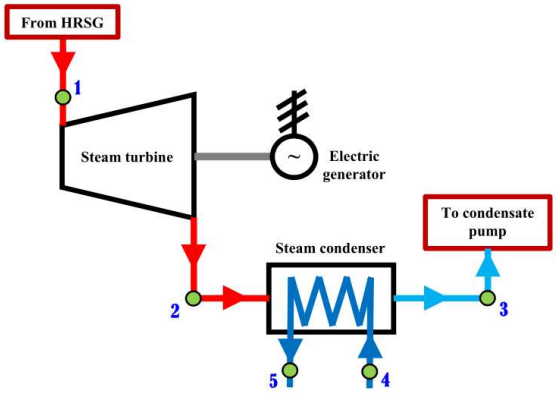


Fig. 1. *General scheme of the analyzed steam turbine and steam condenser along with marked operating points required for the energy (isentropic) and exergy analyses*

Exergy analysis of both steam turbine and steam condenser is performed by using data from the plant exploitation [12]. In the exergy analysis of any plant or a component, only data from the real exploitation conditions are required, there is no need for any comparison with ideal processes.

Energy analysis did not consider parameters of the ambient and therefore, it cannot be performed in a same manner as exergy analysis for any system or a component. For a steam condenser, energy analysis is performed in a standard way (steam condenser is considered as counter flow heat exchanger with two fluid flow streams). Temperatures of both fluid flow streams at the left and right condenser side (at the steam condenser input and output) are presented in Fig. 2 (b).

Considering steam turbine, energy analysis is actually isentropic analysis which shows a comparison between real (polytropic) and ideal (isentropic) steam expansion processes [14]. Regardless of the

observed steam expansion process in the turbine, performed energy (isentropic) analysis did not consider the ambient parameters in any way. Real (polytropic) steam expansion process in turbine (process between operating points 1 and 2, Fig. 2 (a)) is defined by the increase in steam specific entropy. Mentioned increase in steam specific entropy during expansion represents losses which occur in the turbine stages. In comparison to real expansion process, ideal (isentropic) steam expansion process (process between operating points 1 and 2is, Fig. 2 (a)) did not consider any losses in the turbine, so steam specific entropy during ideal expansion remains always the same. For both ideal and real turbine expansion processes, inlet and outlet steam pressures are the same. Steam turbine is a mechanical power producer, so in the ideal (isentropic) expansion process, turbine will produce the highest possible mechanical power. The same steam turbine in the real (polytropic) expansion process will produce lower mechanical power in comparison to the ideal process (because real process involves all losses which occur during expansion) [15].

Operating points of the steam turbine and steam condenser presented in both Fig. 2 parts are consistent with operating points from Fig. 1.

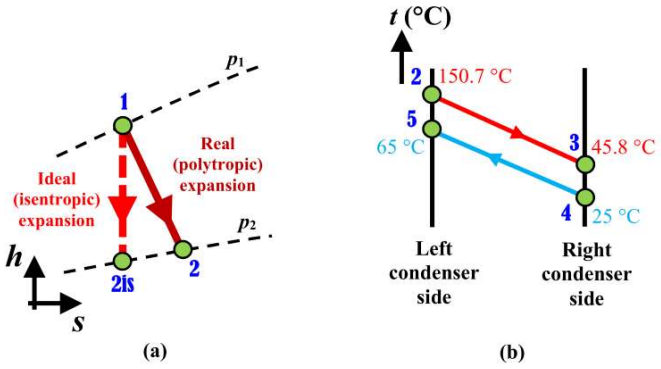


Fig. 2. *Turbine and condenser processes: (a) Ideal and real expansion in the turbine for the energy (isentropic) analysis, (b) Fluid temperatures during the heat exchange in the condenser*

3. Energy and exergy analyses equations

In the energy (isentropic) analysis of any system or component, the ambient parameters (ambient pressure and temperature) are not considered, what means that energy (isentropic) analysis is independent of the environment [16, 17]. In contrast to energy (isentropic) analysis, exergy analysis considers the ambient parameters, therefore, in exergy analysis are considered different kinds of losses in comparison to energy (isentropic) analysis [18, 19]. It should be highlighted that in real exploitation conditions the change in ambient pressure is small and it did not have a notable influence on any system or component exergy parameters, however, the ambient temperature change can be significant and it notably influences exergy parameters of any observed system or component [20]. Energy (isentropic) and exergy analyses equations of the observed steam turbine and steam condenser are defined according to recommendations from the literature [21, 22] as well as by using operating points numeration presented in Fig. 1 and Fig. 2.

3.1. Energy analysis equations of the steam turbine and steam condenser

Turbine:

- Real (polytropic) mechanical power:

$$P_{\text{re,Turbine}} = \dot{m}_1 \cdot (h_1 - h_2) \,, \tag{1}$$

where P is mechanical power, re is an index of real (polytropic) steam expansion process, $\dot{m}$ is fluid (steam) mass flow rate and h is fluid specific enthalpy.

- Ideal (isentropic) mechanical power:

$$P_{\text{id,Turbine}} = \dot{m}_1 \cdot (h_1 - h_{2\text{is}}) \,, \tag{2}$$

where id is an index of ideal (isentropic) expansion process.

- Energy (isentropic) loss:

$$En_{\text{Loss,Turbine}} = P_{\text{id,Turbine}} - P_{\text{re,Turbine}} \,, \tag{3}$$

where En is marking for the energy analysis.

- Energy (isentropic) efficiency:

$$\eta_{\text{En,Turbine}} = \frac{P_{\text{re,Turbine}}}{P_{\text{id,Turbine}}} \,, \tag{4}$$

where η is efficiency. Markings presented in the above four equations remain the same also in all other equations below.

Condenser:

- Total energy input:

$$En_{\text{Input,Condenser}} = \dot{m}_2 \cdot h_2 - \dot{m}_3 \cdot h_3 \,. \tag{5}$$

- Total energy output:

$$En_{\text{Output,Condenser}} = \dot{m}_5 \cdot h_5 - \dot{m}_4 \cdot h_4 \,. \tag{6}$$

- Energy loss:

$$En_{\text{Loss,Condenser}} = En_{\text{Input,Condenser}} - En_{\text{Output,Condenser}} \,. \tag{7}$$

- Energy efficiency:

$$\eta_{\text{En,Condenser}} = \frac{En_{\text{Output,Condenser}}}{En_{\text{Input,Condenser}}} \,. \tag{8}$$

3.2. Exergy analysis equations of the steam turbine and steam condenser

Turbine:

- Total exergy input:

$$Ex_{\text{Input,Turbine}} = \dot{m}_1 \cdot \varepsilon_1 \,, \tag{9}$$

where Ex is marking for the exergy analysis and ε is fluid specific exergy.

- Total exergy output:

$$Ex_{\text{Output,Turbine}} = \dot{m}_2 \cdot \varepsilon_2 + P_{\text{re,Turbine}} \,. \tag{10}$$

- Exergy destruction:

$$Ex_{\text{Destruction,Turbine}} = Ex_{\text{Input,Turbine}} - Ex_{\text{Output,Turbine}} \,. \tag{11}$$

- Exergy efficiency:

$$\eta_{\text{Ex,Turbine}} = \frac{P_{\text{re,Turbine}}}{\dot{m}_1 \cdot \varepsilon_1 - \dot{m}_2 \cdot \varepsilon_2} \,. \tag{12}$$

Condenser:

- Total exergy input:

$$Ex_{\text{Input,Condenser}} = \dot{m}_2 \cdot \varepsilon_2 - \dot{m}_3 \cdot \varepsilon_3 \,. \tag{13}$$

- Total exergy output:

$$Ex_{\text{Output,Condenser}} = \dot{m}_5 \cdot \varepsilon_5 - \dot{m}_4 \cdot \varepsilon_4 \,. \tag{14}$$

- Exergy destruction:

$$Ex_{\text{Destruction,Condenser}} = Ex_{\text{Input,Condenser}} - Ex_{\text{Output,Condenser}} \,. \tag{15}$$

- Exergy efficiency:

$$\eta_{\text{Ex,Condenser}} = \frac{Ex_{\text{Output,Condenser}}}{Ex_{\text{Input,Condenser}}} \,. \tag{16}$$

4. Steam and condensate operating parameters for the energy (isentropic) and exergy analyses

Operating parameters of steam and condensate (water) in real exploitation process are found in [12] and presented in Table 1. Operating parameters which are not known from the literature in each operating point from Fig. 1 are calculated by using NIST-REFPROP 9.0 software [23]. It should be highlighted that at the end of ideal

(isentropic) steam expansion process in the turbine (operating point 2is, Fig. 2 (a)), steam specific enthalpy is equal to 2240 kJ/kg – this specific enthalpy is required for the turbine ideal mechanical power calculation.

The exergy analysis baseline for any system or component is the definition of the base ambient state [24]. In the exergy analysis performed in this paper, the base ambient state is defined by the ambient temperature of 25 °C and the ambient pressure of 1 bar.

Table 1. *Steam operating parameters from turbine and condenser exploitation (real process)*

O. P.*	Temp. (°C)	Press. (bar)	Mass flow rate (kg/s)	Specific enthalpy (kJ/kg)	Specific entropy (kJ/kg·K)	Quality (-)**	Specific exergy (kJ/kg)***
1	575.4	106.4	131.9	3559.20	6.8000	SH	1536.40
2	150.7	0.2	131.9	2783.70	8.3712	SH	292.37
3	45.8	0.1	131.9	191.78	0.6491	SC	2.81
4	25.0	3.0	2044.0	105.10	0.3672	SC	0.20
5	65.0	3.0	2044.0	272.34	0.8935	SC	10.51

* O. P. = Operating point (in accordance to Fig. 1)
** SH = Superheated steam; SC = Subcooled (condensate)
*** At the base ambient state

5. Results and discussion

Energy (isentropic) analysis results of the steam turbine are presented in Fig. 3.

Ideal (isentropic) steam expansion process in the turbine did not consider any losses, so the ideal mechanical power which can theoretically be developed in the turbine is always higher in comparison to the real mechanical power. Ideal mechanical power cannot be developed by the turbine in real exploitation conditions, but it can be a guideline for any turbine improvements and modifications. Real mechanical power is calculated from the real (polytropic) steam expansion process in the turbine which considers all losses during expansion. Observed steam turbine has high energy (isentropic) loss equal to 71.71 MW, and very low energy (isentropic) efficiency of 58.79% only. Considering the fact that observed turbine develop more than 100 MW of mechanical power in real exploitation conditions, obtained energy (isentropic) efficiency is too low for such turbine (it is in the range of low power auxiliary steam turbines [25]). Therefore, steam turbine energy (isentropic) analysis shows that its operation is far from optimal and that it can be notably improved.

Energy analysis results of the steam condenser are not presented. For heat exchangers in general, available literature suggests to avoid energy analysis because it is highly dependable on the accuracy and precision of measuring equipment which is used for obtaining operating parameters [26]. Moreover, any properly operating heat exchanger will always have extremely high energy efficiency (just slightly lower than 100%) and very low energy loss (which can almost be neglected). The same is obtained in the energy analysis of the observed steam condenser. For heat exchangers, only the exergy analysis can be recommended.

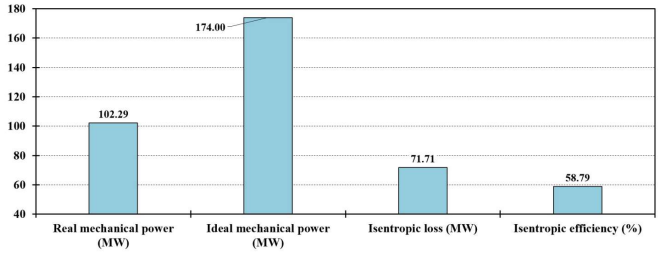


Fig. 3. *Results of the steam turbine energy (isentropic) analysis*

Exergy analysis results of the steam turbine and steam condenser at the base ambient state are presented in Fig. 4.

Comparison of steam turbine and steam condenser total exergy inputs and outputs show that steam condenser has notably lower both total exergy inputs and outputs. Steam turbine has high exergy destruction of 61.80 MW and low exergy efficiency of 62.34%. For a steam turbine which develops real (polytropic) mechanical power higher than 100 MW, Fig. 3, also exergy analysis shows very high exergy destruction and too low exergy efficiency. Both energy and exergy analyses of the observed steam turbine show that its operation can and should be notably improved.

Steam condenser has exergy destruction of 17.12 MW and exergy efficiency of 55.17%, what is in the range of similar steam condensers from the literature [27].

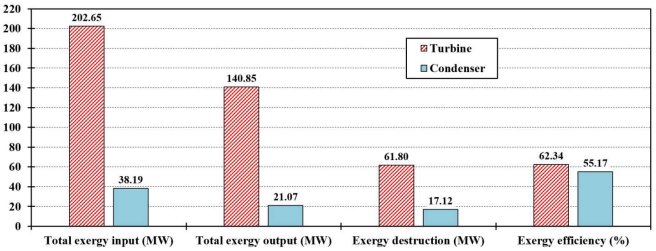


Fig. 4. *Results of the steam turbine and steam condenser exergy analysis at the base ambient state*

Observed steam turbine and steam condenser are also analyzed during the ambient temperature change. Both steam turbine and steam condenser are observed in the ambient temperature range from 5 °C up to 35 °C in steps of 10 °C, Fig. 5. Regardless of the ambient temperature, ambient pressure remains always the same and identical as at the base ambient state. In real exploitation, ambient pressure change is small and its influence on the observed steam turbine or steam condenser exergy parameters can be neglected.

For both steam turbine and steam condenser, increase in the ambient temperature simultaneously increases exergy destruction and decreases exergy efficiency, Fig. 5.

It is clear that steam condenser is much more sensitive to the ambient temperature change than steam turbine. At the ambient temperature of 5 °C steam condenser exergy efficiency is equal to 72.72% and it decreases to 36.82% at the ambient temperature of 35 °C (decrease in exergy efficiency of 35.90%), while in the same temperature range steam turbine exergy efficiency decreases for 2.39% only (from 63.95% up to 61.56%).

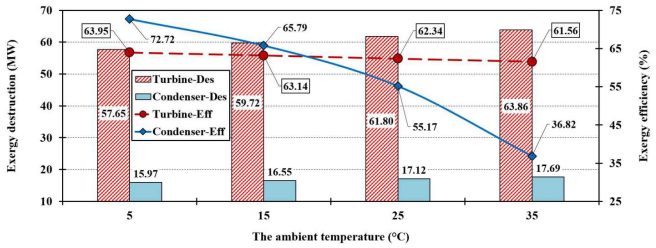


Fig. 5. *Results of the steam turbine and steam condenser exergy analysis during the ambient temperature change*

In further research related to the steam turbine and steam condenser analyzed in this paper will be applied various artificial intelligence procedures with the main aim to optimize performance of both components. As such procedures gives many beneficial results in improving various systems and components from the energy sector [28, 29], it can be expected that performance of the analyzed steam turbine and steam condenser will be notably improved.

6. Conclusions

In this paper are presented energy and exergy analyses results of steam turbine and steam condenser, which operate in commercial combined cycle power plant. For both steam turbine and steam condenser, exergy analysis is performed at the base ambient state and during the ambient temperature variation. The most important conclusions of the performed research are:

- Energy analysis shows that steam turbine has high energy (isentropic) loss equal to 71.71 MW, and very low energy (isentropic) efficiency of 58.79% only, which is in the range of low power auxiliary steam turbines.

- From the energy viewpoint, steam condenser is an almost perfect component. For the observed steam condenser, as well as for any other heat exchanger, only the exergy analysis can be recommended.
- At the base ambient state, steam turbine has high exergy destruction of 61.80 MW and low exergy efficiency of 62.34%. Therefore, both energy and exergy analyses show that steam turbine operation can and should be notably improved.
- Steam condenser has an exergy destruction of 17.12 MW and exergy efficiency of 55.17% at the base ambient state, what is in the range of similar steam condensers.
- For both steam turbine and steam condenser, increase in the ambient temperature simultaneously increases exergy destruction and decreases exergy efficiency.
- Steam condenser is much more sensitive to the ambient temperature change than steam turbine. Increase in the ambient temperature from 5 °C to 35 °C decreases steam condenser exergy efficiency for 35.90%, while the same increase in the ambient temperature decreases steam turbine exergy efficiency for 2.39% only.

7. Acknowledgment

This work was supported by the Croatian Science Foundation under the project number HRZZ-IP-2022-10-2821; University of Rijeka scientific grants uniri-iz-25-6, uniri-iz-25-220 and uniri-iz-25-10 (Funded by the European Union – NextGenerationEU); SPIN projects IP.1.1.03.0120, IP.1.1.03.0028 and IP.1.1.03.0039; University North project UNIN-TEH-25-1-8; the EU NextGeneration under the Juraj Dobrila University of Pula institutional research project number IIP_010144 and IIP_010136; and the EC Digital Europe Programme EDIH Adria 101083838.

8. References

[1] Subramanian, N., & Madejski, P. (2023). Analysis of CO2 capture process from flue-gases in combined cycle gas turbine power plant using post-combustion capture technology. Energy, 282, 128311. (doi:10.1016/j.energy.2023.128311)

[2] Anđelić, N., Lorencin, I., Mrzljak, V., & Car, Z. (2024). On the application of symbolic regression in the energy sector: Estimation of combined cycle power plant electrical power output using genetic programming algorithm. Engineering applications of artificial intelligence, 133, 108213. (doi:10.1016/j.engappai.2024.108213)

[3] Kostyuk, A., & Frolov, V. (1988). Steam and gas turbines. Mir Publishers.

[4] Gülen, S. (2019). Gas turbine combined cycle power plants. CRC Press.

[5] Lorencin, I., Anđelić, N., Mrzljak, V., & Car, Z. (2019). Genetic algorithm approach to design of multi-layer perceptron for combined cycle power plant electrical power output estimation. Energies, 12(22), 4352. (doi:10.3390/en12224352)

[6] Kotowicz, J., & Brzęczek, M. (2018). Analysis of increasing efficiency of modern combined cycle power plant: A case study. Energy, 153, 90-99. (doi:10.1016/j.energy.2018.04.030)

[7] Ibrahim, T. K., Mohammed, M. K., Awad, O. I., Abdalla, A. N., Basrawi, F., Mohammed, M. N., ... & Mamat, R. (2018). A comprehensive review on the exergy analysis of combined cycle power plants. Renewable and Sustainable Energy Reviews, 90, 835-850. (doi:10.1016/j.rser.2018.03.072)

[8] Mrzljak, V., Prpić-Oršić, J., Poljak, I., & Glavan, I. (2022). Energy evaluation of a steam turbine from solar-based combined cycle power plant. In VII International Scientific Conference: High Technologies. Business. Society (pp. 9-12).

[9] Mrzljak, V., Baressi Šegota, S., Prpić-Oršić, J., & Anđelić, N. (2023). Energy evaluation of a three-cylinder steam turbine which operates in combined cycle power plant. In VIII International Scientific Conference" Industry 4.0" 2023-Winter Session (pp. 178-181).

[10] Cihan, A., Hacıhafizoglu, O., & Kahveci, K. (2006). Energy–exergy analysis and modernization suggestions for a combined-cycle power plant. International journal of energy research, 30(2), 115-126. (doi:10.1002/er.1133)

[11] Mrzljak, V., Prpić-Oršić, J., Lorencin, I., & Anđelić, N. (2020). Thermodynamic analysis of three-cylinder steam turbine from combined cycle power plant. Machines. Technologies. Materials., 14(2), 61-64.

[12] Cavalcanti, E. J., Ribeiro, T. J., & Carvalho, M. (2021). Exergoenvironmental analysis of a combined cycle power plant fueled by natural gas from an offshore platform. Sustainable Energy Technologies and Assessments, 46, 101245. (doi:10.1016/j.seta.2021.101245)

[13] Škopac, L., Medica-Viola, V., & Mrzljak, V. (2020). Selection Maps of Explicit Colebrook Approximations according to Calculation Time and Precision. Heat Transfer Engineering, 41, 1-15. (doi:10.1080/01457632.2020.1744248)

[14] Poljak, I., & Mrzljak, V. (2023). Thermodynamic Analysis and Comparison of Two Marine Steam Propulsion Turbines. NAŠE MORE: znanstveni časopis za more i pomorstvo, 70(2), 0-0. (doi:10.17818/NM/2023/2.2)

[15] Elčić, Z. (1995). Steam turbines. ABB, Karlovac, National and University Library Zagreb.

[16] Mrzljak, V., Poljak, I., Jelić, M., & Prpić-Oršić, J. (2023). Thermodynamic Analysis and Improvement Potential of Helium Closed Cycle Gas Turbine Power Plant at Four Loads. Energies, 16(15), 5589. (doi:10.3390/en16155589)

[17] Kanoğlu, M., Çengel, Y. A., & Dinçer, İ. (2012). Efficiency evaluation of energy systems. Springer Science & Business Media.

[18] Mrzljak, V., Jelić, M., Poljak, I., & Medica-Viola, V. (2023). Exergy analysis of supercritical CO2 system for marine diesel engine waste heat recovery application. Pomorski zbornik, 63, 39-62.

[19] Dincer, I., & Rosen, M. A. (2012). Exergy: energy, environment and sustainable development. Newnes.

[20] Kopac, M., & Hilalci, A. (2007). Effect of ambient temperature on the efficiency of the regenerative and reheat Çatalağzı power plant in Turkey. Applied Thermal Engineering, 27(8-9), 1377-1385. (doi:10.1016/j.applthermaleng.2006.10.029)

[21] Erdem, H. H., Akkaya, A. V., Cetin, B., Dagdas, A., Sevilgen, S. H., Sahin, B., ... & Atas, S. (2009). Comparative energetic and exergetic performance analyses for coal-fired thermal power plants in Turkey. International Journal of Thermal Sciences, 48(11), 2179-2186. (doi:10.1016/j.ijthermalsci.2009.03.007)

[22] Mrzljak, V., Jelić, M., Poljak, I., & Prpić-Oršić, J. (2023). Analysis and comparison of main steam turbines from four different thermal power plants. Pomorstvo, 37(1), 58-74. (doi:10.31217/p.37.1.6)

[23] Lemmon, E. W., Huber, M. L., & McLinden, M. O. (2010). NIST Standard Reference Database 23, Reference Fluid Thermodynamic and Transport Properties (REFPROP), version 9.0, National Institute of Standards and Technology. R1234yf. fld file dated December, 22, 2010.

[24] Mrzljak, V., Poljak, I., Prpić-Oršić, J., & Jelić, M. (2020). Exergy analysis of marine waste heat recovery CO2 closed-cycle gas turbine system. Pomorstvo, 34(2), 309-322. (doi:10.31217/p.34.2.12)

[25] Mrzljak, V., Poljak, I., & Mrakovčić, T. (2017). Energy and exergy analysis of the turbo-generators and steam turbine for the main feed water pump drive on LNG carrier. Energy conversion and management, 140, 307-323. (doi:10.1016/j.enconman.2017.03.007)

[26] Mrzljak, V., Lorencin, I., Anđelić, N., & Car, Z. (2021). Thermodynamic Analysis of a Condensate Heating System from a Marine Steam Propulsion Plant with Steam Reheating. Journal of Marine Science and Application, 20, 117-127. (doi:10.1007/s11804-021-00191-5)

[27] Hafdhi, F., Khir, T., Yahyia, A. B., & Brahim, A. B. (2015). Energetic and exergetic analysis of a steam turbine power plant in an existing phosphoric acid factory. Energy Conversion and Management, 106, 1230-1241. (doi:10.1016/j.enconman.2015.10.044)

[28] Ebrahimgol, H., Aghaie, M., Zolfaghari, A., & Naserbegi, A. (2020). A novel approach in exergy optimization of a WWER1000 nuclear power plant using whale optimization algorithm. Annals of Nuclear Energy, 145, 107540. (doi:10.1016/j.anucene.2020.107540)

[29] Baressi Šegota, S., Lorencin, I., Anđelić, N., Mrzljak, V., & Car, Z. (2020). Improvement of marine steam turbine conventional exergy analysis by neural network application. Journal of Marine Science and Engineering, 8(11), 884. (doi:10.3390/jmse8110884)

Theoretical investigation into the influence of a teeth fault to gear train vibrations

Svetlin Stoyanov
University of Ruse "A. Kanchev", 8 Studentska str., POB 7017, Ruse, Bulgaria
SStoyanov@Uni-Ruse.BG

Abstract: *The vibration behavior of a healthy gear train is modelled as a sum of sinusoidal accelerations of a pinion, a gear, and a gear-mesh. A while noise is added trough waveform of normally distributed random numbers. The corresponding time-diagram and spectrogram are obtained. After that, an impulse acceleration waveform is added to simulate a teeth fault. The time-diagram and spectrogram are obtained again and compared. Conclusions are made.*
Keywords*: GEAR TRAIN, FAULT, ACCELERATION WAVEFORMS, GEAR-MESH FREQUENCY, SIDE BANDS, VIBRODIAGNOSTIC, TIME-DIAGRAMS, SPECTROGRAMS, POWER SPECTRUM, CONDITION MONITORING*

1. Introduction

The gear mesh frequency (GMF) is the rate at which a gear tooth make contact, and it appears in the frequency spectrum regardless of the condition of the gears. ***Gear sidebands (GS)*** are frequency peaks appearing symmetrically around the *GMF* peak in a vibration spectrum. By modulating the *GMF* at the rotational speed of a specific gear, the *GS* indicate issues like wear, eccentricity, or misalignment. Analysing *GS* spacing helps diagnose which gear is faulty. This is because the sidebands are spaced at the faulty running speed, so they can indicate problems and are crucial for **predictive maintenance** in gearboxes.

Predictive maintenance is essential for gearboxes because it allows for the **early detection**. Engineers can identify potential failures before they lead to costly breakdowns. This proactive approach significantly **reduces downtime**, ensuring that production remains steady and efficient. Furthermore, it **extends the service life** of the gearbox components by preventing catastrophic damage to the entire system.

2. Prerequisites and means for solving the problem

The complex and multi-element approach is to model a completely gear transmission (including bearings, shafts, box, etc.) and simulate with the help of FEM [1, 3, 4, 5]. This is problematic for the following reasons:

1. The initial modeling is slow, and the time required for the simulation is long even on clusters of powerful computers. Therefore, changing the values of the parameters again and again, requires a lot of calculation time;

2. Many elements influence each other, their influences are mixed, and the dependencies that are the subject of the current study cannot be separated and analyzed. That is, it turns out that the complex model used is not suitable for the specific investigation.

3. Each of the modeled elements has its own parameters to which values must be assigned. But these values are often: not completely clear; dependable by time, load, temperature, etc., and these dependencies cannot be guaranteed to be linear. All of these uncertainties and inaccuracies are very likely to distance the study from real behavior.

As a consequence of the above, **the aim of this investigation** is to obtain results about the ability to identify a fault, analysing *GS* spacing of a phenomenological vibration model of a gear train with presence of white noise environment disturbance.

Therefore, in this investigation the vibration behavior of a healthy gear train is modelled as a sum of sinusoidal accelerations of a pinion, a gear, and a gear-mesh [2, 7, 6]. The influence of other transmission elements and of other mechanisms in the transmission environment, is taken into account adding while noise trough waveform of normally distributed random numbers. Finaly, an impulse acceleration waveform is added to simulate a teeth fault. The time-diagram and spectrogram are obtained and compared. **This is simple, but powerful method, which has flexibility and rapidity.**

3. Solution of the examined problem

The parameter values used is shown in Table 1.

Table 1. Parameter values

Sample rate, KHz	fs	10
Number of pinion teeth	Np	20
Number of gear teeth	Np	81
Rotation speed of pinion, rps	f_{pin}	50
Pinion acceleration amplitude, m/s^2	A_p	0.4
Gear acceleration amplitude, m/s^2	A_g	0.2
Gear-mesh acceleration amplitude, m/s^2	A_{GM}	1

The pinion acceleration waveform is generated according to

$$a_p = A_p \sin(2\pi f_{pin} t). \quad (1)$$

The gear acceleration waveform is generated according to

$$a_g = A_g \sin(2\pi f_{gear} t). \quad (1)$$

The gear-mesh acceleration waveform is generated according to

$$a_{GM} = A_{GM} \sin(2\pi f_{mesh} t). \quad (3)$$

Then, the healthy acceleration is obtained as a sum of (1), (2), and (3). After that, white noise is added trough waveform of normally distributed random numbers – Fig. 1. The time-diagram of the vibration acceleration of the healthy train model is shown on Fig. 2.

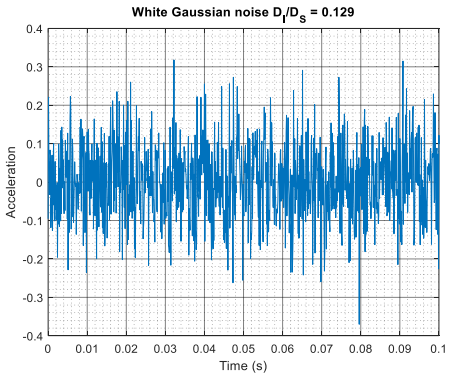


Fig. 1. The time-diagram of the white noise added

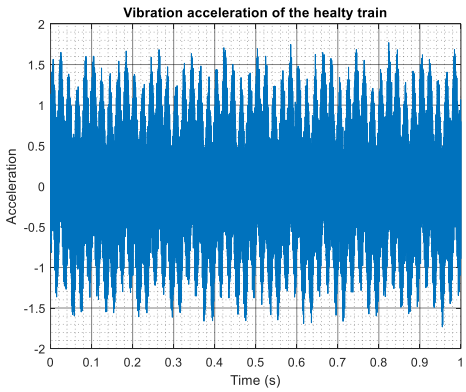


Fig. 2. The time-diagram of the healthy train

The Discrete Fourier Transform is performed according to

$$X(k) = \sum_{n=0}^{N-1} x(t)\ e^{-i\frac{2\pi}{N}kt}, \quad (4)$$

where: x is the input signal in the time area, with length n; X – output signal in the frequency area, with length k; $x(t)$ – the value of the input signal at time t; and $X(k)$ – complex number, carrying amplitude and phase information at frequency k.

Through (4), the spectrogram of the healthy vibration acceleration is obtained and presented on Fig. 3. With red vertical lines are marked gear sidebands frequencies. On Fig. 3, one can observe that there are **six peaks**, that matches with sideband frequencies – they are marked with green circles.

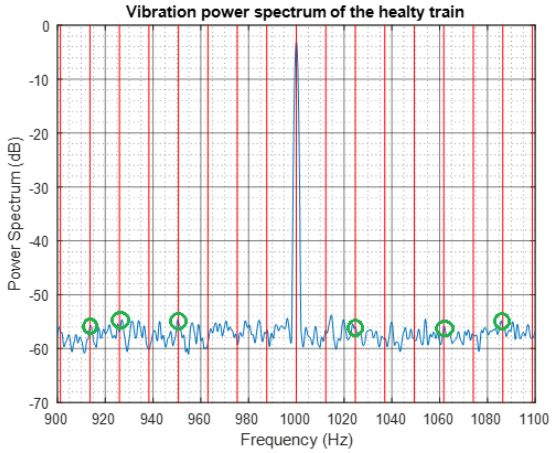


Fig. 3. The spectrogram of the healthy train

The next step is to add an impulse waveform to simulate a teeth fault – Fig. 4.

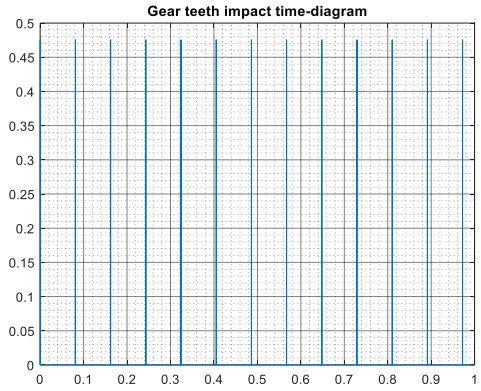


Fig. 4. The time-diagram of the impulse used

The resulting acceleration is shown on Fig. 5. One can observe and compare the time-domain signals from Fig. 2 and Fig. 5. There are not visible differences that indicates signal change and fault presence.

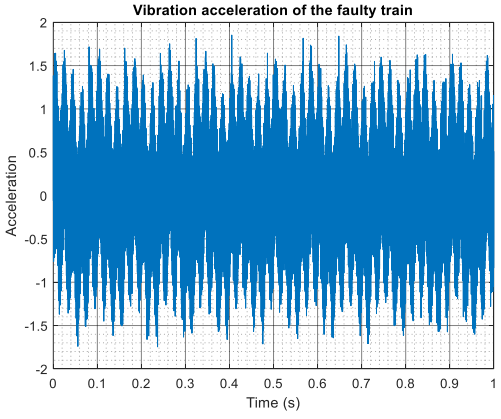


Fig. 5. The time-diagram of the faulty train

After that, the Fourier transform is performed again and the spectrogram of the faulty train is obtained – Fig. 6. One can observe that there are **thirteen peaks**, that matches with sideband frequencies – they are marked with green circles.

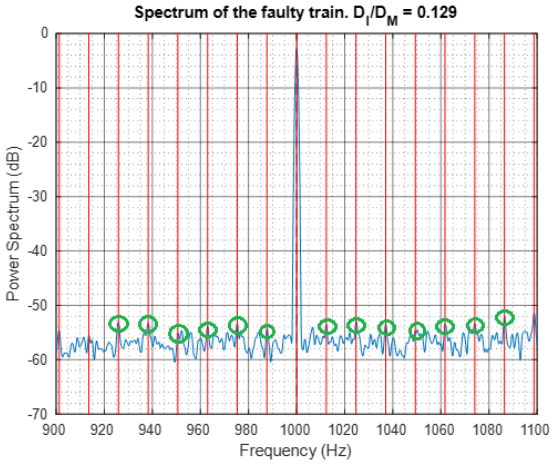


Fig. 6. The spectrogram of the faulty train

4. Conclusions

This investigation shows that by comparing the spectrogram of the healthy gear train model (Fig. 3) and the faulty train model (Fig. 6), one can identify the problem presence. But an interesting question is what is the influence of the white noise density and of the faulty impulse amplitude on this ability the problem presence to be identified. So, this can be marked as a topic for the future investigation.

A basis for this future investigation is the deviation indicator shown in the titles of Fig. 3 and Fig. 6. The standard deviation of the white noise used are calculated and marked with D_I. The standard deviation of the healthy acceleration (obtained as a sum of equations (1), (2), and (3)) are also calculated and marked with D_M. On Fig. 3 and Fig. 6 titles, one can see the indicator obtained by dividing of these deviations. By varying the values if this indicator, the influence of above-described factors will be investigated in the future researches.

5. References

[1] V. Dobrev, S. Stoyanov, A. Dobreva. Design, Simulation and Modal Dynamics of Gears and Transmissions. International Conference on Gears 2015, VDI-Bericht 2255, Munich VDI-Bericht 2255, 3, 695 – 707 (2015)

[2] F. Zhipeng, Z. Ming. Vibration signal models for fault diagnosis of planetary gearboxes. Journal of Sound and Vibration. 331. 4919–4939. 10.1016/j.jsv.2012.05.039 (2012)

[3] S. Stoyanov, V. Dobrev, A. Dobreva. Finite Element Contact Modelling of Planetary Gear Trains Material Science and Engineering, IOP Publishing, 252, 012034 - 38, doi: 10.1088/1757-899X/252/1/012034 (2017)

[4] S. Stoyanov, V. Dobrev, A. Dobreva. Numerical Investigation of Planetary Gear Trains and Transmissions Mechanisms and Machine Science/ 5th International Conference on Power Transmission BAPT, Ohrid, 1, 155-162 (2016)

[5] S. Stoyanov. Explicit dynamics of gear pair using finite element model. Proceedings of the University of Ruse, vol 2/54, pp 67-71, ISSN 1311-3321 (2016)

[6] Y. Juliang, W. Wenyi, M. Zhihong, K. Suiyang. Statistical modeling of gear vibration signals and its application to detecting and diagnosing gear faults. Information Sciences. 259. 295–303. 10.1016/j.ins.2013.03.029 (2014)

[7] Y. Nie, F. Li, L. Wang, J. Li, M. Wang, M. Sun. Phenomenological vibration models of planetary gearboxes for gear local fault diagnosis. Mechanism and Machine Theory, Volume 170, 104698, ISSN 0094-114X (2022)

Bio-electrochemical system based electro-generative pipeline element

Rosen Ivanov
University of Mining and Geology, Bulgaria
r.ivanov@mgu.bg

Abstract: *In the context of a changing climate and the pursuit of sustainable development, any technology or device that produces green energy will help reduce dependence on fossil fuels. This work presents a prototype of an electro-generative pipeline element based on a bio-electrochemical system. The element is suitable for integration into pipelines carrying various liquids. The electro-generative element has shown high efficiency in laboratory conditions, and depending on the passing liquid, it can generate energy in the range of 0.5W - 1.5W. A different number of elements can be located in the pipeline system, depending on its length. Depending on the number of elements in the chain, enough energy can be obtained to power various devices.*
Keywords*: GREEN ENERGY, SEDIMENT MICROBIAL FUEL CELL, BIO-ELECTROCHEMICAL SYSTEMS*

1. Introduction

With the growth of the global population, the demand for natural resources and energy increases. Manufacturing companies expand their operations with new technologies and processes to meet their needs. Rapid development in resource use and energy consumption puts pressure on the environment, increasing pollution, greenhouse gas emissions, and waste generation. Energy and resources are two of the most crucial elements of economic progress. Economic progress is impossible without adequate resources and energy; therefore, resources and energy must be used wisely and efficiently. [4] Climate change and environmental pollution pose significant challenges to the global economy. This problem threatens not only people's health but also their finances and productivity. The urgency to address climate change and environmental pollution has led to significant advancements in renewable energy technologies. With growing global energy needs, developing sustainable and efficient energy solutions is critical. Renewable energy plays a multifaceted role in environmental conservation, providing solutions that generate clean energy and help restore ecosystems. [9]

The number of studies on green energy technologies published so far clearly shows a lack of fragmentation, as research often focuses on specifics such as solar or wind energy, without providing a comprehensive overview of the entire spectrum of available developments. This fragmentation narrows the field of research and hides the interconnectedness of multiple technologies that are critical for the functioning of sustainable energy systems. Green technology is already a branch of science that studies the creation, use, and application of technological tools, as well as how they interact with society, the environment, and human existence. Green inventions are those that benefit the environment and often include recycling, energy efficiency, renewable resources, safety, healthcare, and other areas. [14]

The construction industry is currently undergoing a radical shift towards sustainability, driven by the need to reduce the ecological footprint and improve energy efficiency. Green building is an innovative approach based on sustainable practices aimed at reducing the environmental impact of structures. It offers opportunities to mitigate the negative effects of buildings on the environment and the health of occupants. The water sector, as an integral part of the construction industry, also strives for higher energy efficiency and sustainability. [10] Water supply systems are crucial for providing safe, efficient, and sustainable water services in buildings. However, current design practices are based on outdated assumptions that contribute to stagnation, deterioration of water quality, and compromises between energy and health. Energy efficiency is one of five areas (including hydraulic design, water conservation, water quality, and socio-economic factors) where significant work needs to be done to achieve higher performance of water supply systems. Recognizing the problems of outdated methods of designing water supply and drainage systems, building regulators in developed countries have acknowledged that existing plumbing standards may no longer reflect how water is used in buildings. As a result, new tools and methods are being developed to improve design accuracy. In addition to hydraulics, there is a need to integrate other key areas into the design, including energy efficiency and sustainable development. [2]

Water conservation is a fundamental aspect of the design of water supply and drainage systems, especially in the context of increasing pressure on drinking water resources due to climate variability and population growth. At the same time, energy efficiency has become a critical issue in the design of water supply and drainage systems. This highlights the importance of improving energy efficiency through effective design of water supply systems and integrating systems and devices for generating green energy. [8]

Socio-economic considerations are also crucial for the design, construction, and long-term operational efficiency of water supply systems. Factors such as rising construction costs and material accessibility significantly influence design decisions and project outcomes. Cost-effective solutions that enhance energy efficiency and sustainability are key to addressing this challenge. [4]

Green technologies encompass a wide range of systems and devices. Bio-electrochemical systems are such a technology that can directly convert the available biochemical energy in organic matter into electricity. A variation of bio-electrochemical systems is sediment microbial fuel cells. [6] Sediment microbial fuel cells are special types of microbial fuel cells where the anode is placed in anaerobic sediment, while the cathode is submerged in the surface layer of water. [15] Natural electroactive bacteria break down organic compounds in the sediment, producing electrons and protons. The electrons reach the cathode through an external electrical circuit, while the protons pass through the soil layer, acting as a makeshift membrane. [1]

Oxygen is often preferred as an electron acceptor due to its availability in the cathode region and its high potential. However, reduction reactions of dissolved oxygen are slow and limited due to the limited solubility and diffusion of oxygen. [13] On the cathode, heavy metal ions and other compounds can also be reduced, which will lead to increased generated energy. All this suggests the use of a different fluid in the cathode region. Additionally, the material and configuration of the electrodes are crucial for the efficiency of sediment microbial fuel cells. [3]

Although sediment microbial fuel cells are an interesting and rapidly developing technology, some critical issues need to be addressed before they can be used for more practical purposes. [5] The main limitation of sediment microbial fuel cells is their low output power, which typically ranges from tens to hundreds of milliwatts, insufficient for directly powering various devices requiring watt-level power. [7] The limited energy production in SMFCs results from multiple factors, including undesirable sediment and water characteristics, significant cathodic activation losses, and large ohmic resistance due to the large anode-cathode distance. [11] Another challenge for real-world applications is the materials used for constructing sediment microbial fuel cells. Using expensive electrode materials is not cost-effective given the relatively low generated power. [12]

The aim of the current research is to propose a working practical application of sediment microbial fuel cells. A prototype of an electrogenerative pipeline element based on a sediment microbial fuel cell has been developed. In constructing the prototype, solutions have been found for most challenges limiting the practical, long-term application of sediment microbial fuel cells as a green energy generation technology, as well as improving performance. Inexpensive construction materials with high resistance to environmental factors have been used. The prototype represents a connecting element in pipeline technological schemes, with standardized dimensions, easy to operate and install. Depending on the specific technological scheme and application, a varying number of electrogenerative elements can be included. Connected in a suitable electrical circuit (in parallel or series), they can provide sufficient energy for an extended period.

2. Materials and methods

Construction of electrogenerative pipeline element

The pipeline element represents a sediment microbial fuel cell, which includes anode and cathode parts. The anode part consists of a PVC pipe with a diameter of 110 mm and a length of 250 mm. The bottom of the pipe is closed with a PVC plug. The pipe is filled with river sediment. At the bottom of the pipe, there is a stainless steel electrode AISI 304 with an area of 471 cm², which acts as the anode. At the top of the pipe, a perforated rubber cap filled with clay is placed, serving as a membrane between the anode and cathode zones. The cathode part consists of a PVC branch Ø110/110x87°, in which a curved stainless steel electrode AISI 304 with an area of 407 cm² is located, acting as the cathode. The two structural elements are connected and form an electrogenerative connecting pipeline element based on SMFC. The cathode zone is filled with water with the following chemical characteristics: pH 6.83, Eh 109 mV, and EC 68 µS/cm².

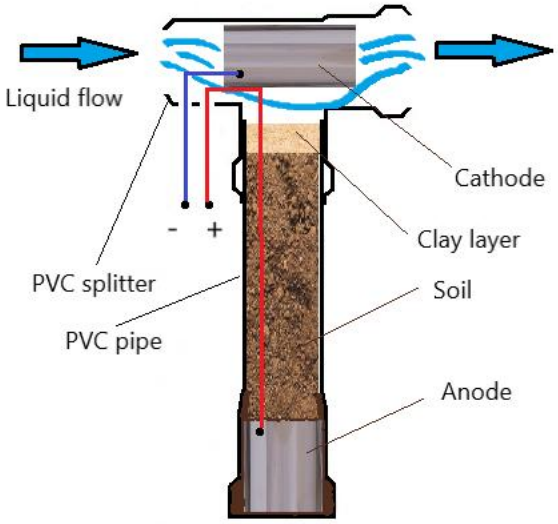


Fig. 1 *The schematic diagram of electrogenerative pipeline element*

Soil sampling

For the purpose of the study, riverside soil was taken from Ivanyanska river, Bulgaria (42°42'27.1"N 23°11'46.4"E), from a depth of 20-30 cm. After taking the river sediment, the larger pieces were removed by sieving through 2 mm. In order to carry out physicochemical analyses, part of the sieved soil was air-dried. The soil is characterized as alluvial-meadow with a high humus content of 6%. The soil has been classified as clay according to the Rutkowski method. Soil pH was measured by pH-meter HANNA HI-9021 determined at 1 : 2.5 (soil:water). Soil electrical conductivity (EC) was measured by WTW LF 197-S determined at 1:5 (soil:water). The main soil physicochemical properties were as follow pH 6.42, EC 288.89 µS cm^{-1}. The Kjeldahl-N content were 0.59% and dissolved organic carbon 74.28 mg kg^{-1}. The amount of total nitrogen measured was 986.5 mg kg^{-1}, phosphorus – 20.2 mg kg^{-1}, potassium – 180.0 mg kg^{-1}. The abundance of exoelectrogenic microorganisms was quantified by 16S rRNA gene. In the sediment *Geobacter* and *Clostridium*, were the most abundant. *Anaeromyxobacter*, *Bacillus*, *Pseudomonas* and *Desulfolobus* were also detected. [18] All these indicators provide sufficient nutrients and substrate for degradation by exoelectrogenic microorganisms in the anode zone. This would ensure long-term and stable operation of the sensor.The soil thus prepared was then used to fill anode area of SMFC based biosensor. (Fig. 1).



Fig. 2 *Photo of electrogenerative pipeline elements*

Electrochemical analysis

To determine the operation and effectiveness of the composter polarization and power curves were obtained by varying external resistances sequentially from 10, 8, 6, 4, 2, 1.5, 1.3, 1, 0.7, 0.5, 0.3 to 0.1 KΩ using MCP lab electronics BXR-04 ResistorBox. The voltage dynamic were measured and recorded in real time with Vernier LabQuest Mini and Logger Lite software.

3. Results and discussion

In order to investigate and validate the operation of the electro-generative pipeline element under laboratory conditions, a series of chemical and electrochemical analyses were conducted. After constructing the element, the time it took to reach its optimal baseline voltage was recorded. The data from the study are presented in Figure 3.

The voltage of the element is directly dependent on the microbiological processes occurring in the soil (the anode zone). From the presented graph, it can be seen that it takes about 10 days for the microorganisms to adapt and initiate stable microbial processes. During this period, the voltage is relatively stable and ranges between 10 to 50 mV. After the tenth day, stable microbial processes have been established in the anode area, and anaerobic processes develop, leading to a significant increase in the potential difference between the soil and water (the cathode area). The voltage increases until the 21st to 22nd day, after which a stable baseline voltage of the electro-generative pipeline element is reached. The baseline voltage of the element when the cathode zone is filled with water is in the range of 425 ± 3 mV and remains so until the end of the experiment (day 31).

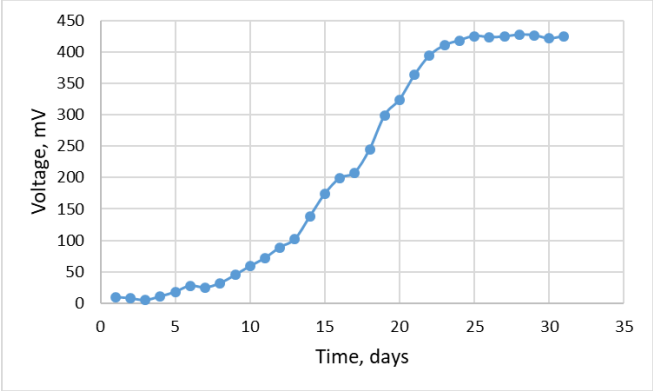


Fig. 3 *Open circuit voltage of electro-generative pipeline element*

The next experiment aimed to determine the dynamics of the open-circuit voltage of the electro-generative pipeline element over time before it was installed in a pipeline network. The data from the experiment are presented in Figure 4.

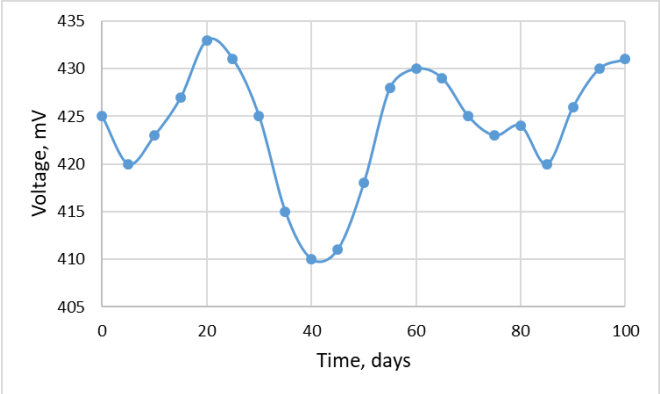


Fig. 4 *Base open circuit voltage of electro-generative pipeline element*

The experiment was conducted over 100 days, during which the open-circuit voltage was continuously monitored and recorded using Vernier LabQuest Mini and Logger Lite software. From the data, it can be seen that the open-circuit voltage remained relatively stable throughout the study period, ranging between 420 ± 15 mV. The slight fluctuations in the voltage of the electro-generative pipeline element can be attributed to temperature differences in the environment. Temperature is a factor that significantly influences microbiological activity in the anode zone, and consequently, the generated voltage of the element.

The next experiments were based on investigating the main electrical parameters of the electro-generative pipeline element. Data from the conducted analyses are presented in Figures 5 and 6.

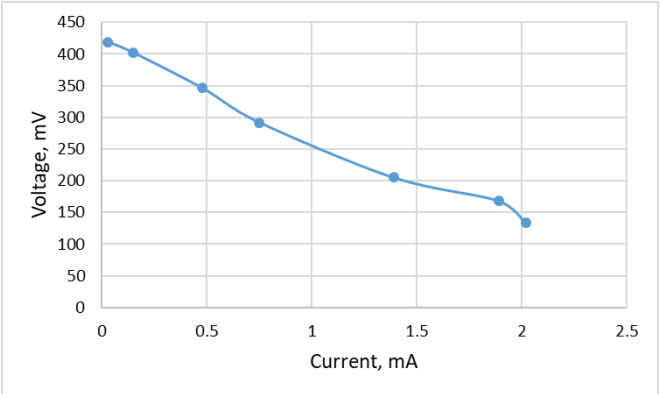


Fig. 5 *V-A characteristic of the electro-generative pipeline element*

Figure 5 shows the volt-ampere characteristic of the electro-generative pipeline element. From the graph, it can be seen that the element reaches a maximum current of 2.02 mA at a voltage of 133 mV and an applied resistance of 1.3 kΩ.

Figure 6 shows the polarization curve of the electro-generative pipeline element.

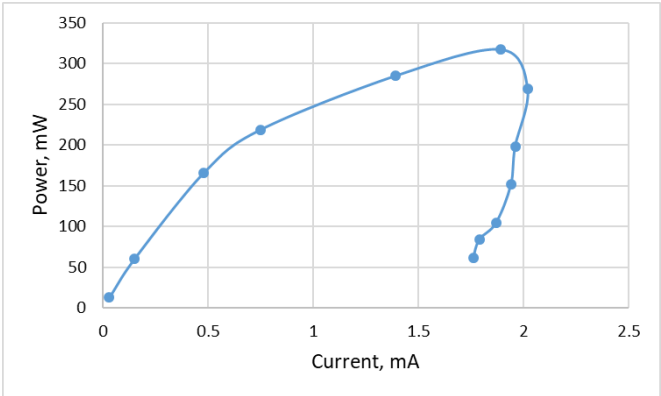


Fig. 6 *Polarization curve of the electro-generative pipeline element*

From the figure, it can be seen that the pipeline element reaches a maximum power of 317.52 mW at a current magnitude of 1.89 mA and a voltage of 168 mV.

It is important to note that the generated voltage and power of the electro-generative pipeline element are highly dependent on the redox potential of the fluid flowing through the cathode zone. The next experiment aimed to determine how the electrical parameters of the pipeline element would change when a solution with a higher redox potential flowed through the cathode zone. For this purpose, a copper solution with a concentration of 2 g/L was prepared, with a redox potential of 384 mV. After filling the cathode zone with this solution, the electrical parameters of the electro-generative pipeline element were measured again. The data from the experiment are presented in Figures 7 and 8.

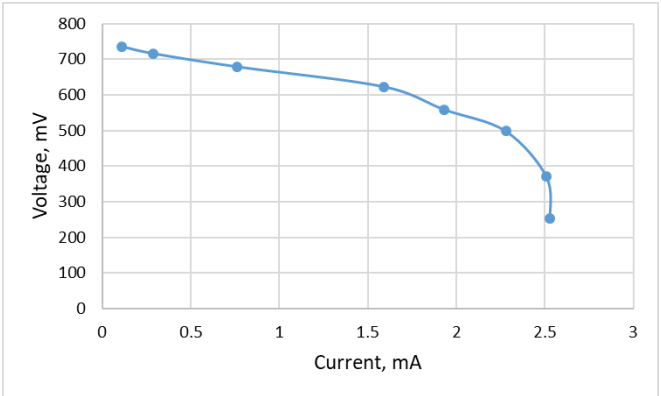


Fig. 7 *V-A characteristic of the electrogenerative pipeline element with high ORP solution*

From the volt-ampere characteristic, it can be seen that there is a significant increase in the open-circuit voltage, reaching up to 736 mV. The maximum current in this experiment reaches 2.53 mA.

From the polarization curve shown in the figure, it is determined that increasing the redox potential leads to a significant increase in the power of the electro-generative pipeline element. In this case, a maximum power of 1135.44 mW is reached at a current magnitude of 2.28 mA and an applied resistance of 1.5 Ω.

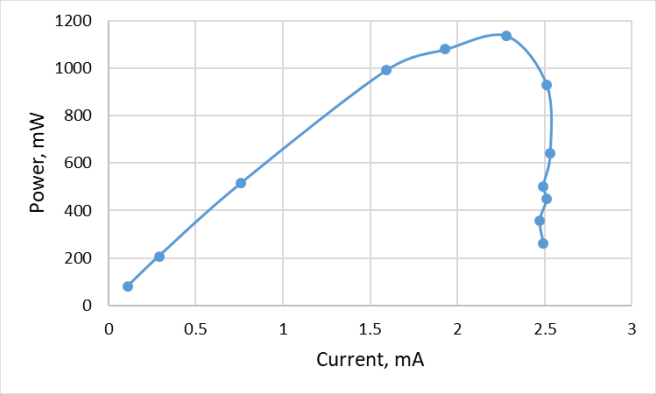


Fig. 8 *Polarization curve of the electro-generative pipeline element with high ORP solution*

4. Conclusion

Green technologies and their integration into practice are key factors for sustainable energy production and use. The article examined and proposed a practical application of bio-electrochemical systems technology for the production of green energy. The developed prototype of an SMG-based electro-generative pipeline element was investigated and validated under laboratory conditions. Analyses showed efficient and stable operation of the pipeline element. Laboratory studies established that the higher the oxidation-reduction potential of the fluid passing through the cathode zone, the higher the power generated by the pipeline element. From the electrical characteristics of the prototype, a maximum generated power of 1.135 W was determined.

Pipeline systems consist of interconnected pipes and pipeline elements with varying lengths. The proposed prototype represents a connecting pipeline element, and the longer the pipeline length, the more electro-generative elements can be incorporated. This will result in the production of greater amounts of energy and its utilization for various needs.

Acknowledgements

This work was funded by Ecodiscover ltd. through the America for Bulgaria Foundation

5. References

1. D. Bose, R. Bhattacharya, M. Pillai, A. Ray, T. Kaur, S. Mondal, A. Mondal, State-of-the-art review on sediment microbial fuel cells: evolution, innovations, challenges, scalability, and policy implications for sustainable development, Water-Energy Nexus 9 (2026) 30–45
2. D. Gasparini, J. Bakens, P. Mulder, N. Pestel, How green are jobs for the energy transition?, Energy Research & Social Science 129 (2025) 104368
3. F. Sun, J. Chen, M. Tang, Y. Yang, Recent research progress, challenges and future directions of sediment microbial fuel cell: A comprehensive review, international journal of hydrogen energy 50 (2024) 870e886
4. G. A. Sundaram, G. R. Muniyandi, Advancements in Renewable Energy: Innovations and Sustainable Solutions for a Greener Future, Next Research 2 (2025) 100482
5. H. Wang, Y. Ye, J. Zhang, H. Ning, Y. Xiang, X. Song, W. Zhao, F. Guo, Power performance improvement in sediment microbial fuel cells: Recent advances and future challenges, International Journal of Hydrogen Energy, 48 (2023) 24426-24446
6. K. Debnath, S. Dutta, Bio-electrochemical system analysis and improvement: A technical review, Cleaner and Circular Bioeconomy 6 (2023) 100052
7. L. Liu, T-Y. Chou, Ch-Y. Lee, D-J. Lee, A. Su, J-Y. Lai, Performance of freshwater sediment microbial fuel cells: Consistency, international journal of hydrogen energy 41 (2016) 4504e4508
8. M. Bilal, S. G. Sandi, B. M. Josey, J. Gong, A review of premise plumbing systems: from design and key performance domains to challenges and future research pathways for full-scale integration, Water Research 293 (2026) 125437
9. N. Khandelwal, S. K. Behera, A. Kumar, V. V. Gedam, Life Cycle Assessment and Circular Economy in Emerging Green and Sustainable Energy Sectors: A Critical Review, Sustainable Energy Technologies and Assessments 81 (2025) 104436
10. O. Humaidan, K. Almazam, O. Agboola, O. Oladokun, Y. A. Dodo, A review on the strategies for green building construction: The role of nanomaterials in green buildings for a sustainable future, Journal of Building Engineering 114 (2025) 114359
11. R. Alipanahi, M. Rahimnejad, G. Najafpour, Improvement of sediment microbial fuel cell performances by design and application of power management systems, International Journal of Hydrogen Energy, 44 (2019) 16965-16975
12. T. Ewing, P. T. Ha, H. Beyenal, Evaluation of long-term performance of sediment microbial fuel cells and the role of natural resources, Applied Energy 192 (2017) 490–497
13. T. Ewing, P. T. Ha, J. T. Babauta, N. T. Tang, D. Heo, H. Beyenal, Scale-up of sediment microbial fuel cells, Journal of Power Sources, 272 (2014) 311e319
14. W. A. Jadayil, G. Shwaheen, M. Ramadan, M. Alkhedher, Green energy management: Combining sustainable technologies for efficient power generation, Energy Strategy Reviews 63 (2026) 102071
15. Y. Hubenova, I. Bardarov, E. Hubenova, E. Slavcheva, Sediment microbial fuel cells capable of powering outdoor environmental monitoring sensors, Sensing and Bio-Sensing Research 46 (2024) 100695

Active damping in cable-stayed-bridge structures using hydraulic actuators

Enkeleda Kokona [1], Helidon Kokona[2], Klodian Dhoska[3]
Faculty of Civil Engineering – Polytechnic University of Tirana, Albania [1]
Structural Engineer - CEO Henars-Engineering ltd, Albania [2]
Faculty of Mechanical Engineering – Polytechnic University of Tirana, Albania [3]
enkeleda.kokona@fin.edu.al

Abstract: *Cable-Stayed-Bridges are an important part of today's constructions in the traffic infrastructure. New materials and computational technology have led to the construction of longer and slender Cable-Stayed-Bridges are under the effect of dynamic loads as wind, traffic or earthquakes. Besides comfort restrictions, the vibrations of large amplitudes effects also the lifetime of the entire structure. Oscillations of Cable-Stayed-Bridges can be reduced significantly by active damping systems. In this paper is represented shortly an electro-hydraulic actuator concept for the active damping of Cable-Stayed-Bridges. This type of control is very efficient even in large bridges (up to 900 m span). Also, the tests on a large-scale bridge show the efficiency of active damping in Cable-Stayed-Bridges using electro-hydraulic actuators. The damping of deck and cables, has become crucial in the design of cable-supported structures. Because of the effectiveness of passive damping systems is limited, this new electro-hydraulic actuator concept is developed.*

Keywords*: CABLE-STAYED, BRIDGE, DAMPING SYSTEMS, OSCILLATIONS*

1. Introduction

Cable-stayed bridges are continuously subjected to dynamic loads such as wind, traffic, and seismic excitations. Beyond issues related to user comfort, large-amplitude vibrations can significantly affect the structural integrity and long-term service life of the entire bridge system [1-3]. Therefore, effective vibration mitigation has become a critical aspect of modern bridge engineering.

Structural oscillations in cable-stayed bridges can be substantially reduced through the implementation of active damping systems. This paper briefly presents an electro-hydraulic actuator concept designed for the active vibration control of cable-stayed bridges. The proposed control approach demonstrates high efficiency, even for large-span bridges reaching up to 900 m. Experimental investigations conducted on a large-scale bridge model further confirm the effectiveness of active damping using electro-hydraulic actuators.

Consequently, the damping of both bridge decks and stay cables has become a crucial consideration in the design of cable-supported structures. Since the performance of traditional passive damping systems is inherently limited, the development of advanced active control solutions, such as the proposed electro-hydraulic actuator system, represents a promising alternative for improving structural performance and durability [4-7]. Figure 1 depict the Normandia bridge – example for a large cable-stayed bridge [8-11].



Fig. 1. *Normandia bridge – example for a large cable-stayed bridge [8]*

2. Damping Concept

Figure 2 illustrates the basic control concept based on the *Integral Force Feedback* (IFF) approach. In this configuration, selected stay cables are equipped with actuators positioned between the stay cable and the bridge deck. The stay cable is modeled by the stiffness c_k, while the bridge deck is represented by the mass m_{st}. The combined structural stiffness of the deck and the stay cables is denoted by c_{st}. The actuator is connected to the stay cable through a force sensor, forming a collocated actuator–sensor pair, which ensures stable and efficient control performance.

For the purpose of explaining the damping concept, the effect of self-weight is neglected. The actuator displacement amplitude *w* is calculated from the dynamic component of the measured force F_D in the stay cable, see equation 1.

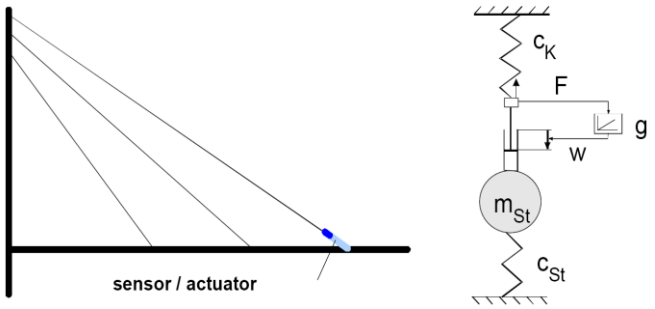


Fig. 2. *Cable-stayed bridge mock-up and active damping model with "Integral Force Feedback"*

$$w = g \cdot \int F_D \cdot dt \tag{1}$$

For an undamped system, the amplification factor approaches the limiting cases (g 0) and (g). When g = 0, a rigid connection exists between the stay cable and the structure; consequently, no oscillation energy is absorbed. In contrast, when g□□□ the cable becomes effectively separated from the structure, causing the actuator forces and therefore the damping effect to vanish.

An optimal amplification value g_{opt} exists at which the total system damping reaches its maximum. For this optimal value, a force oscillation with amplitude F_D produces an actuator displacement amplitude given by

$$\hat{w}\left(g_{opt}\right) = \frac{\hat{F}_D}{c_K} \tag{2}$$

This relationship links the structural parameters directly to the optimal dimensioning of the damping actuator. When the actuator is designed according to this criterion, the *Integral Force Feedback* (IFF) approach guarantees continuous energy dissipation within the system. The corresponding energy flow can be expressed as equation (3).

$$\dot{W} = -F_D \cdot \dot{x}_r = -g \cdot F_D{}^2 \le 0 \quad (3)$$

$\dot{x}_r$ - frequency of the actuator stroke

This damping law enables stable operation for all observable and controllable state variables. However, practical actuators possess limitations related to response time and achievable amplification, which influence the effective feedback gain g and, consequently, the overall damping performance. For effective control, the actuator should have a natural frequency significantly higher than that of the controlled structural system.

Furthermore, actuator placement plays an important role in system efficiency. Positioning actuators on the main (longest) cable is particularly effective, as it both mitigates vibrations of the individual cable and increases the global damping of the entire bridge structure.

3. Electro-Hydraulic Actuator Concept

The primary design objective of active control systems is to ensure minimal energy consumption while maintaining a compact actuator size. To achieve a long service life for cable-supported structures, additional dynamic loads must be minimized through effective active damping. During periods of increased excitation caused by adverse weather or heavy traffic conditions, structural loads should remain below predefined limit values.

In active damping applications, the required dynamic control force is typically less than one-tenth of the corresponding static force. Considering the magnitude of static loads, several design approaches incorporate a separate passive device to sustain static demands, thereby reducing the power consumption of the actuator system. Static load compensation is achieved through the hydraulic component of the actuator. This passive device consists of a hydraulic plunger cylinder connected to a hydraulic accumulator. The passive subsystem can be combined with an additional hydraulic cylinder responsible for generating the active control force.

Compared with purely mechanical solutions, such an actuator configuration offers several advantages:

- The force level of the passive subsystem can be adapted to variations in static loads caused by wind or traffic, enabling variable spring characteristics.
- When combined with a mechanical system, hydraulic pressure can be unloaded during non-active structural periods, improving energy efficiency and reducing component wear over time.

Figure 3 presents different design options for active hydraulic actuators with passive compensation of tension loads. These concepts are classified according to the number of pressure chambers and the actuator control strategy. The number of pressure chambers corresponds to the number of hydraulic oil springs; consequently, a double-acting cylinder provides the highest actuator natural frequency.

Control of a hydraulic cylinder using a variable-displacement pump (displacement control) generally achieves higher efficiency than valve-controlled systems. Nevertheless, a valve-controlled configuration is adopted in this study due to its superior controllability for oscillations characterized by small amplitudes and high frequencies. For large cable-stayed bridges, displacement-controlled systems may offer additional advantages.

To minimize power consumption and extend system lifetime, the control power unit can be switched off during periods when structural oscillations remain within acceptable limits under normal operating conditions.

The experimental investigation focuses on evaluating the effectiveness of the proposed damping concept. For this purpose, a collocated actuator–sensor pair incorporating a valve-controlled double-acting hydraulic cylinder was developed. Figure 4 illustrates the actuator system configuration. A key feature of this design is the integration of passive and active subsystems within a single unit. The passive component combines a hydropneumatics accumulator with a dedicated pressure chamber, enabling the actuator to sustain high tensile forces (cable pre-tensioning) without continuous power flow control during actuator motion. The active subsystem consists of two pressure chambers with nearly identical cross-sectional areas connected to the control ports of a servo valve.

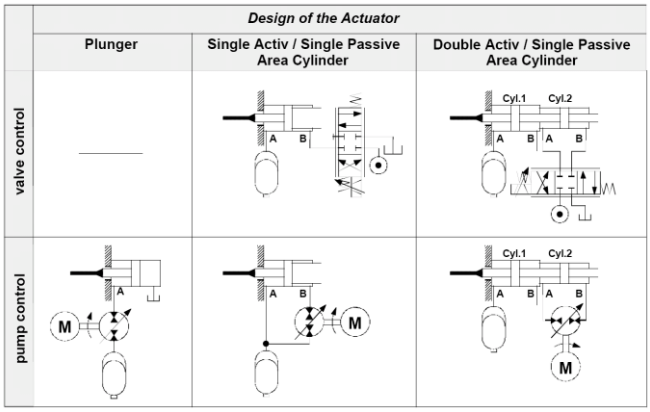


Fig. 3. Systematic of hydraulic actuators with passive load compensation

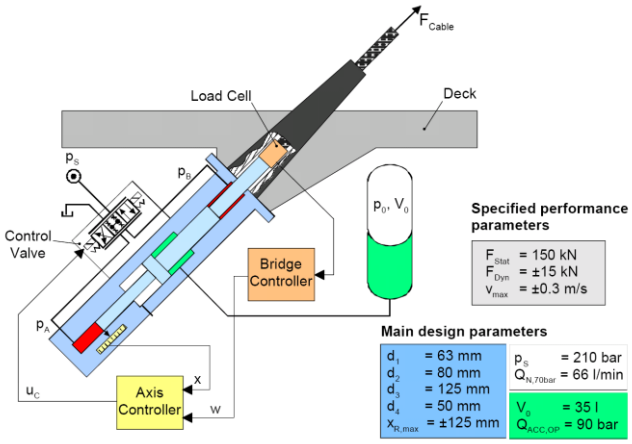


Fig. 4. *Principle design of the prototype actuator and performance requirements*

4. Static and Dynamic Characteristics of The Damping System

The effectiveness of active damping largely depends on the performance capabilities of the actuator. To satisfy both static and dynamic requirements, the actuator must be dimensioned based on an appropriate mathematical model. In addition to accurately describing the actuator dynamics, the model should also represent the complex nonlinear behavior of the bridge structure particularly that of the stay cables — through a suitably linearized system formulation.

4.1 Static and dynamic actuator characteristics

The mathematical model describes the interaction between the actuator and the bridge structure, as well as the internal power characteristics of the actuator, within a frequency range that is not lower than the fundamental frequency of the structure. The actuator dynamics are represented through inertial, stiffness, and damping effects. Damping arises primarily from mechanical friction and hydraulic flow losses, whereas stiffness results from the compressibility of the hydraulic fluid filling the pressure chambers.

The inertial effects are associated with the moving masses, particularly the cylinder rod.

The motion of the piston rod induces an exchange of hydraulic oil between the actuator and the accumulator. A specific characteristic of this actuator is that the dynamic effects associated with oil flow through the connecting pipe cannot be neglected. The oil volume within the pipe is not modeled as a distributed continuous oscillator but rather as a lumped parameter element. Consequently, the model exhibits two degrees of freedom. The inertial effect of the pipe flow can be represented by an equivalent mass, which is greater than the actual mass of the oil contained in the pipe.

Figure 5 illustrates the dynamic characteristics of the actuator model. The formulation accounts for the stiffness contributions of the hydraulic oil volumes in the three pressure chambers, as well as the inertial effects of both the cylinder rod and the hydraulic pipe flow. When the external load is neglected, the system behaves as a two-degree-of-freedom system with two natural frequencies. The model further describes the dynamic interaction between the actuator and the stay cable.

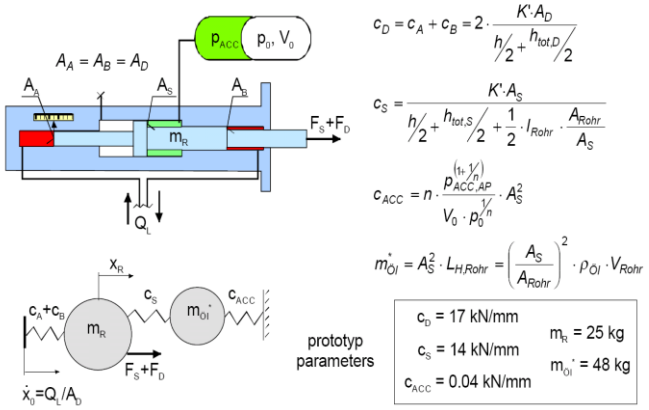


Fig. 5 *Dynamic parameters of the actuator*

4.2 Load Influence on Dynamic Actuator Characteristics

The theory of active damping in cable-stayed bridges must account for various nonlinear effects of the stay cables, including geometric extension and slackening phenomena.

A stay cable can be modeled as a continuous oscillator exhibiting complex dynamic behavior, capable of vibrating in both transverse and longitudinal modes. Since the actuator operates along the longitudinal axis of the cable, only longitudinal forces contribute directly to actuator motion.

The natural frequencies of a restrained cable primarily depend on its length and material properties.

Figure 6 presents the dynamic characteristics of the actuator under loading conditions, illustrating its response within the coupled actuator–cable system.

The most important is, that the stiffness CD of the actively controlled pressure chambers will be higher than the cable stiffness CK. So, the influence of the cable stiffness on the dynamic's actuator characteristics is negligible. The influence of the cable mass on the actuator performance is characterized by: cable mass and stiffness are distributed over the length far from the actuator and do not influence the actuator. Only mass shares nearby the actuator delay the actuator. It can be shown, that the inertial effect of the cable on the control behavior of the actuator can take into account, if a share of the total cable mass is added to the actuator rod mass.

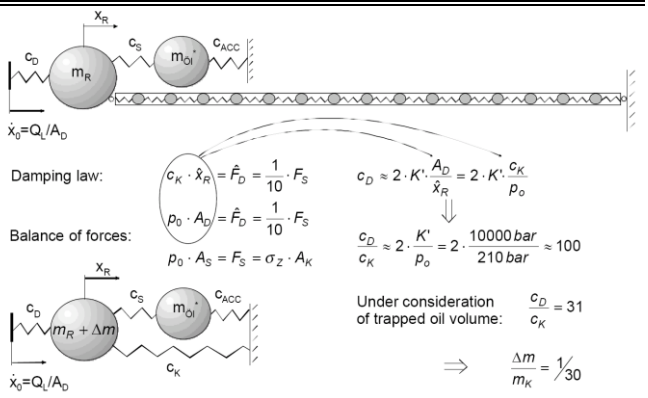


Fig. 6 *Influence of cable mass and stiffness on dynamic actuator characteristics*

5. Summary and Conclusions

Cable-stayed bridges are highly sensitive to dynamic oscillations caused by environmental and operational loads. The proposed Integral Force Feedback (IFF) concept enhances structural damping through collocated sensor–actuator pairs installed between the stay cables and the bridge deck. This approach enables efficient vibration reduction while requiring only minimal external power input under normal operating conditions.

Static loads are compensated by hydraulic accumulators operating without continuous power supply, thereby improving energy efficiency and reducing operational demands. For optimal performance, the actuator system must be designed such that its natural frequency is at least ten times higher than the dominant structural frequencies to be controlled, typically ranging between 0.5 and 3 Hz. This requirement ensures effective damping even under high loading conditions and for long stay cables.

Overall, the integration of active damping with passive hydraulic compensation provides a reliable and energy-efficient solution for mitigating vibrations in cable-stayed bridges, contributing to improved structural durability, operational safety, and extended service life.

6. References

1. Institute of Fluid Power and Motion Control, Dresden University of Technology, 01062 Dresden, Germany.
2. Olosz, A.; Kövesdi, B.; Hegyi, P.; Dunai, L. Improvement of Stockbridge Damper Design for Cable-Stayed Bridges. *Appl. Mech.* **2024**, *5*, 818-838. https://doi.org/10.3390/applmech5040046
3. Bossens, F.; Dumoulin, C.; Magonette, G.;Marazzi, F. Active Control Experiment of a large-scale Cable-Stayed Bridge Mock-Up; 3 rd International Symposium on Cable Dynamics, Trondheim, Norwegen, 16.-18.8.1999.
4. Zhu, X.; Jiang, Y.; Weng, G. Study of the Dynamic Reaction Mechanism of the Cable-Stayed Tube Bridge under Earthquake Action. *Buildings* **2024**, *14*, 2209. https://doi.org/10.3390/buildings14072209
5. Preumont, A.; Helduser, S.; Försterling, H.; Bossens, F.; Bonefeld, R.: Active Tendon Control of Cable-Stayed Bridges: Control Strategy and Actuator Design; IABSE-Conference on: Cable-Stayed Bridges – Past, Present and Future, Malmö, 2.-4.6. 1999
6. Achkire, Y.: Active Tendon Control of Cable-stayed Bridges; Dissertation, Active Structures Laboratory, Université Libre de Bruxelles, 1997
7. Hysenlliu, M., Bidaj, A., Deneko, E., Bilgin, H. Comparative Seismic Assessment and Strengthening of Two Storey URM Dwellings in Kruja Insights from Four Case Studies. *Journal of Integrated Engineering and Applied Sciences*. **2026**; 4(1); 286-305.
8. Port de Normandie. https://www.choosenormandy.com/pont-de-normandie-connecting-normandy/
9. Shi, Z.; Zhong, R.; Jin, N. Seismic Damage Identification of Composite Cable-Stayed Bridges Using Support Vector Machines and Wavelet Networks. *Sustainability* **2023**, *15*, 108. https://doi.org/10.3390/su15010108
10. Preumont, A.: Vibration control of Active Structures: An Introduction; Kluwer Academic Publishes, 1997
11. Liu, Q.; Liu, Z.; Zhao, J.; Lei, Y.; Zhu, S.; Wu, X. Seismic Optimization of Fluid Viscous Dampers in Cable-Stayed Bridges: A Case Study Using Surrogate Models and NSGA-II. *Buildings* **2025**, *15*, 1446. https://doi.org/10.3390/buildings15091446

Two-stroke low-speed engines and maritime transition to net-zero

Ozren Bukovac*, Jelena Kolundžija
University of Rijeka, Faculty of Engineering, Vukovarska 58, Rijeka, Croatia
ozren.bukovac@riteh.uniri.hr

Abstract: *The world's maritime industry is currently undergoing an unprecedented transformation, driven by the climate crisis and the strict regulations imposed by the International Maritime Organization (IMO). The IMO's Greenhouse Gas (GHG) Strategy for 2023 has fundamentally redefined the industry's goals, from gradually reducing carbon intensity to comprehensively phasing out greenhouse gas emissions by 2050. At the heart of this transition is the low-speed, two-stroke engine, which serves as the main source of propulsion for most deep-sea merchant ships. Contrary to being considered a legacy of the limitations of the fossil fuel-dependent era, these engines are being transformed into highly efficient and adaptable platforms capable of using the next generation of carbon-neutral and zero-carbon energy carriers. This analysis examines the technical, operational and regulatory mechanisms that enable the maritime sector to meet its net-zero emission commitments, with a particular focus on dual-fuel engine architectures, advanced combustion control, and the holistic integration of ship energy systems.*

Keywords*: TWO-STROKE LOW-SPEED ENGINES, NET-ZERO 2050, ALTERNATIVE MARINE FUELS, EMISSION REDUCTION*

1. Introduction

Two-stroke slow-speed diesel engines are used in majority on big containers ships. The two-stroke low-speed engine prevails in maritime applications because of its endurance and high thermal efficiency, generally exceeding 50%. Low-speed engines have an extended combustion stroke, enabling the complete burning of complex fuels. This feature makes the two-stroke engine a strong option for using alternative fuels.

The adoption of the 2023 IMO GHG Strategy represents a historic deal in the fight against climate change and signifies a breakthrough in reducing the environmental impact of international shipping. This revised strategy replaces the 2018 initial target of a 50% reduction in emissions by 2050 with a much more ambitious goal of reaching well-to-wake (WTW) net-zero emissions. The WTW perspective is critical, as it accounts for emissions throughout the entire fuel lifecycle, from production and transport to combustion at sea, thereby preventing the mere shifting of emissions to other industrial sectors [1].

To provide the industry with a clear trajectory, the IMO established a series of ambition levels and indicative checkpoints for 2030 and 2040. These milestones are designed to ensure that the global fleet stays on track with the Paris Agreement's 1.5°C temperature goal [2].

Table 1: *IMO Decarbonization Targets (Base Year 2008).*

Milestone Year	Minimum Ambition Level	Strive Target (1.5°C Aligned)	Primary Regulatory Mechanism
2030	20% Absolute GHG Reduction	30% Absolute GHG Reduction	CII Rating / EEXI Compliance
	40% Carbon Intensity Reduction	—	Fuel GHG Intensity Standard
	5% ZNZ Fuel Uptake	10% ZNZ Fuel Uptake	Early Market Incentives
2040	70% Absolute GHG Reduction	80% Absolute GHG Reduction	Global Fuel Standard / Pricing
2050	Net-Zero GHG Emissions	—	Net-Zero Framework (NZF)

The IMO's Net-Zero Framework (NZF) is the regulatory response to these goals [3]. The NZF sets a goal-based marine fuel standard that controls the gradual decrease of GHG intensity. It also includes an economic aspect: the first-ever global maritime GHG emissions pricing mechanism. Starting in 2028, this mechanism is expected to set an initial price of about USD 100 per ton, which would bring in between USD 11 billion and USD 13 billion a year. These funds will help pay for the development of zero- and near-zero (ZNZ) fuels, which will help close the big price gap between regular heavy fuel oil (HFO) and alternative fuels, which are usually three to four times pricier. The NZF only applies to ships that are more than 5,000 gross tons and travel across oceans. These ships are responsible for 85% of all emissions.

The framework's adoption was pushed back by a year in late 2025, but the need to cut carbon emissions is still strong. The move is a clear sign to shipowners that the time of using fossil fuels is coming to an end.

Classic regulations often looked only at tank-to-wake (TTW) emissions, or what comes out of the exhaust, so, e.g., "green" gases or e-fuels seemed perfect. When you turn on WTT, you see that some fuels have very low TTW emissions (e.g., hydrogen, ammonia) but can have high WTT emissions if produced from fossil sources without capturing CO_2 . Conversely, some fuel may have moderately high TTW emissions but a very favorable WTT if, for example, it is an advanced biofuel from waste.

To meet plans of net zero using two-stroke slow-speed engines alternative fuels like hydrogen, methanol and ammonia have to be used (Fig. 1). The MAN B&W ME series and WinGD X-engines exhibit a trend towards electronic regulation. Electronically controlled engines can accurately regulate fuel injection timing and pressure to accommodate the diverse physical and chemical properties of alternative fuels. Marine two-stroke engines have a high volume-to-surface ratio. This reduces heat loss through the walls and makes the temperature in the combustion chamber more even. This feature is especially useful when burning fuels like ammonia and methanol. Also, the dual-fuel design lets these engines run on regular fuels until the bunkering infrastructure for alternative fuels is ready.

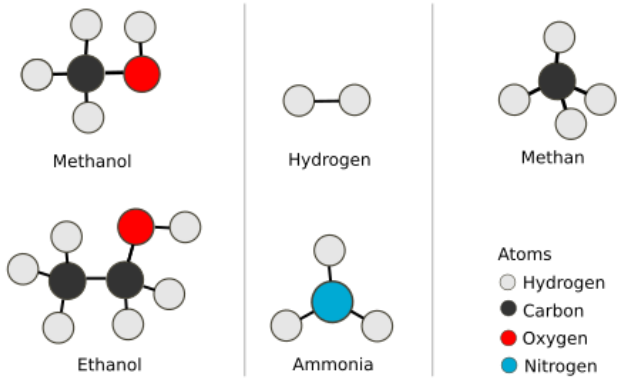


Fig. 1 *Fuels that are in consideration for use in future to meet net-zero or near neto-zero emissions in maritime.*

2. Analysis of alternative fuels and other measures

Methanol and Ethanol

Methanol has become a leading and economically viable option for reducing carbon emissions in shipping. This is due to its liquid state at room temperature and the technological advancements that have been made.

Two-stroke methanol engines, such as the MAN B&W ME-LGIM, have been in operation since 2016, primarily on methanol carriers [5]. Recently, this technology has expanded into the Very Large Container Vessel (VLCV) segment, with hundreds of orders placed by major carriers.

When produced as green methanol using renewable hydrogen and captured CO_2, this fuel has almost no emissions throughout its life cycle. From a tank-to-wake perspective, burning methanol significantly reduces emissions and almost eliminates particulate matter. The diesel-cycle methanol engine utilizes a high-pressure direct injection system, where a small amount of pilot fuel is used to initiate combustion, maintaining the high efficiency associated with the conventional diesel process.

Ethanol is gaining traction as a secondary alcohol fuel, particularly in regions where bioethanol is produced competitively from agricultural biomass [6]. WinGD has pioneered the development of the first ethanol-fueled two-stroke engine, with deliveries scheduled to begin in 2026 [6]. This engine is an adaptation of the X-DF-M methanol platform, utilizing the same combustion concept and safety regulations [7].

Ethanol's technical challenges include its higher energy density compared to methanol. This requires changes to the fuel injector nozzle design and control systems to optimize the injection volume [6]. Research starting in 2014, like the EU-funded HERCULES 2 project, has confirmed the use of flexible injectors for different alcohol fuels, giving shipowners more options for fuel [6].

Ammonia

Ammonia is fuel that does not have carbon atoms so when burning it does not generate CO_2 emissions, but it does generate NO_x emissions and postprocessing is necessary to annulate them.

Ammonia (NH_3) is widely regarded as a critical enabler for the 2050 net-zero target because it contains no carbon and can be produced at scale as green ammonia using renewable energy [8]. However, its slow burning velocity, high auto-ignition temperature, and toxicity present formidable engineering hurdles.[4]

Major engine designers have achieved significant milestones in ammonia propulsion. MAN Energy Solutions completed full-scale testing of its two-stroke ammonia dual-fuel engine in Copenhagen in late 2024 [4]. Similarly, WinGD delivered its first X-DF-A ammonia-fueled engine for installation on an EXMAR LPG carrier in 2025 [7] In Japan, the Green Innovation Fund project has supported the construction of the MAN B&W 7S60ME-Ammonia engine by Mitsui E&S, which will power a Newcastlemax bulk carrier built by Imabari Shipbuilding [9].

Ammonia combustion in two-stroke engines typically utilizes a diesel-cycle combustion process with a 5% mass (or energy) of diesel pilot fuel [8]. This approach addresses ammonia's poor ignition properties and allows for controlled combustion timing. A major concern with ammonia is the production of nitrous oxide, a greenhouse gas that is 298 times more effective at trapping heat than CO_2 [10]. Research indicates that advancing the pilot fuel injection timing (e.g., to 30° BTDC) can significantly reduce NO_x and unburned ammonia emissions. [11]

Advanced Combustion Control and Aftertreatment Systems

To comply with the IMO's Tier III limits while operating on alternative fuels, two-stroke engines rely on a combination of sophisticated in-cylinder measures and external exhaust aftertreatment.

Modern combustion control strategies involve the use of Variable Compression Ratio (VCR) and electronic injection timing to adapt to different fuel reactivities [12]. For ammonia engines, multi-pulse or split injection of pilot fuel has been shown to improve mixture preparation and reduce pressure oscillations [11]. Injector orientation and nozzle spray angles are also being optimized; vertical orientations with symmetric spray angles can reduce formation by up to 85% compared to conventional diesel combustion [13].

Selective Catalytic Reduction (SCR) remains the primary technology for abatement. In ammonia engines, SCR systems are particularly vital as they can also neutralize any ammonia slip that escapes the combustion chamber [14]. For LNG engines, the introduction of Intelligent Control by Exhaust Recirculation (iCER) has proven effective in reducing methane slip by 50% while improving thermodynamic efficiency [12].

Integrated, on-engine aftertreatment solutions are becoming the industry standard, allowing for more compact engine room designs and lower installation costs. These systems ensure that vessels remain compliant with air quality regulations while pursuing global GHG targets.

Integration and Hybridization

Decarbonization cannot be achieved by engine technology alone; it requires the optimization of the entire ship's energy system. As alternative fuels are more expensive and possess lower energy densities, the "efficiency first" is very important principle.

The integration of battery energy storage systems (BESS) with the main two-stroke engine allows for peak shaving and optimized spinning reserves [12]. By utilizing shaft generators—also known as Power Take-Off (PTO) systems—vessels can generate electrical power from the efficient main engine, reducing the need to operate less efficient auxiliary diesel generators.

Hybrid control systems, exemplified by WinGD's X-EL, regulate energy distribution among the main engine, shaft generator, and batteries, thereby maintaining the main engine's optimal operational efficiency. This strategy can diminish overall fuel consumption by 0.1–0.5 tons daily, translating to potential annual savings of up to USD 320,000 per vessel, contingent upon fuel type and operational parameters [15].

Furthermore, waste heat recovery systems, which harness thermal energy from exhaust gases to power steam turbines or supply process heat, are becoming increasingly vital on vessels utilizing cryogenic or ammonia-based fuels.

Hybrid arrangements incorporating fuel cells and batteries have shown promise in reducing emissions associated with shipboard power generation [16].

Operational Efficiency: EEXI, CII, and the Role of Slow Steaming

Operational measures provide the most immediate pathway to emission reductions, often requiring minimal capital expenditure compared to technical retrofits [17]. The regulatory drivers for these measures are the Energy Efficiency Existing Ship Index (EEXI) and the Carbon Intensity Indicator (CII).

A ship's speed and its fuel consumption are related in a way that isn't straightforward. Reducing speed, often called "slow steaming," can significantly lower fuel use and is often the main method ships use to improve their CII ratings [17]. Moreover, digital tools, such as data-driven voyage planning and weather routing, help improve operational efficiency.

Calculations suggest that if shipowners only focus on changing fuels without improving efficiency, the industry won't meet the 2030 indicative checkpoint [1]. This highlights the importance of these measures.

Table 2: *Effectiveness of Short-Term Operational and Technical Efficiency Measures*

Strategy	Estimated GHG Reduction Potential	Implementation Difficulty	Regulatory Context
Vessel Size Optimization	47%	High (Fleet Planning)	EEDI / EEXI
Speed Reduction / Slow Steaming	20–30%	Low (Operational)	CII Compliance
Hull Shape Optimization	15%	Moderate (Newbuild)	EEDI Phase 3
Air Lubrication Systems	8%	Moderate (Retrofit)	CII Improvement
Advanced Hull Coatings	5%	Low (Maintenance)	SEEMP Part III

Future Scenarios to 2050: Biofuels, Nuclear, and Arctic Routes

As the industry approaches 2050, several distinct pathways emerge depending on fuel availability and technological breakthroughs.

Sustainable biofuels, such as Hydrotreated Vegetable Oil (HVO) and Fatty Acid Methyl Esters (FAME), offer a "drop-in" solution that is fully compatible with existing two-stroke engines. While biofuels are crucial for achieving immediate objectives, their sustained utility may be constrained by the availability of feedstocks and competition from the aviation and terrestrial transportation industries.

For sectors where zero-carbon fuels are not feasible because of energy density constraints, like Ultra-Large Container Vessels (ULCVs) operating on high-speed routes, nuclear propulsion is being re-evaluated as a potentially disruptive technology [18]. Contemporary Small Modular Reactors (SMRs) present a high-power density and a 20-year operational lifespan, which could eliminate all bunker expenses and carbon-related costs. Lloyd's Register's analysis suggests that a 15,000 TEU nuclear-powered containership could attain a 38% greater annual cargo capacity by maintaining a speed of 25 knots, in contrast to slow-steaming vessels [19].

The opening of the Arctic Sea Route due to polar ice melt offers the potential to reduce voyage distances between Europe and Asia by 40%. While this could reduce emissions per voyage, modeling suggests that increased total traffic and the lack of strict fuel standards in the region could raise global shipping emissions by 8.2% by 2100 unless a net-zero strategy is strictly enforced in Arctic waters [20].

Economics of the Global Fuel Transition

A global carbon pricing system is crucial for encouraging the transition from fossil fuels. Without such a system, the higher cost of green methanol or ammonia is often a barrier for many operators. The International Maritime Organization's proposed price of USD 100 per ton of CO_2 is a starting point, but researchers suggest that higher prices may be needed to meet the 1.5°C limit [21]. Investing in energy efficiency on ships can significantly reduce the overall cost of this transition. Each percentage point of increased efficiency lowers the total need for expensive alternative fuels, which in turn reduces the investment needed for green fuel production infrastructure [1].

3. Conclusion

The maritime industry is no longer at a crossroads; it has chosen the path of decarbonization. The continued innovation in two-stroke propulsion and shipboard energy management ensures that this journey toward net-zero is not only technically feasible but also commercially sustainable for the global fleet.

To meet the needs of the world's clean energy fleet, currently unavailable amounts of renewable solar and wind energy are needed. Not only ships compete for this energy, but also land transport, heavy industry and households. The two-stroke engine's ability to burn methanol, ammonia, ethanol, and biofuels ensures that the global fleet can adapt to the most available and cost-competitive green fuels as they emerge. The shift from a single-engine focus to an integrated ship energy system—incorporating hybridization, shaft generators, and waste heat recovery—is essential for making the use of zero-carbon fuels economically viable. The IMO's 2023 Strategy and the subsequent Net-Zero Framework provide the long-term certainty required for shipowners to invest in expensive newbuilds and retrofits. Short-term goals will be met primarily through efficiency improvements and slow steaming. While biofuels and alcohols will lead the transition in the current decade, ammonia and potentially nuclear propulsion represent the long-term solutions for a truly zero-carbon maritime industry by mid-century. Nuclear propulsion would likely render two-stroke slow-speed "diesel" engines obsolete.

3. References

1. https://www.zerocarbonshipping.com/files/implications-of-the-2023-imo-ghg-strategy-for-the-shipping-industry.pdf 2026.
2. https://www.imo.org/en/ourwork/environment/pages/2023-imo-strategy-on-reduction-of-ghg-emissions-from-ships.aspx 2026.
3. https://www.imo.org/en/mediacentre/pressbriefings/pages/imo-approves-netzero-regulations.aspx 2026.
4. https://www.man-es.com/docs/default-source/marine/tools/man-b-w-two-stroke-engine-operating-on-ammonia.pdf 2026.
5. https://www.everllence.com/discover-stories/two-stroke-engine-future-technologies 2026.
6. https://wingd.com/news-media/news/wingd-to-introduce-first-ethanol-fuelled-marine-two-stroke-engine-in-2026 2026
7. https://wingd.com/news-media/news/the-year-shipping-hit-the-decarbonisation-crossroads-and-how-2026-could-decide-the-route-ahead 2026.
8. https://www.ammoniaenergy.org/wp-content/uploads/2020/01/engineeringthefuturetwostrokegreenammoniaengine1589339239488-2.pdf 2026.
9. https://ammoniaenergy.org/articles/mitsui-o-s-k-lines-ammonia-fueled-capesize-bulkers-chemical-tankers-to-hit-the-water-from-next-year/ 2026.
10. https://ghgprotocol.org/sites/default/files/2024-08/Global-Warming-Potential-Values%20%28August%202024%29.pdf
11. A. Yousefi, H. Guo, M. Birouk, Fuel, **212**, 332-346, (2018)
12. https://oneweb.wingd.com/news-media/news/wingd-takes-holistic-approach-to-marine-decarbonisation-with-ecosystem-of-solutions
13. E. Shim, H. Park, C. Bae, Fuel, **262**, 116436, (2020)
14. https://www.classnk.or.jp/hp/pdf/research/rd/2024/10_e05.pdf
15. M. Tadros, E. Boulougouris, A. M. Ypsilantis, N. Hadjioannou, V. Sakellis, Energies, **18**, 6070, (2025)
16. M. Altosole, F. Balsamo, U. Campora, E. Fasano, F. Scamardella, Energies, **17**, 2498, (2024)
17. https://www.dnv.com/publications/net-zero-guide-practical-approaches-for-global-shipping-companies 2026.
18. https://www.dnv.com/news/2025/nuclear-propulsion-is-a-viable-solution-for-maritime-decarbonization/ 2026.
19. https://www.lr.org/en/knowledge/press-room/press-listing/press-release/2025/nuclear-powered-containerships-could-unlock-$68-million-in-annual-savings-and-eliminate-ghg-emissions/ 2026.
20. P. Zhao, Y. Li, C. Zhang, T. Kang, Z. He, G. Huang, S. Zhang, X. Zhang, Y. Xu, W. Kong, Nature Communications, **16**, 8431, (2025)
21. https://transport.ec.europa.eu/news-events/news/landmark-agreement-towards-achieving-net-zero-emissions-global-shipping-2050-2025-04-11_en 2026.

Investigation of Cutting Edge Radius Influence on Tool Wear Using FEM Simulation in DEFORM 3D

Martin Necpal[1,*], Marek Vozár[1]
Slovak University of Technology in Bratislava, Faculty of Material Science and technology in Trnava, Slovakia[1]
martin.necpal@stuba.sk

Abstract: *This article presents a study of the influence of cutting edge rounding on the wear of monolithic milling tools using the finite element method (FEM) and DEFORM 3D software. After manufacturing by grinding, monolithic milling tools have considerably sharp cutting edges that are prone to breakage and chipping. Industrial practice and cutting edge zone theory recommend edge preparation to create a defined cutting edge radius. The optimal radius value depends on the machined material, cutting conditions, and other factors, and remains unclear. This study investigates the influence of the cutting edge radius on tool wear using 3D FEM simulation with the Usui wear model, which is considered suitable for machining processes. Initial simulations with sharp cutting edges were performed to determine the sensitivity of wear predictions to the Usui model constants. Subsequently, different cutting edge radii were simulated under identical cutting conditions. The simulation results demonstrate the relationship between cutting edge radius and wear progression. The findings provide guidelines for selecting suitable cutting edge preparation parameters to minimize tool wear when milling with monolithic tools.*
Keywords*: CUTTING EDGE RADIUS, TOOL WEAR SIMULATION, FEM, DEFORM, USUI MODEL, MILLING*

1. Introduction

Tool wear is the primary mechanism that limits tool life in milling and directly affects surface quality and machining costs [1, 2]. After grinding, monolithic milling tools have very sharp cutting edges. Industrial experience shows that such edges are prone to rapid wear and micro-chipping [3]: the geometry is mechanically unstable and cannot withstand the concentrated stresses at the cutting edge during material removal. Tool manufacturers therefore recommend edge preparation by multitude of available methods to create a controlled cutting edge radius [4].

The cutting edge radius (also called edge rounding or hone radius) affects cutting forces, heat generation, chip formation, and wear mechanisms [5]. A larger radius distributes the load over a greater contact area, improving edge stability, but also increases cutting forces and heat generation. A smaller radius keeps forces lower but leaves the edge susceptible to premature failure. The optimal value depends on workpiece material, cutting conditions, and tool material [6]. Finite element method (FEM) simulation has become standard practice for studying machining processes [7], enabling investigation of stress and temperature distributions in the cutting zone that are difficult to measure directly. Several commercial packages support machining simulation, including DEFORM, AdvantEdge, and Abaqus [8].

Tool wear prediction in FEM simulation requires a wear model. The Usui wear model is commonly used for this purpose [9]. This model relates wear rate to interface variables:

$$\frac{dW}{dt} = A.\sigma_n.v_s.exp\left(-\frac{B}{T}\right) \quad (1)$$

where W is wear depth, σ_n is normal stress, v_s is sliding velocity, T is interface temperature, and A and B are material constants that must be calibrated [10]. This study investigates the influence of cutting edge radius on tool wear in milling using 3D FEM simulation in DEFORM. First, the Usui wear model is calibrated using simulations with a sharp cutting edge. The sensitivity of wear predictions to constants A and B is analyzed. Then, simulations with three different cutting edge radius (5 µm, 15 µm, and 45 µm) are performed to determine the optimal radius for minimal wear. inner layer means higher accuracy, but longer production time).

2. Materials and Methods

2.1. Simulation setup

The FEM simulations were performed using DEFORM software. Two simulation approaches were used: 2D simulations for Usui wear model calibration with a sharp cutting edge, and 3D simulations for investigation of different cutting edge radius. The 2D calibration model is defined identically to the 3D wear model in terms of material properties, constitutive models, and cutting conditions. The dimensional reduction to 2D was chosen solely to reduce computation time during calibration. The only variable between the 3D simulations is the cutting edge radius; all other parameters remain constant.

The cutting tool geometry was derived from the commercial SECO Tools JS754 100E2C.0Z4-HXT end mill. The tool material is cemented carbide grade CTS20D, which corresponds to ISO classification K20–K40. The tool was modeled as a rigid body, which is standard practice in machining FEM when tool deformation is negligible compared to workpiece deformation. Consequently, only thermal properties are assigned to the tool material (Table 1). The method used to extract the 2D and 3D model geometry from the commercial tool follows the same principle as described in [17].

Table 1: *Thermal properties of the tool material (carbide, rigid body).*

	Value	Unit
Thermal conductivity	59	$Wm^{-1}K^{-1}$
Specific heat	290	J/Kg.K
Density	15 600	$Kg.m^{-3}$

The workpiece material behavior was described by the Johnson-Cook constitutive model [11, 12]:

$$\bar{\sigma} = (A + B\bar{\varepsilon}^{n})\left(1 + C\ ln\frac{\dot{\bar{\varepsilon}}}{\dot{\varepsilon}_0}\right)\left(1 - \left(\frac{T - T_{room}}{T_{melt} - T_{room}}\right)^{m}\right) \quad (2)$$

where $\bar{\sigma}$ is the equivalent flow stress, $\bar{\varepsilon}$ is the equivalent plastic strain, $\dot{\bar{\varepsilon}}$ is the equivalent strain rate, $\dot{\varepsilon}_0$ is the reference strain rate, T is temperature, T_{room} is room temperature, and T_{melt} is the melting temperature. The constants A, B, n, C, and m characterize the workpiece material. The workpiece material was AISI316L. Johnson-Cook constants and thermal properties for the workpiece are listed in Table 2.

Table 2: *Workpiece material Johnson-Cook constants and thermal properties*

	Symbol	Value	Unit
Yield stress	A	310.8	MPa
Strain hardening coefficient	B	881.38	MPa
Strain hardening exponent	n	0.178	-
Strain rate sensitivity	C	0.19	-
Thermal softening exponent	m	1.25	-
Thermal conductivity		18.9	$Wm^{-1}K^{-1}$
Specific heat		500	J/Kg.K
Density		8000	$Kg.m^{3}$

The 3D simulation setup is shown in Figure 1. To reduce computational demands, the model was simplified by representing only a segment of the tool containing the main cutting edge rather than the full tool geometry. This allows the simulation to capture the cutting mechanics and chip formation without excessive computation time.

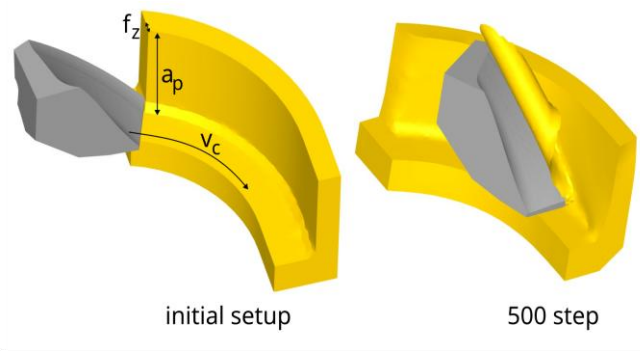


Fig. 1 *3D FEM simulation setup in DEFORM: simplified model showing the main cutting edge segment and chip formation*

The cutting conditions were kept constant for all simulations (Table 3):

Table 3: *Thermal properties of the tool material (carbide, rigid body).*

Cutting Parameter	Symbol	Value	Unit
Cutting speed	v_c	190	m/min
Feed per tooth	f_z	0.09	mm
Axial depth	a_p	3	mm
Radial depth	a_e	3	mm

2.2. Tool geometry and cutting edge radius

The monolithic milling tool geometry was modeled according to standard tool parameters. A sharp edge (as-ground condition, radius < 2 µm) was used exclusively in the 2D calibration model. Following cutting edge radii sizes were investigated in the 3D wear simulations: $r_{\_n}$ = 5, 15, and 45 µm. Figure 2 shows the FEM mesh of the tool with the three edge radius configurations.

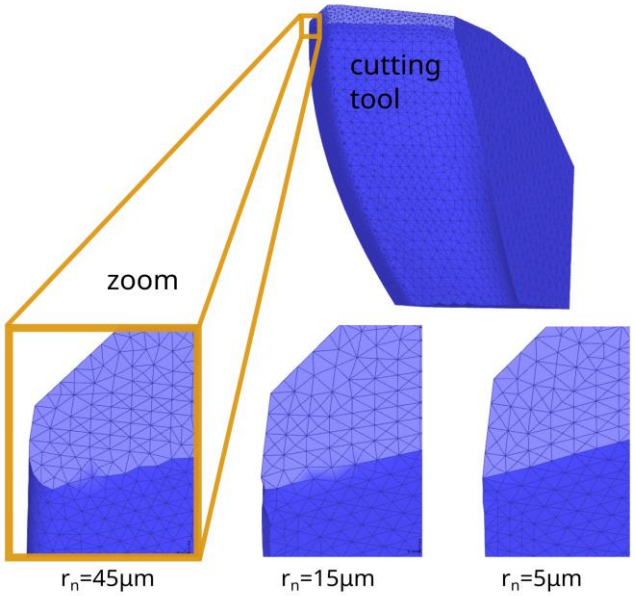


Fig. 2 *Edge radius configurations: r_n = 5, 15, and 45 µm.*

2.3. Usui wear model calibration

The Usui wear model (Equation 1) requires calibration of constants A and B. These constants depend on the tool-workpiece material combination and must be determined experimentally or through inverse analysis [13]. Binder et al. [14] applied a similar calibration procedure for coated carbide tools in turning, showing that constant selection strongly affects predicted wear.

Due to the substantially lower computational cost compared to 3D simulation, calibration was performed using 2D simulations of milling with a sharp cutting edge. Three combinations of constants were evaluated, as summarized in Table 4.

Table 4: *Tested Usui constant and resulting wear rates from 2d calibration simulation*

No.	A	B	Wear
1	$1x10^{-7}$	2000	$6.7\ x10^{-3}$ m.m^{-3}s^{-1}
2	$1x10^{-8}$	2500	$3\ x10^{-4}$ mm^{-3}s^{-1}
3	$1x10^{-9}$	3000	$1\ x10^{-5}$ mm^{-3}s^{-1}

Cutting speed was held constant throughout the calibration. Although varying cutting speed would provide broader validation of the constants, the available experimental data for sharp cutting edge wear were obtained under constant cutting conditions, which constrained the calibration accordingly.

2.4. Simulation procedure

The simulation procedure consisted of two phases. In the calibration phase, a 2D FEM model with a sharp cutting edge was constructed and simulations were run with different combinations of constants A and B. Wear distribution and depth were analyzed and the constants that best matched available experimental reference data were selected for further use.

In the edge radius investigation phase, the calibrated Usui constants were applied to three 3D models with cutting edge radius of 5, 15, and 45 µm. All simulations were run under identical cutting conditions and wear development was compared across the three configurations.

3. Result and Discussion

3.1. Calibration result

The 2D calibration simulations with a sharp cutting edge showed clear sensitivity of predicted wear to both Usui constants (Table 4). Increasing A by one order of magnitude from 10^{-8} to 10^{-7} increased the wear rate by more than twenty times. Decreasing A to 10^{-9} produced negligible wear, inconsistent with experimental observations for sharp cutting edges.

Based on comparison with experimental results for sharp cutting edge wear and in agreement with values reported in the literature [14], the constants A = 10^{-8} and B = 2500 were selected, yielding a wear rate of 0.0003 m^{3}s^{-1}. These calibrated constants were applied to all subsequent 3D simulations of the cutting edge radius influence.

3.2. Influence of cutting edge radius on wear

Using the calibrated Usui model, simulations were performed for the three edge radius. Figure 3 shows the wear distribution on the tool rake face for each configuration.

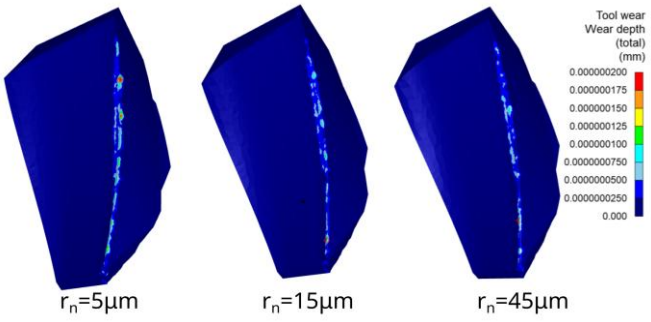


Fig. 3 *Wear distibution on cutting edge*

The results show that cutting edge radius affects both the location and magnitude of maximum wear. Key simulation output

variables extracted from the DEFORM results are compared in Table 5.

Table 5: *Simulation output variables for the tree cutting edge radius*

Parameter	R_n=45µm	R_n=15µm	R_n=5µm	Unit
Sl. velocity flank	3240	3240	3240	mms^{-1}
Sl. velocity rake	2025	2025	2025	mms^{-1}
Max interface press.	25.7	18.2	17.7	GPa
Max wear rate	$2.46x10^{-3}$	$3.86x10^{-3}$	$5.66x10^{-3}$	mm^3s^{-1}
Max wear dept	121	116	241	µm

Interface pressure increases with radius (17.7 to 25.7 GPa), as the blunter edge enlarges the contact zone and raises local contact stress. Despite this, the wear rate decreases with increasing radius: the sharp 5 µm edge produces the highest wear rate (0.00566 mm/s) because heat concentrates in a small volume at the tip, driving the exponential term in the Usui model. Maximum wear depth shows the clearest separation — 241 µm at 5 µm versus 116 and 121 µm at 15 and 45 µm — with the 15 µm radius offering the best overall result.

3.3. Analysis of wear mechanism

The wear mechanism shifts with edge radius. At 5 µm, stress and heat concentrate at the tip, producing rapid localized removal and the deepest wear (241 µm). At 15 µm, the thermal load spreads over a wider contact zone (Figure 4), yielding the lowest wear depth (116 µm) and a moderate wear rate — a balance between edge strength and contact pressure. At 45 µm, the larger contact area raises interface pressure to 25.7 GPa, promoting ploughing and resulting in wear depth (121 µm) comparable to the 15 µm case but under significantly higher stress, indicating less efficient edge geometry.

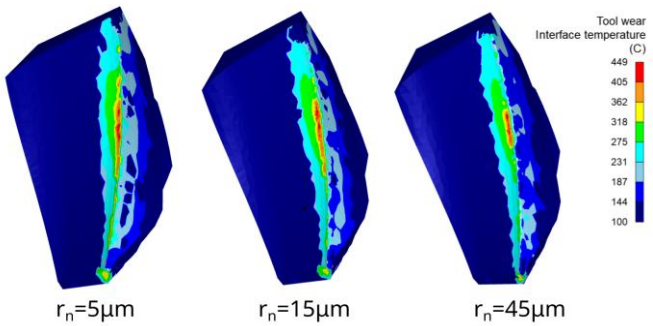


Fig. 4 *Temperature distribution on cutting edge for different edge radius*

3. Discussion

Figure 5 shows a comparison between the experimentally observed wear land on the cutting tool (left) and the numerically simulated tool wear (right) for identical cutting conditions as those used in the dissertation by Vozár [16].

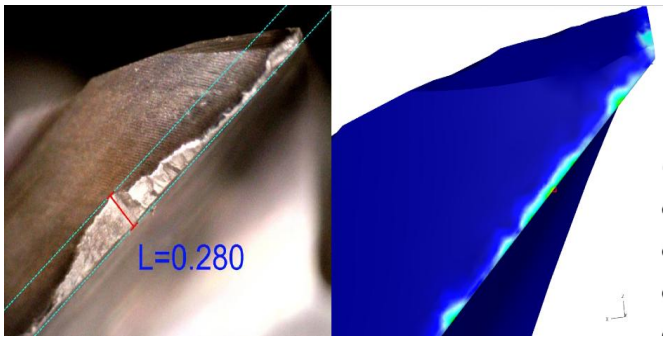


Fig. 5 *Comparison of the experimentally observed worn cutting tool (left) and numerically simulated tool wear (right) under identical cutting conditions as in the dissertation by Vozár [16].*

The FEM results show that cutting edge radius affects tool wear in milling. The Usui wear model, after proper calibration, can predict wear trends for different edge geometries. The calibration phase showed that both constants A and B must be carefully selected. Small changes in these values produce large differences in predicted wear. Calibration against experimental data is therefore necessary. Limitations of this study include the simplified tool geometry, the assumptions inherent in the Johnson-Cook material model, and the use of a single set of cutting conditions. Future work should extend the investigation to multiple cutting speeds and feed rates, and validate simulation results against experimentally measured wear data.

4. Conclusion

This study investigated the influence of cutting edge radius on tool wear in milling using 3D FEM simulation in DEFORM. The Usui wear model requires careful calibration of constants A and B. the 2D calibration simulations demonstrated high sensitivity to both parameters, with a one-order-of-magnitude change in A altering the predicted wear rate by more than twenty times. The constants $A = 10-8 and B = 2500, yielding a wear rate of 0.0003, were found to best match the available reference data and were applied to all subsequent 3D simulations.

Cutting edge radius affects both the distribution and magnitude of wear on the rake face. The as-ground sharp edge showed increased tool wear and higher temperature concentrations along the cutting edge. Among the tested radii of 5, 15, and 45 µm, the 15 µm radius size produced the lowest wear depth under the investigated cutting conditions. The optimal cutting edge radius is a compromise between edge stability and cutting performance. Based on the simulation results, a radius of approximately 15 µm is recommended for the investigated tool-workpiece combination. The FEM approach demonstrated here can inform edge preparation decisions ahead of experimental trials, shortening the development cycle for monolithic milling tools.

Acknowledge

This work was supported by the Slovak Research and Development Agency under the contract No. APVV-21-0071. This work was supported by the Science Grant Agency - project VEGA 1/0266/23.

Referencess

1. Y. Altintas, Manufacturing Automation (Cambridge Univ. Press, 2012)
2. V.P. Astakhov, Tribology of Metal Cutting (Elsevier, 2006)
3. B. Denkena, D. Biermann, CIRP Ann. 63, 631 (2014)
4. C.J.C. Rodriguez, Cutting edge preparation (PhD Thesis, Kassel Univ., 2009)
5. C.F. Wyen, K. Wegener, CIRP Ann. 59, 93 (2010)
6. T. Özel, T.K. Hsu, E. Zeren, Int. J. Adv. Manuf. Technol. 25, 262 (2005)
7. P.J. Arrazola et al., CIRP Ann. 62, 695 (2013)
8. DEFORM User Manual (Scientific Forming Technologies Corp., Columbus, OH, 2023)
9. E. Usui, T. Shirakashi, T. Kitagawa, Wear 100, 129 (1984)
10. Y.C. Yen et al., J. Mater. Process. Technol. 146, 82 (2004)
11. G.R. Johnson, W.H. Cook, Proc. 7th Int. Symp. Ballistics, 541 (1983)
12. S.P.F.C. Jaspers, J.H. Dautzenberg, J. Mater. Process. Technol. 122, 322 (2002)
13. A. Attanasio et al., CIRP Ann. 57, 61 (2008)
14. M. Binder, F. Klocke, D. Lung, Wear 330-331, 600 (2015)
15. N.E. Karkalos, A.P. Markopoulos, Procedia Manuf. 22, 107 (2018)
16. M. Vozár, Influence of cutting edge microgeometry (Dissertation, STU Bratislava, 2022)
17. M. Necpal, T. Vopát, M. Vozár, Acta Tech. Napoc. 67(1s) (2024)

Kinetic investigation of copper ions adsorption onto corn stalks

Milan Gorgievski *, Miljan Marković, Nada Štrbac, Vesna Grekulović, Milica Zdravković, Marina Marković, Kristina Božinović,
University of Belgrade Technical Faculty in Bor, Vojske Jugoslavije 12, 19210 Bor, Serbia
mgorgievski@tfbor.bg.ac.rs

Abstract: *Corn stalk was used as a biosorbent for the adsorption of copper ions from synthetic solutions. To examine the mechanism of the adsorption process and identify the potential rate-determining step, the following kinetic models were used in this study: the pseudo-first order kinetic model, the pseudo-second order kinetic model, the Elovich kinetic model, and the interparticle diffusion model. Kinetic studies show that copper ions adsorption followed the pseudo-second order kinetic model. The maximum adsorption capacity was 5.5 mg g^{-1}. The results indicate that corn stalk can be successfully used as a biosorbent for the adsorption of copper ions from synthetic solutions.*
Keywords*: CORN STALK, COPPER IONS, ADSORPTION, KINETIC INVESTIGATION*

1. Introduction

The increasing discharge of heavy metals into aquatic environments poses a serious threat to ecosystems and public health, necessitating the development of efficient and sustainable wastewater treatment methods. Agricultural by-products, such as corn stalks, represent a promising class of low-cost, environmentally friendly adsorbents for removing metal ions from contaminated water.

Owing to their lignocellulosic composition and abundance of functional groups, modified or untreated corn stalks can effectively capture heavy metal ions through adsorption processes. To better understand the mechanisms and efficiency of these systems, kinetic modelling plays a crucial role. The application of kinetic models – such as pseudo-first-order, pseudo-second-order, and Elovich kinetic model – provides insights into the rate-controlling steps and adsorption dynamics, contributing to the optimisation of treatment parameters for practical applications.

2. Materials and methods

Corn stalks collected from agricultural fields near Bor were used as the adsorbent. The material was first ground and sieved, and the sieve fraction (-1 + 0.4) mm was used for adsorption experiments.

2.1. Adsorption of Cu^{2+} ions onto corn stalks – experimental procedure

Adsorption experiments of Cu^{2+} ions onto corn stalks were carried out in a stirred batch reactor with a magnetic stirrer operating at 300 rpm. Before the experiments, the adsorbent was washed with distilled water, and pH and conductivity were monitored.

A synthetic Cu^{2+} solution (0.2 g dm^{-3}) served as the aqueous phase, with 0.5 g of adsorbent mixed with 50 mL of solution. After a specified contact time, the suspension was filtered, and the filtrate was analysed for residual copper, alkali metals, and alkaline earth metals. The amount of adsorbed copper and the adsorption capacity were determined by mass balance, and pH variation was monitored during adsorption. All experiments were conducted at room temperature.

The adsorption capacity, defined as the amount of metal adsorbed per unit mass of adsorbent, was calculated using the following equation:

$$q_{(t)} = \frac{c_i - c_{(t)}}{m} V \quad (1)$$

where: $q_{(t)}$ is the adsorption capacity (mg g^{-1}); c_i and $c_{(t)}$ are the initial and time-dependent metal concentrations in solution (mg dm^{-3}); V is the solution volume (dm^3); m is the mass of adsorbent (g).

3. Results and discussion

3.1 Kinetics of the adsorption process

To investigate the adsorption mechanism and identify the rate-limiting step, the following kinetic models were applied: pseudo-first-order, pseudo-second-order, Elovich, and intraparticle diffusion models, commonly used for liquid–solid adsorption systems [1,2].

Adsorption experiments were conducted at an initial Cu^{2+} concentration of 200 mg dm^{-3} and stopped after 90 minutes, assumed sufficient to reach equilibrium [3].

The adsorption capacity increased rapidly during the first 10 minutes, reflecting abundant active sites on the corn stalks. Thereafter, the rate slowed as available sites decreased and Cu^{2+} concentration in solution declined, approaching equilibrium after ~ 60 minutes, when the amount of adsorbed copper remained constant.

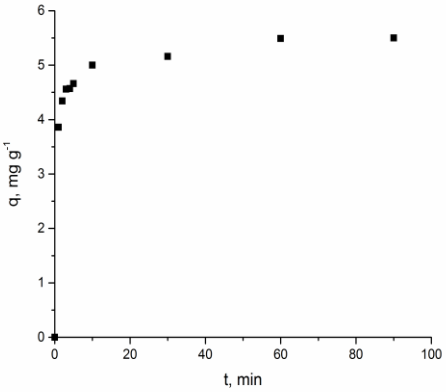


Fig. 1 *Change of copper ion adsorption capacity with time on corn stalks.*

3.1.1. Pseudo-first-order kinetic model (Lagergren model)

The pseudo-first-order kinetic model was proposed by Lagergren and is often referred to as the Lagergren model. This model assumes that the adsorption kinetics occur as a reversible process based on the adsorption capacity [4]. In differential form, the pseudo-first-order model can be expressed by equation (2):

$$\frac{dq_{(t)}}{dt} = k_1\left(q_e - q_{(t)}\right) \quad (2)$$

where: $q_{(t)}$ is the adsorbent capacity defined as the mass of metal adsorbed per unit mass of adsorbent at time t (mg g^{-1}); q_e is the equilibrium adsorption capacity (mg g^{-1}); k_1 is the rate constant for the pseudo-first-order kinetic model (min^{-1}).

For practical application, the following equation can be used:

$$\log(q_e - q_{(t)}) = \log(q_e) - \frac{k_1}{2,303} \cdot t \qquad (3)$$

A plot of $\log(q_e\text{-}q_{(t)})$ versus t provides a linear relationship, from which k_1 and q_e can be determined from the slope and intercept, respectively. Results are shown in Table 1.

As shown in Table 1, the pseudo-first-order model exhibits a correlation coefficient $R^2 = 0.89$, indicating a moderate fit. The calculated and experimental adsorption capacities differ significantly, suggesting limited applicability of this model.

Table 1: *Pseudo-first-order kinetic parameters for Cu^{2+} adsorption.*

Parameter/Ion	k_1 (min^{-1})	$q_{e,exp}$ (mg g^{-1})	$q_{e,cal}$ (mg g^{-1})	R^2
Cu^{2+}	0.082	5.5	1.76	0.89

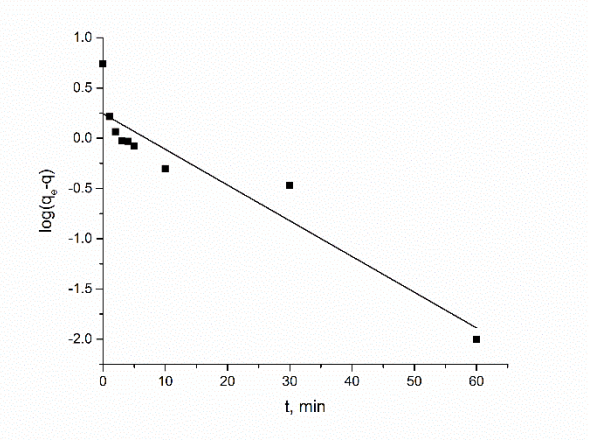


Fig. 2 *Pseudo-first-order kinetic model for copper ion adsorption on corn stalks.*

3.1.2. Pseudo-second-order kinetic model

The pseudo-second-order kinetic model assumes that both adsorption and ion exchange occur at the adsorbent surface, with chemisorption controlling the binding of the adsorbate [5]. The nonlinear form of the pseudo-second-order model is expressed as [6]:

$$\frac{dq_{(t)}}{dt} = k_2\left(q_e - q_{(t)}\right)^2 \qquad (4)$$

where: $q_{(t)}$ is the adsorbent capacity defined as the mass of metal adsorbed per unit mass of adsorbent at time t (mg g^{-1}); q_e is the equilibrium adsorption capacity (mg g^{-1}); k_2 is the rate constant for the pseudo-second-order kinetic model (g mg^{-1} min^{-1}).

For practical application, the following equation can be used:

$$\frac{t}{q_{(t)}} = \frac{1}{k_2 q_e^{\,2}} + \frac{t}{q_e} \qquad (5)$$

Values of k_2 and q_e were determined from the intercept and slope of the $t/q_{(t)}$ vs. t plot. The results are shown in Table 2.

Table 2: *Pseudo-second-order kinetic parameters for Cu^{2+} adsorption*

Parameter/Ion	k_2 (g mg^{-1} min^{-1})	$q_{e,exp}$ (mg g^{-1})	$q_{e,cal}$ (mg g^{-1})	R^2
Cu^{2+}	0.205	5.5	5.5	1

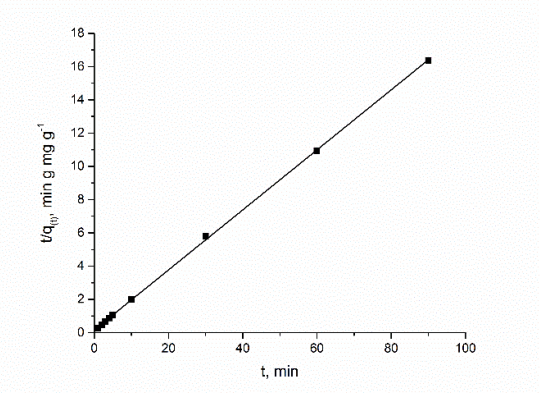


Fig. 3 *Pseudo-second-order kinetic model for copper ion adsorption on corn stalks.*

The perfect correlation ($R^2 = 1$) indicates excellent agreement between the experimental data and the pseudo-second-order model, confirming that chemisorption and ion exchange govern Cu^{2+} adsorption on corn stalks.

3.1.3. Elovich kinetic model

Originally developed for gas chemisorption on heterogeneous solid surfaces, the Elovich model is widely used for solution-phase adsorption [6]. It assumes that the adsorption rate decreases exponentially with increasing adsorbate coverage. In the literature, it is most commonly presented in the following form [7]:

$$\frac{dq_{(t)}}{dt} = \alpha e^{-\beta q(t)} \qquad (6)$$

where: α is the initial adsorption rate (mg g^{-1} min^{-1}); β is a parameter related to surface coverage and activation energy (g mg^{-1}); $q_{(t)}$ is the adsorbent capacity (mg g^{-1}).

For practical application, the following equation can be used:

$$q_{(t)} = \frac{1}{\beta}\ln(\alpha\beta) + \frac{1}{\beta}\ln t \qquad (7)$$

The values of the parameters α and β were determined from the intercept and slope of the $q_{(t)}$ vs. ln$t$ plot (Figure 4), and are presented in Table 3 together with the correlation coefficient R^2 for copper ions.

Table 3: *Elovich kinetic parameters for Cu^{2+} adsorption.*

Parameter/Ion	α (mg g^{-1} min^{-1})	β (g mg^{-1})	R^2
Cu^{2+}	4.073	0.4	0.958

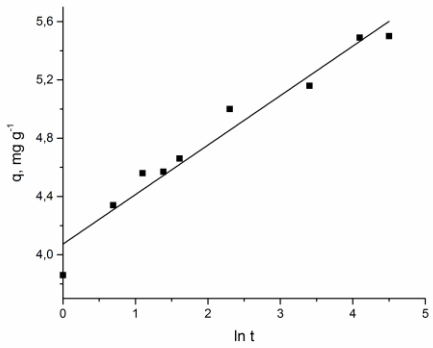


Fig. 4 *Elovich kinetic model for copper ion adsorption on corn stalks.*

From Table 3, based on the obtained value of the correlation coefficient $R^2 = 0.958$, it can be observed that the Elovich kinetic model describes very well the kinetics of copper ion adsorption onto corn stalks, indicating that copper ions bind to the adsorbent predominantly through chemisorption.

4. Conclusions

The kinetics of the copper ion adsorption process onto corn stalks were analyzed according to three theoretical kinetic models: the pseudo-first-order model, the pseudo-second-order model, and the Elovich model. Comparison of R^2 values for all models (Tables 1–3) demonstrates that the pseudo-second-order model provides the best fit ($R^2 = 1$), indicating that chemisorption is a possible mechanism of copper ion binding to the surface of corn stalks.

5. Acknowledgment

The research presented in this paper was done with the financial support of the Ministry of Science, Technological Development and Innovation of the Republic of Serbia, within the funding of the scientific research work at the University of Belgrade - Technical Faculty in Bor, according to the contract with registration number 451-03-34/2026-03/200131.

6. References

1. L. Largitte, R. Pasquier, *Chem. Eng. Res. Des.* **109** (2016), 495-504.
2. H. Qiu, L.V. Lu, B. Pan, Q. Zhang, W. Zhang, Q. Zhang, *J. Zhejiang Univ. Sci. A.* **10(5)** (2009), 716-724.
3. D. Božić, M. Gorgievski, V. Stanković, N. Štrbac, *Ecol. Eng*. **58** (2013), 202-206.
4. S. Lagergren, *Kungl. Svenska Vetenskapsakad. Handl.* **241** (1898), 1-39.
5. N.T. Coleman, A.C. McClung, D.P Moore, *Science* **123** (1956), 330-331.
6. Y.S. Ho, G. McKay, *Process Biochem*. **34(5)** (1999), 451-465.
7. A. Štrkalj, Z. Glavaš, G. Matijašić, *Mat. Technol*. **48(5)** (2014), 619-622.

Implementation of slow stress rating test method (SSRT) in determination susceptability to hydrogen embritlement of P460NL1 steel

Sveto Cvetkovski[1], Dr Rudolf Vallant[2], Fabian Bobner[2], Tobias Walder[2], Thomas Staubman[2], Fernando Warchomicka[2]
Faculty of Technology and Metallurgy, Ss Cyril and Methodius University, Skopje, Republic of North Macedonia[1]
IMAT, TU Graz Austria[2],
sveto@tmf.ukim.edu.mk

Abstract: *The hydrogen embrittlement susceptibility of P460NL1 pressure-vessel steel was assessed by slow strain rate testing (SSRT) with in situ electrochemical hydrogen charging. An electrochemical cell integrated with a tensile testing machine was used to generate hydrogen in a 3.5 wt.% NaCl solution containing 1 g/L thiourea. Cathodic charging was applied at a constant current of −20 mA (approximately −1.4 V). SSRT was performed at a strain rate of 10^{-5} s^{-1} in accordance with ASTM G129-21. Tensile specimens extracted from the base material and welded joints were tested in air and under hydrogen-charging conditions. The methodology enabled controlled hydrogen introduction during deformation of tensile probes and allowed comparison of hydrogen-assisted cracking susceptibility between base metal and welded material. Tested brocken tensile probes were subjected to determination of dissolved hydrogen. Tensile probes were first tested in the air and after that in prepared solution.*
To analyse hydrogen embritlement of investigated steel hydrogen embritlement index was determined through determination of fracture elongation and reduction of Area (RA) of the brocken specimen. Light and SEM microscopy was used to analyse possible location of the present defects in material i.e. hot rolled steel. Types of non-metallic inclusions were determined too.
KEYWARD*: HYDROGEN EMBRITLEMENT, P460NL1 STEEL, SLOW STRESS RATE TESTING (SSRT), TENSILE PROBE, FRACTURE ANALYSIS, SCANING ELECTRON MICROSCOPE (SEM)*

1. Introduction

Hydrogen embrittlement in installations for the transportation and storage of crude oil, natural gas, and oil derivatives has been known for more than one hundred years. However, due to current global energy challenges, this problem has become increasingly acute. For this reason, hydrogen embrittlement is a critical issue for steel producers (raw material suppliers), manufacturers of steel pipes, crude oil refineries, and similar industries.
In other words, steel producers must prove to pipe manufacturers that their materials—such as hot-rolled plates, steel sheets, and strips—are resistant to hydrogen embrittlement. More specifically, the produced equipment and installations must be safe during service with respect to hydrogen embrittlement. Refineries, their equipment, reservoirs, and tanks all depend on the long-term reliability of the steels used in their construction. Therefore, all users of steel products need assurance that the materials they build into their facilities are safe for long-term operation.
If hydrogen embrittlement occurs in such equipment, it can lead to material damage, environmental pollution, and, in many cases, loss of human lifes.
The question arises: how can it be proven that the delivered steel fulfills the requirements for resistance to hydrogen embrittlement?
Generally, two methods are mainly used: the slow strain rate testing (SSRT) and the fracture toughness (KIc) method. Based on a literature review and our own knowledge and experience, we decided to use the SSRT method. The investigated steel has a yield strength of 460 MPa. For medium-strength steels, SSRT is recommended, whereas the KIc method is typically used for high-strength materials (steels) with yield strengths above 800–900 MPa.

1 material and experimental

For determination tendency to hydrogen embritlement of P460NL1 steel, slow stress rate testing was implemented (SSRT). Generally, it can be said that this method give real and reproductive results. For implementation of this method experimental, electrochemical cell was constructed Figure 1.
This cell was mounted to tensile testing machine. After putting the tensile probe in the testing machine, the cell was filled with prepared solution (Electrolyte: 3.5% NaCl, 1g/L Thiourea) Hydrogen was additioanaly added in the cell during testing - in-situ charging during SSRT with flow rate of **,,,,** l/m. After breaking of the tensile probes concetration of dissolved hydrogen in the probes was determined. It value is approximately about**,,,,**

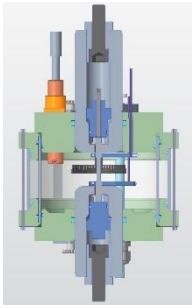


Figure 1 *Experimental electrochemical cell*

1.1 Investigated Material

P460NL1 steel was used for experimental work in this paper. The steel is produced in electric arc furnace (EAF) with capacity of 100 tons molten metal. As a raw material was used steel scrap. Chemical composition and mechanical properties of produced steel plates are given in the Tables 1 and 2. They are in accordance with standard requirements/

Table 1 *Chemical composition of P460NL1 steel*

El.	C	Si	Mn	P	S	Al	N	Cr
	0.16	0.25	1.22	0.016	0.005	0.055	0.08	0.07

Cu	Ni	Mo
0.3	0.25	0.1

Ceqv=0.427

Table 2 *Mechanical properties – transversal of P460NL1 steel*

	Rah (MPa)	Rm (MPa)	A %	ISO-V(-20) J
value	512	627	28.8	144

Molten metal was continuously casted in slabs. Produced slabs were hot rolled in wide plates with thickness of 12 mm. From the plates were taken pieces for machining tensile probes. Besides, from the plates, welded pieces were prepared in order to obtain tensile probes from the welded joints. These probes are with the same dimensions as probes from the plates. Loacation of the weld is in the midle of the probe.

Used welding process is SAW. As Welding wire was chosen BOHLER EMS 2 Mo // BB 24 - ϕ4. Used Welding flux is Bohler BB24. Tandem welding was performed figure 2.

Rounded tensile probes were prepared. Dimensions of probes are shown in the figure 3.

So, it was prepared tensile probes from the plates and from the welded pieces. The idea was to compare results of the both types of probes. The probes were tested in the air an in the experimental prepared solution.



a ***b***

Figure 2 *Macro picture of welded joint (a), Microstructure of coarse grained HAZ (b)*

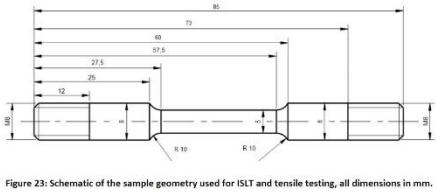


Figure 3 *Rounded tensile probes for SSRT testing*

What means designation P460NL1 steel?

P460NL1 is a European (EN) steel designation. Each part tells something specific about the steel. P460NL1 is a normalized (normalized rolling) fine-grain pressure-vessel steel with a minimum yield strength of 460 MPa and guaranteed impact toughness at −40 °C.

Figure 4 show nonmetallic inclusions present in the investigated steel. Magnification is x100 according standard. Mainly oxide inclusions are detected at this magnification.



Figure 4 Non-metallic inclusions

Microstructure of steel is ferrite-perlite with more than 70% ferrite (figure 5) and grain size of steel is 9 (figure 6).

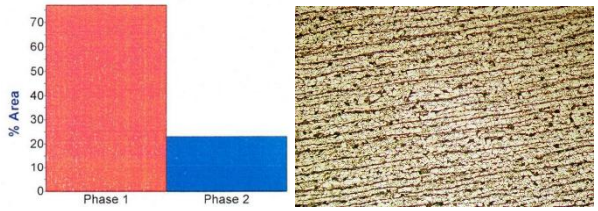


Figure 5 Microstructure of investigated steel P460NL1

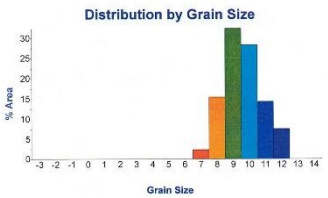


Figure 6 *Grain size of steel*

1.1 Performed investigations

Prepared tensile probes were first tested in the air. After that they were tested in the experimental electrochemical cell. It was concluded that base metal plate showed better resistance to hydrogen embritlement compared to welded joints. Tested probes in electrochemical cells showed lower values which is in accordance with our espectations.

The tensile test was carried out with a Zwick / Roell ZMART.PRO testing machine. As a strain rate was accepted 10^{-5} s^{-1} (figure 8). Altough some preliminary investigations was performed with strain rate of 10^{-4} s^{-1} (figure 7). The hydrogen charging (H-charging) was done with our Electrochemical Charging Cell (ECC) containing a solution of 3.5% NaCl and 1g/L Thiourea as an inhibitor to reduce the recombination of atomic H to H_2 on the surface of the working electrode. During H-charging the strain rate for the tensile test was reduced to 10^{-5} s^{-1} (Slow Strain Rate Test/SSRT). As a potentiostat a Metrohm Autolab PGSTAT128N was used with a constant applied voltage of -1.1V (cathodic polarisation).

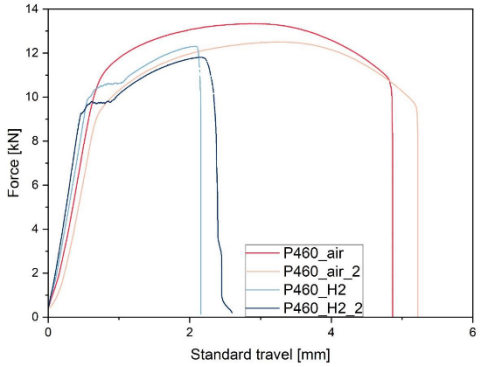


Figure 7 *Diagram force/standard travel strain rate 10^{-4} s^{-1}*

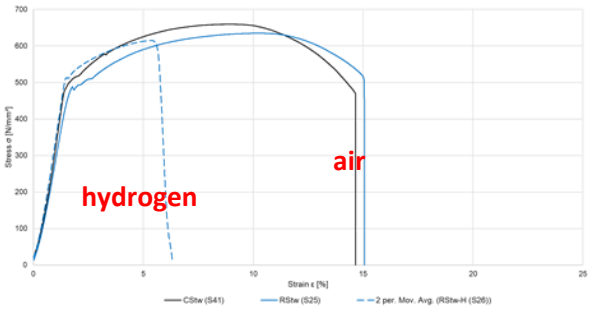


Figure 8 *Diagram force/standard travel strain rate 10^{-5} s^{-1}*

The question which has to be answered is what is tendency of investigated steel to hydrogen embritlement?

More concretely, How susceptibility to environmentally assisted cracking (EAC) can be determined?

SSRT - Evaluate the susceptibility to EAC according to: ASTM G129 – 21. Suggested strain rate range 10^{-4}/s to 10^{-7}/s - Slow enough for H diffusion vs. fast enough to produce cracking in reasonable time period. We mainly used strain rate 10^{-5} s.

Parameters we used in investigations were taken from the tested tensile probes. Tensile specimen: l_0= 25 mm, d_0=5 mm, Strain rate: 10^{-5}/s (15µm/min).

Evaluation of hydrogen embritlement (HE) was determined by Hydrogen Embrittlement Indices:

Fracture Elongation A5: $HEI_E(\%) = \frac{A5_{air} - A5_H}{A5_H}$

Reduction of Area RA: $HEI_E(\%) = \frac{RA_{air} - RA_H}{RA_{air}}$

Figure 9 shows broken tensile probes from which was detrmined A5, elongation after testing in the air and in the cell. Figure 10 show type of fracture.



Figure 9 Brocken tensile probes



Figure 10 *Type of fracture in tensile probess*

Tested tensile probes from welded joints were subjected to hardness measurement (figure 11).
Submerged Arc Welding (SAW) process:
- weld hardness ca. 250HV1
- base material hardness ca. 230HV1

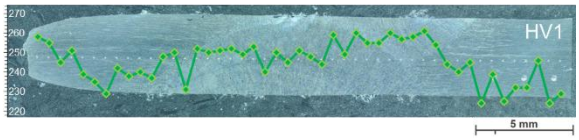


Figure 11 *Hardness measurement of tensile probe from the welded joint*

Figure 12 show how cross section of tested tensile probes was measured. Obtained values were used in order to determine reduction of area.

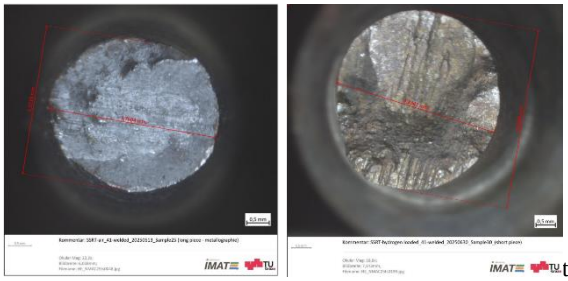


table 1

Figure 12 *Measuring cross section of investigated tensile probes*

Using determined values for elongationn end reduction of area, hydrogen embritlement index (HEI) was determened. Obtained results are in the table 3.

Table 3 *Determination of hydrogen embritlement index HEI which*

steel	Yield strength R_{eL} (MPa) *average*	Tensile strength R_m (MPa) *average*	Fracture elong. A_5* (%) *average*	**HEI A5 (%)**	Reduction of Area RA (%) average	**HEI RA (%)**
RSt	451	637	20.3	**62.1**	66.9	**85.9**
RSt -H	475	615	7.7		9.4	
RStw	483	635	14.6	**50.7**	58.0	**71.7**
RStw -H	502	626	7.2		16.4	

1.2 Metallographic investigations

Scaning and optical microcroscopy was used for investigation of microstructrure and present defects in investigated steel. Figure 13 clearly show detected defect on the polished and etched specimen.

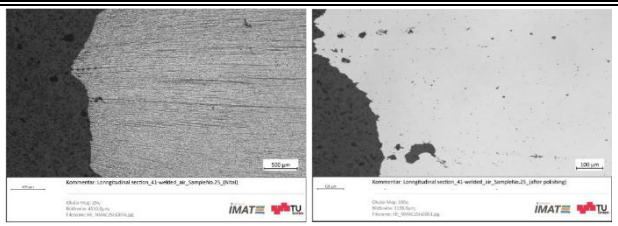


Figure 13 *Detected defects in the specimen – tensile probes*

From the figure14 was concluded that presence of defects was in the perlitic bands

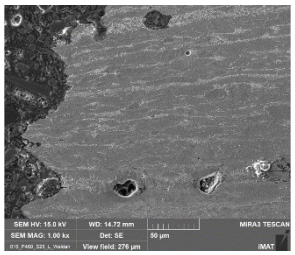


Figure 14 *Defects in steel located in perlitic bands*

From the figure 15 and 16 can be concluded that formed cracks on the probe surface propagate towards the probe interior. It can be seen too that some cracks are formed in pearlitic bands and are arested in ferrite.

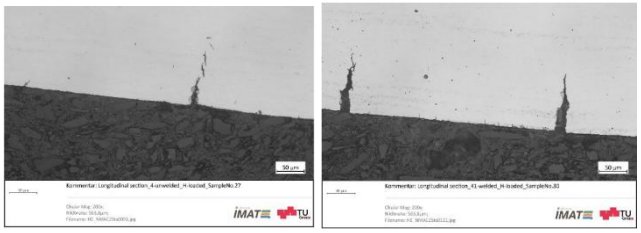


Figure 15 *Polished specimed – cracks formed on the surface*

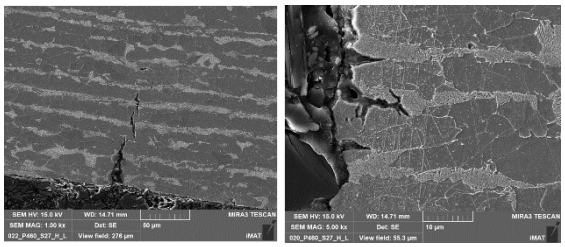
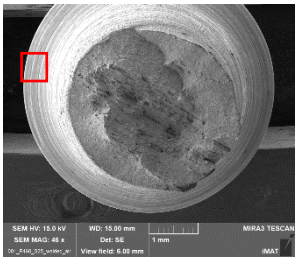


Figure 16 *Cracks formed in pearlite and stoped in ferritic bands*

Figure 17 presents macro fracture of broken tensile probes tested in the air and in the solution. Fragments of fractured surfaces inside the red squares are shown in the figure 18. It was concluded from the SEM figures that probe tested in the air shows typical dimple fracture while probe tested in the electrochemical solution has quasi cleavage fracture as results of influence of hydrogen to fracture.



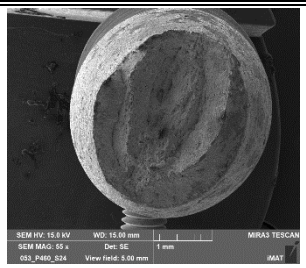


Figure 17 *Macro fracture of tensile specimens*

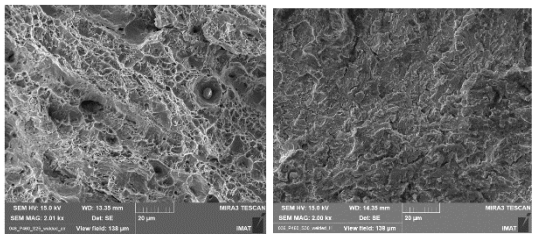
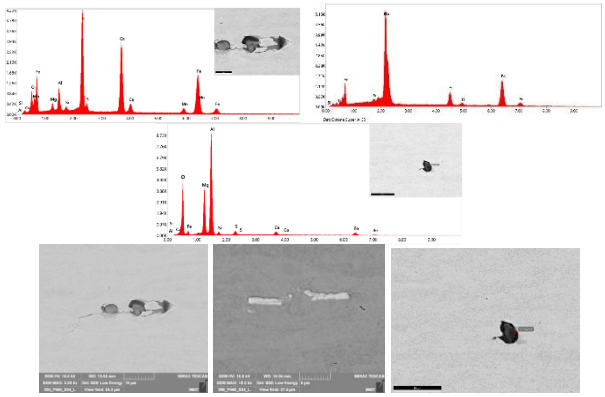


Figure 18 *Types of micro fracture*

1.3 SEM analysis

SEM with EDAX system was used for determination of different types of small inclusions. Nonmetallic NMI CaS-type and NMI AlMgO type were detected. Metallic inclusions MI NbTi-type: were detected too, figure 19.



NMI CaS-type *MI NbTi-type* *NMI AlMgO type*

Figure 19 *Inclusions detected by SEM*

Discussion

The results obtained from slow strain rate testing clearly demonstrate that P460NL1 [1,2] steel is susceptible to hydrogen embrittlement, with a pronounced difference between the base metal and welded joints. The susceptibility to environmentally assisted cracking (EAC) increases significantly when hydrogen is introduced electrochemically, which is consistent with the observed degradation of plastic properties.

Effect of Hydrogen on Mechanical Properties

Hydrogen charging caused a substantial reduction in fracture elongation (A5) and reduction of area (RA) for both base metal and welded specimens. The calculated Hydrogen Embrittlement Index (HEI) values confirm that elongation is more sensitive to hydrogen than tensile strength, which remained relatively unchanged. This behaviour is typical for hydrogen embrittlement, where hydrogen primarily reduces ductility rather than strength [3,4].

The base metal exhibited higher resistance to hydrogen embrittlement compared to welded joints. This is attributed to the microstructural heterogeneity introduced by welding, particularly in the weld metal and heat-affected zone (HAZ), where local hardening and residual stresses are present. The higher hardness measured in the weld region (~250 HV1) compared to the base metal (~230 HV1) further supports the increased hydrogen susceptibility of welded joints [6].

The ferrite–pearlite microstructure with more than 70% ferrite generally provides good resistance to hydrogen embrittlement due to the relatively high hydrogen solubility and low diffusivity in ferrite. However, the presence of banded pearlite significantly influences crack initiation and propagation [7].

Metallographic observations revealed that defects and crack initiation sites are predominantly located in pearlitic bands. During hydrogen charging, cracks initiated at the specimen surface and propagated along pearlitic regions, while ferritic areas often acted as crack arresters [8,9]. This indicates that pearlite, due to its higher strength and cementite lamellae, provides favourable paths for hydrogen-assisted cracking.

Fracture Behaviour and Hydrogen-Assisted Cracking Mechanism

Fractographic analysis showed a clear transition in fracture mode caused by hydrogen. Specimens tested in air exhibited a ductile dimple fracture, characteristic of microvoid coalescence. In contrast, hydrogen-charged specimens showed quasi-cleavage fracture, confirming the presence of hydrogen-assisted cracking mechanisms [10].

The observed fracture morphology suggests that hydrogen promotes localized plasticity and decohesion, leading to premature crack initiation and rapid crack propagation. The quasi-cleavage features are particularly pronounced in welded specimens, indicating a synergistic effect of hydrogen, microstructural inhomogeneity, and residual welding stresses.

Role of Non-Metallic Inclusions

SEM–EDAX analysis identified CaS, AlMgO, and NbTi-type inclusions, which can act as hydrogen trapping sites. These inclusions contribute to local hydrogen accumulation, increasing the likelihood of crack initiation under applied stress. In particular, elongated or clustered inclusions within pearlitic bands intensify hydrogen-assisted damage, explaining the preferential crack initiation observed in these regions [11].

Assessment of EAC Susceptibility by SSRT

The applied SSRT strain rate of 10^{-5} s^{-1}, in accordance with ASTM G129, proved suitable for evaluating hydrogen embrittlement susceptibility. The significant reduction in A5 and RA under hydrogen charging confirms that SSRT is an effective method for assessing EAC susceptibility in P460NL1 steel.

Overall, the results indicate that welding significantly increases the susceptibility of P460NL1 steel to hydrogen embrittlement, and that the combined effects of hydrogen charging, microstructural banding, inclusions, and local hardening govern the EAC behaviour.

Conclusion

P460NL1 steel exhibits a measurable susceptibility to hydrogen embrittlement, which becomes pronounced under electrochemical hydrogen charging, as evidenced by a significant reduction in fracture elongation and reduction of area.

Welded joints show substantially higher hydrogen embrittlement susceptibility than the base metal. This is attributed to microstructural heterogeneity, increased hardness in the weld metal and heat-affected zone, and the presence of residual welding stresses.

Hydrogen charging has a limited effect on yield and tensile strength, while ductility-related parameters (A5 and RA) are strongly degraded, confirming that hydrogen primarily affects plastic deformation and fracture behaviour.

Crack initiation and propagation preferentially occur in pearlitic bands, whereas ferritic regions tend to impede crack growth, indicating the critical role of microstructural banding in hydrogen-assisted cracking.

Fractographic analysis revealed a transition from ductile dimple fracture in air to quasi-cleavage fracture under hydrogen charging, confirming the operation of hydrogen-assisted cracking mechanisms.

Non-metallic inclusions (CaS, AlMgO) and NbTi-based metallic inclusions act as hydrogen trapping sites and contribute to local stress concentration, promoting crack initiation.

The SSRT method at a strain rate of 10^{-5} s^{-1}, in accordance with ASTM G129, proved to be an effective approach for evaluating susceptibility to environmentally assisted cracking in P460NL1 steel.

Overall, microstructure, inclusion characteristics and welding-induced hardening, highlighting the importance of welding procedure control for applications involving hydrogen-containing environments, govern the resistance of P460NL1 steel to hydrogen embrittlement.

Literature

[1] BS EN 10028-3:2017 Flat products made of steels for pressure purposes - Weldable fine grain steels, normalized

[2] BS EN 10028-2:2009 Flat products made of steels for pressure purposes Part 2: Non-alloy and alloy steels with specified elevated temperature properties

[3] N. Saidani, A. Mihi, R. Benbouta Fracture process of C–Mn steel embrittled by hydrogen, University of Bahrain; Journal of the Association of Arab Universities for Basic and Sciences

[4] Hirth, J.P., Johnson, H.H., 1976. Hydrogen problems in energy

[5] Woodward, J., Procter, R.P.M., 1988. Fatigue of offshore related technology. Corrosion 32, 3.structures. In: Dover, W.D., Glinka, G. (Eds.), Proceedings of International Conference, London.

[6] Wu, T.I., Wu, J.K., 2002. Effects of thiourea and its derivatives on the electrolytic hydrogenation behavior of Ti–6Al–4V alloy. Materials Letters 53, 193.

[7] Vergani, Laura; Colombo, Chiara; et al. (2014).“Hydrogen effect on fatigue behavior of a quenched and tempered steel”. Procedia Engineering. Elsevier. 74 (XVII International Colloquium on Mechanical Fatigue of Metals (ICMFM17)): 468–71.doi:10.1016/j.proeng.2014.06.299. Retrieved 9 May 2015.

[8] ASTM STP 543, “Hydrogen Embrittlement Testing”

[9] Jewett, R.P. (1973). Hydrogen Environment Embrittlement of Metals. NASA CR-2163.

[10] Raymond L (1974). Hydrogen Embrittlement Testing. ASTM International. ISBN 978-0-8031-0373-3.

[11] Tartaglia, John; Lazzari, Kristen; et al. (March2008). “A Comparison of Mechanical Properties and Hydrogen Embrittlement

Machine Learning Prediction of Mechanical Properties for Al-Cu Alloys Using Monte Carlo Data Augmentation

Mihail Kolev[1,5], Tatiana Simeonova [1,2,5*] Ivo Lozanov [3], Vilyana Kazanlaklieva[4], Viktoria Gerdzhikova [4]

[1] Institute of Metal Science, Equipment and Technologies with Hydro- and Aerodynamics Centre "Acad. A. Balevski", Bulgarian Academy of Sciences, Sofia, 1574, Bulgaria
[2] Institute of Mechanics, Bulgarian Academy of Sciences, Sofia, 1113, Bulgaria
[3] Department of Inorganic Chemistry, Faculty of Chemistry and Pharmacy, Sofia University "St. Kliment Ohridski", Sofia, Bulgaria
[4] University of Chemical Technology and Metallurgy Sofia, Bulgaria
[5] National Center for Mechatronics and Clean Technologies, 8 "Kliment Ohridski" Blvd., Building 8, 1756 Sofia, Bulgaria
* Corresponding author: tsimeonova@imbm.bas.bg

Abstract: *This study presents a machine learning framework for predicting the mechanical properties of 2xxx series Al-Cu alloys (2024, 2219, 2524) across 11 temper conditions. Monte Carlo augmentation generated 8,800 synthetic samples from compositional specification ranges of a literature-mined dataset. Three regression models, Random Forest, Gradient Boosting, and SVR-RBF were evaluated via 5-fold cross-validation (CV) to predict ultimate tensile strength (UTS), yield strength (YS), and elongation. All models achieved coefficient of determination $R^2 > 0.991$, with Mean Absolute Error MAE ≤ 7.4 MPa for UTS, ≤ 5.4 MPa for YS, and ≤ 0.51% for elongation. Feature importance analysis revealed that temper condition encoding dominated predictions (>75% importance), while individual compositional features contributed <5% each. The high predictive accuracy reflects the effectiveness of the augmentation scheme in capturing within-group property–composition–temper relationships, though generalization to unseen alloy–temper conditions remains to be validated. The results illustrate the potential of combining corpus-mined data with Monte Carlo augmentation for rapid alloy property screening.*
Keywords*: Al-Cu ALLOYS; MACHINE LEARNING; MECHANICAL PROPERTIES; MONTE CARLO AUGMENTATION; RANDOM FOREST; GRADIENT BOOSTING*

1. Introduction

The 2xxx series Al-Cu alloys (2024, 2219, 2524) are critical structural materials in aerospace applications, valued for their high strength, fatigue resistance, and damage tolerance [1,2]. Their mechanical properties depend strongly on both composition and temper condition, making property prediction across alloy-temper combinations a non-trivial task. Machine learning (ML) methods have shown promise for materials property prediction [3–5], but limited dataset sizes per alloy-temper condition remain a challenge [6,7]. Monte Carlo augmentation, which generates synthetic samples by sampling from compositional specification ranges, offers a physically motivated strategy to expand training datasets [8]. In this work, we apply three ML regression models to predict UTS, YS, and elongation of three 2xxx alloys across 11 temper conditions, using Monte Carlo-augmented data derived from a publicly available dataset.

2. Materials and Methods

Composition and property data were obtained from the dataset compiled by Pfeiffer et al. [9] and uploaded in Materials Cloud Archive, which contains aluminum alloy data extracted from scientific literature and US patents. Three alloys were selected: 2024 (T3, T351, T4, T6, T8), 2219 (O, T6, T62, T851), and 2524 (T3, T351). The feature space comprised 10 elemental compositions (Al, Cu, Mn, Si, Mg, Zn, Cr, Fe, Ti, Zr), 3 alloy-type and 8 temper-type one-hot encodings, and 1 ordinal temper code (22 features total). Figure 1 presents the mean experimental properties for each alloy-temper combination.

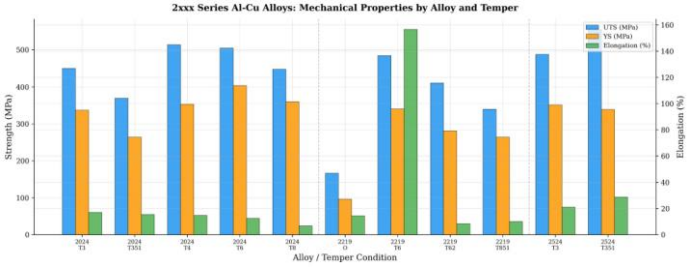


Fig. 1 *Mechanical properties (UTS, YS, elongation) by alloy and temper for 2xxx series Al-Cu alloys.*

For each of the 11 conditions, 800 synthetic samples were generated (8,800 total) by uniformly sampling element concentrations from specification ranges, computing Al as the balance, and adding 2% Gaussian noise to mean experimental property values. Three models were trained: Random Forest (RF, 200 trees, max depth 12, min samples split 5), Gradient Boosting (GBR, 200 trees, max depth 6, lr = 0.1, min samples split 5), and SVR-RBF (C = 100, ε = 0.1, γ = scale, features standardized). Performance was assessed by 5-fold cross-validation using coefficient of determination R^2, Mean Absolute Error (MAE), and Root Mean Square Error (RMSE).

3. Results and Discussion

Table 1 summarizes model performance. All models achieved $R^2 > 0.991$ for all targets. RF provided the best overall accuracy (UTS MAE = 7.04 MPa, YS MAE = 5.08 MPa, elongation MAE = 0.46%). The marginal differences among models indicate that the augmented dataset effectively captured property-composition-temper relationships. Figure 2 shows predicted vs. actual plots confirming tight clustering along the 1:1 diagonal across all alloy clusters.

Table 1: *Cross-validation metrics for ML models.*

Model	Target	R^2	MAE	RMSE
Random Forest	UTS (MPa)	0.9924	7.04	9.06
	YS (MPa)	0.9931	5.08	6.56
	Elongation (%)	0.9994	0.46	1.03
Gradient Boosting	UTS (MPa)	0.9921	7.20	9.24
	YS (MPa)	0.9928	5.19	6.69
	Elongation (%)	0.9993	0.49	1.11
SVR (RBF)	UTS (MPa)	0.9916	7.39	9.52
	YS (MPa)	0.9923	5.32	6.90
	Elongation (%)	0.9993	0.50	1.06

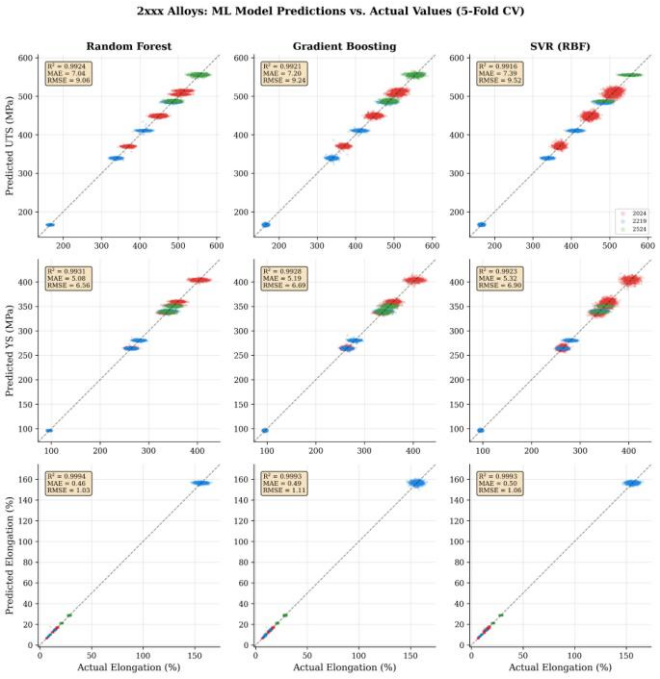


Fig. 2 *Predicted vs. actual values for RF, GBR, and SVR-RBF models (5-fold CV), colored by alloy: 2024 - red, 2219 - blue, and 2524 - green.*

Feature importance rankings (Fig. 3) show that temper-related features dominated all property predictions. For UTS, the temper code and O temper indicator together accounted for ~80% of importance. For elongation, the T6 indicator was most important (RF: 0.42), reflecting the anomalous 2219-T6 elongation (156.5%). This value should be interpreted with caution: the source dataset contains only two elongation records for 2219-T6 (11.0% and 302.0%), and the 302% value is physically unrealistic for a conventional precipitation-hardened Al-Cu alloy, where typical elongation ranges from 10 to 17%. The resulting mean (156.5%) is therefore likely dominated by a data extraction error in the original corpus and may inflate the elongation R^2 through a lever-arm effect. Individual compositional features contributed <5% each, consistent with the fact that within the 2xxx system, property differences arise primarily from thermomechanical processing history rather than minor compositional variations [10,11].

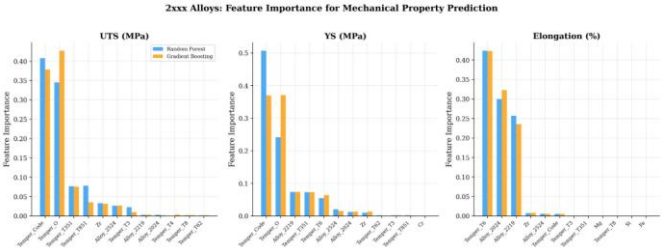


Fig. 3 *Feature importance from RF and GBR models for UTS, YS, and elongation prediction.*

The correlation heatmap (Fig. 4) confirms strong UTS-YS correlation (r = 0.93), a strong negative correlation between O temper and strength (r = −0.81 to −0.85), and weak negative Cu-strength associations (r ≈ −0.16). The augmented property distributions (Fig. 5) show that Monte Carlo sampling preserved realistic property ranges for all conditions, with the noted exception of the 2219-T6 elongation discussed above.

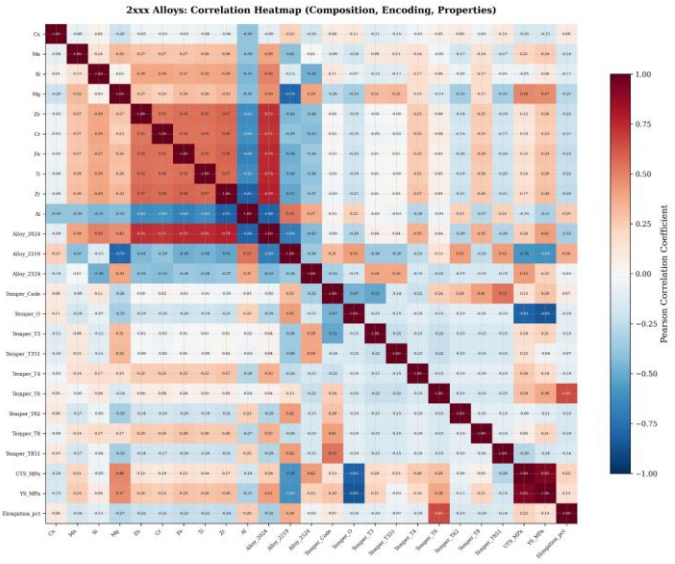


Fig. 4 *Pearson correlation heatmap of compositional features, encoding variables, and mechanical properties*

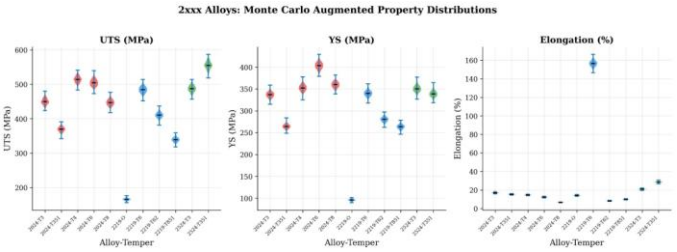


Fig. 5 *Monte Carlo augmented property distributions (violin plots) for each alloy-temper combination.*

4. Conclusions

A Monte Carlo augmented ML framework was developed for predicting UTS, YS, and elongation of 2024, 2219, and 2524 Al-Cu alloys across 11 temper conditions. All three models (RF, GBR, SVR-RBF) achieved $R^2 > 0.991$ for all targets. RF provided the best performance with MAE of 7.04 MPa (UTS), 5.08 MPa (YS), and 0.46% (elongation). Temper condition dominated feature importance (>75%), while compositional features contributed <5% each. It should be noted that the high R^2 values partly reflect the augmentation design: since all synthetic samples within a given alloy–temper condition share the same mean property values with only 2% noise, the cross-validation task effectively reduces to recovering group means from categorical encodings. The present results therefore demonstrate strong interpolative accuracy within the training domain but do not establish extrapolative generalization to unseen alloy–temper conditions. Additionally, the 2219-T6 elongation data should be treated with caution due to a likely outlier in the source dataset. Future work should evaluate leave-one-condition-out cross-validation to assess true predictive capability, and incorporate broader alloy systems to improve compositional sensitivity. Despite these limitations, the framework illustrates how combining literature-mined datasets with Monte Carlo augmentation can serve as a practical tool for rapid property screening of aluminum alloys within known compositional and processing domains.

5. Funding

This research was funded by the Bulgarian National Science Fund, Project **КП-06-Н77/5** "Self-lubricating hybrid aluminum metal matrix composites: synthesis, experi-mental and computer modeling of mechanical and tribological properties".

6. Acknowledgement

The work in this publication was performed using equipment funded by project BG16RFPR002-1.014-0006 “National Center for Mechatronics and Clean Technologies”.

7. References

1. Li, S.-S.; Yue, X.; Li, Q.-Y.; Peng, H.-L.; Dong, B.-X.; Liu, T.-S.; Yang, H.-Y.; Fan, J.; Shu, S.-L.; Qiu, F.; et al. Development and Applications of Aluminum Alloys for Aerospace Industry. *J. Mater. Res. Technol.* **2023**, *27*, 944–983, doi:10.1016/j.jmrt.2023.09.274.

2. García-Aguirre, K.A.; Holguín-Momaca, J.T.; Ruiz-Esparza-Rodriguez, M.A.; Guía-Tello, J.C.; Garay-Reyes, C.G.; Estrada-Guel, I.; Martínez-Sánchez, R. Microstructural Evolution and Strengthening Mechanisms in a 2xxx Series Modified Al Alloy. *Microsc. Microanal.* **2022**, *28*, 2854–2856, doi:10.1017/s1431927622010753.

3. Elkatatny, S.; Alsharekh, M.F.; Alateyah, A.I.; El-Sanabary, S.; Nassef, A.; Kamel, M.; Alawad, M.O.; BaQais, A.; El-Garaihy, W.H.; Kouta, H. Optimizing the Powder Metallurgy Parameters to Enhance the Mechanical Properties of Al-4Cu/XAl2O3 Composites Using Machine Learning and Response Surface Approaches. *Appl. Sci. (Basel)* **2023**, *13*, 7483, doi:10.3390/app13137483.

4. Hu, H.; Zhao, F.; Yong, W.; Jiang, L.; Zhang, Z.; Xie, J. A Machine Learning Strategy to Achieve Dual-Synchronous Property Improvement of Aviation Al-Cu-Mg Alloy. *J. Mater. Sci. Technol.* **2026**, *244*, 208–230, doi:10.1016/j.jmst.2025.04.036.

5. Fu, C.; Lin, X.; Huang, H.; Yue, C.; Zuo, X.; Zheng, B.; Du, K.; Zheng, W. Synergistic Enhancement of Strength and Plasticity in Al-Cu Alloys Using Interpretable Machine Learning Algorithms. *Mater. Sci. Eng. A Struct. Mater.* **2025**, *942*, 148702, doi:10.1016/j.msea.2025.148702.

6. Shawon, A.R.; Ghosh, R.; Islam, M.A. Analysis of Thermal Conductivity of Aluminum Alloys by Compositions and Tempering Process Using Machine Learning. *Sci. Rep.* **2025**, *15*, 33352, doi:10.1038/s41598-025-15868-y.

7. J. Soofi, Y.; Rahman, M.A.; Gu, Y.; Liu, J. A Feasibility Study of Machine Learning-Assisted Alloy Design Using Wrought Aluminum Alloys as an Example. *Comput. Mater. Sci.* **2022**, *215*, 111783, doi:10.1016/j.commatsci.2022.111783.

8. Park, J.; Yoon, H.-K. Methodology for Generating Diverse Geotechnical Datasets Using Monte Carlo Simulation and Genetic Algorithms. *Comput.-aided Civ. Infrastruct. Eng.* **2025**, *40*, 5494–5511, doi:10.1111/mice.70106.

9. Pfeiffer, O.P.; Liu, H.; Montanelli, L.; Latypov, M.I.; Sen, F.G.; Hegadekatte, V.; Olivetti, E.A.; Homer, E.R. Aluminum Alloy Compositions and Properties Extracted from a Corpus of Scientific Manuscripts and US Patents 2021.

10. Zhou, Y.; Lin, X.; Kang, N.; Huang, W.; Wang, Z. Mechanical Properties and Precipitation Behavior of the Heat-Treated Wire + Arc Additively Manufactured 2219 Aluminum Alloy. *Mater. Charact.* **2021**, *171*, 110735, doi:10.1016/j.matchar.2020.110735.

11. Zhang, L.; Huang, G.; Wang, L.; Lu, G.; Guan, S. Microstructure-Strengthening Correlation of 2219 Al Alloy Subjected to Ultrasonic Melt Treatment, Hot Rolling and Heat Treatment. *J. Mater. Res. Technol.* **2023**, *27*, 7470–7481, doi:10.1016/j.jmrt.2023.11.167.

Analytical-numerical approach for computation of welding residual stresses in large shell structures

Nikolay Doynov[1,2*], Vesselin Michailov[1,3], Hartmut Pasternak[4]
IMSETHAC, Bulgarian Academy of Science, 67. Shipchenski prohod Blvd., 1574 Sofia, Bulgaria[1]
National Centre of Excellence Mechatronics and Clean Technologies, 8 bul. Kliment Ohridski, 1756 Sofia, Bulgaria[2]
Department of Joining and Welding Technology, BTU Cottbus-Senftenberg, Konrad-Wachsmann-Allee 17, 03046 Cottbus, Germany [3]
Department of Steel and Timber Structures, BTU Cottbus-Senftenberg, Konrad-Wachsmann-Allee 2, 03046 Cottbus, Germany[4]
nikolay.doynov@ims.bas.bg

Abstract: *In this paper, the inherent strain method is employed for the purpose of predicting welding residual stresses in large shell structures. Such structures include roof structures in the construction industry and deck sections in the shipbuilding industry. The study focuses on the numerical aspect of the inherent strain method, with the objective of investigating the most appropriate technique for transferring analytically calculated inherent strains into the elastic finite element model of the structure. The approach under consideration takes into account the thermally induced stresses, to the extent that they are considered to be significant for the structures and their behaviour in question, with the objective of determining the field of welding residual stresses over the entire structure (macro-scaled). The work proposes theoretical parameters for the alignment of finite element meshes within the weld seam domain. The discussion in the conclusion encompasses the general application capabilities, limitations, and challenges for further development.*
Keywords*:* COMPUTATIONAL WELDING MECHANICS, VIRTUAL MANUFACTURING, INHERENT STRAIN METHOD, WELDING RESIDUAL STRESSES, WELDING IMPERFECTIONS

1. Introduction

Stiffened shell structures are now being increasingly used in different sectors of industry like shipbuilding, construction industry, etc. The structure typically consists of a thin outer skin and, if applicable, inner skin, which is stiffened by longitudinal and transverse stiffeners. This structural design enables extremely efficient and material-minimized built up. Due to the use of slender metal sheets, the buckling influence needs to be taken into account. A geometrically and materially nonlinear analysis [1] of the imperfect shell corresponds to the theoretically highest degree of realism. The quality of proofs depends decisively on whether the imperfections introduced into the computational model adequately describe the effect of, in particular, the welding residual stresses and distortions, of real structures [2]. For this purpose, in general, more appropriate is not the stress distribution in a small vicinity of the weld, but rater than the stress field over the whole structure. It means that more relevant is not the local maxima but their integral values, i.e. the tensile and the compressive loaded domains.

Today, it is basically possible to reliably predict welding residual stresses by means of thermo-mechanical numerical welding simulation [3, 4, 5], denoted also as transient thermal, metallurgical and elastic-plastic mechanical analysis (TMMA). The extensive modeling and computational costs, however, prevent its practical application. It becomes even more inapplicable if the aspects of component assembling and their accompanying measures, e.g. thermal or mechanical straightening operations, should be taken into account. The employment of the inherent strain method, first suggested by [6], enables to overcome these difficulties and to serve practicable simulation tools. Today this method is generally used to predict the welding distortions. Hence, there is a demand for its development concerning the prediction of welding residual stresses.

The essence of the inherent strain method is the loading the finite element **(FE)** model of the structure with initial strain, tendon forces, etc., and running a simple elastic analysis. Usually, elastic shell elements are used for modeling the structure. The inherent strain is the residual irreversible strain arising in a vicinity of the weld. It can be estimated either experimentally/analytically, or using numerical or analytical models [7-17]. The relevance of the analytical models is due to an easy-to-use and fast solution it offers. Hence, the concept of analytical-numerical hybrid model for distortion prediction [18-20] will be followed in this work.

The material of regarded structures is either non-alloyed or austenitic structural steel and the applied welding processes (gas metal arc welding, submerged arc welding) are generally characterized by slow cooling rates. Thus the phase transformations in the heat affected zone have very limited significance. Therefore, it is assumed that the thermally induced stresses are reasonable for the regarded applications.

The scope of this work is to propose an applicable analytical-numerical method for simulation of thermally induced residual welding stresses in large shell structures. It is supposed that this method shall enable in addition a coupling with different models, such as for calculation of the load-carrying capacity of welded structures.

2. Theoretical background of the approach

As stated above, in this work the inherent strain is assumed to be equal to the plastic strain and acts in the plastic deformed zone. The plastic strain depends on the temperature distribution, the thermo-mechanical material properties and the reaction of structure - structural stiffness and initial stress. The analytical solution, e.g. in [20] enables to take into account all relevant influences. Thus it allows an accurate calculation of the plastic strain distribution. But, by the large structures the FE mesh must be rather coarse and the plastic deformed zone is presented usually by only one or two rows of elements along the weld path. It means that the plastic strain components must be transferred into the FE-model as integral values (sketched domain on fig.1). This aspect must be taken into account by the formulation of the working hypothesis.

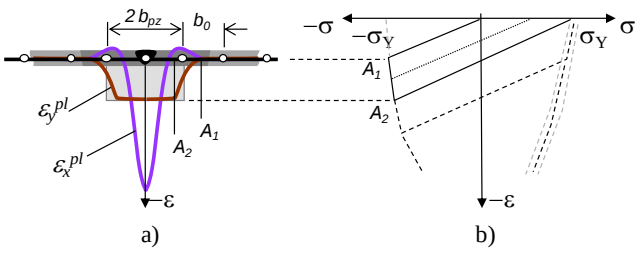


Fig. 1 *Sketch of the numerical experiment: a) transverse distribution of the plastic strain mapped on the FE-model (points are the element nodes) and b) kinetics of the accumulation of longitudinal plastic strain*

After revision of the theoretical models [21-25] it could be found a strong relation between some characteristic points of both the plastic strain distribution and the residual stress distribution. Here, more critical appears to be the distribution of longitudinal stress, because of the rather higher gradients. The point (transverse distance from the weld axis) of transition from tensile to compressive residual stress corresponds to the point (A_1) where the plastic strain differs from null, see fig. 1. The point where the plastic strain attains its maximal value is very close to the point (A_2) where the tensile residual stress correlates with the yield limit. The

leading hypothesis of this work is therefore to take into account these two points by the calculation of stress distribution.

3. Calculation of inherent strain and A_1 and A_2 coordinates

The inherent strain is assumed to be equal to the sum of plastic strain ε^{pl} and residual strain ε, if any, represented by the equation:

$$\varepsilon = \varepsilon^{el} + \varepsilon^{pl} + \varepsilon^{th}$$

where ε^{el} and ε^{th} are the elastic and thermal strain respectively.

Applying an analytical solution, e.g. in [20], which is derived from the shrinkage volume model suggested from [21-25] the strain components can be calculated as follow.

- longitudinal shrinkage volume v_y:

$$v_y = \varepsilon_y^* b_{pz} s = \int_0^s \int_0^\infty \varepsilon_y^{pl} dx dz = s \int_{\varepsilon_1}^{\varepsilon_2} x\left(\varepsilon_{\max}^{th}\right) d\varepsilon_{\max}^{th}$$

- transverse shrinkage volume v_x :

$$v_x = \varepsilon_x^* b_{pz} s \;\; and \;\; \varepsilon_x^* = \frac{1}{b_{pz} s} \int_0^s \int_0^\infty \varepsilon_x^{pl} dx dz$$

In case of welding of flat and relatively width sheets, i.e. with very high stiffness [23, 8, 15, 25], the residual strain is equal to zero. The simple form is than given by the equation:

$$\varepsilon_y^* b_{pz} = \int_{\varepsilon_1}^{\varepsilon_2} x\left(\varepsilon_m^{th}\right) d\varepsilon_m^{th} =$$

$$= -\frac{1}{2\sqrt{\chi}} \int_{\varepsilon_1}^{\varepsilon_2} \sqrt{\left(W_0\left(\frac{1}{\pi e} \left(\frac{\alpha}{\rho c} \frac{q}{vs} \sqrt{\chi} \right)^2 \frac{1}{\varepsilon_m^{th^2}} \right) + 1 \right)^2 - 1}\, d\varepsilon_m^{th}$$

$$\varepsilon_y^* = \varepsilon_2 - \varepsilon_1 = -\left(\varepsilon_Y - \varepsilon_{ini} - \varepsilon_{y1} + \varepsilon_{y2}\right) \approx -\left(\varepsilon_Y - \varepsilon_{ini} - \varepsilon_y\right)$$

where ε_Y is the strain at yield point and ε_y is the residual caused by the limited stiffness of the structure. Thus:

$$\varepsilon_1 = \varepsilon_Y + \varepsilon_{ini} + \varepsilon_y \;\; \text{and} \;\; \varepsilon_2 = 2\left(\varepsilon_Y + \varepsilon_y\right)$$

Hereby the Lamberd function $W_0(u)$ can be solved using either Fritsch's or Halley's interpolation, combined with Newton's method [26].

The transition between tensile and compressive stress corresponds to the point where plastic strain goes to zero, i.e. point A_1. The strain equation for longitudinal component, i.e. the weld axis aligns to Y-axis, either straight or curved, becomes:

$$\varepsilon_Y + \varepsilon_y + \varepsilon_{ini} = \alpha \Delta T_m\left(b_{pz,0}\right)$$

However, if sheets have a curvature along the weld their stiffness is limited and therefore the residual strain differs from zero [27, 28]. To simplify the expression it can be introduced by functions $K_{R,i}=f(R,s)$, applied to the strain vector components, i.e. entity. Here R and s are the radius of curvature and sheet thickness respectively. Thus, the residual strain along the sheet curvature can be written as follows:

$$\varepsilon_y = v_y \left(\frac{1}{B\, s} + \frac{x_w}{I_z} x_w + \frac{z_w}{I_x} z_w \right) \frac{K_{R,v_y}}{K_{Rb_{pz}}} =$$

$$= v_y \left(\frac{1}{B\, s} + \frac{x_w}{I_z} x_w + \frac{z_w}{I_x} z_w \right) K_{R,\varepsilon}(R,s)$$

In that case the proportion function $K_{R,i}=f(R,s)$, can be determined by the moment of inertia equation, considering the stiffness of the curvature, as follows:

$$K_{R,\varepsilon}(R,s) = \frac{\varepsilon_y}{\varepsilon_{y,\infty}} = 1 + b_{pz} s \left(\frac{1}{b\, s} + \frac{z_c}{I_x} z_c \right) + b_{pz} \frac{\sqrt[4]{3\left(1-\nu^2\right)}}{\sqrt{R\, s}} =$$

$$= 1 + \frac{b_{pz}}{b} + b_{pz} \frac{\sqrt[4]{3\left(1-\nu^2\right)}}{\sqrt{R\, s}} ,$$

In addition, a limited stiffness of flat sheets as well as a presence of initial strain also contribute to the inherent strain, s. [20], but in the current study these will be neglected due to the reasonability of the considered welded joints. Hence, in a first approximation, the point A_1 can be calculated by equalizing the maximal thermal strain to the yield strain and analogues the point A_2 – to two times to the yield strain.

$$A_1 = \frac{p}{2\sqrt{\chi}} \sqrt{\left(W_0\left(\frac{\chi}{\pi e} \left(\frac{\alpha q}{\rho c v s} \right)^2 \frac{1}{\left(\varepsilon_Y + \varepsilon_{ini} + \varepsilon_k\right)^2} \right) + 1 \right)^2 - 1} +$$

$$+ \left(1-p\right) \sqrt{\frac{2}{\pi e} \frac{\alpha q}{\rho c v} \frac{1}{\left(\varepsilon_Y + \varepsilon_{ini} + \varepsilon_k\right)} - z_s^{\,2}}$$

and

$$A_2 = \frac{p}{2\sqrt{\chi}} \sqrt{\left(W_0\left(\frac{\chi}{\pi e} \left(\frac{\alpha q}{\rho c v s} \right)^2 \frac{0.25}{\left(\varepsilon_Y + \varepsilon_{k'}\right)^2} \right) + 1 \right)^2 - 1} +$$

$$+ \left(1-p\right) \sqrt{\frac{2}{\pi e} \frac{\alpha q}{\rho c v} \frac{0.5}{\left(\varepsilon_Y + \varepsilon_{k'}\right)} - z_s^{\,2}}$$

where z_s = s/2 for the middle surface in case of thin sheets, ε_k is the strain caused by limited stiffness and is usually equal to zero, p is the weld form factor that depends on the process and becomes 1 for deep penetration weld, i.e. line heat source, and near 0 for surface weld of relatively thick wall joints, i.e. point heat source.

3. Approval of the working hypothesis

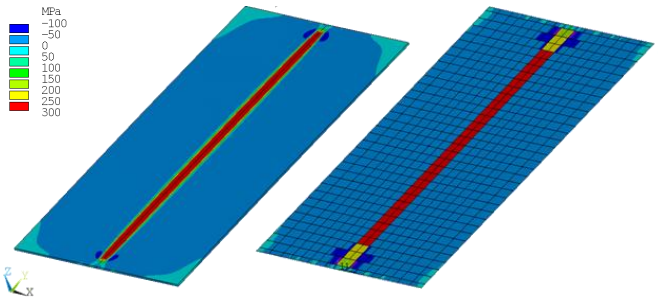
To prove the reasonability of this hypothesis a simple numerical experiment is considered. Assuming a known distribution of the plastic strain we try to load it as an integral value on different FE meshes (shell FE model). In this trial we will keep the width of the target elements equal to the width of the plastic zone (b_{pz}) at its centroid, i.e. the middle point between A_1 and A_2, s. fig. 2. The width of the other elements (b_0, see fig. 1) we will vary relative to it. The results are than compared with the nominal stress distribution. Here nominal denotes the stress and strain distribution calculated by benchmark studies using 3D TMMA. The calculation experiment performed considers a non-alloyed reference structural steel, e.g., S235J2 with a yield strength of 290 MPa, with thickness of 5 mm, and a reference parameter of a GMAW process, applying single-pass double welds. The parameters are as follow: top side: 168±8 A, 20,6 V, 10 mm/s and bottom side: 225±25 A, 26,6 V, 12 mm/s.

The first case represents a butt weld of flat plates, while the second case represents a butt weld of plates with longitudinal curvature. For flat plates, the samples are 1 m long and 500 mm wide, and for curved plates, the weld length is 500 mm and the joint width is 1 m. These two cases result in different levels of stress distribution due to the different stiffness of the joints.

The analysis of the residual stress calculation was only performed on the thermally induced residual stresses in the longitudinal direction. In the transverse direction of the seam, the calculations show only marginal residual stresses in both the flat sheets and the curved shells. The subject of the analyses performed here is both the mathematically determined transition from the

tensile to the compressive zone and the stress distribution in the compressive zone.

In case of welding of flat plates the tensile stress near the weld are equalized by nearly constant compressive stresses outside this zone, see fig. 2 and the doted curve of fig.3. For the analytical-numerical calculation the meshing parameter b_0 was varied relatively to the width of the plastic deformed zone b_{pz}, starting with relation ratio from 4/3 the width of b_{pz} until 1/4 of it.



a) *b)*

Fig. 2 *Cualitative comparison of the calculated welding residual stress fields (longitudinal stresses) in flat structures using: a) transient thermal mechanical Simulation and b) the analytical-numerical hybrid model*

The results show that, despite the variation, the equalizing compressive stress remains unchanged, fig.3. In the same time, the position of the turning point from the tensile range to the compressive range is highly dependent on the meshing, i.e. b_0-parameter. After adjusting the mesh in the plastic strain range to a value equal to A_1 and A_2 respectively, in that case the 1/4-value, the analytical-numerical hybrid calculation delivers results that are approximately the same as those obtained from the TMMA-calculation. The deviations can be described as marginal.

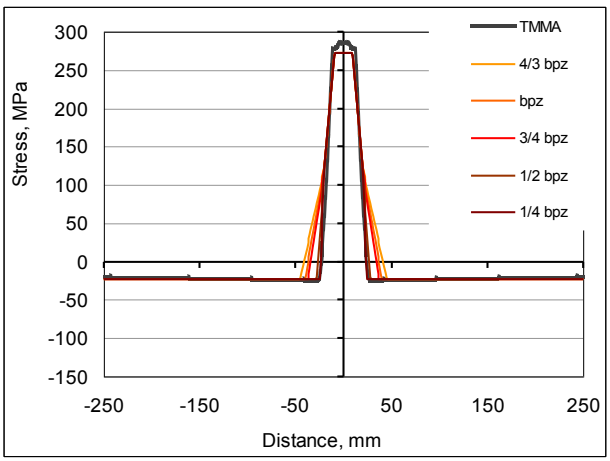
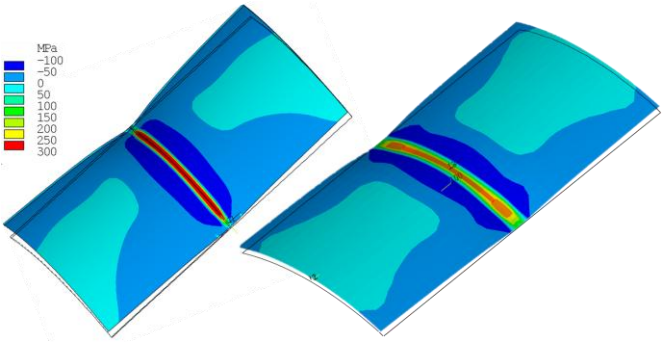


Fig. 3 *Calculated transverse distribution of the thermally induced longitudinal welding residual stress in flat sheet structures after variation of b_0 parameter*

In the curved specimens (fig. 4), the residual stress fields from the TMMA simulation show an asymmetrical distribution along the weld seam. This is due to the inconsistent development of plastic strain along the seam, which was also observed in the distortion calculation. The results of the calculations with the analytical-numerical hybrid model, on the other hand, are symmetrical. However, this can generally be described as a minor effect.

Both calculations also show a non-linear distribution of the longitudinal compressive residual stresses in the transverse direction, see fig.5. The quantitative comparison based on the transverse distribution of the longitudinal residual stresses in the center of the specimen illustrates the significance of the hybrid model, when adjusting the b_0 parameter, i.e. nodes location to A_1 and A_2 respectively (fig. 5, curve 1/8 bpz). However, a slight deviation can be seen between the TMMA (dashed curve) and the stress curves calculated with the analytical-numerical hybrid model (1/8 bpz) in the transition area from tension to compression. The reason for this is primarily the lower mesh density in the analytical-numerical hybrid model. Better agreement can be achieved by refining the FE mesh or using shell elements with a quadratic shape function. However, at small distances from the transition point, the stress distributions correlate very well.



a) *b)*

Fig. 4 *Cualitative comparison of the calculated welding residual stress fields (longitudinal stresses) in curved structures using: a) transient thermal mechanical Simulation and b) the analytical-numerical hybrid model*

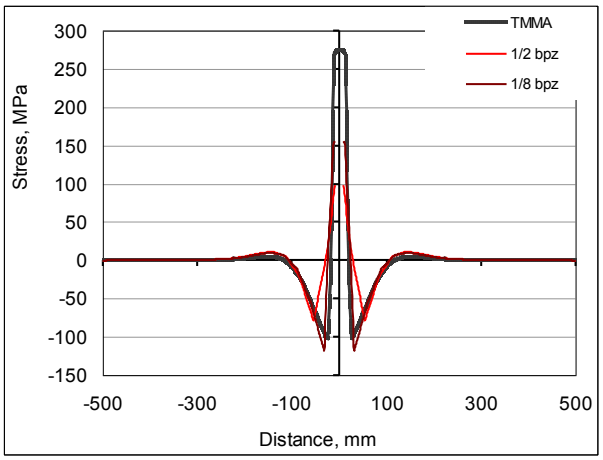


Fig. 5 *Calculated transverse distribution of the thermally induced longitudinal welding residual stress in curved sheet structures after variation of b0 parameter*

The results clearly show that although the maximum compressive stress value remains unchanged, the transition point from tension to compression can be strongly influenced by the mesh. When the FE mesh is adjusted using parameters A_1 and A_2, both the continuous and analytical-numerical simulations deliver virtually identical results.

It is worth mentioning that performing a calculation of the distribution of residual welding stresses using the analytical-numerical hybrid model takes seconds and does not place any particular demands on computer power.

4. Conclusions

The analytical-numerical hybrid model has already been successfully applied to a large number of components of varying complexity. However, the focus was on weld distortions. Little attention was paid to the local stress state in the vicinity of the seam. However, this influences the load-bearing behavior of welded

components. Verification of the stresses calculated with the hybrid model against the results of continuous thermo-mechanical numerical calculations showed good agreement. To improve this agreement, a new meshing strategy was suggested and developed.

The study is limited to thin sheet structures, where the plastic deformed zone penetrate the sheets. Analytical expressions, that support the determination of the characteristic FE parameters, specially derived for this purpose is suggested. For thick sheet structures, additional approval of the analytical expressions is necessary.

The analytical-numerical hybrid model provides a practical methodology for calculation of residual stress distribution in large structural components.

To obtain a proper distribution of welding residual stresses the finite element mesh must be aligned with the lower limit of the plastic zone.

The analytical-numerical hybrid model has a great relevance especially for the practice, because of incomparable calculation times and power against the common calculation approaches.

Acknowledgments:

Part of this work was supported by European Regional Development Fund under "Research Innovation and Digitization for Smart Transformation" program 2021-2027 under the Project BG16RFPR002-1.014-0006 "National Centre of Excellence Mechatronics and Clean Technologies".

Another part of the work was carried out under IGF project No. 19173 BR of the German Research Association for Steel Application (FOSTA). This project is funded by the German Federal Ministry of Economic Affairs and Energy (BMWi) by the AiF (German Federation of Industrial Research Associations) as part of the program for support of the Industrial Cooperative Research (IGF) on the basis of a decision by the German Bundestag.

5. References

1. Norm DIN EN 1993-1-5. 2010-12. Eurocode 3: Bemessung und Konstruktion von Stahlbauten - Teil 1-5: Plattenförmige Bauteile
2. Stapelfeld C., Launert B., Pasternak H., Doynov N. Michailov V.: Traglastberechnung versteifter Platten und Schalen unter Berücksichtigung realer Schweißimperfektionen. Bauingenieur 93 (2018) 403-411
3. Radaj D.: Welding residual stresses and distortion. Calculation and measurement, DVS-Verlag, Duesseldorf (2003)
4. Lindgren L.-E.: 'Computational welding mechanics: thermomechanical and microstructural simulations'; 2007, Cambridge, Woodhead Publishing
5. Michaleris P.: Modelling welding residual stress and distortion: current and future research trends, Science and Technology of Welding and Joining, 2011, 16(4), 363-368, DOI: 10.1179/1362171811Y.0000000017
6. Fujimoto T.: A method for analysis of welding residual stresses and deformations based on the inherent strain, Journal of the Japan Welding Society (1970) 39, 236–252. doi: 10.2207/qjjws1943.39.4_236 (in Japanese)
7. Ueda Y., Kim K., Yuan M.G.: A predicting method of welding residual stress using source of residual stress (report I), Transactions of JWRI, 1989, 18(1), pp. 135–141.
8. Ueda Y., Yuan M.G.: Prediction of residual-stresses in butt welded plates using inherent strains', Journal of Engineering Materials and Technology – Transactions of the ASME, 1993, 115 (4), pp. 417–423.
9. Yuan M.G., Ueda Y.: 'Prediction of residual stresses in welded T-and I-joints using inherent strains', Journal of Engineering Materials and Technology – Transactions of the ASME, 1996, 118 (2), pp. 229–234.
10. Mun H.S., Jang C.D.: 'Prediction of welding deformation of hull panel blocks using an advanced inherent strain analysis method considering the heat equivalent layer effect', *Met Mater Int*, 2011, 17(6): pp. 993–1000.
11. Michaleris P., Debiccari A.: Prediction of welding distortion, *WJ*, 1997, 76(4): pp. 172-180
12. Murakawa H., Okumoto Y., Rashed S., Sano M.: 'A practical method for prediction of distortion produced on large thin plate structures during welding assembly', *Weld World*, 2013, 57, pp. 793–802.
13. Duan Y. G., Vincent Y. et al.: 'Prediction of welding residual distortions of large structures using a local/global approach', *Journal of Mechanical Science and Technologie*, 2007, 21(10), pp. 1700-1706.
14. Tsirkas S. A., Papanikos P. et al.: 'Evaluation of distortions in laser welded shipbuilding parts using local-global finite element approach', *Science and Technology of Welding and Joining*, 8(2), pp. 79-88, 2003
15. Ma N., Wang J., Okumoto Y.: 'Out-of-plane welding distortion prediction and mitigation in stiffened welded structures', *Int J Adv Manuf Technol*, 2016, 84, pp. 1371–1389.
16. Ikushima K., Itoh S., Shibahara M.: 'Numerical analysis of welding deformation for large-scale structure', *Q J Japan Weld Soc*, 2013, 31(4), pp. 138s–142s.
17. Deng D., Serizawa H., Murakawa H.: Theoretical Prediction of Welding Distortion Considering Positioning and the Gap between Parts, Trans. JWRI, 2001, 30(2), 89-96
18. Michailov V.G., Doynov N., Ossenbrink R., Dinkov P., Hristov S.: 'Advanced analytical-numerical approach for simulation of welding distortions', *J Mater Sci Technol (Bulgaria)* 15(3), pp. 139–150, 2007.
19. Michailov V.G., Doynov N., Stapelfeld C., Ossenbrink R.: 'Hybrid model for prediction of welding distortions in large structures', *Front. Mater. Sci.*, 2011, 5(2), pp. 209–215.
20. Doynov, N; Stapelfeld, C; Michailov, VG; Pasternak, H; Launert, B: Distortion analysis of large scaled welded structures, In: Mathematical Modeling of Weld Phenomena 12, Eds.: C. Sommitsch, N. Einzinger, P. Mayr, Verl. TU-Graz, 2019, 254-280, doi: 10.3217/978-3-85125-615-4
21. Nikolaev G. A.: *Svarochnie konstrukcii*. Maschgiz Moskau, Moskau, 1962. (in Russian)
22. Okerblom N. O.: Welding Stresses in Metal Structures, Mashinostroenie, Moskau/Leningrad (1955) (in Russian)
23. Kuzminov S. A.: Welding Deformations of Ship-Structures, Sudostroenie, Leningrad (1974) (in Russian)
24. Gatovskii K. M., Karkhin V. A.: *Theoria svarochnih deformaciy i napriajeniy*, LKI, Leningrad, 1980. (in Russian)
25. Michailov V.G., Karkhin V. A., Petrov P.P.: *Principles of welding*, Politechnic Uni. Publ. St. Petersburg, 2016.
26. Veberic D.: Lambert W function for applications in physics: Computer Physics Communication, 2012, 18(12), 2622-2628
27. Luo Y., Ishiyama M.and Murakawa H., Welding Deformation of Plates with Longitudinal Curvature, Trans. JWRI, 28(2), 1999
28. Pasternak H., Stapelfeld C., Launert B., Michailov, VG, Doynov, N., Kaya CA: Ermittlung der Tragfähigkeit neuartiger stählerner Schalenbauwerke unter realitätsnaher Berücksichtigung des Schweißverzugs, Book Series FOSTA Forschungsberichte; P 1126, Verlag und Vertriebsgesellschaft mbH, Düsseldorf, 2020

Fiberglass casing string cementation operations in wellbore

Igor Medved, Borivoje Pašić
University of Zagreb, Faculty of Minning, Geology and Petroleum Engineering, Pierrotijeva 6, 10 000 Zagreb, Croatia
igor.medved@rgn.unizg.hr, borivoje.pasic@rgn.unizg.hr

Abstract: *Casing string is critical component in wellbore construction, defining wellbore diameter and providing structural integrity throughout drilling and production operations. Traditionally, steel casings are generally used due to their mechanical strength; however, problems connected with corrosion, particularly in environments containing hydrogen sulfide or saline formation water, presents significant operational and financial challenges. This paper explores the use of fiber-reinforced plastic (FRP) casing as a corrosion-resistant alternative, focusing on glass fiber-reinforced epoxy composites, especially concerning cementing operation. FRP casing properties depend on the fiber–matrix composition, fiber type, and manufacturing quality, which affect tensile and compressive strength, thermal stability, and resistance to environmental degradation. Laboratory and field studies, including pilot projects in Argentina, Oman, Brunei, and Kuwait, evaluated casing handling, rig down speed, anchoring, and cement bonding. Special attention was given to cementation procedures, fluid formulations for mud cake removal, and ultrasonic methods for assessing casing-to-cement bonding, adapted for the acoustic characteristics of FRP materials. Results indicate that while steel casings exhibit superior cement bonding, FRP casings can achieve adequate structural performance when mechanical stresses during handling and installation are carefully controlled and proper chemical compatibility between fluids and cement is ensured. Field data show that FRP casings can be deployed with only minor reductions in installation speed for smaller diameters and that optimized handling and cementation practices are crucial for operational success. These data demonstrate that FRP casings offer a technically feasible and economically advantageous alternative for wells in highly corrosive environments. However, their successful implementation requires tailored operational procedures, including modified handling equipment, optimized fluid systems, and specialized evaluation methods. Further field studies are needed to develop comprehensive guidelines for widespread adoption.*

Keywords*: CASING, FIBER-REINFORCED PLASTIC (FRP), CEMENTATION, CORROSION, CASING-TO-CEMENT BONDING*

1. Introduction

Casing string is an extremely important part of the wellbore, as it defines the diameter of the wellbore and, among many other tasks, protects it from collapse. In order to ensure the long-term successful performance of the well, it is necessary to properly dimension casing string, which means that the appropriate inner and outer diameters should be selected along with the appropriate material and its quality and installation depth for each individual series of casing. The most commonly used casing is made of steel (of a certain quality), which remains the ideal material for most wells [1]. However, this material is prone to corrosion, which poses a major problem in certain locations during the production life of the well [2]. Corrosion is considered one of the most expensive problems in the oil and gas industry, even in modern times that offer various effective solutions to prevent its occurrence [3]. This phenomenon is defined as the deterioration of a metal or its properties and represents a major problem not only during drilling, but also throughout each subsequent phase of well operations. The process of corrosion occurs due to chemical reactions with substances containing oxygen, chlorine or hydrogen sulfide, which is a common occurrence during oil or gas production. Special emphasis should be placed here on hydrogen sulfide, a highly corrosive acid gas that causes major corrosion-related problems. In most oil wells around the world, formation (salt) water is produced along with oil and natural gas and is also a natural corrosive substance. With a longer production life, the proportion of formation water increases, which further worsens the situation in the well. Metals in the tubular tool oxidize and form their corresponding oxides and salts, which results in a decrease in the strength of the metal, i.e. the loss of the initial properties of the casing string. The ultimate consequence may be the replacement of the entire string to avoid production losses [4]. This problem, apart from the production phase, can also occur during special oilfield services, such as acid treatment of the underground formation, but also during the increasingly common enhanced oil recovery projects that involve injecting water or gases through existing or newly drilled wells.

Given all the important functions of casing, it is of utmost importance that the string can withstand high pressures, temperatures and forces that can lead to material failure over the long term. If the casing structure were to degrade, the worst consequence would be the collapse of the wellbore, making it almost impossible to replace the string in the well, especially if it is a small diameter wellbore. In that case, it would be necessary to start drilling and completion of a new well, which creates large direct and indirect financial losses. In order to reduce, and possibly eliminate such consequences of corrosion on the casing string, the industry has begun to research cost-effective composite materials that could withstand the expected stresses in the wellbore conditions with better corrosion resistance than steel [5]. Composite materials are structurally heterogeneous materials consisting of two or more different phases that are chemically or mechanically bonded [6]. They can be produced by appropriate thermal and mechanical treatment, but many composites are produced by mixing individual components in such a way that they bind together. The properties of a composite depend not only on the intrinsic properties of the reinforcement (fibers) and the properties of the matrix, but also on the geometry (size and shape) of each component. In addition, the properties depend on the characteristics of the interface between the different components. Therefore, mechanical damage of composite material is associated not only with the breakage of the reinforcement and the matrix, but also with their separation at the interface [7]. This last characteristic depends on the bond between the two components. Surface roughness is also important, as it affects the degree of mechanical bonding of the components [6].

The introduction of composite materials into the oil and gas industry has provided many alternatives to expensive alloy steel, which, in addition to corrosion resistance and overall financial benefit, also has some other advantages such as easier handling of equipment since it is a material with a significantly lower unit mass. One of these materials is fiber-reinforced polymer, or so-called FRP. There are many types of fibers with which a polymer can be reinforced, such as aramid fibers, basalt fibers, carbon fibers or glass fibers. This type of composite is produced by mixing individual components in such a way that they bind, such as, for example, the incorporation of glass fibers into epoxy resin to produce fiberglass. Fiberglass consists of two different materials that together form a whole, namely a polymer and glass fibers. Epoxy resin is an example of a frequently used polymer resin, and in order for fiberglass to have satisfactory properties, it is reinforced with thin glass fibers. Epoxy resin has an excellent strength-to-density ratio, while glass provides additional strength under tensile and compressive stress. Thus, fiberglass equipment is lightweight due to the low density of epoxy resin, with significant strength due to the glass fibers in the structure [8]. The composition and proportions of epoxy resin and glass fibers primarily depend on the purpose of the fiberglass equipment, which means that the composition of the fiberglass material can vary significantly. For example, a pipe tool (such as a casing) made of fiberglass can be quite resistant to tensile and compressive stresses, but at the same

time it does not need to be designed to have good properties when subjected to torsion. It is also important to know that the matrix, in this case epoxy resin, defines the behavior of fiberglass with respect to environmental conditions, which is extremely important for downhole equipment.

Glass fibers are, along with carbon fibers, the most commonly used reinforcement for composites. A fiber can be described as an elongated, uniform material with a more or less uniform cross-section of less than 250 μm, with a length-to-diameter ratio that is typically greater than 100 [9]. The primary tasks of fibers are to absorb the load (in structural composites, fibers carry 70 to 90% of the load), provide strength, stiffness, and thermal stability, and to provide electrical conductivity or insulation, depending on the purpose of the composite [10]. The main component of glass fibers is SiO_2, the proportion of which is usually above 50% [11]. The most commonly used glass fibers for fiberglass are E-glass fibers and S-glass fibers.

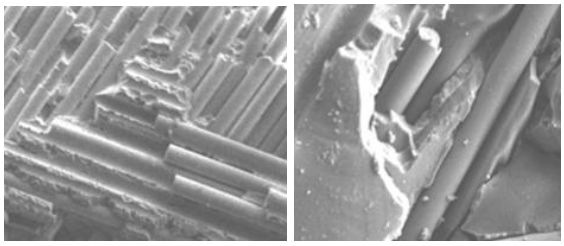


Fig. 1 *A view of glass fibers in epoxy resin taken with a scanning electron microscope (SEM) [6]*

In many composite materials, the main functions of the matrix are to transfer the load to the fibers and to maintain the structure and properties of the material under certain environmental conditions [12]. In addition, the matrix can affect the compressive strength, shear properties within the composite structure and the interaction of the matrix with the fibers [13]. The thermal stability of fiberglass is largely determined by the thermal resistance and stability of the polymer matrix. The heat resistance of polymeric materials is determined by their shape stability, which includes deformation when heated, and thermal stability is determined by the ability of the material to maintain chemical stability during heating [11].

2. Cementing operation

The cementation operation itself is carried out in a conventional manner, but it is necessary to pay attention to certain phases during cementation, which are considered critical when it comes to this type of material. It is necessary to adjust the cementation operational program in order to prevent breakage of fiberglass casing, given their weaker mechanical properties compared to steel casing, which primarily refers to resistance to burst and collapse, as well as axial loads [14]. Significant adjustments are required to properly handle the fiberglass casing at the rig floor and running in hole, and to ensure satisfactory bonding of the cement rock to the fiberglass after cementation. Conventional tools used for this purpose on drilling rigs are adapted to handle steel casing, including casing handling tools. Certain tools can be used for fiberglass casing without any modification, but the proportion of such equipment on site is insignificant. Accordingly, field reports show that improper handling on rig floor is a more common cause of damage to fiberglass casing than during casing running in hole, cementation, and post-cementation processes [15]. The solution to this problem lies either in modifying the equipment intended for handling fiberglass casing or in adding reinforcement to the contact surface of casing and handling tool. Handling equipment adapting most often involves tools that have a softer contact surface to minimize the possibility of damaging the outer wall of the fiberglass casing. The use of softer materials is particularly important for slips, rig tongs and elevators since each pipe is in contact with the aforementioned group of tools.

On the other hand, pipe adaptation is most often performed by coating a certain area of the pipe near the threaded joints (which are in contact with the handling tool) with a layer of appropriate material that prevents mechanical damage to the outer wall of the fiberglass casing. The described fiberglass casing have been successfully used on several projects in Argentina, Oman and Brunei [16]. In addition to all of the above, it is worth adding observations from Kuwait where fiberglass casing was handled on more than 20 wells [14]:

- when transferring casing to the rig site, only braided slings were used;
- for the initial manual tightening, special tightening tongs were used, made of a softer material that does not damage the outer surface of the fiberglass casing;
- to achieve the prescribed tightening torque for casing, an automatic pipe wrench (tongs) was used, but a significantly lower torque was used than for steel pipes, i.e. the tightening was performed to the torque prescribed by the manufacturer of fiberglass casing;
- pneumatic slips were used, instead of manual slips;
- only an annular preventer was used for well control.

If drilling rig has equipment adapted to handle fiberglass casing, it is possible to achieve a downhole speed that is close to that of a conventional steel string. For example, a project in Argentina has shown that the speed of fiberglass casing running in hole up to 0.0889 m (3 ½ inches) in diameter is only 5.7% slower than that of an equivalent steel casing string [17]. The overall tripping time is somewhat worse, however, since the fiberglass casing is usually slightly shorter than the standard steel casing, which means that more time is spent overall due to the greater number of casing make-ups. When running in hole larger diameter casings, e.g. 0.2445 m (9 5/8 in), the difference in speed is still significant. The fiberglass casings were run in hole at an average speed of 0.3048 m/s (1 ft/s), which is three times slower than the 0.9144 m/s (3 ft/s) recorded for the steel string [14]. Fiberglass casings could withstand higher speeds of running in hole, but it is more important to avoid breakage caused by excessive axial load. Running in hole can be considered the riskiest part of the entire cementing process, since a significantly lower value of the tension is available in the event of string failure. In order to minimize such a possibility, the stability of open hole must be ensured by drilling. Therefore, the use of fiberglass casing string depends on the type of rock drilled, as well as on the level of quality of the drilled wellbore. Also, slightly larger ratios of the diameter of the wellbore to the outer diameter of the casing joints are taken into account, than is the case with steel casing.

Before cementing, due to the significantly lower total weight of the fiberglass casing, the string should be anchored to the borehole walls so that the lifting of the string, which is a direct consequence of buoyancy, does not cause critical pressure loads that can result in buckling or breakage. For this purpose, an anchor with stop rings without nuts is used in the open hole to prevent damage to the fiberglass casing, and the string thus manages to resist the compressive force. Also, this type of tool acts as a kind of centralizer, to enable uniform penetration of the cement slurry in the annular space between the string and the wellbore walls, and thus better cementing job. An alternative to casing anchoring is to use a lower density cement slurry [18], which in some cases is technically not feasible. Steel casing can also be used at the bottom of the string to provide additional weight and thereby reduce the negative buoyancy effect. Testing the quality of cement bonding behind fiberglass casing string (cement bonding) poses a significant challenge for conventional methods since there is a large difference in the acoustic properties of fiberglass compared to steel [19]. In wellbores lined with steel casing, methods based on measuring ultrasonic signals sent perpendicular to the casing have been successfully used for many decades. Pulse echo tool, which is

immersed in the fluid inside the casing, work by sending and receiving return signals with a frequency of 200 kHz to 400 kHz, which are used to calculate the acoustic impedance of the cement rock when the sound signal passes through the steel casing wall, the cement rock and the formation [20]. The parameters required for calculating the acoustic impedance of cement stone are shear velocity, compressional velocity and the acoustic impedance of steel and drilling fluid in the well, in which the ultrasonic probe is immersed. Among other things, the reliability of the method lies in the fact that the properties of steel are well known, and the changes in properties between different manufacturers of steel casings are insignificant. Due to the significant difference in the speed of sound and resonant frequency when passing through fiberglass compared to steel, the classic use of these tools is not possible, since the listed properties in the case of fiberglass are below the measurement range of typical ultrasonic scanning tools [21]. The cement bond log method, which measures the attenuation of the first return sound pulse, is also unusable in the case of cementation of fiberglass casing. The reason lies in the fact that waves passing through the cement stone and formation interfere with the slower return pulses from the fiberglass, making them almost impossible to isolate for the purpose of precise evaluation of the results.

Instead of conventional methods that calculate the boundary between steel and cement stone, the acoustic impedance of the cement stone located in the annular space between the fiberglass casing and the formation is calculated from the amplitudes between the first two pulses [20]. The first ultrasonic signal (echo) is from the boundary between the drilling fluid inside the casing and the inner wall of the fiberglass casing, while the second signal is a reflection from the boundary between the outer wall of the fiberglass casing and the cement stone, as shown in Fig. 2.

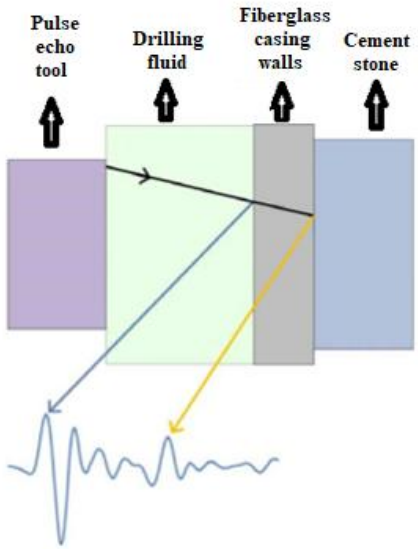


Fig. 2 *View of the echoes from the boundary between the drilling fluid inside the casing and the inner wall of the fiberglass casing and from the boundary between the outer wall of the fiberglass casing and the cement stone [21]*

This method of measurement can only give accurate results if the wall of the fiberglass casing is thick enough to keep the first and second signals separate. Also, the fiberglass casing must not have a structure that can significantly attenuate the signal as it passes through the wall, otherwise the second signal is unusable. The parameters needed to calculate the acoustic impedance of the cement stone and the wall thickness of the fiberglass casing are the compression rate, the acoustic impedance of the fiberglass, the attenuation factor of the signal as it passes through the fiberglass, and the acoustic impedance of the fluid inside the well. If the above parameters can be accurately determined by laboratory research, it is possible to determine the quality of the cement stone behind the fiberglass casing, as well as its wall thickness, with an ultrasonic probe. In addition to the above conditions that must be met, differences in the composition of the fiberglass casing also pose a problem. There are several parameters that can affect the acoustic impedance of fiberglass [20]:

- a type of plastic polymer, primarily due to differences in density;
- glass fiber content (average content is about 70%);
- fiberglass casing production method;
- surface treatment method, surface smoothness;
- cavities in the wall of the fiberglass casing created during manufacturing.

Due to the lack of a database that includes different variants of fiberglass casings, the assessment of the possibility of using an ultrasonic probe (existing field equipment that does not involve additional investments) must be done separately for each well, which presents additional operational problems. Laboratory research and field results related to a project in Argentina, in which 70 wells were cased with fiberglass casings [16], provided an interesting insight into the level of casing to cement bonding of this material in relation to steel pipes. The experimental phase also included measurements of the quality of mud cake removal from the wellbore walls before cementing. An Intevep cell can be used to simulate the above process [22], and the mud cake is generated on Whatman #50 filter paper. Thus, with this device shown in Fig. 3, a quantitative evaluation of the effectiveness of a particular mud cake removal fluid formulation can be performed. Laboratory tests have shown that the best results were achieved with a water-based fluid portion containing 7% citric acid, 0.2% nonionic surfactant and 251 kg of calcium chloride ($CaCl_2$) per 1 m^3 of portion, followed by another water-based fluid feed containing 3% sodium carbonate (Na_2CO_3) and 2% anionic surfactant, which removed 80% of the mud cake [16].



Fig. 3 *Device for laboratory testing of mud cake removal quality [22]*

Also, laboratory tests were conducted to compare the bond quality of cement stone for fiberglass casing compared to steel ones. Before cementing the pipes, their outer surface is immersed in drilling fluid and then washed with a portion of fluid of the aforementioned composition, to remove the mud cake. The testing was carried out in such a way that segments of fiberglass pipe (smooth and rough surfaces) were cemented inside a larger diameter mold, and the cement slurry was dried for 48 hours at a temperature of 55°C [16]. The pipe is then axially loaded until a displacement in the opposite direction occurs, which indicates the force required to break the contact surface between the fiberglass pipe and the cement stone. The same procedure was performed with the steel pipe, so that the results could be compared. As expected, this study proved that steel protective pipes bond best to the cement stone, and a force of 23,350 N was required to move the cemented pipe, while the bond between the cement stone and the fiberglass protective pipe with a smooth (treated) surface was broken at an axial force of 13,900 N [16]. On the other hand, the bonding of the rough-surfaced fiberglass casing to the cement stone was extremely poor,

since this pipe surface remained saturated with the mud cake flushing fluid, which created poor bonding conditions at the interface due to the inefficient hydration process caused by the chemical incompatibility of the mud cake flushing fluid and the cement slurry. This is also evidence that in addition to the quality of mud cake removal, chemical compatibility between the different fluids is also extremely important. It should be noted that these results refer to a cement slurry with a density of 1649 kg/m^3 (13.76 ppg), and similar results were obtained after cementing the pipes with a cement slurry with a density of 1849 kg/m^3 (15.43 ppg), which proves that the change in density does not affect the quality of the bond. [16].

3. Conclusion

The use of fiberglass casing string represents a technically viable alternative to steel casings in corrosive environments. However, their successful implementation directly depends on a carefully designed and controlled cementation operation. Key success factors include limiting mechanical loads during handling and running in hole, ensuring string centering during running in hole, optimizing fluid systems and chemical compatibility, and adapted cement bond evaluation methods. However, for more accurate analyses of the cementation success of composite casings, significantly more projects of this type should be implemented in order to draw more detailed conclusions.

4. References

[1] Duthie L., Almarri, H., Saiood, H., Lata, A., Radhakrishnan, G., *Effective Corrosion Mitigation Exploiting Glass Reinforced Epoxy Lined Tubulars in Offshore Producing & Injection Wells*, Offshore Technology Conference, 6-9 May, Houston, Texas, doi:10.4043/29266-MS (2019)

[2] Zaripov, I. M., Iskhakov, A. R., Kateev, R. I., Zaripov, A. M., *Tatneft's experience in well completion using fiberglass-reinforced plastic casing strings*, Oil Industry Journal (2018)

[3] Rauf, A. A., *Performance of Fiberglass Casing and Tubing in Highly Corrosive Environments*, SPE Annual Technical Conference and Exhibition, 28-30 September, Houston, Texas, USA, doi:10.2118/178729-STU (2015)

[4] Hawkins, R. C., *Replacing Corroded and Failed Metallic Pipe with Corrosion Resistant FRP Pipe Design and Installation Requirements and a Case History*, ASME, March 16-20, New Orleans, Louisiana, USA (2008)

[5] Simpson, J., Radhakrishnan, G., *Developments and Experience in Non-Metallic Alternatives to Combat Corrosion in the Oil and Gas Business*, Effective Environment Management Through Continual Corrosion Control Conference, 25-26 November, Bidholi, Dehraddun, India (2006)

[6] Al-Hashem, A., Tarish, H., Fallatah, G., *Cavitation erosion behavior of epoxy-, vinyl ester-and phenolic-based fiber glass composites in sea water*, Corrosion Conference & Expo, NACE International (2009)

[7] Hull, D., *An Introduction to Composite Materials*, Cambridge Press, New York (1987)

[8] Yao, W., *Mechanical Properties of hybrid fiber-reinforced concrete and low fiber volume fraction*, Cement and Concrete Research, 33(1), 27–30 (2003)

[9] Zhang, M., Matinlinna, J. P., *E-glass fiber reinforced composites in dental applications*, Silicon, 4(1), 73-78 (2012)

[10] Singh, P., Pramanik, D., Singh, R. V., *Finite Element Analysis of Pilot's Helmet Design Using Composite Materials for Military Aircraft*, Journal of Aerospace Technology and Management, 8(1), 33-39 (2016)

[11] Bakhareva, V. E., Sargsyan, A. S., *New heat-resistant electrical insulating fiberglass*, Inorganic Materials: Applied Research, 8(6), 881-885 (2017)

[12] Righetti, L., Edmondson, V., Corradi, M., Borri, A., *Fiberglass grids as sustainable reinforcement of historic masonry*, Materials, 9(7), 603 (2016)

[13] Soares, C. A. M., Soares, C. M. M., Freitas, M. J., *Mechanics of composite materials and structures*, Springer Science & Business Media, (Vol. 361) (1999)

[14] Al-Oqab, M., Kaushik, P., Ahmad, A. T., Kumar, S., *Fiber Glass Casing Design, Planning and Installation Experience in Observation Wells*, SPE/IADC Middle East Drilling Technology Conference and Exhibition, 29-31 January, Abu Dhabi, UAE (2018)

[15] Sharif, Q. J., Esmail, O. J., Radhakrishnan, G., Simpson, J. A., Bremner, M. R., *Experience with Fiberglass (GRE) Lined Carbon Steel Tubular for Corrosion Protection for Oil Production Applications*, SPE Annual Technical Conference and Exhibition, 8-10 October, San Antonio, Texas, USA (2012)

[16] Romera, G. A., Robles, J. L., Peacock, H., Morris, W., Peralta, D., *Glass-Reinforced Epoxy Casing: Lessons Learned After Cementing and Completion of 70 Wells*, In SPE Annual Technical Conference and Exhibition. Society of Petroleum Engineers (2008)

[17] Peralta, D., Maggioni, A., Garcia, R., Martin, D., *Successful Application of Glass Reinforced Epoxy (GRE) Casing in Hydraulically Fractured Water Injection Wells*, SPE Annual Technical Conference and Exhibition, 24-27 September, San Antonio, Texas, USA (2006)

[18] Amani, M., Rauf, A. A., *An Update on the Use of Fiberglass Casing and Tubing in Oil and Gas Wells*, International Journal of Petroleum and Petrochemical Engineering (IJPPE), 3, 43-53 (2017)

[19] Abugreen, Y., Kalyanraman, R., Al-Hajeri, M., Raturi, S., Hamadah, A., Al-Qahtani, F., 2018. *Application of a New Concept for Enhanced Well Integrity Evaluation in Unconventional Completions with Fiberglass Casings in Kuwait*, Abu Dhabi International Petroleum Exhibition & Conference, 12-15 November, Abi Dhabi, UAE (2018)

[20] Edwards, J., Kalyanaraman, R. S., Renard, S., Kuijk, R. V., Froelich, B., *Cement Evaluation of Fibre-Reinforced Plastic Casing for EOR Observation*, SPE EOR Conference at Oil and Gas West Asia, 31 March – 2 April, Muscat, Oman. Society of Petroleum Engineers (2014)

[21] Tello, L. N., Hesse, K., Pawlowski, M. K., Kozak, M. Z., Audouin, O., Hirsinger, L., *A New and Innovative High Frequency Ultrasonic Method for Evaluating Cement Bond and Casing Thickness in Wells with Fiberglass Casing Applied in the French Paris Basin*, SPWLA 57th Annual Logging Symposium, 25-29 June, Reykjavik, Iceland, Society of Petrophysicists and Well-Log Analysts (2016)

[22] Robles, J. L., Morris, W., Criado, M. A., Jensen, E. L., *Dynamic Mudcake-Removal Evaluation Under Annulus Hydrodynamic Conditions*, SPE Latin American and Caribbean Petroleum Engineering Conference, 20 – 23 June, Rio de Janeiro, Brazil. Society of Petroleum Engineers (2005)

Analysis of workover operations over a ten-year period in an oil and gas field with sucker rod pump production

Borivoje Pašić[1,*], Igor Medved[1], Antonio Knežević[1]
University of Zagreb, Faculty of Mining, Geology and Petroleum engineering[1]
borivoje.pasic@rgn.unizg.hr

Abstract: *At the start of exploitation of any hydrocarbon or geothermal water reservoir, production of reservoir fluids is driven by natural energy in the form of reservoir pressure. Therefore, the primary task for production engineers is to maintain this reservoir pressure for as long as possible, ensuring long-term economic production. Unfortunately, sooner or later it becomes necessary to introduce mechanical methods of fluid lifting. Today, there are numerous solutions on the market for mechanical lifting of reservoir fluids (progressing cavity pumps-PCP, electric submersible pumps-ESP), and one of the oldest mechanical methods for producing reservoir fluids is the sucker rod pump. In the Republic of Croatia, sucker rod pumps are among the most commonly used mechanical methods for lifting reservoir fluids. Although Croatian production engineers have significant experience working with sucker rod pumps, operational problems are common and are accompanied by additional expenses related to workover operations. This paper presents an analysis of workover operations over a ten-year period (from 2011 to 2022) in an oil and gas field in the Republic of Croatia. Based on the collected data, an analysis was conducted to determine the volume of fluid not produced during equipment maintenance and repair, the waiting time for repairs, the duration of equipment maintenance as well as the cost-effectiveness of the repairs. Special attention is given to the analysis of the causes of problems in using sucker rod pumps and the identification of problematic wells.*

Keywords*: SUCKER ROD PUMP, PROBLEMATIC WELLS, WORKOVER OPERATIONS, FAILURES OF DOWNHOLE EQUIPMENT, CAUSES OF EQUIPMENT FAILURES*

1. Introduction

At the start of the exploiting of any hydrocarbon or geothermal water reservoir, production of reservoir fluids is driven by natural energy in the form of reservoir pressure. This reservoir pressure, depending on the location of the reservoirs (depth, density of overburden layers, regional tectonics), may be normal, overpressure or underpressure. Under normal circumstances, it is about normal reservoir pressure which corresponds to the pressure of the column of formation water from sea level to the depth of the reservoir. Unfortunately, starting production of the reservoir fluid (oil, gas, or geothermal water) inevitably causes a decline in reservoir pressure. These trends in reservoir pressure decline can be mitigated through reservoir management strategies, and one of the most commonly strategies is reinjection of the produced water in water-driven reservoirs or gas in gas-cap driven reservoirs.

Therefore, the primary task for production engineers is to maintain reservoir pressure for as long as possible, ensuring long-term economic production. However, sooner or later it becomes necessary to introduce some form of artificial fluid lifting. According to Perrin (1999), at the end of the 1990s artificial lift was used in 75% of the world's production wells (excluding the USA) or even more (90%) if data relating to the USA is included. Artificial method for reservoir fluid lifting can be divided into two groups [1]:

- mechanical lifting by pumping, and
- reduction of reservoir fluid density by mixing the reservoir fluid with gas (natural gas, carbon dioxide) injected into lower part of the production string.

Today, there are numerous solutions on the market for mechanical lifting of reservoir fluids (progressing cavity pumps-PCP, electric submersible pumps-ESP), but one of the oldest and most widely used mechanical methods for producing reservoir fluids is the sucker rod pump. The most important part of the sucker rod pumping system is the positive-displacement pump driven from the surface by rod strings. Despite availability of different and modern solutions for reservoir fluid pumping, the sucker rod pumping system still occupies a large share of the market today. For example, according to data published in 2012, in China there were 118000 wells equipped with sucker rod pumping system, representing 96% of all producing wells [2]. Also, according to data from Matanović i Moslavac (2011), at the beginning of 2000 in the Republic of Croatia were 1,133 active wells, of which 484 were equipped with sucker rod pumping systems while 310 were equipped with gas lift systems [3]. The reason for this probably lies in the fact that it is the oldest artificial system, with extensive technical and engineering experience in its operation.

2. Sucker rod pumping system

As mentioned earlier, the sucker rod pumping system is probably the oldest and most widely used mechanical system for pumping reservoir fluid. The sucker rod pumping system, shown in **Fig. 1**, consists of surface pumping units (usually mechanical or hydraulic propulsion systems) powered by an electric motor or engine (gas or diesel) as well as a pumping head, and a subsurface part which includes the rod string, tubing, and a positive-displacement pump at the bottom.

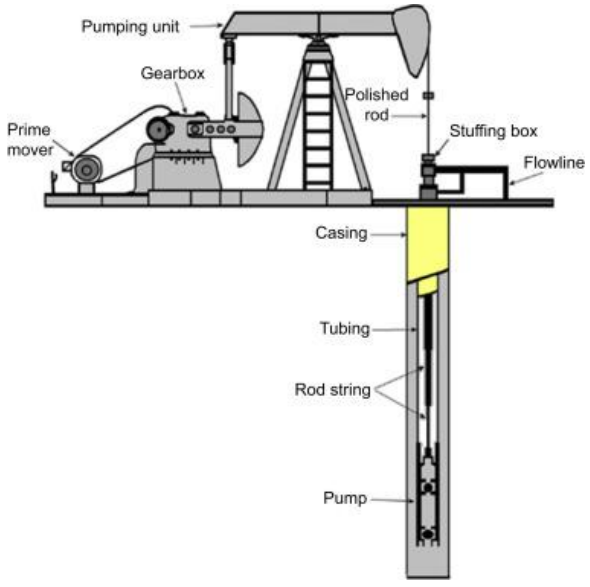


Fig. 1 *Sucker rod pumping system* [4]

Despite technological improvements over the years, the basic working principles of positive-displacement pumping remain unchanged. The core of the system is a positive-displacement pump composed of a cylinder (pump barrel) with a standing valve at the bottom and a hollow plunger with a travelling valve. The hollow plunger is connected to the surface system by a steel rod string, and fluid pumping is achieved by the reciprocating motion of the hollow

plunger and the alternating operation of the valves mentioned above. Depending on their installation method, sucker rod pumps can be classified as rod pumps (R pumps) and tubing pumps (T pumps), each with specific advantages and disadvantages (**Fig. 2**).

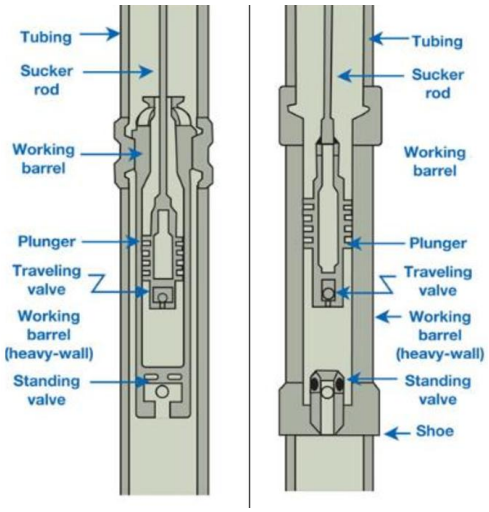


Fig. 2 *Rod pump (left) and Tubing pump (right)* [5]

The pumping unit is installed on the surface and, using electric motors or various types of engines, ensures continuous reciprocating movement of the rod string in opposite direction, enabling the pumping of reservoir fluids accumulated within the wellbore. In additional to the power source for driving the pumping unit, the methods of converting rotational motion from the power unit into linear motion of the rod string is also important. The oldest system, still relevant today, is the mechanical walking beam (**Fig. 3**), balanced with a mechanical counterweight or compressed air. Beside this, there are also hydraulic types of pumping units, as well as various derivatives of these two basic types, such as the linear rod pumping unit (LRP) and other commercial solutions.



Fig. 3 *Mechanical walking beam balanced with counterweight*

The design of the sucker rod pumping system and the selection of the appropriate pump and pumping unit are specific to each location and depend on various parameters, such as the depth of the reservoir, production index, static level of the reservoir fluid column within the wellbore, inside diameter of the installed production casing, pressure required to lift the reservoir fluid and transport it to surface facilities, and the amount of gas within the reservoir fluid, etc.

3. Sucker rod pumping system

As mentioned earlier, the sucker rod pumping system is the oldest method of artificial lifting of reservoir fluid. Given the extensive engineering experience accumulated over 150 years of practical application, the sucker rod pumping system represents a long-term production solution with low operating costs and significant potential for process automation [6]. Despite these advantages, the sucker rod system is accompanied by numerous problems, which can lead to operational halts and associated production losses. Outages in the sucker rod system result in two distinct costs: the first is related to the workover operation required to resolve the cause of the outage, and the second, equally important, is the cost of fluid production interruption (unrealized production of reservoir fluid). Accordingly, from the production engineer's perspective, it is very important to schedule workover operations at specific locations, as reducing the time between problem detection and taking corrective action lowers the costs associated with lost production. This is especially important for large fields with several hundred sucker rod pumping systems installed and possibly only a small number of workover units available in the area.

The sucker rod system outage is most often caused by mechanical wear and material fatigue but can also result from corrosion or their combined effects. The first issue mentioned relates to well construction and system operating principles. Unfortunately, some wells, even those designed as vertical, contain wellbore sections with unwanted changes in inclination and azimuth. Ideally, any contact between the moving rod string and the fixed tubing string within the wellbore should be avoided, but this is practically impossible. According to Hart (2003), between 10% and 20% of the inside surface of the tubing comes into contact with rod couplings [7]. This contact causes excessive wear of the rod couplings and creates a groove on the inner side of the tubing along the length corresponding to the pump stroke. This wear leads to tubing leakage and system downtime, necessitating the removal of the damaged tubing joint from the production string, even though more than 80% of the tubing surface area remains untouched (**Fig. 4)**.

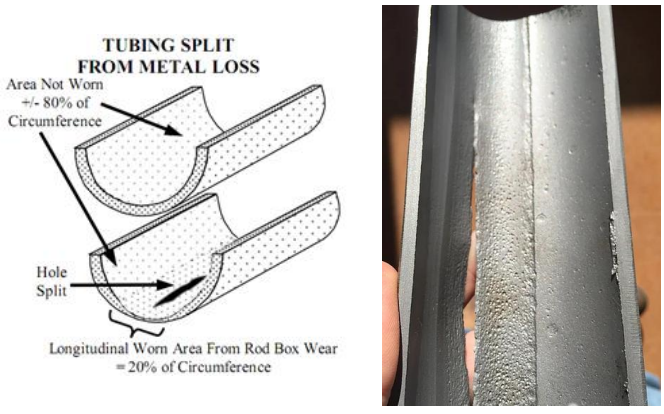


Fig. 4 *Mechanical wear of the tubing* [8]

Apart from mechanical wear, problems also arise from corrosion, especially when the produced fluid contains various admixtures such as carbon dioxide, hydrogen sulfide, or a high proportion of reservoir water. The subsurface components of the sucker rod pump production system, damaged by mechanical action, are particularly susceptible to these processes. Specifically, movement of the rod string inside the tubing removes both the corrosion product and corrosion inhibitors from the inner surface of the tubing, allowing these processes to continue [9]. The chemical

effect of the reservoir fluid on the inner surface of the tubing is shown in **Fig. 5**.



Fig. 5 *Pitting corrosion of the tubing* [10]

Considering all the above, it is very important to detect the primary mechanism of tubing and rod wear as soon as possible. The initial assessment can be made based on chemical analysis of the produced reservoir fluid. In the case of mechanical wear, the produced fluid will contain only metal shavings, whereas in the case of corrosion, the produced fluid will contain products of steel corrosion such as FeS, FeCO3, or iron oxide [7].

4. Analysis of workover operations in an oil and gas field over a ten-year period – Case study from Republic of Croatia

The Republic of Croatia has a long tradition of exploiting hydrocarbon reservoirs both onshore and offshore, as well as geothermal water reservoirs. The oil-gas field under consideration is located in the continental part of the country. Of the 195 wells drilled in this field, only 30 are currently active (less than 15%), of which 29 are production wells and one is an injection well. There are also 43 observation wells (**Tab. 1**) [11].

Table 1. Status of the wells in the oil-gas field under consideration.

Well status			Well number
Active	Oil wells	Sucker Rod Pumps	26
		Electrical Submersible Pumps (ESP)	1
		Natural flowing wells	2
	Injection wells		1
Inactive	Oil wells		39
	Gas wells		2
	Injection wells		6
Observation wells			43
Abandoned wells			75

During the period under consideration, 292 workover operations were conducted on 60 wells. According to the available information, of the 60 wells where workover operations were carried out, one was horizontal, 44 were vertical, and for 15 wells (or 25% of workover operations) there was no information about the type of well (**Fig. 6**) [11].

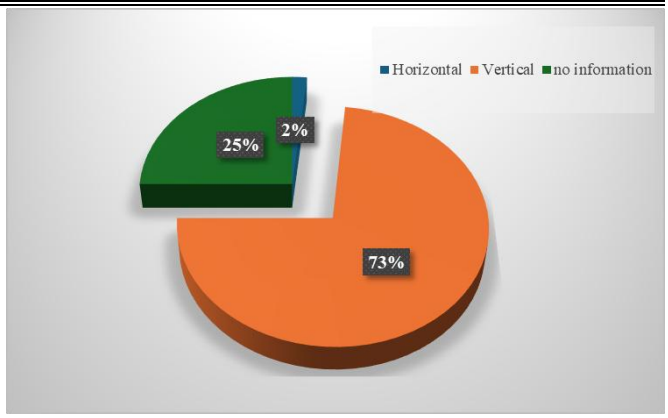


Fig. 6 *Type of wells under workover operation in the period from 2011 to 2022*

Of the 292 workover operations mentioned above, 263 (90%) were conducted in vertical wells, 3 (1%) in horizontal wells, while for 26 operations (9%) there was no information about the type of well construction. Furthermore, 94% of all workover operations during the period from 2011 to 2022 were carried out in wells with a sucker rod pump production system (**Fig. 7**). In addition, 273 workover operations were conducted on rod-type pumps, while information about the type of installed pump was missing for only two operations.

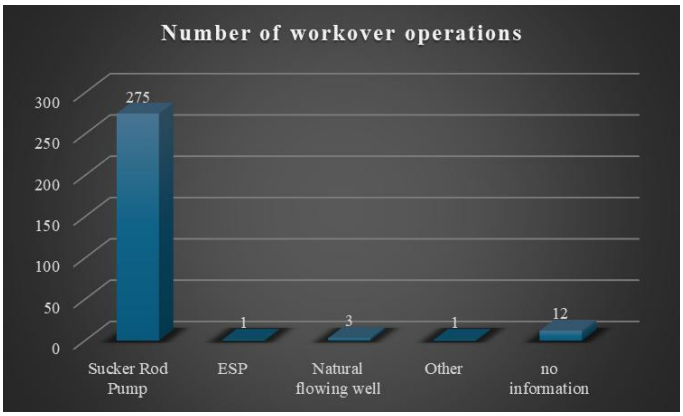


Fig. 7 *Number of workover operation during the period from 2011 to 2022 by production system*

It is particularly interesting to examine the reasons for stopping production and conducting workover operations. Most workover operations (43%) are caused by tubing failure, followed by sucker rod pump failure at 20% and rod string failure at 11% (**Fig. 8**). In 95% of tubing string failures, leakage was the cause, while 87% of rod string failures were due to breakage. Unfortunately, a large number of workover operations lack accurate information about the cause of production stoppage and the need for workover operations. This lack of accurate information makes analysis of the problem more difficult, and in some cases, impossible.

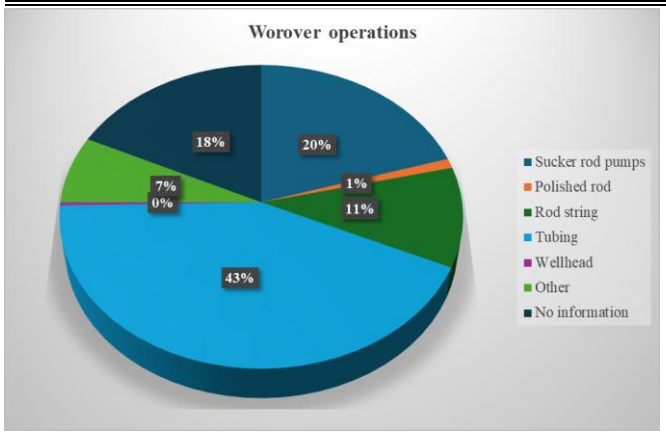


Fig. 8 *Workover operations during the period from 2011 to 2022 in relation to the part of the production system in failure*

In addition to identifying the problematic part of the installed production system, determining the failure type is equally important for a thorough analysis. According to the available information, of the 123 workover operations conducted between 2011 and 2022, 42% were related to leakage, 11% (32 operations) to breakage, and 66 operations to other types of failure. For a large number of workover operations (71), accurate information about the failure type is missing. The cause of problems related to the sucker rod pump is particularly unclear. Based on the available data, in 47 (80%) of the workover operations attributed to the sucker rod pump, the specific cause of the problem remains unknown. The exact cause of the pump-related problem is stated for only 20% of these workover operations (for example, paraffin or formation sand) (**Fig. 9).**

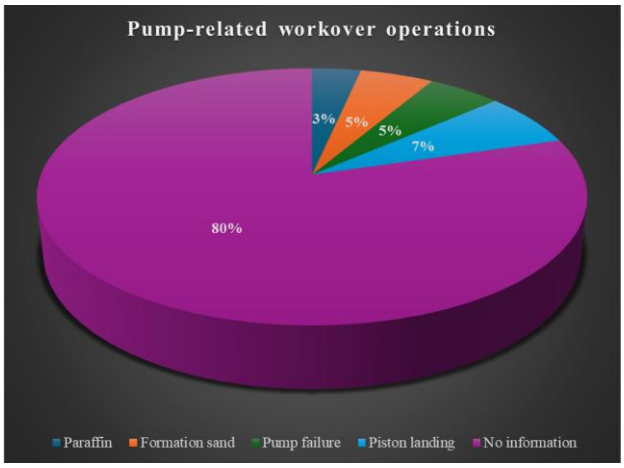


Fig. 9 *Workover operations during the period from 2011 to 2022 related to problems with sucker rod pumps*

Also, the cost of the workover operation varies considerably between operations, ranging from €3,500 per operation to more than €450,000 per workover operation and well. Half of the workover operations cost between €11,000 and €20,000 (**Fig. 10**). The data in Fig. 10 show that 15 workover operations cost between €40,000 and €450,000, while for 57 workover operations, information about the cost is missing [11].

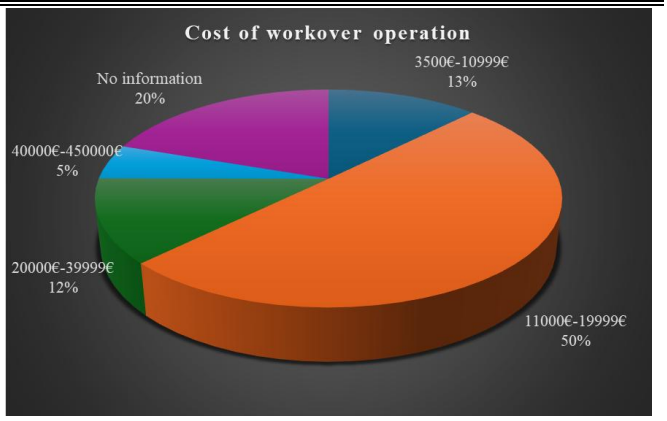


Fig. 10 *Cost of workover operations during the period from 2011 to 2022*

5. Conclusions

Despite being a well-established technology with over 150 years of global use, the sucker rod pumping system experiences problems related to its mode of operation. As expected, most issues with installed sucker rod pumping systems in the oil-gas field studied were associated with the subsurface equipment, primarily the tubing, but also the rod string and the pump itself. The analysis presented in the paper highlighted issues with the consistent collection of all relevant data and the absence of important information. Unfortunately, without all relevant information, identifying problematic wells and implementing preventive actions is significantly more difficult.

6. References

1. D. Perin, *Well Completion and Servicing* (1999), Editions Technip, Paris, France.
2. R. Zhao, J. Li, Z. Tao, M. Liu, J. Shi, C. Xiong, H. Huang, C. Sun, Y. Zhang, X. Zhang, *Research and Application of Rod/Tubing Wearing Prediction and Anti-Wear Method in Sucker Rod Pumping Wells* (2019), SPE conference paper 194955-MS, Manama, Bahrain.
3. D. Matanović, B. Moslavac, *Opremanje i održavanje bušotina* (2011) University of Zagreb, Zagreb, Croatia.
4. https://www.sciencedirect.com/topics/engineering/rod-pumping-system
5. I. Medved, P. Mijić, K. Peric, *Analysis of Workover Causes for Wells With Installed Downhole Sucker-Rod Pumps* (2019.), Intern. Scientific Journal "Machines, Technologies, Materials", Year XIII, Issue 2, p.p. 66-69.
6. R. D. Lacy, *The Rotating Tubing Hanger System: A Unique New System Designed to Extend the Run Time of Rod Pumped Wells* (1992.). SPE conference paper 23977-MS, Midland, Texas, USA
7. P. E. Hart, *Manual Tubing Rotation Reduces Rod Pumping Failures by 76%* (2003), SPE conference paper 80886-MS, Oklahoma City, Oklahoma, USA
8. *https://production-technology.org/tubing-rotator/*
9. K. P. Mccaslin, *A Study of the Methods for Preventing Rodwear Tubing Leaks in Sucker Rod Pumping Wells* (1987), SPE conference paper 16198-MS, Oklahoma City, Oklahoma, USA.
10. *https://www.semanticscholar.org/paper/Pitting-and-crevice-corrosion-of-offshore-stainless-Schiroky-Dam/7b183dc00ddd193eff458ffb4d6cd2ac7e7a72bb*
11. A. Knežević, *Analysis of Repair Works in a Ten-Year Period on the Example of an Oil And Gas Field in The Republic Of Croatia* (2023), Masters thesis, University of Zagreb Faculty of Mining, Geology and Petroleum Engineering, Zagreb, Croatia.

Forecast-oriented optimization of production plans: closed-loop decision-making and model risk management

Belozyorov M., Kalashnikov E.
Department of Information and Communication Technologies – The Federal State Autonomous Educational Institution of Higher Education "National Research Technological University "MISIS", Moscow, Russia
E-mail: mnbelozyorov@gmail.com, e.a.kalashnikov@mail.ru

Abstract: *This paper presents a forecast-oriented optimization framework for production and technological planning in modern metallurgical manufacturing systems. Forecasts of demand, raw material availability, and external constraints are widely used in the development of production plans; however, in traditional optimization models, forecast information is typically treated as a fixed input parameter, which leads to model risk and reduced robustness of decision-making. Within the proposed framework, forecasts are interpreted as dynamic and potentially inaccurate elements of the control system, and planning is performed in a closed-loop feedback structure integrating forecasting, model risk management, and optimization. The paper describes the architecture of an integrated forecast-oriented planning system and reports the results of computational experiments on the problem of forming a technological production plan for secondary aluminum alloys. The results demonstrate the impact of forecast accuracy on product cost and the computational complexity of the optimization process.*

KEYWORDS: *FORECAST, OPTIMIZATION, PRODUCTION PLANNING, MODEL RISK, INTEGRATED CONTROL SYSTEMS, METALLURGY*

1. Introduction

Under conditions of industrial digitalization, forecasts of demand, raw material availability, as well as logistical and market constraints are becoming a key element of production planning processes. In practice, such forecasts are typically incorporated into optimization models as fixed input parameters, which corresponds to a cascade control scheme of the form "forecast → optimization → execution." This approach remains widespread in industrial planning systems despite the increasing uncertainty and dynamism of the external environment [7, p.1030].

However, numerous studies demonstrate that the direct inclusion of forecast values into the constraints and objective functions of optimization problems leads to systemic suboptimality of solutions in the presence of forecasting errors [1, p.454]. Even relatively small deviations in forecast parameters may result in a significant reduction in economic efficiency and robustness of production plans, which is particularly critical for metallurgical industries characterized by rigid technological and resource constraints. From the perspective of optimization theory, this effect manifests itself as the "price of robustness" and highlights the necessity of explicitly accounting for uncertainty when formulating managerial decisions [2, p.36].

In this context, there arises a need to transition from cascade control schemes to integrated systems in which forecast uncertainty is addressed in a systematic manner, and the process of plan generation and adjustment is carried out within a closed-loop feedback framework.

2. Preconditions and means for resolving the problem

2.1. Limitations of Traditional Approaches to the Use of Forecasts in Optimization

Existing classes of production management systems (ERP, MES, APS) incorporate individual elements of forecasting, optimization, and execution control; however, in most cases, these elements do not form a unified closed-loop decision-making framework. The characteristic properties of cascade control systems and their limitations are systematized in Tables 1 and 2.

Table 1*. Key Characteristics of Cascade Interaction*

Characteristics	*Description*
1.Sequential Operation	*Each subsystem waits for the completion of the preceding one before initiating its own operation.*
2.Absence of Feedback	*Subsystems do not exchange data in real time. If an error or a change occurs at a certain stage, it is not transmitted backward for corrective adjustment.*
3.Isolation	*Subsystems do not take into account the state of other subsystems, which may lead to conflicts or suboptimal decisions.*
4.Rigidity	*The system exhibits poor adaptability to changes, such as variations in demand or equipment failures.*

Table 2. Key Drawbacks of the Cascade Approach

Characteristics	*Description*
1.Delays in Data Transmission	*Each subsystem processes data and then transfers it to the next one, which increases the overall decision-making time. Under conditions of rapidly changing demand or production environments, such delays may result in data obsolescence and suboptimal decisions.*
2.Information Loss	*During data transmission between subsystems, simplification or loss of critical information may occur. For example, demand forecasts may be aggregated and fail to account for specific requirements that are essential for technological preparation.*
3.Lack of Feedback	*The approach largely does not provide feedback mechanisms between subsystems. For instance, if the material and technical supply system encounters problems (e.g., raw material shortages), it cannot promptly adjust tasks for the technological preparation system or rapidly revise demand forecasts.*
4.Low Flexibility	*Cascade interaction exhibits poor adaptability to changes. If a failure or a change in conditions occurs at any stage (e.g., changes in demand volume or equipment breakdowns), the entire chain may require revision, which is time- and resource-consuming.*
5.Difficulty in Coordinating Multi-Criteria Objectives	*Each subsystem may pursue its own objectives and optimization criteria. For example, the demand forecasting system aims to maximize accuracy, whereas the material and technical supply system focuses on cost minimization. The cascade approach does not always allow these conflicts to be properly addressed, which may lead to suboptimal solutions.*
6.Suboptimality of Decisions	*Each subsystem optimizes its own task without considering global system-wide objectives.*

7.Error Accumulation	*Errors or inaccuracies at one stage (e.g., in demand forecasting) may be amplified as data are passed to subsequent subsystems. This can result in significant deviations in the planning and execution of production processes.*
8.Limited Scalability	*The approach scales poorly as system complexity increases. The addition of new subsystems or modification of existing ones requires substantial integration and configuration efforts.*

ERP systems are primarily oriented toward rule-based and balance planning, MES systems focus on execution monitoring and dispatching, while APS systems are designed to optimize plans given predefined input data. At the same time, forecasts of demand and resources are typically generated in subsystems external to the optimization model and transferred to it without accounting for their reliability or potential deviations.

Even in advanced planning and scheduling (APS) systems, demand and resource forecasts are usually produced by subsystems external to the optimization model and are treated as exogenous parameters. Scenario-based and robust approaches used to account for uncertainty can improve the robustness of decisions; however, they rely on static specification of scenarios or parameter intervals and do not account for the dynamic evolution of forecast quality [3, p.50].

Recent surveys of decision-making methods under uncertainty emphasize that the lack of linkage between forecast quality and optimization models represents one of the key limitations of traditional approaches [6, p.3]. As a result, the model risk associated with forecasting models manifests itself already at the plan execution stage and necessitates frequent manual adjustments.

2.2. Forecasts as a Source of Model Risk in Planning Problems

Let us consider the production planning optimization problem in a generalized form (1):

$$(1) \qquad \min_{x \in X(\hat{d}_t)} f(x, \hat{d}_t)$$

where x – denotes the vector of decision variables (production volumes, technology selection, routing), and $\hat{d}$ – represents the forecast parameters.

Forecast error (2):

$$(2) \qquad \varepsilon_t = d_t - \widehat{d_t}$$

This leads to a situation in which the optimal solution obtained on the basis of forecast data does not coincide with the optimal solution corresponding to the actual parameter values (3) [7, p.1034].

$$(3) \qquad x^*(\hat{d}_t) \neq x^*(d_t)$$

It is fundamentally important that forecast parameters enter not only the objective function but also the system of constraints, thereby shaping the feasible set $X(\hat{d})$.

Consequently, a forecasting error leads to a deformation of the feasible decision space rather than merely to a shift of the optimum. This effect is interpreted as model risk within the production planning loop [4, p.151].

Modern data-driven approaches emphasize the distinction between parametric uncertainty and the structural impact of data on the optimization model, which is particularly important when forecasts are obtained using machine learning methods [5, p.240].

The main sources of model risk in forecasting models (data, methods, assumptions, implementation errors, and the human factor) are systematized in table 3.

Table 3. Key Sources of Model Risk

Sources of Model Risk	*Description*
1.Data	*Data constitute the foundation for model development and operation. However, their quality, completeness, and representativeness may serve as significant sources of model risk.*
2.Errors in Data Transformation	*At the data preparation stage, various transformations are typically applied. Common transformations include data cleaning, normalization, aggregation, removal of duplicates and inconsistencies, and imputation of missing values. Errors introduced at this stage may distort model outputs and compromise their validity.*
3.Algorithms	*The selection and calibration of algorithms may also represent sources of model risk. An inappropriate choice of method or incorrect parameter settings can lead to inaccurate results. For instance, the use of linear regression to model nonlinear relationships (e.g., forecasting real estate prices under conditions of sharp market volatility) may result in substantial forecasting errors.*
4.Implementation	*Errors in the software implementation of a model, including coding errors or improper integration with other systems, may give rise to model risk.*
5.Model Assumptions and Limitations	*Models are constructed based on certain assumptions that may not hold in practice. For example, a market risk assessment model assuming normally distributed returns may underestimate the probability of extreme events (e.g., financial crises), leading to inadequate risk evaluation.*
6.Human Factor	*Errors at the stages of model development, deployment, or interpretation of results also constitute sources of risk. An analyst may misinterpret model outputs, resulting in incorrect strategic decisions, such as launching a new product into the market.*
7.Regulatory and Ethical Aspects	*Models may fail to comply with regulatory requirements or ethical standards, which also generates risks. For example, the use of a model that discriminates against certain groups of individuals (e.g., based on age, gender, or racial background) may lead to legal and reputational consequences for a company.*

For metallurgical production systems, where forecasts are increasingly generated using machine learning methods, the management of this risk becomes a critically important task.

2.3. Forecast-Oriented Optimization and Closed-Loop Control

This paper proposes the principle of forecast-oriented optimization, in which the forecast is treated as a dynamic and potentially inaccurate element of the control system. The formation of production plans is carried out within a closed-loop feedback framework integrating forecasting, model risk management, and optimization.

Figure 1 illustrates that, in existing ERP, MES, and APS systems, forecasting models are not integrated into the optimization and feedback loop, in contrast to the proposed forecast-oriented approach.

Fig.1 *A Methodological Classification of Production Control Systems Based on the Use of Forecasts, Optimization, and Feedback*

Class of Control Systems	Use of Forecasting Models	Optimization Logic in Plan Formation	Feedback at the Execution Level	Feedback at the Forecasting Model Level	Feedback at the Optimization Model Level
ERP	✗ Absent	✗ Absent	⚠ Limited	✗ Absent	✗ Absent
MES	✗ Absent	✗ Absent	✓ Implemented	✗ Absent	✗ Absent
APS	⚠ Limited	⚠ Limited	⚠ Limited	✗ Absent	✗ Absent
Data-driven MES	⚠ Limited	✗ Absent	✓ Implemented	⚠ Limited	✗ Absent
Proposed Approach	✓ Systemic	✓ Systemic	✓ Implemented	✓ Implemented	✓ Implemented

The architecture of interaction between forecasting models, optimization procedures, and intelligent agents is presented in Figure 3, while an extended scheme involving the decision-maker is shown in Figure 2.

Fig.2 *High-level structural diagram of the modeling algorithm*

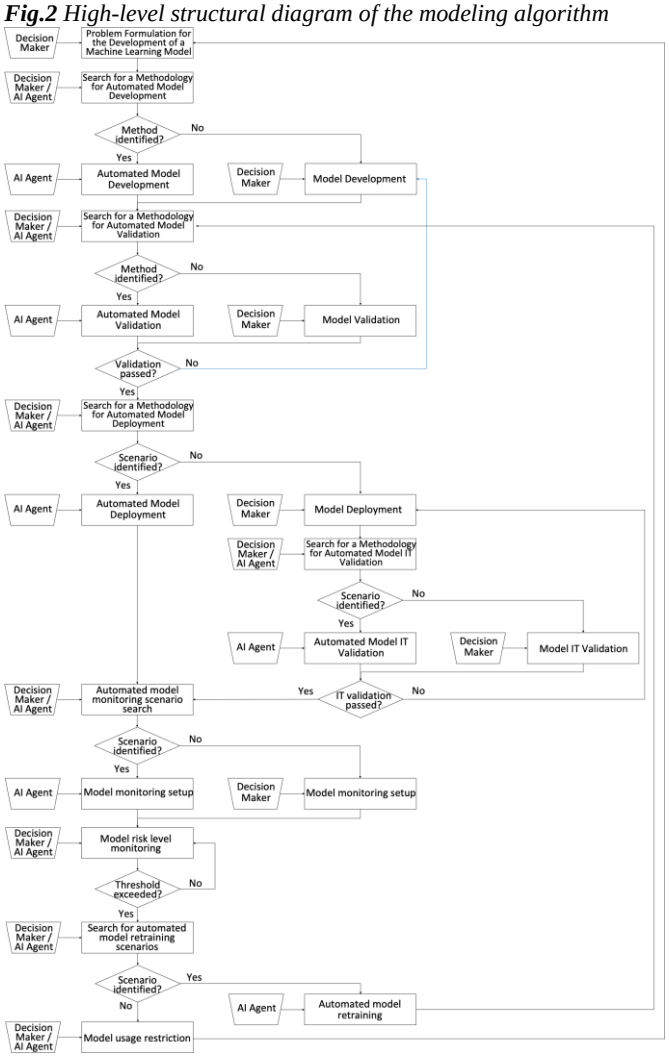
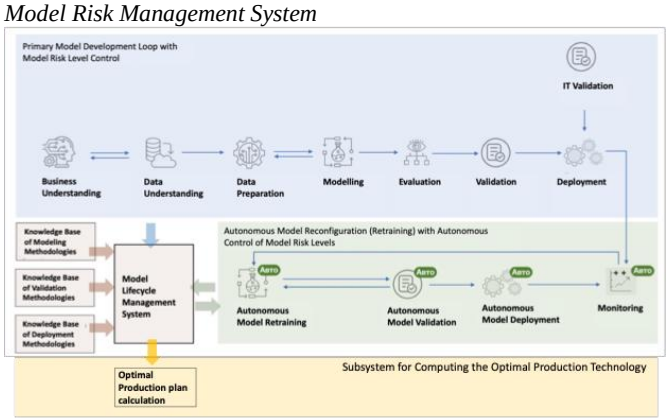


Fig.3 *Interaction Scheme of the Components of an Automated Model Risk Management System*



Formally, the closed-loop structure can be represented as shown in (4):

$$\hat{d}_{t+1} = \mathcal{F}(\mathrm{X}_{t+1}, \theta_t, x_t) \quad (4)$$

where the parameters of the forecasting model and the forecasts themselves are adapted based on the results of optimization and actual execution. Such a logic is consistent with modern concepts of closed-loop optimization in intelligent manufacturing [8, p.2] and is closely related to industrial implementations of model predictive control (MPC) [9, p.1705].

2.4. Architecture of an Integrated Forecast-Oriented Planning System

The practical implementation of forecast-oriented optimization requires the integration of three functional components: a forecasting subsystem, a model risk management subsystem, and an optimization subsystem. The composition and functions of these modules are presented in table 4.

Table 4*. Description of Functional Modules*

Functional Component	*Description*
1.Forecasting Subsystem	*This subsystem performs the analysis of historical data, current trends, and external factors (demand, raw material availability, and logistics) in order to construct scenarios for the development of the production process. By employing machine learning methods and statistical modeling techniques, it generates forecasts that serve as a basis for managerial decision-making. For example, demand forecasting enables the adjustment of material procurement volumes, avoiding both shortages and excessive inventories.*
2.Model Risk Management Subsystem	*This subsystem is aimed at the identification, assessment, and mitigation of risks associated with the adoption of new modeling technologies, changes in standards, or fluctuations in market conditions.*
3.Subsystem for Computing the Optimal Production Technology	*This subsystem enables the application of multi-criteria optimization algorithms, including the use of duality theory, to select rational variants of the technological process that maximize efficiency under given constraints. It integrates forecasting data and risk assessments to generate decisions that balance economic benefits and associated risks.*

The forecasting subsystem generates estimates of future states of the production system and development scenarios; the model risk management subsystem assesses the reliability of forecasts and identifies critical deviations; and the optimization subsystem uses this information to construct production and technological plans while accounting for an acceptable level of risk. Such an architecture enables a transition from the isolated use of individual models to their joint calibration and operation within a unified control loop.

2.5. Empirical Results

The viability of the proposed approach was confirmed by computational experiments on the problem of formulating a production plan for secondary aluminum alloys. The initial data for the groups of charge components are presented in Fig. 4, the admissible charge compositions in terms of chemical composition are shown in Fig. 5, and the constraints on raw material availability and production plan are given in Fig. 6.

Fig.4 *Available raw material groups*

Charge materials	Designation	Price Cj	Principal components, mass fraction, %				Impurities, mass fraction, %	
			Cu	Si	Mg	Mn	Fe	Total Impurities
Aluminium turnings (BIII)	a1	1800	4,5	0,8	1,8	1,9	1,0	2,7
A IX	a2	1400	2,6	0,7	0,3	0,5	0,5	2,8
Grade A III can scrap	a3	1700	0,1	0,5	0,1	0,1	0,8	2,6
A III	a4	1850	4,5	0,8	1,8	1,9	1,0	2,7
A VI	a5	1950	3,0	8,0	1,4	0,3	1,0	2,9
Grade AVIII (Al-Mg) scrap	a6	1900	0,1	0,8	1,5	0,1	0,5	2,2
Grade AI (AZh) charge material	a7	1900	0,05	0,5	1,3	1,2	0,9	2,3
A X	a8	1200	2,6	0,7	1,00	0,5	0,9	2,8

Fig.5 *Available burdening options*

Burden	a1	a2	a3	a4	a5	a6	a7	a8	Price
Recipe 0	0,00	0,18	0,23	0,00	0,46	0,00	0,00	0,13	1680,00
Recipe 1	0,00	0,26	0,18	0,00	0,46	0,02	0,00	0,09	1696,80
Recipe 2	0,00	0,30	0,15	0,00	0,46	0,03	0,00	0,07	1713,77
Recipe 3	0,00	0,35	0,12	0,00	0,45	0,04	0,00	0,04	1730,91
Recipe 4	0,00	0,18	0,23	0,00	0,46	0,00	0,00	0,13	1748,21
Recipe 5	0,00	0,16	0,25	0,00	0,46	0,00	0,00	0,13	1765,70
Recipe 6	0,00	0,22	0,23	0,00	0,46	0,00	0,00	0,09	1783,35
Recipe 7	0,00	0,13	0,27	0,00	0,46	0,00	0,00	0,14	1801,19
Recipe 8	0,00	0,24	0,23	0,00	0,46	0,00	0,00	0,07	1819,20
Recipe 9	0,00	0,25	0,23	0,00	0,46	0,00	0,00	0,06	1837,39
Recipe 10	0,00	0,27	0,23	0,00	0,46	0,00	0,00	0,05	1855,77
Recipe 11	0,00	0,28	0,23	0,00	0,46	0,00	0,00	0,03	1874,32
Recipe 12	0,00	0,30	0,23	0,00	0,46	0,00	0,00	0,02	1893,07
Recipe 13	0,00	0,07	0,32	0,00	0,46	0,00	0,00	0,15	1912,00
Recipe 14	0,00	0,18	0,24	0,00	0,49	0,00	0,00	0,09	1931,12
Recipe 15	0,00	0,04	0,34	0,00	0,46	0,00	0,00	0,16	1950,43
Recipe 16	0,00	0,03	0,35	0,00	0,46	0,00	0,00	0,16	1969,93
Recipe 17	0,00	0,18	0,25	0,00	0,50	0,00	0,00	0,07	1989,63
Recipe 18	0,00	0,18	0,26	0,00	0,51	0,00	0,00	0,05	2009,53
Recipe 19	0,00	0,18	0,26	0,00	0,53	0,00	0,00	0,03	2029,62
Recipe 20	0,00	0,18	0,27	0,00	0,54	0,00	0,00	0,01	2049,92
Recipe 21	0,03	0,00	0,50	0,00	0,47	0,00	0,00	0,00	2070,42
Recipe 22	0,03	0,00	0,50	0,00	0,47	0,00	0,00	0,00	2091,12
Recipe 23	0,06	0,00	0,48	0,00	0,46	0,00	0,00	0,00	2112,03
Recipe 24	0,08	0,00	0,46	0,00	0,46	0,00	0,00	0,00	2133,15

Fig.6 *Raw Material Inventory and Production Plan*

	a1	a2	a3	a4	a5	a6	a7	a8
Stock Availability (tons)	2	10	20	2	30	4	6	2
Required Product Volume (tons)	20							

An example of the optimal solution is shown in Fig. 7

Fig.7 *Optimal solution*

	recept_0	recept_1	recept_3	Price
Optimal solution	10	6	4	33 904

To analyze the impact of forecast uncertainty, the planned production volume was varied over a range corresponding to a demand prediction error of 0 to 120% in terms of the MAPE metric Fig. 8. This resulted in the dependencies of technology selection on the production plan Fig. 9, the impact of forecast accuracy on product cost Fig. 10, and the relationship between the computation time for finding the optimal solution and the magnitude of the forecast error Fig. 11.

Fig.8 *Modeled experiment scenarios*

Error of model, MAPE	0%	10%	20%	30%	40%	50%	60%	70%	80%	90%	100%	110%	120%
Production plan (scenario)	20	22	24	26	28	30	32	34	36	38	40	42	44
Real production volume	20												

Fig.9 Production technologies as a function of the production plan

Error of model, MAPE		0%	10%	20%	30%	40%	50%	60%	70%	80%	90%	100%	110%
Production plan (scenarios)		20	22	24	26	28	30	32	34	36	38	40	42
Production cost		33 904	37 399	40 929	44 460	47 901	51 364	54 895	59 764	64 989	69 794	75 394	79 505
Production cost per ton		1 695	1 700	1 705	1 710	1 711	1 712	1 715	1 758	1 805	1 837	1 885	1 893
Burden:	Price	Production plan for scenarios											
recept_0	1680	10	7	8	9	1	0	1	0	1	2	0	0
recept_1	1697	6	6	3	0	6	16	13	5	1	1	0	0
recept_2	1714	0	7	6	5	18	1	0	14	0	0	0	0
recept_3	1731	4	2	7	12	3	13	18	5	9	1	0	0
recept_4	1748	0	0	0	0	0	0	0	0	2	0	8	1
recept_5	1766	0	0	0	0	0	0	0	0	0	1	0	0
recept_6	1783	0	0	0	0	0	0	0	0	2	0	1	1
recept_7	1801	0	0	0	0	0	0	0	0	0	0	0	0
recept_8	1819	0	0	0	0	0	0	0	0	0	0	0	0
recept_9	1837	0	0	0	0	0	0	0	0	0	0	0	0
recept_10	1856	0	0	0	0	0	0	0	9	21	33	4	24
recept_11	1874	0	0	0	0	0	0	0	0	0	0	0	1
recept_12	1893	0	0	0	0	0	0	0	0	0	0	1	0
recept_13	1912	0	0	0	0	0	0	0	0	0	0	3	0
recept_14	1931	0	0	0	0	0	0	0	1	0	0	21	10
recept_15	1950	0	0	0	0	0	0	0	0	0	0	0	0
recept_16	1970	0	0	0	0	0	0	0	0	0	0	0	0
recept_17	1990	0	0	0	0	0	0	0	0	0	0	0	0
recept_18	2010	0	0	0	0	0	0	0	0	0	0	2	0
recept_19	2030	0	0	0	0	0	0	0	0	0	0	0	0
recept_20	2050	0	0	0	0	0	0	0	0	0	0	0	5
recept_21	2070	0	0	0	0	0	0	0	0	0	0	0	0
recept_22	2091	0	0	0	0	0	0	0	0	0	0	0	0
recept_23	2112	0	0	0	0	0	0	0	0	0	0	0	0
recept_24	2133	0	0	0	0	0	0	0	0	0	0	0	0

Fig.10 *Influence of prediction accuracy on production costs*

Error of model, MAPE	0%	10%	20%	30%	40%	50%	60%	70%	80%	90%	100%	110%
Production plan (scenario)	20	22	24	26	28	30	32	34	36	38	40	42
Production cost	33 904	37 399	40 929	44 460	47 901	51 364	54 895	59 764	64 989	69 794	75 394	79 505
Production cost per ton	1 695	1 700	1 705	1 710	1 711	1 712	1 715	1 758	1 805	1 837	1 885	1 893
⇧delta cost per ton	0,0%	0,3%	0,6%	0,9%	0,9%	1,0%	1,2%	3,7%	6,5%	8,3%	11,2%	11,7%

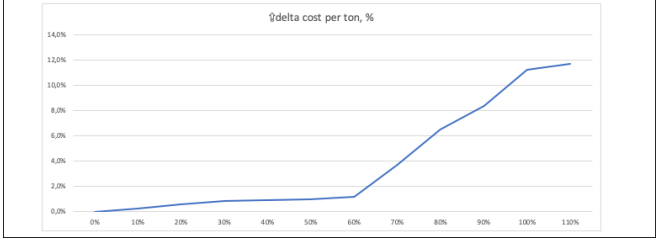


Fig.11 *Dependence of the optimal solution search time on the magnitude of the model error*

Error of model, MAPE	0%	10%	20%	30%	40%	50%	60%	70%	80%	90%	100%	110%	120%
Calculation time per variant, s	< 1	< 1	< 1	< 1	< 1	< 1	< 1	< 1	< 1	< 1	1 645	200 000	> 200 000. Processing incomplete

The experimental results show that an increase in the forecasting error leads both to a higher production cost per ton and to a substantial rise in computational costs. A similar growth in computational complexity in stochastic planning is also observed in other metallurgical applications [10, p.8].

3. Conclusion

The article demonstrates that using forecast data as fixed input parameters for optimization models is methodologically insufficient and leads to increased model risk and reduced robustness of production plans. The principle of forecast-informed optimization is substantiated, based on a closed feedback loop integrating forecasting, model risk management, and optimization. Computational testing on a metallurgical production problem shows that forecast accuracy significantly impacts both economic performance indicators and the computational complexity of optimal solution search. The proposed approach can be utilized in the development and modernization of metallurgical production planning systems to enhance their adaptability and resilience.

4. References

1. *Ben-Tal A., Nemirovski A. Robust optimization – methodology and applications // Mathematical Programming. 2002. Vol. 92, no. 3. P. 453–480. DOI:10.1007/s101070100286.*
2. *Bertsimas D., Sim M. The price of robustness // Operations Research. 2004. Vol. 52, no. 1. P. 35–53. DOI:10.1287/opre.1030.0065.*
3. *Bertsimas D., Sim M. Robust discrete optimization and network flows // Mathematical Programming. 2003. Vol. 98, no. 1–3. P. 49–71. DOI:10.1007/s10107-003-0396-4.*
4. *Bertsimas D., Thiele A. A robust optimization approach to inventory theory // Operations Research. 2006. Vol. 54, no. 1. P. 150–168. DOI:10.1287/opre.1050.0238.*
5. *Bertsimas D., Gupta V., Kallus N. Data-driven robust optimization // Mathematical Programming. 2018. Vol. 167, no. 2. P. 235–292. DOI:10.1007/s10107-017-1125-8.*
6. *Sadana U., Bampis C., Gupta V. A survey of contextual optimization methods for decision-making under uncertainty // European Journal of Operational Research. 2024. Article 110369. DOI:10.1016/j.ejor.2024.03.020.*
7. *Elmachtoub A. N., Grigas P. Smart "Predict, then Optimize" // Management Science. 2021. Vol. 67, no. 2. P. 1029–1052. DOI:10.1287/mnsc.2020.3922.*
8. *Zhang W., Huang X., Xu C. Closed-loop process optimization in smart manufacturing: A systematic review and future trends // Computers in Industry. 2024. Vol. 150. Article 104131. DOI:10.1016/j.compind.2024.104131.*
9. *Schwenzer M., Kirsch A., Hölzle W. Review on model predictive control: an engineering perspective // The International Journal of Advanced Manufacturing Technology. 2021. Vol. 114, no. 5–6. P. 1701–1724. DOI:10.1007/s00170-021-07682-3.*
10. *Wu J., Tang Z., Liao T. Approximated dynamic programming for production and inventory planning problem in cold rolling process of steel production // Mathematics. 2024. Vol. 12, no. 24. Article 3922. DOI:10.3390/math12243922.*

Rolling element bearing fault detection using accelerometer and laser displacement measurements

Mihaela Vještica[1], Braut Sanjin[1], Goranka Štimac Rončević[1,*]
University of Rijeka Faculty of Engineering, Vukovarska 58, 51000 Rijeka, Croatia[1]
[*]goranka.stimac@uniri.hr

Abstract: *Rolling element bearing fault detection is of significant importance due to the widespread use of bearings across numerous industrial applications. In this study, vibration measurements using an accelerometer and a laser displacement sensor are carried out on a laboratory bearing test rig under different operating conditions, including a healthy state and bearings with localized inner- and outer-ring faults. Measurements are conducted at a constant rotational speed of 1700 rpm and the acquired signals are analysed to extract characteristic features associated with potential bearing faults. The results demonstrate that the applied methodology enables indicative bearing fault detection using both measurement approaches.*

Keywords*: ROLLING ELEMENT BEARINGS, FAULT DETECTION, ACCELEROMETER, LASER DISPLACEMENT SENSOR*

1. Introduction

Rolling element bearings are critical components in rotating machinery, and their reliable operation is essential for the safety and efficiency of numerous industrial systems. Defects in the inner race, outer race, rolling elements, or cage are among the most common causes of mechanical failure and can lead to increased vibration levels, noise, and eventual catastrophic breakdowns if not detected at an early stage. Localized bearing defects generate impulsive vibration responses that excite structural resonances; however, these responses are often masked by background noise and other machine-related vibrations, making bearing fault diagnosis particularly challenging. Consequently, vibration-based condition monitoring has become a central topic in rolling element bearing diagnostics.

Envelope analysis is a well-established technique for detecting localized bearing faults, as it enables the demodulation of high-frequency resonance responses and reveals characteristic fault frequencies related to bearing geometry and rotational speed [1,2]. Randall and Antoni demonstrated that envelope analysis can effectively extract these fault-related features, provided that appropriate band-pass filtering is applied prior to demodulation [2]. To further enhance fault detection under noisy operating conditions, Antoni introduced spectral kurtosis as a frequency-dependent indicator capable of identifying impulsive, non-Gaussian signal components associated with bearing defects [3]. Based on this concept, the kurtogram was proposed as a systematic tool for selecting the optimal frequency band for envelope analysis in rotating machinery diagnostics [4]. This method was later refined into a fast, multi-resolution implementation, significantly improving its computational efficiency and practical applicability [5].

In recent years, the increasing implementation of data-driven and machine learning-based diagnostic techniques has intensified the need for high-quality, well-labeled experimental datasets. Antunovic et al. [6] evaluated machine learning performance using the CWRU bearing dataset, based on accelerometer measurements on the roller element bearing (REB) housing, directly connected to the REB outer ring. In simulation models, the primary degree of freedom is the radial displacement of the sleeve, directly connected to the inner ring. Since measurements focused on the inner ring are generally rare or unavailable, this study was motivated to perform vibration measurements using both an accelerometer and a laser displacement sensor on a laboratory test rig under different operating conditions, including a healthy state and bearings with localized inner- and outer-ring faults. The signals measured at a constant rotational speed of 1700 rpm were processed to extract fault-related features, enabling comparison of the two diagnostic approaches. Accelerometer data were processed using envelope spectrum analysis, while laser displacement signals were evaluated in the order domain to isolate defect-related components.

2. Experimental setup

The experimental setup is based on the DyLab Bearing Test Simulator (BTS-100) and is shown in Fig. 1. Sensor locations are indicated as follows: (1) accelerometer, (2) laser displacement sensor and (3) integrated single-pulse-per-revolution (1 PPR) analog tachometer reference sensor. A PCB 352C34 piezoelectric accelerometer is mounted vertically on the bearing housing to capture high-frequency vibration responses and has a nominal sensitivity of 100 mV/g. A Micro-Epsilon ILD2300-50LL laser displacement sensor is used to measure radial shaft displacements, providing a maximum sampling rate of 49.13 kHz with a reduced measuring range of 25 mm.

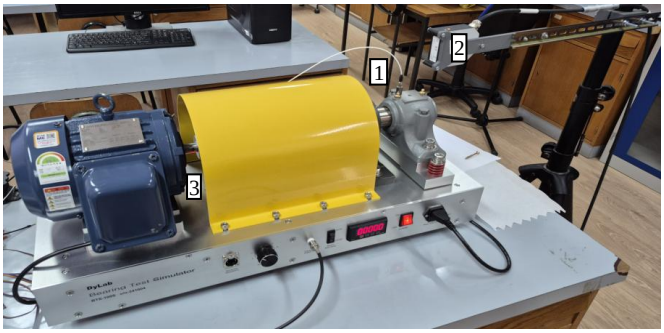


Fig. 1 *Laboratory bearing test rig with sensors (1 – accelerometer, 2 – laser displacement sensor, 3 – phase reference sensor)*

A relatively rigid shaft is supported by two healthy REBs, with the faulty deep grove REB mounted on an overhung section of the shaft. The drive unit consist of a 0.75 kW electric motor, capable of operating at rotational speeds up to 1800 rpm. Data acquisition is carried out using a DEWESoft SIRIUS Modular system, which offers eight simultaneously sampled analog input channels suitable for vibration and acoustic measurements.

3. Characteristic bearing fault frequencies

The characteristic defect frequencies of rolling element bearings are determined by the bearing geometry and the shaft rotational speed. The ball pass frequency outer race (BPFO) corresponds to defects on the outer ring and is calculated as:

$$BPFO = \frac{n}{2} f_r \left(1 - \frac{d}{D}\cos\theta\right), \tag{1}$$

while the ball pass frequency inner race (BPFI) corresponds to defects on the inner ring and is given by:

$$BPFI = \frac{n}{2} f_r \left(1 + \frac{d}{D}\cos\theta\right). \tag{2}$$

Here, n is the number of rolling elements, d is the rolling element diameter, D is the pitch diameter, θ is the contact angle, and f_r is the rotational frequency. These frequencies are critical for bearing fault

diagnosis, as they determine the locations of spectral peaks associated with inner and outer race defects.

4. Time-domain signals

The tested faulty REB (NTN 6307) consists of 8 balls, with harmonics BPFO = 3.06 × and BPFI = 4.94 ×. A sampling frequency of 50 kHz is employed for all measurement channels. Experimental results obtained at a constant rotational speed of 1700 rpm are presented.

Figs. 2–4 illustrate time-domain signals from accelerometer and laser sensors, comparing responses for a healthy bearing against bearings with localized faults on the outer and inner rings. These visualizations typically show lower-amplitude waveforms for healthy bearings, while those with damage exhibit periodic impulses or elevated vibration levels due to fault impacts. Healthy bearing produces steady, low-variance signals in the time domain from both sensors, reflecting uniform rolling without defects. Accelerometer data often appears as baseline noise, and laser measurements indicate minimal displacement variations.

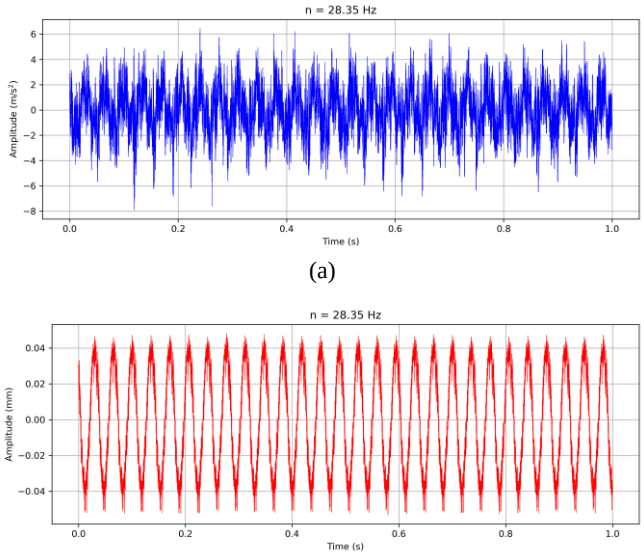


Fig. 2 *Time-domain signal of a healthy bearing: (a) accelerometer, (b) laser sensor*

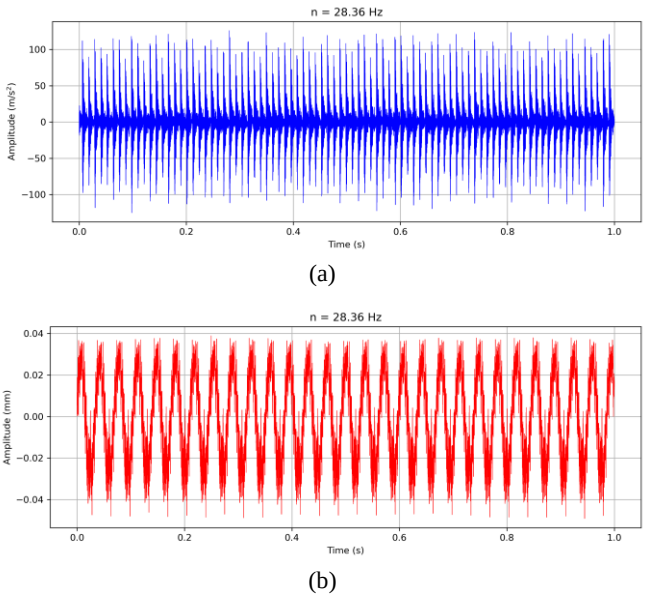


Fig. 3 *Time-domain signal of a bearing with localized fault on the outer ring: (a) accelerometer, (b) laser sensor*

Figures corresponding to outer ring faults display repetitive high-amplitude peaks in accelerometer signals, caused by rolling elements repeatedly striking the defect. Laser sensor data may show correlated displacement spikes, with periods matching ball-pass frequency. Inner ring defects produce less periodic but higher-frequency impulses in time-domain plots, as the defect rotates with the shaft. Accelerometers capture sharper transients compared to outer race faults, while laser sensors detect subtler positional shifts.

Figures 5–7 illustrate the time-domain signals obtained from the accelerometer and laser sensors over a shortened time interval of 0.1 s, allowing clearer visualization of the signal features and transient vibration responses.

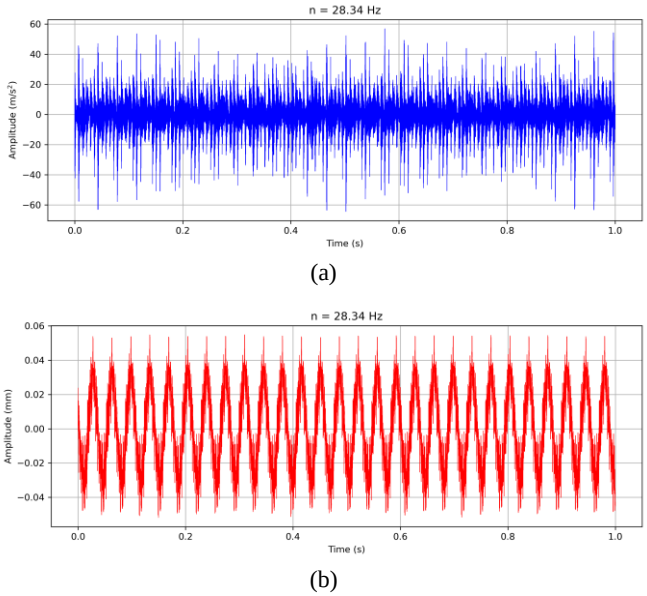


Fig. 4 *Time-domain signal of a bearing with localized fault on the inner ring: (a) accelerometer, (b) laser sensor*

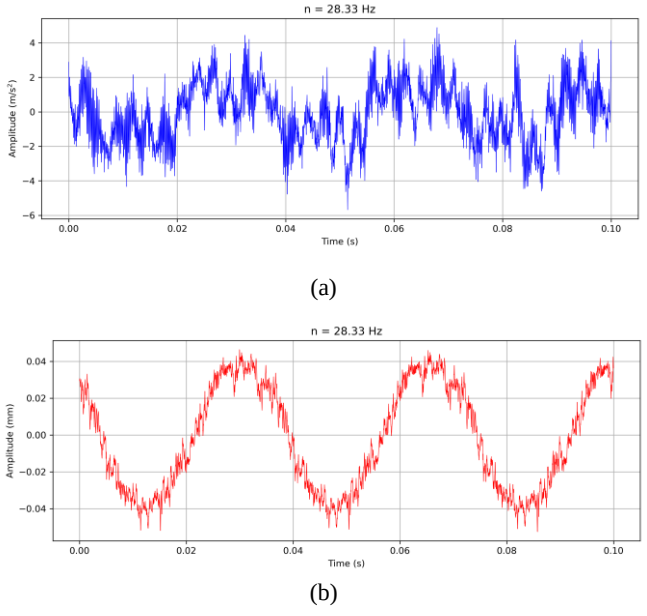
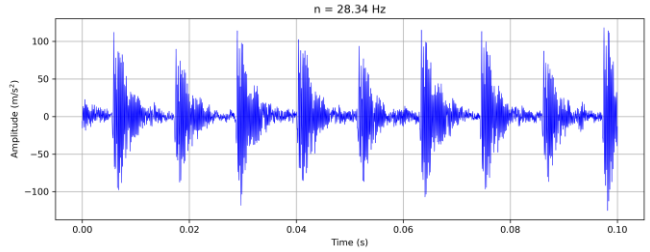
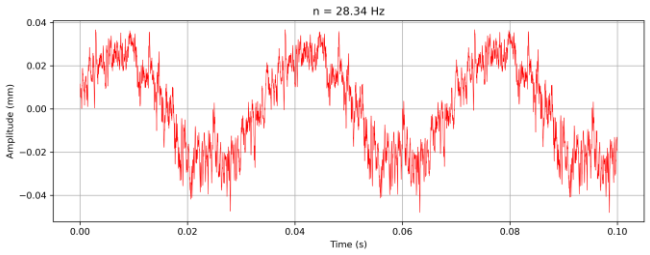


Fig. 5 *Time-domain signal* (0.1 s) *– healthy bearing: (a) accelerometer, (b) laser sensor*

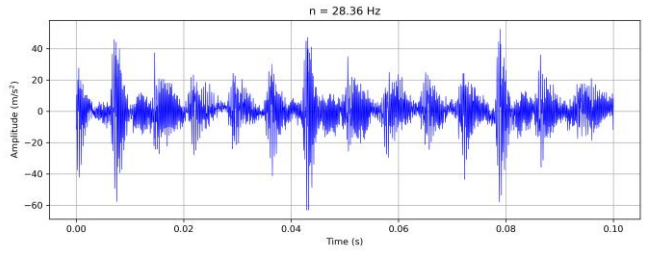


(a)

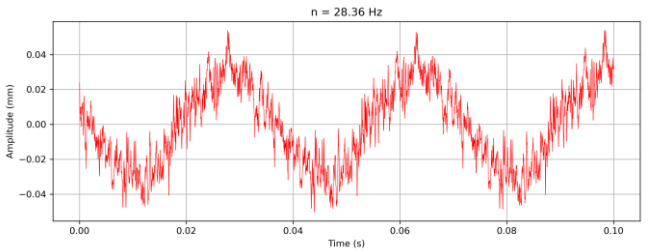


(b)

Fig. 6 *Time-domain signal* (0.1 s) *– bearing with localized fault on the outer ring: (a) accelerometer, (b) laser sensor*



(a)



(b)

Fig. 7 *Time-domain signal* (0.1 s) *– bearing with localized fault on the inner ring: (a) accelerometer, (b) laser sensor*

5. Acceleration signal processing

Figs. 8–10 display the envelope spectra obtained from the accelerometer for a healthy bearing and for bearings exhibiting localized defects on the outer and inner rings. The spectra highlight the harmonic frequencies of BPFO and BPFI associated with bearing faults.

The envelope spectra were obtained using a Hilbert transform–based demodulation procedure applied to the acceleration signal. First, the mean value was removed to eliminate signal offset and improve numerical stability. Next, the analytic signal was computed using the Hilbert transform. The envelope was obtained as the magnitude of the analytic signal. This step removes the high-frequency carrier component and retains the amplitude modulation caused by repetitive bearing impacts. No band-pass filtering is applied prior to demodulation. Finally, the Fast Fourier Transform (FFT) of the envelope signal was calculated, and only the positive frequency components were retained and properly normalized. The resulting envelope spectrum reveals characteristic defect frequencies (BPFI and BPFO) and their harmonics, which are not directly visible in the conventional vibration spectrum.

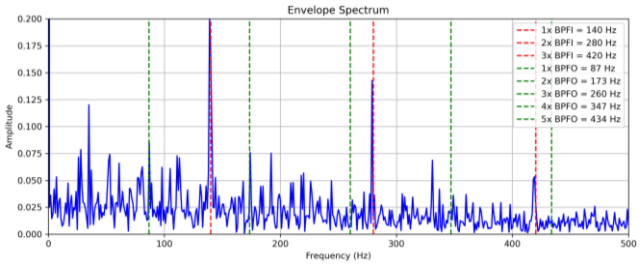


Fig. 8 *Envelope spectrum – healthy bearing*

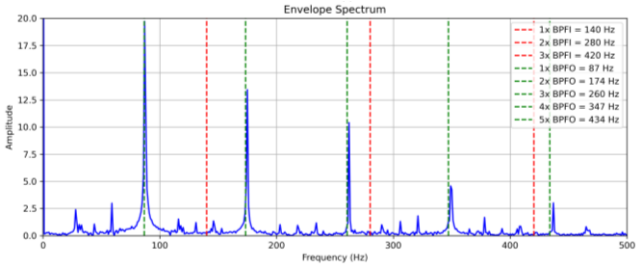


Fig. 9 *Envelope spectrum – bearing with localized fault on the outer ring*

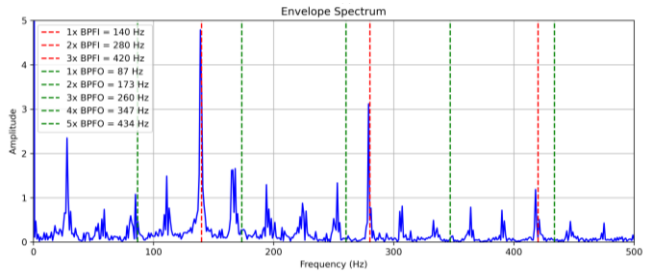


Fig. 10 *Envelope spectrum – bearing with localized fault on the inner ring*

6. Laser displacement signal processing

Since the laser sensor measures displacement rather than acceleration, the impact impulses generated by bearing faults are often insufficiently pronounced for effective envelope spectrum analysis. Therefore, the vibration signal acquired using the laser displacement sensor was processed in the order domain to enable detection of characteristic bearing defect frequencies. First, the laser displacement signal was transformed from the time domain to the angular domain and the mean value was removed to eliminate signal offset. The signal was subsequently resampled into the angular domain using tachometer-based angle synchronization, thereby ensuring constant angular resolution per revolution. To suppress low-order components associated with rotational effects, a high-pass Butterworth filter (HP) with a cutoff at the first two orders (Fig. 11) is applied. Figure 12 presents the tested and filtered signals for the bearing with an outer ring defect, while Figs. 13–15 show the corresponding order-tracked power spectral densities (PSDs) for the healthy bearing and for bearings with outer- and inner-ring defects.

In laser-based radial displacement measurements, the spectral signatures of BPFO and BPFI harmonics are generally less pronounced than in acceleration-based measurements. The outer ring fault (BPFO = 3.06 × shaft order), is dominantly characterized

by the 3× and 4× orders. On the other hand, the inner ring fault (BPFI = 4.94× shaft order) exhibits a clear dominance of the 5× order, which can be considered as a characteristic indication of an inner ring defect. Despite the reduced prominence of fault-related features in displacement-based measurements, the results demonstrate that laser measurements still exhibit characteristic spectral patterns associated with different types of bearing defects.

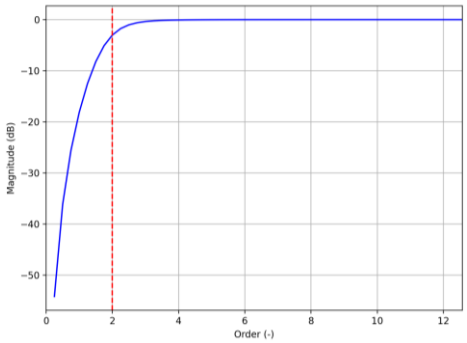


Fig. 11 *Magnitude response of the Butterworth high-pass filter in the order domain*

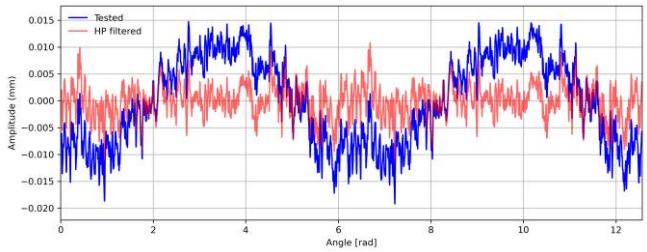


Fig. 12 *Comparison of tested and filtered signals – bearing with localized fault on the outer ring*

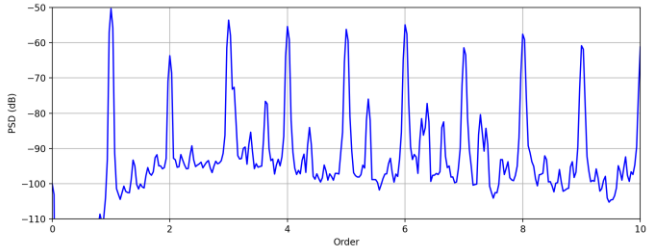


Fig. 13 *Order-tracked power spectral density – healthy bearing*

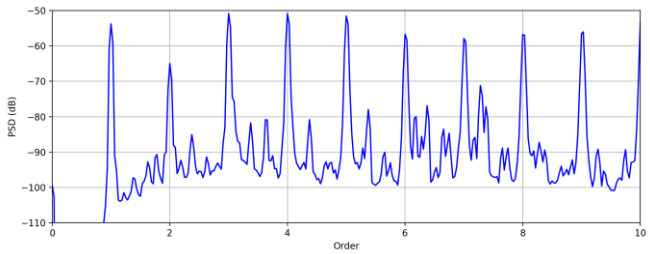


Fig. 14 *Order-tracked power spectral density – bearing with localized fault on the outer ring*

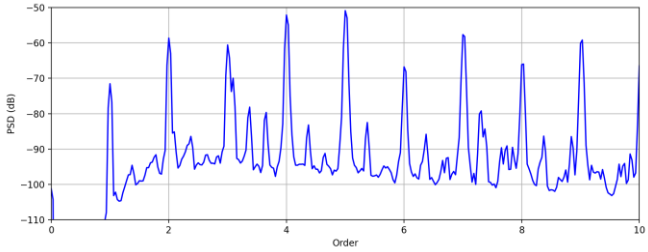


Fig. 15 *Order-tracked power spectral density – bearing with localized fault on the inner ring*

7. Conclusion

The study demonstrates that rolling element bearing faults can be reliably detected under laboratory conditions using vibration-based measurements. Accelerometer signals were analyzed in the time domain and further processed using envelope spectrum analysis, which enabled clear identification of characteristic inner-ring (BPFI) and outer-ring (BPFO) fault frequencies and their harmonics. Laser displacement measurements were evaluated in the order domain to extract defect-related components. A high-pass Butterworth filter was applied to suppress low-order contributions associated with shaft-related effects. Although fault-related orders were detectable, their amplitudes were less pronounced compared to the acceleration-based results, reflecting the lower sensitivity of displacement measurements to high-frequency impulsive events. Overall, the accelerometer combined with envelope analysis provided superior fault detectability and clearer diagnostic indications, whereas the laser displacement sensor represents a valuable non-contact alternative with complementary capabilities and specific practical considerations.

Acknowledgment: This work was supported by the European Union—NextGenerationEU under the project number uniri-iz-25-241.

8. References

1. R. B. Randall, *Vibration-based Condition Monitoring: Industrial, Aerospace and Automotive Applications* (2011)
2. R. B. Randall, J. Antoni, Mech. Syst. Signal Process, **25**, 485–520 (2011)
3. J. Antoni, Mech. Syst. Signal Process, **20**, 282–307 (2006)
4. J. Antoni, R. B. Randall, Mech. Syst. Signal Process **20**, 308–331 (2006)
5. J. Antoni, Mech. Syst. Signal Process **21**, 108–124 (2007)
6. M. Antunović, S. Braut, R. Žigulić, G. Štimac Rončević, M. Lovrić, *Proceedings of the 11th IFToMM International Conference on Rotordynamics*, 406–421 (2024)

Finite Element Modeling of a Flat Reinforced Expanded Polytetrafluoroethylene Gasket

Evlogi Mladenov, Ivo Draganov
University of Ruse „Angel Kanchev“, Studentska str. 8, Bulgaria
iivanov@uni-ruse.bg

Abstract: *The porosity of flat ePTFE gaskets imposes requirements on the compression force during installation. Improving the tightness when using such gaskets is achieved by reinforcing them in a certain area. The combination of the complicated shape and the highly nonlinear properties of the material used necessitates the creation of an appropriate numerical model, through which to determine the compression force necessary to ensure the required tightness. In this work, a simulation using the finite element method has been created and used, which is based on the Marlow material model and a viscoelastic model of shear stress relaxation. Results have been obtained for the hydrostatic stress, the minimum principal strains and the fluid leakage path. The threshold values of the minimum principal strain at different magnitudes of the compression force have been determined.*
Keywords: *ePTFE, FEM, Marlow model, viscoelasticity, leakage path, threshold strain*

1. Introduction

Gaskets are an essential component of the bolted-flange connection and serve to fill and seal the space between two or more working surfaces of fixed parts or details in a system operating at changing temperatures and pressures [1].

Flat gaskets made of ePTFE have high compressibility and show a significant reduction in creep and load retention of bolts while maintaining all the characteristics of chemical resistance of the material. The production of a sealing sheet by bonding and laminating ePTFE membranes is described in a patent of the company GORE [2].

The material models used in the modeling of ePTFE are diverse and are determined by the specifics of the problems being solved. Some authors use the simplest linear model to describe the properties of the material [3]. Since only the stress-strain diagram can be considered linear at very small strain values, Adamek and Jaszak use a bilinear model with reinforcement, with which they solve the problem of the stress-strain state of a spiral wound gasket with ePTFE lamellae [4].

The presence of significant residual strains suggests the possibility of using plastic models. Bergström uses the Drucker-Prager plasticity criterion [5]. He finds that this approach does not give a good approximation for unloading under pressure.

The presence of significant deformation gives reason to seek a solution using hyperelastic material models. Viscoelastic and viscoplastic models are used to account for residual strains. Bergström found that the closest to experimental results are obtained with Dual Network Fluoropolymer (DNF) and Three Network (TN). The use of these models is accompanied by a larger amount of computational work. TN gives slightly better results. An additional evaluation of some models applied to PTFE is given in [6].

In addition to parametric models, there are others, fundamentally different, which are based on a scalar function. Their main representative is the Marlow model [7]. It can be applied to ePTFE by being extended with a viscoelastic model.

A suitable software implementing the finite element method (FEM) and allowing the modeling of an ePTFE gasket with the described properties is ABAQUS [8].

The aim of this work is to create a finite element model and to perform simulations of a flat reinforced ePTFE gasket, through which to identify a suitable characteristic that provides an estimate of the fluid leakage at a given pressure force in the flange connection. Of interest is the determination of the fluid flow path and the threshold value of the minimum principal strain along this path.

2. Mechanomathematical model

Modeling the stress-strain state of an ePTFE gasket requires considering the nonlinear properties of the material and significant changes in the initial shape and dimensions. This necessitates solving the problem as a function of time.

The dynamic problem in FEM is formulated by the following equation [9]:

(1) $\mathbf{M\ddot{u}} + \mathbf{C\dot{u}} + \mathbf{Ku} = \mathbf{f}^{ext}$,

where **M** is the mass matrix, **C** is the damping matrix, **K** is the stiffness matrix, **u**, $\dot{\mathbf{u}}$, и $\ddot{\mathbf{u}}$ are respectively the displacement, the velocity and the acceleration, and $\mathbf{f}^{ext}$ is the vector with the external forces.

There are two formulations of FEM that solve the problem of equation (1) [9]. The first is the implicit formulation, which solves the problem of determining the unknown fields as implicit functions of time by solving a system of algebraic equations at each time step, which is suitable for long-term loads, quasi-static analyses and linear properties of the structure. The second formulation is explicit. In it, the quantities at the next time instant are calculated directly from known values at the previous time instant, without iterative procedures. It is suitable for strongly nonlinear behavior, contact problems, viscoplastic materials, short-time and fast processes, which makes it suitable for the modeling of an ePTFE gasket.

The explicit formulation is most often implemented using the central difference method. The time increment is defined by the equations

(2) $\Delta t^{n+1/2} = t^{n+1} - t^n, \qquad t^{n+1/2} = \frac{1}{2}(t^{n+1} + t^n),$

$\Delta t^n = t^{n+1/2} - t^{n-\frac{1}{2}},$

where t^n is the time in the n-th step, t^{n+1} – the time in the step n+1, $t^{n+1/2}$ and $t^{n-1/2}$ – the times in half step forward and half step back.

The half-step forward velocity is determined by the relationship

(3) $\dot{\boldsymbol{u}}^{n+1/2} \equiv \boldsymbol{v}^{n+1/2} = \frac{\boldsymbol{u}^{n+1} - \boldsymbol{u}^n}{t^{n+1} - t^n} = \frac{1}{\Delta t^{n+1/2}}(\boldsymbol{u}^{n+1} - \boldsymbol{u}^n)$,

where $\mathbf{u}^n$ is the displacement in the n-th step, $\mathbf{u}^{n+1}$ – displacement it the step n + 1.

Acceleration is determined by the equation

(4) $\ddot{\boldsymbol{u}}^{n+1/2} \equiv \boldsymbol{a}^n = \frac{\boldsymbol{v}^{n+1/2} - \boldsymbol{v}^{n-1/2}}{t^{n+1/2} - t^{n-1/2}}$, $\boldsymbol{v}^{n+1/2} = \boldsymbol{v}^{n-1/2} + \Delta t^n \boldsymbol{a}^n$.

The velocity is determined at a midpoint for the time interval (in half-steps). Substituting equation (2) into equation (3) allows the acceleration to be represented directly in terms of the displacement

(5) $\ddot{\boldsymbol{u}}^n \equiv \boldsymbol{a}^n = \frac{\Delta t^{n-1/2}(\boldsymbol{u}^{n+1}-\boldsymbol{u}^n)-\Delta t^{n+1/2}(\boldsymbol{u}^n-\boldsymbol{u}^{n-1})}{\Delta t^{n+1/2}\Delta t^n \Delta t^{n-1/2}}$.

For an arbitrary step *n*, equation (1) can be considered in the form

(6) $\mathbf{M}\boldsymbol{a}^n = \mathbf{f}^n = \mathbf{f}^{ext}(\boldsymbol{u}^n, t^n) - \mathbf{f}^{int}(\boldsymbol{u}^n, t^n)$

as it does not describe discretization in time, but only in space.

In the Marlow material model, the potential strain energy is represented by the equation

(7) $U = U_{dev}(\bar{I}_1) + U_{vol}(J)$,

where U is the strain energy density, U_{dev} – deviatoric part of the strain energy density, U_{vol} – volume fraction of the strain energy density, $\bar{I}_1$ – first invariant of the deviatoric part of the strain tensor, determined by the dependence

(8) $\bar{I}_1 = \bar{\lambda}_1^2 + \bar{\lambda}_2^2 + \bar{\lambda}_3^2$.

In the above equation $\bar{\lambda}_i$ are the principal values of the deviatoric part of the strain tensor, determined by the equation:

(9) $\bar{\lambda}_i = J^{-1/3}\lambda_i$,

where λ_i are the principal strains.

Marlowe proposes that the deviatoric part of the strain energy density be represented only by the first invariant of the deviatoric part of the strain tensor:

(10) $U_{dev} = \int_0^{\varepsilon} \sigma_{dev} d\varepsilon$,

where σ_{dev} is the deviatoric part of the nominal stress, which is determined experimentally.

3. Finite element model

The geometry modeling of the ePTFE gasket was carried out in the ABAQUS environment. An axisymmetric problem is solved, and the body is modeled in one plane. The shape and dimensions (in meters) of the gasket are given in Fig. 1. Radii of curvature are ignored.

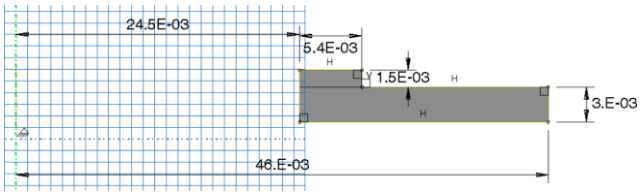


Fig. 1. *Geometrical model*

The discretization of the geometry was performed using bilinear axisymmetric four-node finite elements – CAX4R [8]. They have reduced integration and this requires a check to obtain the "hourglass" effect. The discretization of the seal is realized with 423 elements and 488 nodes – Fig. 2. Two rigid lines (wires) were created to set the boundary conditions, representing the upper and lower pressure plates and having a diameter of 120 mm. They are controlled by using reference points and are discretized with RAX2 elements. Each of them is divided into 38 elements and 39 nodes. The used mesh density was checked for convergence of the results by comparing it with other meshes – one with a higher density and one with a lower one. The check gives satisfactory results with the selected size of the finite elements.

The simulation of the seal includes two explicit steps. The duration of the first step is 180 s. In it, a load is set, which is realized by setting a concentrated force with a magnitude starting from zero at the initial moment and reaching its nominal value at the end of the step. The second step lasts 600 s. In it, the load is held at the value reached in the first step. For both steps, a linear bulk viscosity equal to 0.06 and a quadratic bulk viscosity – 1.2 are set.

In the initial step of the analysis, the reference point of the lower plate is set to zero velocities in all directions. The upper plate is set to zero velocities in the circumferential and radial directions. No value is set for the velocity of the reference point of the upper plate. It is calculated during the analysis.

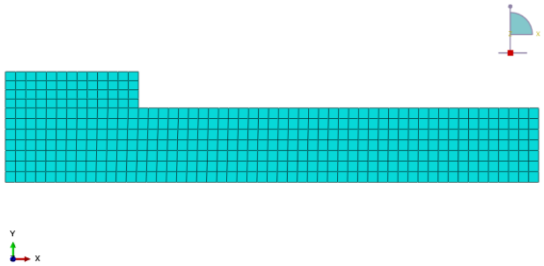


Fig. 2. *Discretization*

A contact is given between the two plates and the gasket. The kinetic contact method is used. A hard contact is given in the normal direction of the contacting surfaces, and friction is given in the tangential direction, using the penalty method. A concentrated normal force is applied to the upper plate, which is a variable parameter.

The gasket is set to self-contact because it is subject to significant deformations.

The material characteristics are set according to Marlow's model, using experimental pressure data – Fig. 3.

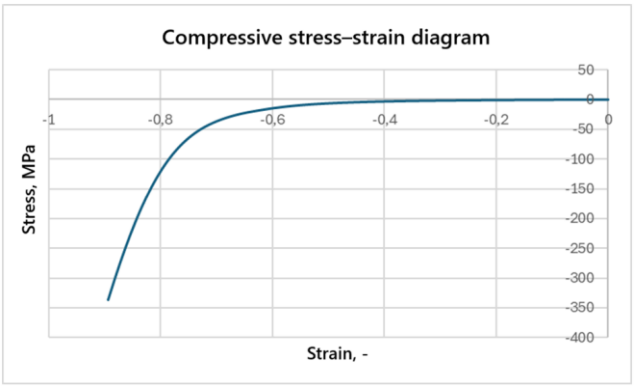


Fig. 3. ***D****iagram of compression in Marlow's model*

Viscoelastic properties are assigned using experimental data from shear stress relaxation testing – Fig. 4.

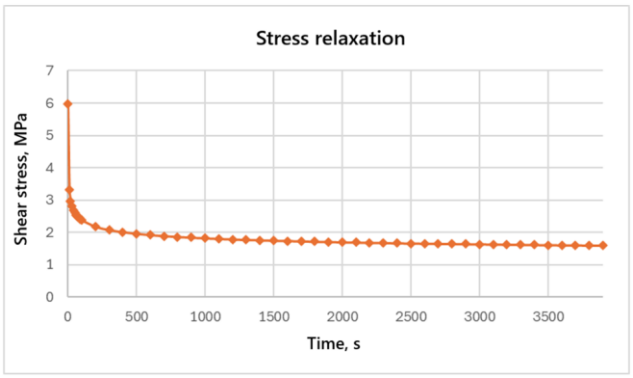


Fig. 4. *Shear stress relaxation*

The remaining material characteristics are given in Table 1.

Mass scaling was used to reduce computation time and scaling factor is 10^6.

Table 1: *Material properties*

Density of ePTFE, [kg/m^3]	Friction coefficient, [-]	Poisson's ratio, [-]
800	0.01	0.05

4. Results and analyses

From the calculations of the created model, results were obtained for the stress-strain state of the ePTFE gasket. Of particular interest is hydrostatic stress. Results for it at a compressive force of 47.6 kN are given in Fig. 5, where the gasket is presented in a three-dimensional form (3/4 in circumferential direction).

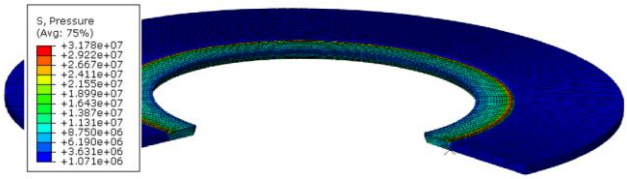


Fig. 5. *Hydrostatyc stress*

The maximum absolute value of the normal stress in the direction of compression has been determined as a function of time – Fig. 6. It is obtained along the outer diameter of the thickened part of the seal.

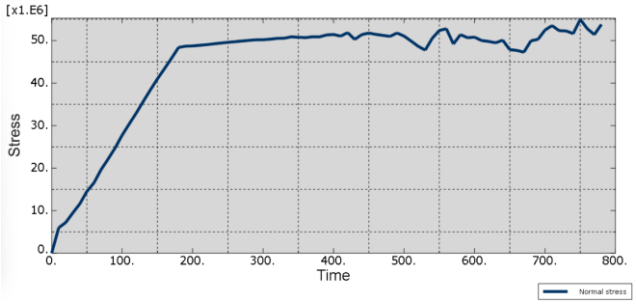
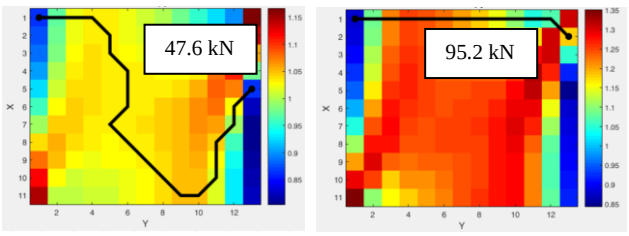


Fig. 6. *Maximal norlan stress as a function of time*

Another important quantity, which is related to the permeability of the seal due to the porosity of the material, is the minimum principal strain in the finite elements. It is used to determine the fluid leakage path. For this purpose, a script was created in MATLAB, based on the Dijkstra algorithm [10], which solves the minimax problem. It determines the connected elements with the minimum principal strain from the inside of the seal to the outside of the zone of increased density. Elements that have common sides and common nodes are considered connected. These elements form the leakage path – Fig. 7, which is given by a black line at different values of the compressive force. The maximum absolute value of the principal strain along the path is determined, which represents the threshold value for leakage. The part of the seal without reinforcement is not considered, since the strain in it are significantly smaller.



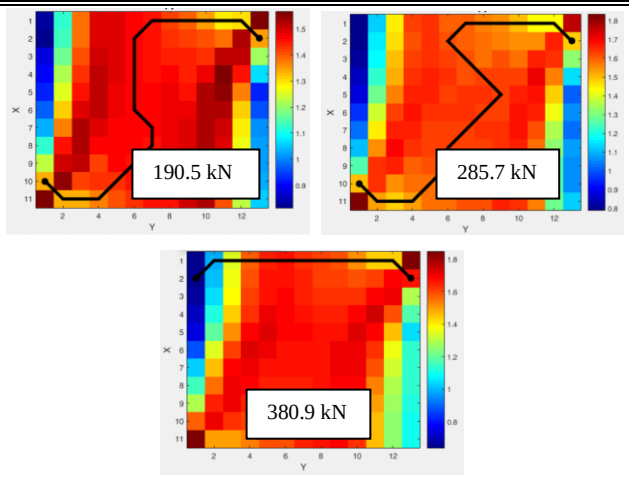


Fig. 7. *Leakage path at different forces*

Fig. 8 shows the vertical displacement of the upper plate as a function of time under a load of 47.6 kN with color diagrams of the strain state at some characteristic moments.

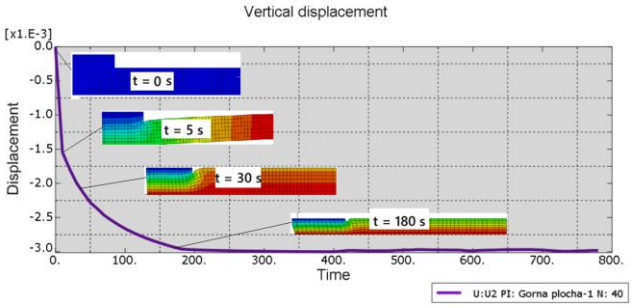


Fig. 8. *Displacemt of the uper plate*

The results at the end of the simulations for the maximum hydrostatic stress, the maximum normal stress in the direction of compression, the threshold principal strain and the maximum displacement of the upper plate, at different values of the compression force, are given in Table 2.

Table 2: *Results*

Pressure force, [kN]	47.6	92.5	190.5	285.7	380.9
Maximum hydrostatic pressure, [MPa]	31.8	91.1	171.7	243.6	203.1
Absolute value of maximum normal stress in the direction of compression, [MPa]	53.77	130.8	269.6	439.2	628.2
Threshold principal strain, [-]	1.0501	1.2546	1.4653	1.6321	1.67
Displacement of the top plate, [mm]	-2.983	-3.256	-3.421	-3.517	-3.583

The obtained values for the maximum hydrostatic stress show that with an initial increase in the compressive force, the stress also increases, but the function is not monotonic. At a force of 380.9 kN, stress decreases.

The results for the maximum normal stress in the direction of compression show fluctuations in the relaxation stage, which occurs after holding the force in the second step of the analysis.

The results for the maximum displacement of the upper plate in the relaxation stage are more stable compared to the results for the hydrostatic stress.

The threshold value along the path of the minimum principal strain is a monotonic function. As expected, it increases with increasing compression force. The fluid outflow path determined by it has different shapes at different loads. There is no clear trend. Excluding the first load, in the remaining cases it is noticeable that the entry-exit points are close to the compression plates.

The obtained results allow us to search for a correlation between the quantities determined by numerical simulations and experimentally obtained data on fluid outflow at different magnitudes of the compression force.

5. References

1. R. Flitney. *Seals and Sealing Handbook*, Elsevier, (2014).
2. H. Hisano, S. Urakami. Expanded porous polytetrafluoroethylene film-laminated sheet, and gasket composed of said sheet, Patent US 8784983B2, (2014).
3. M. Czerwiński, J. Żmudzki, K. Kwieciński, M. Kowalczyk. Finite element analysis of the impact of the properties of dental wedge materials on functional features. Arch. Mat. Sc. Eng., **112**, No.: 1, (2021).
4. K. Adamek, P. Jaszak. Design method of enhancing the tightness of a spiral wound gasket with PTFE filling. J Braz. Soc. Mech. Sci. Eng. **45**, 332, (2023).
5. J. Bergström. Accurate Finite Element Simulations of PTFE Components. SIMULIA Com. Con, (2012).
6. J. Bergström. *Mechanics of Solid Polymers*. Elsevier Inc. (2015).
7. R. Marlow. A general first-invariant hyperelastic constitutive model. Const. Mod. Rub., 157-160, (2003).
8. Dassault Systèmes SIMULIA. Analysis User's Guide. Ver. 6.14, (2014).
9. T. Belytschko, W. Liu, B. Moran. *Nonlinear Finite Elements for Continua and Structures*. John Wiley & Sons Ltd, (2000).
10. T. Cormen, C. Leiserson, R. Rivest, C. Stein. *Introduction to Algorithms.* The MIT Presss, (2009).

Preparation of biocompatible hydrogels incorporating sensing nanoparticles

Nadya Nikolova[1], Stanislav Baluschev[2,3], Ivanka Nikolova[1]
[1]Stephan Angeloff Institute of Microbiology, Bulgarian Academy of Sciences, Sofia,, Bulgaria
[2]Max Planck Institute for Polymer Research, Mainz, Germany
[3]Optics and Spectroscopy Department, Faculty of Physics, Sofia University "St. Kliment Ochridski", Bulgaria
mail: inikolova@microbio.bas.bg

Abstract: *The overarching goal of the presented here HypoVir project is to develop a research tool capable of revealing the real-time distribution of local oxygen concentrations in the liquid microenvironment of cell cultures exposed to viral infections. Particular attention is devoted to drastically reducing free surfactant levels in the extra-cellular an aqueous microenvironment. Procedures that avoid UV- or photo-induced crosslinking, as well as radical-mediated gel formation will be preferred.*

Introduction

Unlike traditional approaches that measure average respiratory activity in bulk cultures, the *HypoVir* sensing platform allows for the detection of subtle, infection-induced shifts in cellular respiration that in the case for example of infected cells may correspond to distinct stages of viral entry, replication, or immune evasion. Such granular metabolic profiling is particularly critical in the study of viruses, whose replication and pathogenesis are closely linked to host cell metabolic states [1]. *HypoVir* can perform oxygen sensing at the below-lying layers of multilayer cultures in contrast to other respirometric technologies allowing for the study of more physiologically relevant cell models [2].

Prerequisites and means for solving the problem

The *HypoVir* project chose two viruses – a RNA virus (poliovirus-1 (PV-1)) and a DNA virus (adenovirus type 5 (Ad5)) – with different pathogenetic mechanisms, and organism-specific responses, providing a rich basis for analyzing hypoxic processes, used as a viral models.

The poliovirus is an RNA virus that causes poliomyelitis – a highly contagious disease most commonly affecting children under the age of five. Most infections are asymptomatic (>90%), about 0.1–0.5% lead to infection of the nervous system and paralysis [3], and the mortality rate among paralyzed patients is 2–10%. Even in countries where poliomyelitis has been eliminated, there remains a risk of importation or circulation of vaccine-derived strains — such as the cases reported in the USA and the United Kingdom in 2022 [4]. The poliovirus serves as a suitable model for studying the molecular biology of RNA viruses and mechanisms of viral pathogenesis.

Human adenoviruses are DNA viruses that are widely distributed, with most people becoming infected in childhood [5]. They typically cause mild respiratory or gastrointestinal symptoms, but in immunosuppressed patients the infection can be severe and life-threatening. There is no specific antiviral

treatment, and therapy is supportive. The virus is stable in the environment and resistant to many disinfectants. It spreads easily via respiratory droplets, direct contact, and the fecal–oral route. Due to its broad tropism for different tissues, it serves as a valuable model for studying hypoxic responses in diverse cellular environments.

As an entirely novel research approach applicable to the visualization and monitoring of viral infection and oxygen dynamics in cell liquid microenvironment, the *HypoVir*-proposal is both well-justified and innovative. The selection of poliovirus and human adenovirus for the project is based on their complementary biological and pathogenic profiles, which are ideally suited for studying hypoxia-related processes during viral infection.

Poliovirus, a small, non-enveloped RNA virus with a well-characterized replication cycle and strict neurotropism, offers an opportunity to investigate hypoxia dynamics in highly specialized and metabolically active cells such as neurons [6]. In contrast, human adenoviruses are large, non-enveloped DNA viruses with broad tissue tropism, infecting epithelial, gastrointestinal, and respiratory cells, where hypoxia is often a result of both direct cytopathic effects and inflammatory responses [7].

The combination of an RNA virus with acute, lytic infection and a DNA virus with the ability to persist or establish latent states enables the comparative analysis of how fundamentally different viral replication strategies influence oxygen consumption, cellular metabolism, and microenvironmental oxygen gradients. Furthermore, both viruses are well-established in laboratory models, have extensively studied genomic and structural properties, and can be safely handled in controlled research conditions (BSL-2 for most laboratory-adapted strains). Studying these viruses under controlled optical modulation of hypoxia will not only advance our understanding of virus–host interactions in distinct cellular contexts but also help develop new real-time imaging and diagnostic approaches applicable to a wide range of viral pathogens.

Solution of the examined problem

The *HypoVir* sensing platform aims to develop an innovative approach for monitoring viral infection status by employing optical control of hypoxia dynamics within the intercellular microenvironment. By enabling real-time, minimally-invasive monitoring of infection progression and cellular responses under controlled microenvironmental conditions, the project addresses key societal challenges such as preparedness for emerging infectious diseases, improved diagnostic capabilities, and support for precision medicine

(**1**): material composition of the oxygen nanosensor, including solubility characteristics of the optically active materials; oxidation efficiency of the SSOS – materials; cell toxicity and solubility parameters of the used SSOS – materials; solubility of oxygen into the nanosensor core; last, but crucially important – CMC value of the used for NP-preparation surfactant.

(**2**): spectral content of the excitation light; peak excitation intensity and integral optical dosage of the testing light; this group predetermine the level of electromagnetic stress, caused by the sensing procedure.

(**3**): compulsory change of the *experimental parameters for cell growth, such as absence of Reporter-protein (for instance mCherry; dTomato*; *eGFP*; *LSSmKate1*; *LSSmKate2*, etc) or pH-reporter (Phenol red), as a consequence of excitation spectrum overleaping; or forced alteration of the ionic strange and salt content of the cell media; mechanical stress, introduced to the cell lines, during the drive-in or drive-out of the external sensor heads, etc. .

Results and discussion

Synthesis of *oil-in-water* NC - for stabilization of oil-in-water nanoconfined objects, commonly surfactants with high HLB–value and high solubility in water are used [8]. The use of highly water soluble surfactants has a major disadvantage: the molecular concentration of free surfactant in the extracellular water microenvironment is high, with a pronounced cell-toxic effect [9, 10]. Originally, for the first time in the field of TTA-UC based sensing, for stabilization of the lipophilic sensing-NC we used surfactant dedicated for type, namely water-in-oil dispersion, such as Octadecyl Trimethyl Ammonium Chloride (OTAC, with low HLB = 15.4, defined following the Davies' method), and very low solubility in water (1.759 mg/L at 25 °C, or less than 0.02% wt. (OTAC Percent Purity = 95%) [11]), NC will be prepared using the miniemulsion solvent evaporation method: in brief, two immiscible phases were emulsified in the hot state to form surfactant stabilized

wax-oil droplets including the upconversion dyes and the dissolved beeswax in the effective solvent (ethyl acetate). The particle formation took by cooling the molten droplets below 40°C and subsequent evaporation of the volatile solvent. The great advantage of adopting such hydrophobic surfactant is the extremely low concentration of free surfactant in the water phase, and therefore, dramatically reduced cell-toxicity of the sensing-NC.

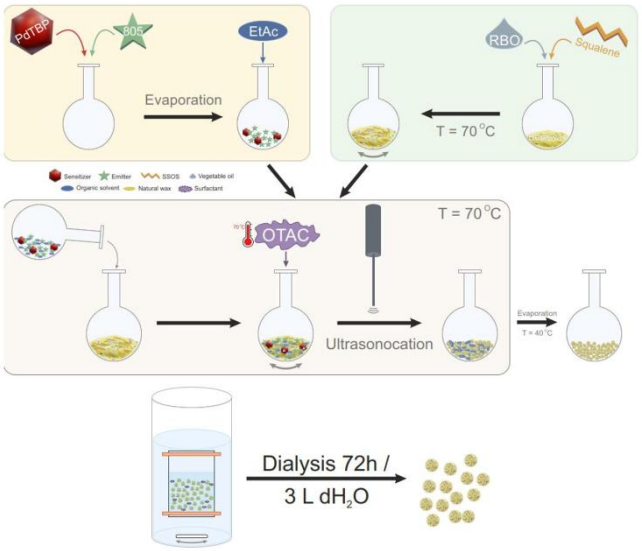


Figure 1: *Scheme of modified preparation procedure for TTA-UC-nanoparticles. The Zeta-potential of the synthesized TTA-UC soft particles is +64mV.*

Preparation of hydrogel-based NC-sensing scaffolds (NC-SS): Identification and preparation of hydrogels, bearing the sensing-NC. Procedures avoiding UV - photo induced cross linking or radical driven gel formation is preferred. Various candidate materials including solubilized basement membrane matrix derived from Engelbreth-Holm-Swarm (EHS) mouse sarcoma cells, jellyfish collagen, nanofibrillar cellulose, and alginate will be utilized to fabricate 2D hydrogel scaffolds for cell culture. These hydrogels, with or without embedded sensing-NC, will be compared in human cancerous epithelial cell line **HEp-2**, as well as the normal diploid fibroblast cell line **MRC-5**.

Cytotoxicity of the hydrogel-based NC-SS - *In vitro* cytotoxic effects of the NC-SS will be investigated using the human cancerous epithelial cell line HEp-2**,** as well as the normal diploid fibroblast cell line MRC-5. Their viability will be monitored in order to assess the potential toxicity of the hydrogels and/or the embedded oxygen-sensing nanocomponents. The obtained results may reveal possible effects of these materials on cell viability and provide insights into the tolerance and adaptation of the cells to the different matrices.

Validation of the proof-of-principle is carried out using an *in vitro* culture of epithelial cells susceptible to the target virus. Well-characterized viruses, such as poliovirus and adenovirus, will be used as a models for correlation of the viral replication activity (defined by classical methods, [12, 13]) and dynamics of hypoxia in the intercellular microenvironment (obtained by the *HypoVir* - technology). The temporal dynamics of the oxygen consumption of the cell cultures will be studied according to the duration of the replication cycle (marked further as $\boldsymbol{\tau_{RC}}$) of the respective viruses:

Poliovirus: it is a RNA virus with a rapid replication cycle ($\boldsymbol{\tau_{RC}}$~6–8 hours).

Adenovirus: it is a DNA virus with a slower replication cycle ($\boldsymbol{\tau_{RC}}$~24–48 hours).

Planed time points for measurements: $\tau = \mathbf{0}$ (*infection*); $\tau = {}^{\mathbf{1}}/_{\mathbf{2}}\,\boldsymbol{\tau_{RC}}$; $\tau = \boldsymbol{\tau_{RC}}$; $\tau = {}^{\mathbf{3}}/_{\mathbf{2}}\,\boldsymbol{\tau_{RC}}$; $\tau = 2\boldsymbol{\tau_{RC}}$; $\tau = {}^{\mathbf{5}}/_{\mathbf{2}}\,\boldsymbol{\tau_{RC}}$, etc.

Samples can be taken at selected time points to titrate the intracellular virus and to correlate measured hypoxia parameters with viral replication. This assay will be performed under normoxic and hypoxic conditions to assess the influence of oxygen availability on viral replication efficiency and cytopathogenic potential.

Viral Titration: Quantification of infectious virus will be performed using the $\mathbf{CCID_{50}}$ assay (50% Cell Culture Infective Dose) [14]. The $\mathbf{CCID_{50}}$ assay is used to determine the infectious virus titer by measuring the dilution at which 50% of the cell cultures show cytopathic effects (CPE). It estimates the amount of virus required to infect half of the cell cultures in a given sample, providing a quantitative measure of viral infectivity. Serial dilutions of virus-containing supernatants will be applied to cell monolayers in 96-well plates. The presence or absence of CPE (cytopathic effect) will be scored, and viral titers will be calculated using the Reed-Muench method [15].

The *HypoVir* platform is be integrated into the **O_2-HSC** hydrogel cancerous epithelial cell line **HEp-2** or normal diploid fibroblast cell line **MRC-5,** in order to enable real-time, spatially resolved monitoring of oxygen consumption during viral infection.

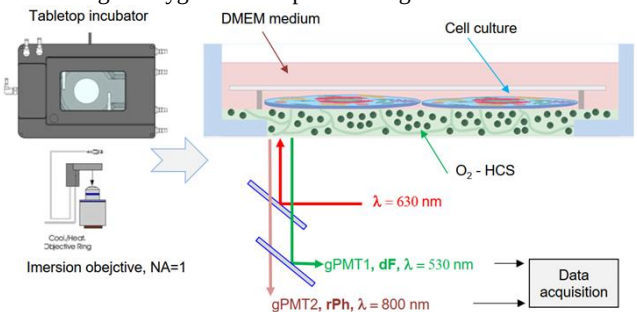


Figure 2*: Set-up for optical sensing of the oxygen content.*

We observe oxygen gradients in 2D cell model and correlate viral replication (reporter-viruses PV-1 and HAdV-5) with local metabolic activity and oxygen profiles. A FluoroDish™ vessel, covered with the **O_2-HSC** hydrogel and supporting healthy cell monolayer is translated to the top incubator *PECON P-Set 2000*, Figure 2. The optical quality window (d = 125 µm thickness) allows application of high numerical aperture apochromatic objective HCPL-APO 63x/1.2 W CORR CS2 (*Leica Microsystems*). Further, the acquisition of the optical signals of dF and rPh, can be performed following the set-up shown in Figure 2**b**, WP1. The oxygen content in the cell microenvironment, (***i***) healthy and (***ii***) subjected to viral infection will be compered, following time table corresponding to the specific replication cycles.

Conclusion

The overarching goal of the presented here *HypoVir* project is to develop a research tool capable of revealing the real-time distribution of local oxygen concentrations in the liquid microenvironment of cell cultures exposed to viral infections. We demonstrate preparation of a hydrogel (incorporating the sensing NC) with drastically reducing free surfactant levels in the extra-cellular an aqueous microenvironment. The applied procedure, based on self-organization in nanoconfinement, avoids UV- or photo-induced crosslinking, as well as radical-mediated gel formation will be preferred.

References

[1] Serebrovska, Z.O., Chong, E.Y., Serebrovska, T.V. et al. Hypoxia, HIF-1α, and COVID-19: from pathogenic factors to potential therapeutic targets. Acta Pharmacol Sin 41, 1539–1546 (2020). doi.org/10.1038/s41401-020-00554-8

[2] Evenou F, Fujii T and Sakai Y, Spontaneous Formation of Highly Functional Three-Dimensional Multilayer from Human Hepatoma Hep G2 Cells Cultured on an Oxygen-Permeable

Polydimethylsiloxane Membrane, Tissue Engineering Part C: Methods, doi.org/10.1089/ten.tec.2009.0042
[3] https://www.who.int/news-room/fact-sheets/detail/poliomyelitis
[4] Morbidity and Mortality Weekly Report https://www.cdc.gov/mmwr/volumes/73/wr/mm7341a1.htm .
[5] Amber Arnold and Eithne MacMahon. Adenovirus infections, *Medicine*, **2021**, 49 (12), 790-793
[6] T. Pipiya, H. Sauthoff, Y. Q. Huang, B. Chang, J. Cheng, S. Heitner, S. Chen, W. N. Rom, J. G. Ha, Hypoxia reduces adenoviral replication in cancer cells by downregulation of viral protein expression, *Gene Therapy*, **2005**, Vol. 12, 911–917.
[7] A. Reyes, L. F. Duarte, M. A. Farias, E. Tognarelli, A. M. Kalegris, S. M. Bueno, P. A. Gonzales. Impact of Hypoxia over Human Viral Infections and Key Cellular Processes, *Int. J. Mol. Sci*., **2021**, 22(15), 7954.
[8] K. Landfester in *Colloid Chemistry II. Topics in Current Chemistry, Vol. 227* (Eds.: Antonietti, M.), Springer, Berlin, Heidelberg, **2003**, pp. 75–123.
[9] Â. S. Inácio, K. A. Mesquita, M. Baptista, J. Ramalho-Santos, W. L. Vaz, O. V. Vieira, "In vitro surfactant structure-toxicity relationships: implications for surfactant use in sexually transmitted infection prophylaxis and contraception" *PLoS One* **2011,** *6(5)*, e19850.
[10] M. Manaargadoo-Catin, A. Ali-Cherif, J.-L. Pougnas, C. Perrin, "Hemolysis by surfactants — A review" *Advances in Colloid and Interface Science* **2016,** *228*, 1–16.
[11] Fisher Scientific Chemicals, "n-Octadecyltrimethylammonium chloride – Product Specifications", can be found under https://www.fishersci.se/shop/products/n-octadecyltrimethylammonium-chloride-95-thermo-scientific/15407148 (accessed: 28.05.2025).
[12] Ren L, Zhang W, Zhang J, Zhang J, Zhang H, Zhu Y, Meng X, Yi Z, Wang R. Influenza A Virus (H1N1) Infection Induces Glycolysis to Facilitate Viral Replication. *Virol Sin*. **2021**, 36(6):1532-1542. doi: 10.1007/s12250-021-00433-4.
[13] Tomaskova J, Oveckova I, Labudova M, Lukacikova L, Laposova K, Kopacek J, Pastorekova S, Pastorek J. Hypoxia induces the gene expression and extracellular transmission of persistent lymphocytic choriomeningitis virus. *J Virol*. **2011**, 85(24):13069-76. doi: 10.1128/JVI.00829-11.
[14] Hierholzer, J.C., & Killington, R.A. (1996) Virus isolation and quantitation. Virology Methods Manual (pp. 25-46). Academic Press.
[15] Reed, L.J., and Muench, H. (1938) Simple method of estimating fifty percent endpoints, American Journal of Hygiene, 27(3), 493-497.

Acknowledgements:
SB acknowledge the European Union-*NextGenerationEU* project, through the National Recovery and Resilience Plan of the Republic of Bulgaria, project № BG-RRP-2.004-0008-C01". IN, SB acknowledge the Bulgarian National Science Fund, project КП-06-H97/4 / 05.12.2025 / *HypoVir* - „Monitoring Viral Infection Status via Optical Control of Hypoxia Dynamics in the Intercellular Microenvironment" for the financial support.

Possibilities for accelerating chemical-thermal treatment

Valery M. Konstantinov, Vladislav A Leshok
Faculty of Mechanical Engineering – Belarusian National Technical University, Belarus

Abstract: *The intensification methods for carburizing and nitrocarburizing investigated in this study include the use of biochar, preliminary oxidation, and plastic deformation. The possibility of combining oxidation and plastic deformation was also examined.*
***KEYWORDS**: INTENSIFICATION OF CHEMICAL–THERMAL TREATMENT, CARBURIZING, NITROCARBURIZING, BIOCARBON, OXIDATION, PLASTIC DEFORMATION, ACCELERATION OF DIFFUSION PROCESSES*

1. Introduction

Chemical–thermal treatment (CTT) occupies an important place in mechanical engineering, being widely used to improve the properties of steel parts and tools. For example, in the automotive industry up to 70% of products are strengthened by carburizing, nitrocarburizing, and nitriding [1]. However, a common drawback of these technologies is the low rate of diffusion-layer formation [2]. Since the emergence of CTT as a scientific discipline, developments have followed two main paths: the creation of new CTT processes and the acceleration (intensification) of established ones. In this context, the search for and investigation of effective methods to accelerate CTT processes becomes particularly significant, as it directly contributes to resource-saving objectives [3]. A number of intensification approaches are known [4–14], and their combination is a promising direction.

The aim of this study is to investigate the feasibility of using biochars as a replacement for conventional carbon-containing components in saturating mixtures for pack carburizing and pack nitrocarburizing, as well as to evaluate the effect of combining oxidation and plastic deformation on subsequent gas nitrocarburizing.

2. Results and Discussion

Process acceleration was evaluated using the degree of intensification, defined as the relative increase in diffusion-layer thickness compared with the baseline regime:

$$\Delta = \left(\frac{h_i - h_0}{h_0}\right) \cdot 100\%, \quad (1)$$

where h_i is the layer thickness after the corresponding intensification method, and h_0 is the layer thickness under the baseline regime without intensification.

The carburized layer thickness was taken as the distance from the surface to the point where the microhardness reached 550 HV. The nitrocarburized layer thickness was taken as the distance to the point where the microhardness exceeded the core hardness by 50 HV.

A promising direction for improving pack carburizing and pack nitrocarburizing is to modify the composition of saturating mixtures [12–14]. This topic has been successfully developed by the scientific school of L. G. Voroshinin at the Belarusian National Technical University, where positive results have been obtained [7, 9].

In the present study, the possibility of replacing traditional carbon-containing components with alternative ones–specifically, biochars–is considered. These materials are produced by pyrolysis of biologically derived wastes (e.g., from the food, agricultural, and other industries) [15]. It is known [16] that biochars possess a well-developed porous structure, which may potentially enhance the saturating capacity of CTT mixtures.

The relevance of this research is supported by the fact that hundreds of millions of tonnes of biological waste are generated worldwide every year [17]. The main disposal methods still remain landfilling and incineration. Incorporating this type of waste into industrial processes such as CTT is a pathway toward rational resource use and the development of secondary recycling.

Pack carburizing and pack nitrocarburizing in powder media based on biochar and charcoal were studied experimentally. The results showed that biochar-containing mixtures provide a higher degree of process intensification compared with charcoal-based mixtures. The increase reached 21% (Fig. 1a).

At the next stage, the effect of preliminary oxidation and plastic deformation on subsequent gas nitrocarburizing was investigated. Previously, the school of Professor L. G. Voroshinin (Department of Materials Science in Mechanical Engineering, Belarusian National Technical University) reported positive results when applying these intensification methods. In particular, studies [3, 10] examined the effect of preliminary oxidation on accelerating carburizing and boriding of micro-objects, while studies [8, 11] demonstrated a positive effect of plastic deformation on accelerating boriding of micro-objects.

In the present study, an extremal dependence of the degree of intensification on preliminary oxidation temperature was identified, leading to an increase in intensification up to 38% (Fig. 1b). It was also established that the deformation degree affects the intensification nonlinearly, resulting in an increase up to 52% (Fig. 1c). These experimental findings are consistent with earlier results reported by Professor Voroshinin's school [3, 8, 10, 11].

When oxidation and plastic deformation are combined, one might expect an intensification degree of 90% as the additive sum of the individual effects (38% + 52%). However, the experimentally determined intensification degree for the combined treatment was 118%. Thus, the non-additive increment amounted to 28% (Fig. 1d).

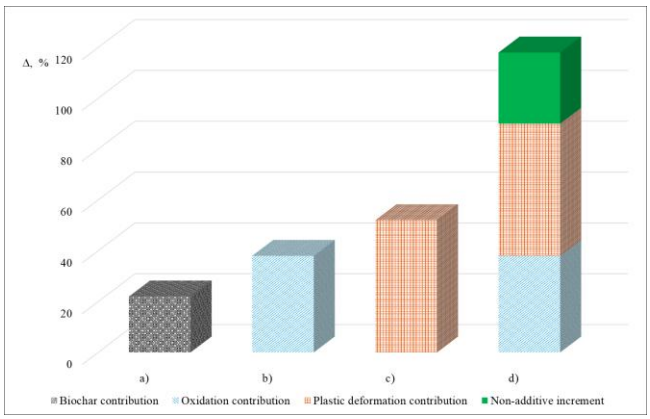


Fig. 1. Degree of intensification of carburizing and nitrocarburizing as a function of intensification methods: (a) use of biochar; (b) oxidation; (c) plastic deformation; (d) combined oxidation and plastic deformation.

3. Conclusions

1. The use of biochar as a carbon-containing component in powder saturating mixtures for pack carburizing and pack nitrocarburizing provides higher process intensification than conventional charcoal-based mixtures; the maximum increase in diffusion-layer thickness reached 21%.

2. Preliminary oxidation prior to gas nitrocarburizing exhibits an extremal dependence on oxidation temperature and can increase the degree of intensification up to 38%.

3. Preliminary plastic deformation affects the degree of intensification nonlinearly, with the maximum increase reaching 52%.

4. Combining preliminary oxidation and plastic deformation results in an intensification degree of 118%, exceeding the additive expectation (38% + 52% = 90%); the non-additive increment is 28%.

5. The investigated intensification approaches (biochar application, preliminary oxidation, preliminary plastic deformation, and their combination) demonstrate practical potential for industrial implementation and contribute to resource-saving by involving bio-waste-derived materials in CTT processes.

4. References

1. Voroshnin L.G., Mendeleeva O.L., Smetkin V.A. Teoriya i tekhnologiya khimiko-termicheskoi obrabotki: uchebnoe posobie [Theory and technology of chemical-thermal treatment: study guide]. Moscow; Minsk, Novoe znanie Publ., 2010. 304 p. (in Russian).

2. Konstantinov V.M., Kukareko V.A. Puti energosberezheniya pri termicheskoi i khimiko-termicheskoi obrabotke stalei za schet uskoreniya diffuzionnykh protsessov [Approaches to energy saving in thermal and thermochemical treatment of steels through acceleration of diffusion processes]. Lit'e i metallurgiya [Foundry production and metallurgy], 2023, no. 4, pp. 72–80 (in Russian).

3. Voroshnin L.G., Konstantinov V.V. Aktual'nye problemy khimiko-termicheskoi obrabotki [Topical problems of chemical-thermal treatment]. Nauka i tekhnika, 2002, no. 4, pp. 22–26 (in Russian).

4. Panteleenko F.I., Liakhovich L.S., Kukharev B.S. O klassifikatsii sposobov intensifikatsii protsessov khimiko-termicheskoi obrabotki metallov i splavov [On the classification of methods for intensification of thermochemical treatment of metals and alloys]. Metallurgiya: respubl. mezhvedom. sb. nauch. tr. [Metallurgy: Republican interdepartmental collection of scientific papers]. Minsk, Vysheishaya shkola Publ., 1980, pp. 5–6 (in Russian).

5. Petrova L.G., et al. Intensifikatsiya protsessov khimiko-termicheskoi obrabotki stalei [Intensification of thermochemical treatment processes of steels]. Moscow, MADI Publ., 2019. 160 p. (in Russian).

6. Kukareko V.A., Gatsuro V.M., Grigorchik A.N., Chichin A.N. Matematicheskoe modelirovanie i mekhanizm ukrupneniya austenitnogo zerna pri vysokotemperaturnom nagreve legirovannykh konstruktsionnykh stalei [Mathematical modeling and mechanism of austenite grain coarsening during high-temperature heating of alloyed structural steels]. Mekhanika mashin, mekhanizmov i materialov, 2019, no. 3(48), pp. 58–68 (in Russian).

7. Voroshnin L.G., Voroshnin A.L. Novye podkhody k sozdaniyu i ispol'zovaniyu poroshkovykh nasyshchayushchikh sred dlya khimiko-termicheskoi obrabotki [New approaches to the development and use of powder saturating media for chemical-thermal treatment]. Vesci ANB. Seryya FTN., 1997, no. 3, pp. 13–17 (in Russian).

8. Konstantinov V.M. Diffuzionno-legirovannye splavy dlya zashchitnykh pokrytii. Diss. dokt. tekhn. nauk [Diffusion-alloyed alloys for protective coatings. Dr. tech. sci. diss.]. Minsk, 2008. 474 p. (in Russian).

9. Protasevich G.F., Voroshnin L.G. Izobretatel'skaya rabota v oblasti khimiko-termicheskoi obrabotki metallov [Inventive activity in the field of chemical-thermal treatment of metals]. Metallovedenie i termicheskaya obrabotka metallov, 1988, no. 5, pp. 26–30 (in Russian).

10. Konstantinov V.M., Leshok V.A. Aktivatsiya termodiffuzionnogo nasyshcheniya nizkouglerodistoi stali metodom okisleniya poverkhnosti [Activation of thermodiffusion saturation of low-carbon steel by surface oxidation]. Fundamental'nye issledovaniya i innovatsionnye tekhnologii v mashinostroenii: nauch. tr. VIII Mezhdunar. nauch. konf., Moscow, 19–20 November 2024 [Fundamental research and innovative technologies in mechanical engineering: Proc. 8th Int. Sci. Conf.]. Moscow, Institut mashinovedeniya im. A.A. Blagonravova RAN, 2024, pp. 117–118 (in Russian).

11. Konstantinov V.M., Leshok V.A., Shtempel' O.P. Analiz vliyaniya predvaritel'noi i tsiklicheskoi plasticheskoi deformatsii na khimiko-termicheskuyu obrabotku konstruktsionnykh stalei [Analysis of the effect of preliminary and cyclic plastic deformation on chemical-thermal treatment of structural steels]. Mekhanika mashin, mekhanizmov i materialov, 2024, no. 1(66), pp. 37–42. doi: 10.46864/1995-0470-2024-1-66-37-42 (in Russian).

12. Luksha L.K. Tverdyi karbyurizator [Solid carburizer]. Author's certificate SU 111009, publ. date 01 Jan 1957 (in Russian).

13. Chuchkalov M.V., et al. Sostav karbyurizatora dlya tsementatsii detalei iz nizkouglerodistoi stali [Carburizer composition for carburizing parts made of low-carbon steel]. Patent RU 2690630, publ. date 04 Jun 2019 (in Russian).

14. Spiridonova I.M., et al. Karbyurizator dlya tsementatsii stal'nykh izdelii [Carburizer for carburizing steel products]. Author's certificate SU 1836486, publ. date 23 Aug 1993 (in Russian).

15. Misyukova A.D., Yankovskii S.A., Gorshkov A.S. Otkhody pererabotki tsitrusovoi biomassy kak energeticheskii tsennyi produkt [Citrus biomass processing wastes as an energy-valuable product]. Mezhdunarodnyi zhurnal prikladnykh i fundamental'nykh issledovanii [International Journal of Applied and Fundamental Research], 2021, no. 11, pp. 76–80. doi: 10.17513/mjpfi.13316 (in Russian).

16. Ding Y., Wang T., Dong D., Zhang Y. Using Biochar and Coal as the Electrode Material for Supercapacitor Applications. Frontiers in Energy Research, 2020, vol. 7, art. 159.

17. Laimon M., Mai T., Goh S., Yusaf T. Energy sector development: System dynamics analysis. Applied Sciences, 2020, vol. 10, art. 134. doi: 10.3390/app10010134.

Analytical solutions for boundary value problems of transport phenomena in the design of multilayer structures

Renat Sadykov[1], Airat Osipov[1], Artem Akhmerov[1]
[1] Kazan State Power Engineering University, st. Krasnoselskaya, 51, 420066, Kazan, Russia
E-mail: sadykov_r_a@mail.ru, nord7077@yandex.ru, akhm@mail.ru

Abstract: *This article provides a systemic analysis of the application of analytical methods for solving differential equations of heat and mass transfer for the design of building envelopes in the context of modern energy efficiency requirements and the digitalization of the construction industry. It is demonstrated that analytical solutions remain critical for the design of multilayer walls and roofs, thermal stability and vapor permeability calculations, and the verification of BIM models and smart home systems. A review of classic and new analytical results from 2015–2025 is presented, including the use of physically-informed neural networks (PINN) for real-time thermal protection optimization. Examples of implementation in regulatory documents, software, and microclimate management systems are provided.*
KEY WORDS: BUILDING ENVELOPES, THERMAL CONDUCTIVITY, MOISTURE TRANSFER, ANALYTICAL SOLUTIONS, BUILDING ENERGY EFFICIENCY, PINN, DIGITAL TWINS, BIM

1. Introduction

Building envelopes, which include external walls, roofs, ceilings over unheated basements and driveways, and translucent enclosures, are a key element determining the energy efficiency of the building as a whole. According to the International Energy Agency [1], building envelopes account for up to 40% of total energy consumption in residential and public sectors, making accurate calculations of their thermal performance paramount.

Modern building energy efficiency requirements, formulated in regulatory documents such as SP 50.13330.2012 [2] in the Russian Federation, ASHRAE Standard 90.1 [3] in the United States, as well as voluntary standards such as PassivHaus, BREEAM, and LEED, place increasingly stringent demands on the accuracy of thermal calculations. In particular, designers must ensure reliable predictions of transient temperature fields within the building envelope under diurnal and annual fluctuations in outdoor air temperature, correctly assess the intensity of moisture transfer and identify potential condensation zones in multilayer structures, calculate the thermal stability of rooms under intermittent heating conditions, and optimize the relative positions of thermal insulation layers and vapor barrier membranes.

It should be noted that, despite the rapid development of numerical methods and related software such as ANSYS, COMSOL Multiphysics, EnergyPlus, and WUFI, analytical solutions to differential equations of heat and mass transfer remain an indispensable tool in the design engineer's arsenal. This circumstance is explained by the fact that analytical solutions form the basis of the current regulatory calculation methods regulated by the documents of the SNiP, SP, DIN and ISO systems, ensure the possibility of performing rapid engineering calculations at the pre-project stages, serve as a standard for the verification of complex BIM models and CFD calculations, and also form the basis of the algorithms of "smart home" systems and predictive control of heating and ventilation.< 0.030 W/(m·K), as well as design solutions that minimize thermal bridges and ensure airtightness.

Over the past five years, rapid advancements have been observed both in innovative insulation materials and intelligent insulation systems that combine energy efficiency, environmental sustainability, and durability.

2. Classical analytical solutions in building thermal physics

For an n-layer flat wall, the temperature field is determined by the exact solution[4]:

$$T(x) = T_{int} - \frac{T_{int} - T_{ext}}{R_0} \sum_{i=1}^{k} \frac{\delta_i}{\lambda_i},$$

where the total thermal resistance is:

$$R_0 = \frac{1}{\alpha_{int}} + \sum_{i=1}^{n} \frac{\delta_i}{\lambda_i} + \frac{1}{\alpha_{ext}},$$

This solution is the basis of SP 50.13330.2012 and has been used in 100% of projects since 1958.

Problem of Diurnal Fluctuations in Outdoor Temperature [5,6]:

$$T_{ext\,(t)} = T_m + A_{ext} \sin(\omega t),$$

For a semi-infinite body, the exact solution is:

$$T(x,t) = T_m + A_{ext} \exp\left(-x\sqrt{\frac{\omega}{2a}}\right) \sin\left(\omega t - x\sqrt{\frac{\omega}{2a}}\right),$$

where the amplitude attenuation is characterized by the coefficient

$$\mu = \sqrt{\frac{\omega}{2a}} = \sqrt{\frac{\pi}{aP}},$$

P is the oscillation period (24 hours for daily fluctuations, 8760 hours for annual fluctuations).

Thermal stability criterion (SNiP II-3-79*, SP 23-101-2004):

$$\xi = \frac{A_{internal}}{A_{external}} \leq 0.5,$$

Fourier solution for a multi-layer wall with a harmonic boundary condition [7]:

$$\theta(x,t) = \sum_{k=1}^{\infty} A_k \exp(-\mu_k x) \sin(\omega t - \mu_k x + \varphi_k),$$

where the eigenvalues μ_k are determined from the layer coupling conditions.

Practical application: Calculating the surface heat-gain coefficient s (W/(m²•°C)) according to GOST 26254-84:

$$s = \sqrt{\lambda c \rho \omega},$$

This is a critical parameter for assessing the comfort of spaces with intermittent heating.

The equation for the transient diffusion of water vapor [8,9]:

$$\frac{\partial e}{\partial t} = \frac{\partial}{\partial x}\left(\frac{\delta(e)\partial e}{\partial x}\right),$$

where e is the partial vapor pressure and δ(e) is the vapor permeability coefficient.

For steady-state operation, the exact solution (SP 50.13330.2012):

$$e(x) = e_{int} - \frac{e_{int} - e_{ext}}{R_{\text{п}}} \sum_{i=1}^{k} \frac{\delta_i}{\delta_{\text{п},i}},$$

where R_n is the vapor permeability resistance.

The condensation zone is determined from the condition:

$$e(x) \geq E\big(T(x)\big),$$

where E(T) is the saturated vapor pressure at temperature T.

3. Industrial Applications in Building Practice

Analytical solutions to heat conduction problems remain the methodological foundation of all key regulatory documents. In Russia, SP 50.13330.2012 (2023 revision) relies on the steady-state heat conduction solution for a multilayer wall to determine the required thermal resistance of building envelopes [2], while the thermal stability

methodology per SP 23-101-2004 (2024 revision) is based on A.M. Shklover's results on the attenuation of harmonic temperature oscillations [5]. Internationally, DIN 4108-2 (2024) employs Fourier's solution for periodic thermal processes, ISO 13786:2017 defines dynamic characteristics of building components through complex heat transfer coefficients, and the ASHRAE Handbook (2021) applies the Mitalas–Arseneau Transfer Function Method (1971) — a discretized form of the analytical solution.

Professional software is likewise grounded in analytical solutions — either implemented directly or used for verification. THERM 7.8 (Lawrence Berkeley National Laboratory) calculates heat transfer through window systems and junction details using Fourier's solution. WUFI Pro 6.7 (Fraunhofer Institute for Building Physics) integrates A.V. Lykov's solutions for coupled heat and moisture transfer along with the Glaser method. DesignBuilder 7.0 uses the EnergyPlus core based on the Conduction Transfer Function (CTF) method — a discrete analogue of the analytical solution. The Russian program "Teremok" 3.1 (Research Institute for Building Physics, RAASN) implements B.F. Vasiliev's solution for thermal stability of enclosures under Russian climatic conditions, while Elcut 6.5 employs exact analytical solutions as a benchmark for FEM verification.

Online calculators are widely used: SmartCalc.ru (dew point and condensation zone calculations, over 10,000 queries per day) and Teploraschet.rf (compliance checks against SP 50.13330.2012). Insulation manufacturers — Rockwool, Knauf Insulation — provide their own online tools for selecting optimal insulation thickness based on classical analytical formulas.

Analytical solutions are particularly important in automated building climate control systems, where computationally intensive numerical methods are impractical due to real-time performance requirements. Tesla Powerwall 3 with HVAC integration (2024) implements predictive heating control with a forecast horizon of up to 6 hours based on an exponential cooling model:

$$T_{room\,(t+\Delta t)} = T_{ext\,(t)} + \left[T_{room\,(t)} - T_{ext\,(t)}\right] exp\left(-\frac{\Delta t}{\tau}\right),$$

here $\tau = \frac{C_{bldg}}{kA_{env}}$.

The 4th-generation Google Nest Learning Thermostat (2023) adjusts heating start times to account for the thermal inertia of enclosing structures, achieving energy savings of 18–23% compared to algorithms that disregard dynamic thermal characteristics [10]. Siemens Desigo CC (2024 update) integrates analytical solutions into its thermal load calculation module [11]: accounting for the thermal stability of massive walls reduces the required peak boiler capacity by 12–15% without compromising thermal comfort.

4. New Analytical Solutions for Building Envelopes

Phase transitions in materials with variable properties: Tariku et al. (2015) [12] derived an exact solution for a wall with moisture phase change (freezing/thawing):

$$\frac{\partial}{\partial t}\left[\rho_0 w(T)\right] = \frac{\partial}{\partial x}\left[D_w(T,w)\frac{\partial w}{\partial x}\right],$$

where w(T) is the moisture content accounting for ice. Applied in WUFI Pro 6.5+ for climates with freeze–thaw cycling through 0°C.

Solution for walls with infrared film and electric heating: Zukowski (2019) [13] obtained an analytical solution for a wall containing a planar heat source:

$$T(x) = T^0 + \frac{q_{src}}{2\lambda}(L - |x|)\ for\ -L \le x \le L,$$

Used in the design of Caleo, RexVa, and Teplolux heating systems in Russia (2023–2025).

Optimization of vapor barrier placement by variational calculus: Qiu & Haghighat (2020) [14] presented the first analytical solution for the optimal position of a vapor barrier layer based on the criterion of minimum accumulated moisture:

$$\min\ x_{vb} \int_0^L \left[e(x) - E\left(T(x)\right)\right]^+ dx,$$

Result: for the climate of Moscow, the optimum is x_vb = 0.73δ_total from the interior surface (rather than 2/3 as prescribed in SP [15]).

Dynamic thermophysical characteristics of composite panels: Mazzeo et al. (2021) [16] derived an exact solution for sandwich panels with honeycomb core under harmonic oscillations, yielding the complex heat transfer coefficient:

$$U^* = |U|e^{i\varphi} = \frac{1}{\sum R_i + i\omega \sum C_i R_i^2},$$

Applied in the design of rapidly erected buildings (Kingspan, Ruukki, 2024).

5. The Role of Neural Networks in Calculating Building Enclosures

The latest approach to calculating building envelope heat and moisture conditions is physically-informed neural networks (PINNs), which combine machine learning with the application of physical laws in the form of differential equations.

Zhang et al. (2022) [17] developed a PINN trained on A.V. Lykov's exact solutions for 500 material types. The network predicts the moisture content field w(x,t) in a multilayer wall in ~2 ms with an accuracy of ≤0.5%, while WUFI requires 40 minutes. Based on this development, the Moisture Guard Pro mobile app (iOS/Android) was released in 2024: a builder scans a material's QR code and instantly receives a condensation zone estimate for a specific structure.

A team from the Polytechnic University of Milan (2023) [18] trained the DeepONet network on 10^6 accurate analytical solutions for thermal conductivity for various combinations of materials and thicknesses. In ~50 ms, the network determines the optimal arrangement of 5 layers from 20 available materials, subject to cost and required R_0 constraints. The technology is integrated into the Knauf Insulation online configurator (2024): the architect enters requirements, and the system instantly suggests three optimal options with a 30-year NPV calculation.

Integrating analytical solutions with reinforcement learning opens up possibilities for optimal HVAC control. In a joint study by MIT and Siemens (2024) [19], an RL agent was trained on accurate solutions for a building cooling problem under various ventilation conditions and automatically controls the dampers of a supply and exhaust system. A trial at the MIT.nano building (Cambridge, USA) demonstrated a 27% reduction in energy consumption without compromising thermal comfort.

The use of symbolic regression for the automatic derivation of engineering formulas also holds promise. Cranmer (2023) [20] applied the PySR system to 50,000 exact solutions of the Shklover problem for the attenuation of temperature fluctuations for various climatic zones and automatically derived a new formula for the attenuation coefficient:

$$\xi = \frac{1}{1+0.85\sqrt{\frac{R_0 s_{вн}}{P}}},$$

This formula is 34% more accurate than the old empirical relationships from current codes and is proposed for inclusion in draft SP 50.13330.2025.

6. Verification and Validation of Calculation Methods

The reliability of thermal calculation results for enclosing structures, whether analytical, numerical, or hybrid, must be confirmed by verification using standard test problems with a known exact solution.

The BESTEST methodology, regulated by ANSI/ASHRAE standard 140, includes a set of test cases based on the analytical solutions of Shklover and Vasiliev and is used to verify software packages such as EnergyPlus, DesignBuilder, and IDA ICE. Test problems developed within the IEA ECBCS Annex 24 project are based on the Fourier solution for a multilayer wall and are used to verify WUFI, DELPHIN, and COMSOL Multiphysics. EN ISO 13791:2012 defines simplified test cases for validating thermal stability calculation methods, which are used for certification of national software in all European Union countries.

Along with verification using test problems, experimental validation of calculation methods by comparing them with the results of in-kind measurements is of fundamental importance.

The Fraunhofer Institute for Building Physics conducted a large-scale in-kind experiment at the Holzkirchen test site in Germany from 2020 to 2023 [28]. During the experiment, 12 types of wall structures were exposed to real-world climatic conditions, with temperature T(x,t) and moisture content w(x,t) measurements taken every 10 minutes for three years.

A comparison of measurement results with calculated data showed that accurate analytical solutions provide temperature deviations of less than 0.3°C and moisture content deviations of less than 1.5%, while one-dimensional numerical models in the WUFI program yield deviations of 0.3–0.5°C and 1.5–2.8%, respectively, and three-dimensional CFD calculations yield deviations of up to 1.2°C due to the uncertainty of boundary conditions. Thus, accurate analytical solutions not only remain relevant but also outperform numerical methods in accuracy for problems with regular geometry.

7. Comparative Analysis of Calculation Methods

A systematic comparison of various methods for calculating the thermal regime of enclosing structures allows us to formulate recommendations for selecting the optimal approach depending on the nature of the problem being solved.

In terms of temperature determination accuracy, analytical solutions provide a reference accuracy of approximately ±0.1°C within the applicability limits of the corresponding physical model. One-dimensional numerical methods implemented in the WUFI program provide an accuracy of approximately ±0.3–0.5°C, while two- and three-dimensional CFD calculations are characterized by an error of ±0.5–1.5°C, primarily due to the uncertainty of the boundary conditions. Hybrid methods based on PINN provide an accuracy of approximately ±0.15°C thanks to training on arrays of accurate analytical solutions.

In terms of humidity accuracy, analytical solutions provide an error of approximately ±0.5%, while WUFI numerical methods provide an error of ±1.5–3%, CFD methods provide an error of ±3–5%, and hybrid PINN methods provide an error of ±0.8%.

Significant differences are observed in calculation time: for an annual cycle problem with an hourly resolution, an analytical solution requires less than 1 second, a one-dimensional numerical solution requires 5–20 minutes, CFD requires 10–50 hours, and a hybrid PINN solution requires 5–10 seconds.

However, analytical solutions have limitations with regard to the geometry of the problem: they do not allow for direct consideration of thermal bridges, whereas numerical methods allow for approximate calculations, and CFD and PINN provide full consideration of two- and three-dimensional effects.

In terms of operator skill requirements, analytical and numerical one-dimensional methods are characterized by a moderate level of complexity, CFD requires high skill levels, and hybrid PINN methods are low due to the automation of the calculation process. Software costs range from zero for analytical formulas and open-source PINN libraries to 50,000–150,000 rubles for commercial one-dimensional programs and 0.5–2 million rubles for CFD packages.

8. Practical Recommendations

Based on the analysis performed, the following practical recommendations can be formulated for choosing a method for calculating the thermal conditions of enclosing structures.

An analytical solution is the method of choice in the following cases: when calculating standard flat multilayer structures without significant thermal bridges, during preliminary calculations and feasibility studies of design solutions, when verifying complex numerical models, for educational purposes and to develop an understanding of the physics of heat and mass transfer processes, and when developing algorithms for embedded controllers of smart home systems.

The use of numerical methods is necessary in cases of complex fencing geometry, including corners, junctions with balconies and window units, with two- or three-dimensional heat and moisture transfer, in the presence of phase transitions with a moving phase boundary, when using non-standard materials with unstudied or significantly nonlinear properties, and also when

9. Conclusions

The analysis of the current state of analytical methods in building thermal physics allows us to formulate the following key conclusions.

Analytical solutions to heat and mass transfer equations in building envelopes will retain and strengthen their position as the foundation of regulatory and technical design in 2025, as all current codes, DIN, ISO, and ASHRAE standards are based on precise analytical solutions obtained between the 1950s and 1990s.

The critical importance of analytical methods for engineering calculation practice is determined by the fact that verifying the compliance of a designed structure with the requirements of SP 50.13330 takes no more than 2 minutes with manual calculations or 10 seconds using an online calculator, whereas numerical calculation of the same problem requires significantly more time and operator skill.

The indispensability of analytical solutions for verifying numerical models stems from the fact that no numerical code can be certified for practical use without testing on analytical benchmark problems with a known exact solution.

The resurgence of interest in analytical methods observed in recent years is largely due to their synergy with artificial intelligence technologies: physically-informed neural networks (PINNs), DeepONet architectures, and symbolic regression methods allow calculations to be accelerated by 100-1000 times, new precise formulas to be obtained for previously unsolved problems, and the physics of heat and mass transfer to be integrated into predictive microclimate control systems.

The practical significance of accurately calculating thermal stability using analytical formulas is confirmed by the achievable energy savings of 15-25% compared to simplified calculation methods.

Promising areas for the development of analytical methods in building thermal physics include the automatic

derivation of new analytical solutions using transformer neural network architectures [29], the development of quantum algorithms for the instantaneous solution of eigenvalue problems [30], the integration of analytical solutions into building information modeling systems (Revit, ArchiCAD) with automatic report generation according to building codes, and the creation of blockchain-based verification systems for energy efficiency calculations for green mortgage programs.

Thus, in the era of digitalization of construction, classical analytical methods that laid the foundation for building thermal physics between 1950 and 2020, combined with modern neural network technologies for 2020–2025, are forming a new standard for the design of energy-efficient buildings, ensuring an optimal combination of accuracy, speed, and the physical validity of calculation results.

References

1. International Energy Agency. Energy Efficiency 2023. Paris: IEA Publications, 2023. 250 p.
2. SP 50.13330.2012. Thermal Protection of Buildings. Updated Version of SNiP 23-02-2003. Moscow: Ministry of Regional Development of the Russian Federation, 2012. 96 p.
3. ASHRAE Standard 90.1-2022. Energy Standard for Buildings Except Low-Rise Residential Buildings. Atlanta: ASHRAE, 2022. 284 p.
4. Fokin, K.F., Thermal Engineering of Building Envelopes. 5th ed. Moscow: AVOK-PRESS, 2006. 256 p.
5. Shklover, A.M., Heat Transfer under Periodic Thermal Effects. Moscow: Gosenergoizdat, 1961. 160 p.
6. Vasiliev, B.F., “Field Studies of the Temperature and Humidity Regime of Panel Walls.” Moscow: Stroyizdat, 1965. 176 p.
7. Tabunshchikov, Yu.A., Brodach, M.M., “Mathematical Modeling and Optimization of Thermal Efficiency of Buildings.” Moscow: AVOK-PRESS, 2002. 194 p.
8. Lykov, A.V., “Transfer Phenomena in Capillary-Porous Bodies.” Moscow: GITTL, 1954. 296 p.
9. Ilyinsky, V.M., “Structural Thermal Physics (Enclosing Structures and Microclimate of Buildings”). Moscow: Vysshaya Shkola, 1974. 320 p.
10. Google Nest Labs. Energy Savings White Paper 2023. Mountain View: Google LLC, 2023. 48 p.
11. Siemens Smart Infrastructure. Desigo CC Performance Report 2024. Zug: Siemens AG, 2024. 64 p.
12. Tariku F., Kumaran K., Fazio P. Transient model for coupled heat, air and moisture transfer through multilayered porous media // International Journal of Heat and Mass Transfer. 2015. Vol. 78. P. 1207–1220.
13. Zukowski M. Analytical model of heat transfer in electric floor heating systems // Applied Thermal Engineering. 2019. Vol. 150. P. 681–689.
14. Qiu X., Haghighat F. Optimization of vapor retarder position in building envelopes: A variational approach // Building and Environment. 2020. Vol. 182. Article 107117.
15. Gagarin V.G., Kozlov V.V. On the calculated position of the vapor barrier in multilayer enclosing structures // AVOK. 2004. No. 2. pp. 56–61.
16. Mazzeo D., Oliveti G., Arcuri N. Analytical model for dynamic thermal characteristics of sandwich panels // Applied Thermal Engineering. 2021. Vol. 184. Article 116276.
17. Zhang L., Wang Y., Chen X. Physics-informed neural networks for moisture transfer in building envelopes // Building Simulation. 2022. Vol. 15, No. 6. P. 1047–1062.
18. Poli R., Mazzarella L. DeepONet-based rapid optimization of multilayer wall configurations // Energy and Buildings. 2023. Vol. 285. Article 112901.
19. Wang Z., Hong T. Reinforcement learning for building HVAC control using physics-based models // Applied Energy. 2024. Vol. 355. Article 122245.
20. Cranmer M. Interpretable machine learning for science with PySR and SymbolicRegression.jl. arXiv preprint arXiv:2305.01582, 2023.
21. Fast P., Gaffikin J. Brock Commons Tallwood House: Construction and thermal performance // Journal of Architectural Engineering. 2018. Vol. 24, No. 3. Article 05018003.
22. Favoino F., Jin Q., Overend M. Design and control optimization of adaptive insulation systems for office buildings // Applied Energy. 2023. Vol. 330. Article 120356.
23. Baetens R., Jelle B.P., Gustavsen A. Aerogel insulation for building applications: A state-of-the-art review // Energy and Buildings. 2011. Vol. 43, No. 4. P. 761–769.
24. Alam M., Singh H., Limbachiya M.C. Vacuum Insulation Panels for building construction: A review // Renewable and Sustainable Energy Reviews. 2011. Vol. 15, No. 8. P. 3897–3908.
25. Li Y., Fu Q., Yu S. et al. Optically transparent wood: Recent progress and opportunities // Advanced Optical Materials. 2020. Vol. 8, No. 1. Article 1901939.
26. Nika D.L., Balandin A.A. Phonons and thermal transport in graphene // Reports on Progress in Physics. 2017. Vol. 80, No. 3. Article 036502.
27. Siemens. Building Digital Twins: From concept to reality. Siemens White Paper. Zug: Siemens AG, 2024. 32 p.
28. Künzel H.M., Zirkelbach D. Long-term hygrothermal performance of building envelopes: Experimental validation // Journal of Building Physics. 2023. Vol. 46, No. 4. P. 387–405.
29. Hao Z., Liu S., Zhang Y. et al. Physics-informed machine learning: A survey on problems, methods and applications. arXiv preprint arXiv:2211.08064, 2022.
30. Cao Y., Romero J., Aspuru-Guzik A. Potential of quantum computing for drug discovery // IBM Journal of Research and Development. 2018. Vol. 62, No. 6. P. 6:1–6:20..

Cathodic Protection Modeling of Steels in Corrosive Chemical Environments Using COMSOL Multiphysics

Julieta Daniela Chelaru
Babeș-Bolyai University, Cluj-Napoca, Romania
julieta.chelaru@ubbcluj.ro

Abstract: This study investigates the electrochemical performance of Sacrificial Anode Cathodic Protection (SACP) systems for offshore steel structures using Finite Element Analysis (FEA). Two structural substrates, S235JR carbon steel and S550QL high-strength steel, were modelled in a 3 wt.% NaCl electrolyte. A comparative analysis was performed between two sacrificial anode materials: a conventional Al-5Mg alloy and a quaternary Al-6Zn-0.2In-1Mg-0.03Ti alloy. The simulations evaluate the influence of anode placement errors by comparing an ideal symmetric distribution (90°) with a clustered configuration (10°). The results show that geometric clustering significantly alters the potential distribution along the structure. For S235JR steel, the clustered configuration produces localized underprotection with potentials reaching −0.78 V (vs. Ag/AgCl). In contrast, for S550QL steel, the same configuration results in localized over-polarization (≈ −0.96 V), thereby increasing the risk of hydrogen-induced stress cracking (HISC). The study demonstrates that improper anode placement may compromise cathodic protection efficiency even when high-performance anode alloys are used. These findings highlight the importance of accurate anode distribution and support the use of numerical simulations in digital twin approaches for offshore corrosion management.

***Keywords**: SACRIFICIAL ANODES, DIGITAL TWIN, CATHODIC PROTECTION, COMSOL MULTIPHYSICS*

1. Introduction

Corrosion remains a persistent and costly challenge in offshore industrial environments, particularly in aggressive maritime conditions. If left unmonitored, electrochemical degradation can lead to catastrophic structural failures and significant economic losses [1]. To mitigate these risks, Cathodic Protection (CP) using sacrificial anodes is the most widely adopted method for preserving submerged offshore assets [1,2].

The effectiveness of CP systems depends on electrochemical thresholds that vary with substrate metallurgy. According to EN ISO 15589-2, standard carbon steels such as S235JR require a polarized potential maintained between −0.85 V and −1.05 V (vs. Ag/AgCl) for full corrosion immunity [1]. High-strength steels such as S550QL introduce a narrow operational window: while they require cathodic polarization to prevent mass loss, they are highly susceptible to Hydrogen-Induced Stress Cracking (HISC) if the potential drops below −1.10 V (vs. Ag/AgCl) [2, 3]. Achieving a uniform potential distribution is therefore a structural necessity.

Although theoretical designs assume perfect anode symmetry, industrial constraints and installation errors often result in asymmetric or clustered arrangements [4–6]. Such non-ideal configurations reduce the system's "throwing power," creating localized "shadowing effects" that leave areas vulnerable to accelerated corrosion or hydrogen-induced damage. Under Industry 4.0, Digital Twins allow engineers to simulate these non-ideal scenarios and predict structural behavior before failure occurs [1, 5, 7].

This study utilizes COMSOL Multiphysics® [8] to quantify the electrochemical impact of geometric clustering errors, specifically where anodes are placed at 10° intervals instead of the ideal 90° symmetry. Two sacrificial anode chemistries—the binary Al-5Mg alloy and the quaternary Al-6Zn-0.2In-1Mg-0.03Ti alloy—are compared across S235JR carbon steel and S550QL high-yield steel substrates. This analysis provides critical data for predictive maintenance strategies, supporting the transition toward Corrosion 4.0 [9].

2. Methodology

The numerical investigation was conducted using the Corrosion Module of COMSOL Multiphysics® [8]. whether Secondary or Tertiary Current Distribution interface was used, and which kinetic boundary conditions were applied.

Model Geometry and Environmental Conditions
The computational domain consists of a cylindrical cathode (15 m height) representing a submerged structural pile. Two thermal scenarios were evaluated: 20 °C for the S235JR substrate and 15 °C for the S550QL substrate, as temperature significantly influences electrolyte resistivity and oxygen solubility. While an isothermal comparison would isolate electrochemical kinetics, this study intentionally differentiates the thermal profiles (15°C for S550QL vs. 20°C for S235JR) to reflect the distinct operational depths and geographic deployments of these structural steels. This dual-variable approach (geometry + temperature) provides a more robust 'stress-test' for the Digital Twin's predictive
Anode Materials: Two distinct sacrificial alloys were defined. The traditional Al-5Mg alloy and the quaternary Al-6Zn-0.2In-1Mg-0.03Ti alloy. The latter is characterized by the addition of Indium (0.2%), which acts as an activator to ensure continuous activation and prevent the formation of a passive alumina film [3, 7]
Boundary Conditions: The anodes were modeled with an equilibrium potential E_{eq} relative to the Ag/AgCl reference electrode, following DNV-RP-B401 guidelines [7].
Simulation Scenarios: To quantify the impact of installation non-conformities, two geometric configurations were compared:
- Standard Configuration (Control): 4 anodes distributed with perfect 90° radial symmetry.
- Clustered Configuration (Error): A deliberate error where a group of anodes is positioned at a 10° interval (5 anodes), simulating spatial constraints or human error in the process industry [4].
The electrolyte was modeled as a substitute ocean water with a constant salinity of 3 wt.% NaCl (conductivity (σ_l) of 4.78 S/m). This concentration was chosen to simulate a standard aggressive marine environment, providing a baseline for analyzing the impact of temperature on ionic mobility. At this salinity, the transition from 20˚C to 15˚C induces a non-linear increase in kinematic viscosity and a corresponding decrease in the diffusion coefficient of dissolved oxygen, which are critical factors for the cathodic reaction kinetics [10, 11]. The study adopts a context-specific thermal mapping, simulating each alloy under its most frequent operational environment.

3. Results and Discussion

The surface potential analysis of the pile (Fig. 1) highlights the system's sensitivity to both geometric configuration and anode composition. According to DNV-RP-B401 [7], the optimal protection criteria for steel in seawater requires a potential between -0.80 V and -1.05 V (vs. Ag/AgCl). Results indicate that the Al-6Zn-0.2In-1Mg-0.03Ti alloy achieves a deeper polarization (approaching -1.08 V in adjacent zones) compared to the Al-5Mg alloy, which maintains a more conservative potential. This performance gap is attributed to the presence of Indium, which prevents anode surface passivation. However, in the 10° clustering error scenario, both materials fail to protect the distal ends of the pile (reaching -0.78 V), confirming that the superior chemical activation of the quaternary alloy cannot overcome the ionic

shielding induced by asymmetric distribution [12, 13]. For the S235JR carbon steel substrate, this error leads to localized underprotection, posing a direct risk of generalized corrosion. In contrast, for the S550QL high-strength steel, the same geometric error drives the potential near the cluster toward -1.10 V. While this represents over-polarization, for high-strength steels, such levels are hazardous as they promote hydrogen evolution and subsequent absorption into the metal lattice, triggering Hydrogen-Induced Stress Cracking (HISC) [14].

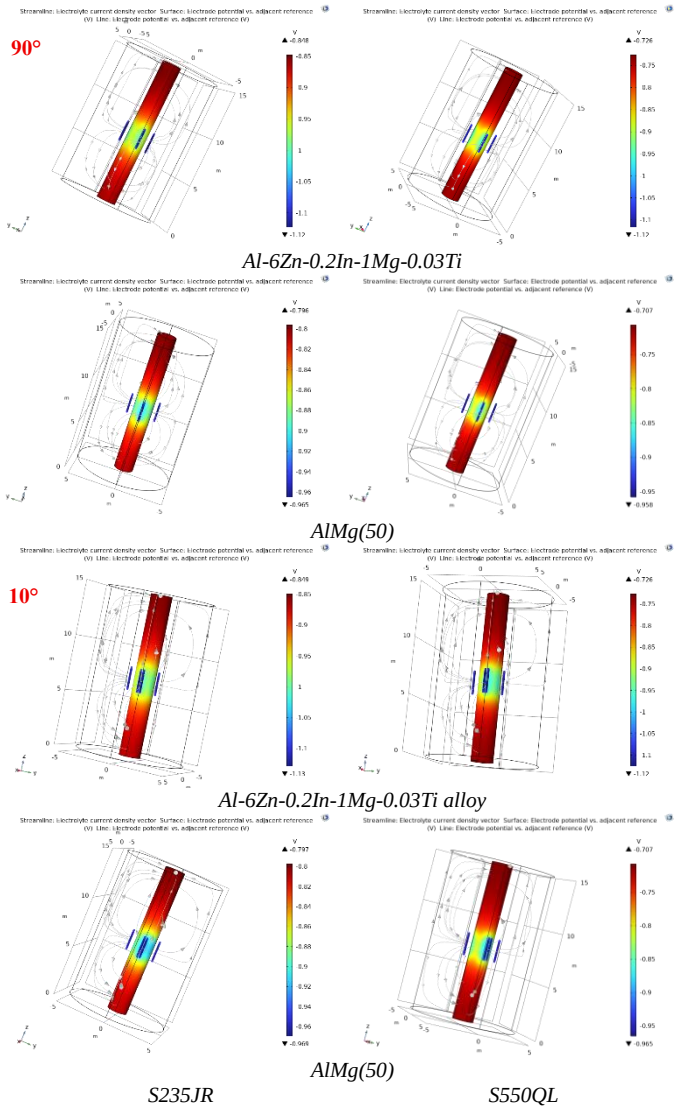


***Fig. 1**. Surface electrode potential distribution on S235JR and S550QL piles protected by Al-Zn-In-Mg-Ti and Al-Mg sacrificial anodes under symmetric (90°) and clustered (10°) configurations.*

The multislice electrolyte potential plots (Fig. 2) reveal the physical mechanisms behind underprotection: the 'potential shadow' effect and the ohmic IR drop. The quaternary alloy generates a more extensive potential field in the electrolyte due to its higher electrochemical activity. However, on the S550QL substrate, this drives the potential toward the critical -1.10 V threshold. Conversely, the Al-5Mg alloy offers a higher safety margin against hydrogen embrittlement but demonstrates significantly lower 'throwing power'. The IR drop is most pronounced in the 10° clustering case, where the density of equipotential lines indicates a massive ohmic resistance that isolates the leeward side of the pile, a well-documented phenomenon by Peabody [15]. The S550QL high-strength steel shows a higher vulnerability to the IR drop generated by clustering. The 'potential shadow' effect is more critical for this substrate because its electrochemical safety window is significantly narrower: it must be polarized below -0.80 V to ensure corrosion protection but maintained above -1.10 V to avoid hydrogen damage. This delicate balance is easily disrupted by the 10° anode positioning error.

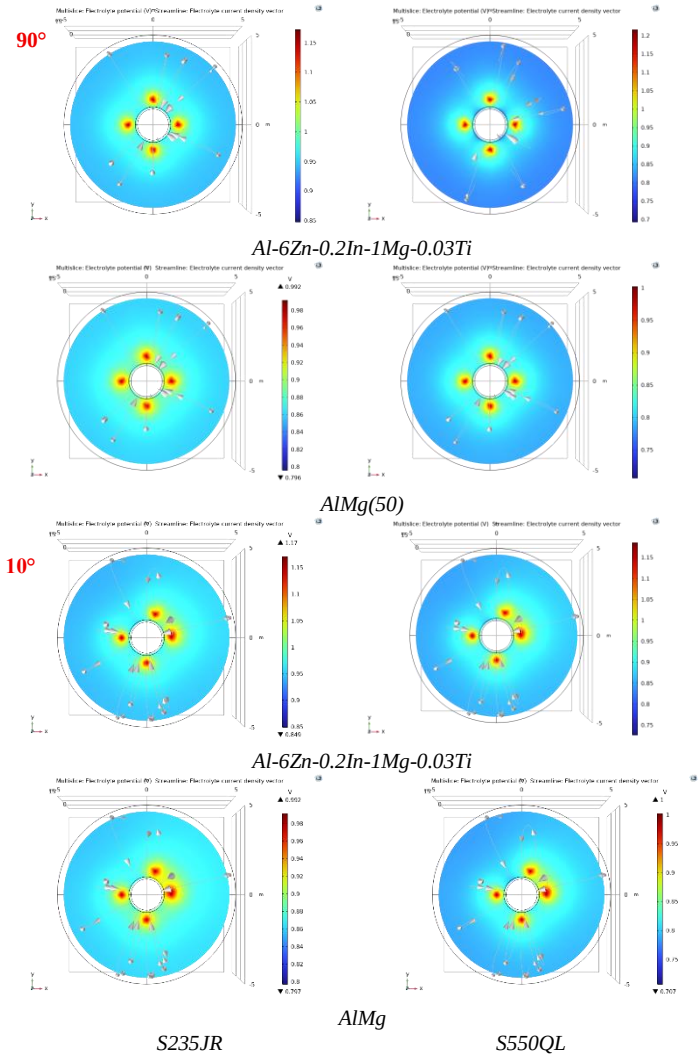


***Fig. 2.** Multislice electrolyte potential (φl) and current streamline distribution for S235JR and S550QL substrates: (a) clustered anode configuration (10°); (b) symmetric configuration (90°).*

The visualization of current streamlines (Fig. 3) emphasizes the 'current crowding' effect and the overall current conversion efficiency of the system. The Al-6Zn-0.2In-1Mg-0.03Ti alloy delivers a significantly higher local current density, which is particularly advantageous in colder waters (15 °C} where electrolyte resistivity increases according to Sharqawy's correlations [11]. In contrast, the Al-5Mg alloy tends to passivate more rapidly under these thermal conditions, restricting the flux lines and failing to reach critical zones of the structure. In the 10° clustering scenario, negative interference is observed as adjacent anodes 'compete' for the same ionic pathways, leading to an inefficient distribution of protective current. This demonstrated inefficiency underscores the value of a Digital Twin framework [16, 17] in detecting 'hidden' current hotspots that could lead to premature anode consumption without ensuring total structural protection. The simulation quantifies a 'divergent failure mode': the 10° error leads to material loss (corrosion) in S235JR steel and structural embrittlement (HISC) in S550QL steel. While the quaternary alloy's high current output is beneficial for polarizing the S235JR pile in resistive environments, it becomes a liability for the S550QL substrate by creating localized zones of high current density that exceed the safe hydrogen evolution limits defined by DNV-RP-B401 [3].

In conclusion, the results highlight that cathodic protection design must consider the operational potential window of the protected steel. While conventional structural steels such as S235JR

require sufficient polarization to avoid corrosion, high-strength steels such as S550QL exhibit a narrower safe potential range due to the risk of hydrogen-induced damage.

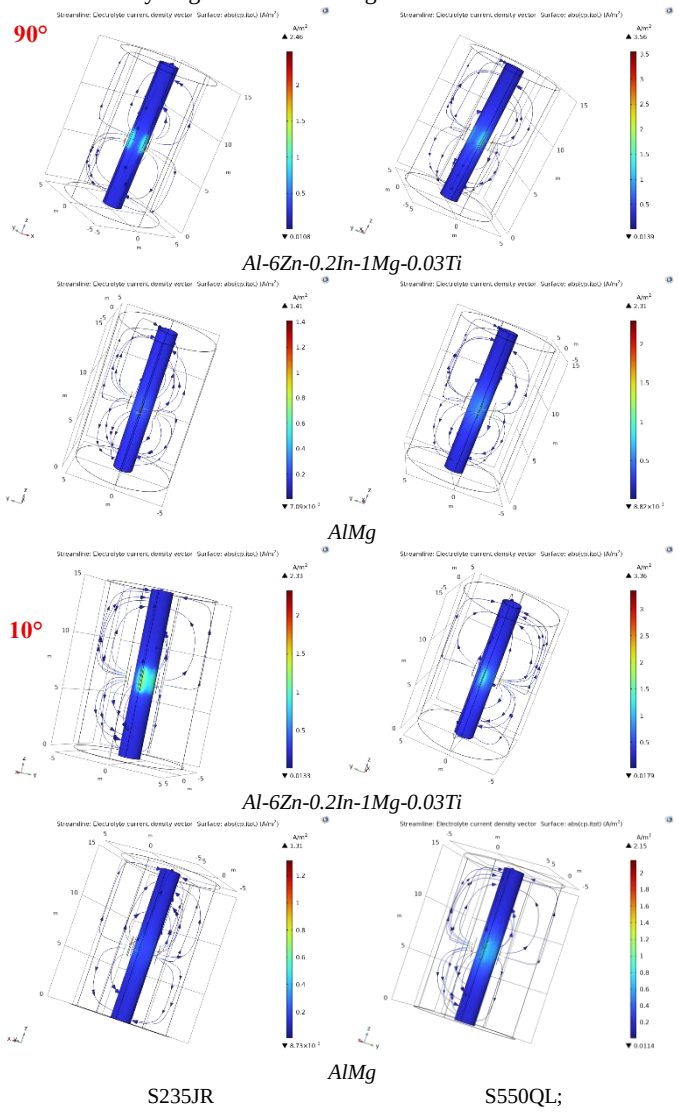


Fig. 3 Electrolyte current density and streamline distribution illustrating current flow for S235JR and S550QL substrates with Al-Zn-In-Mg-Ti and Al-Mg sacrificial anodes under symmetric (90°) and clustered (10°) configurations.

3. Conclusions

The numerical investigation into the cathodic protection of offshore structural piles under geometric and environmental stress yields the following key findings:

Impact of Geometric Non-Conformity: The simulations indicate that anode placement is the primary determinant of system integrity. A 10° clustering error creates a "potential shadow" effect, leaving structural extremities at potentials more positive than -0.80 V (vs. Ag/AgCl). Consequently, localized corrosion may occur despite the use of high-performance sacrificial alloys, as the configuration fails to meet ISO 15589-2 protection standards.

Divergent Failure Modes: Identical geometric faults produce distinct risks depending on the steel grade. For S235JR carbon steel, localized underprotection leads to material loss through oxidation. For S550QL high-strength steel, the clustering of quaternary anodes drives local potentials to be more negative than -1.10 V, introducing a critical risk of Hydrogen-Induced Stress Cracking (HISC) due to excessive cathodic polarization.

Anode Chemistry and Environmental Sensitivity: The quaternary Al-6Zn-0.2In-1Mg-0.03Ti alloy exhibits superior "throwing power" in colder, more resistive electrolytes (15 °C) compared to the binary Al-5Mg alloy. However, its higher electrochemical activity requires precise spatial distribution to prevent the formation of localized over-polarization "hotspots" on the substrate.

Predictive Modeling and Industry 4.0: The correlation between electrolyte potential (φ_l) and current streamline dynamics confirms that multi-physics modeling can identify shielded regions not detectable by traditional surface-only measurements. This underlines the necessity of integrating Digital Twin frameworks into predictive maintenance strategies within the Corrosion 4.0 paradigm.

3. References

1. J. Zhang, X. Wang, Digital Twins for Corrosion Management in Offshore Structures, Journal of Marine Science and Engineering, 10 (2022) 456.
2. P.R. Roberge**,** *Handbook of Corrosion Engineering*, 3rd ed., McGraw-Hill Education, New York, 2019.
3. DNV-RP-B401**,** *Cathodic Protection Design*, Det Norske Veritas (DNV), 2021.
4. E. Bardal, *Corrosion and Protection*, Springer Science & Business Media, Trondheim, 2004.
5. R. Javaherdashti, *Corrosion Management in the Chemical Process Industries*, CRC Press, 2015.
6. L. Wright, S. Davidson**,** *How to Tell the Difference Between a Model and a Digital Twin*, Advanced Modeling and Simulation in Engineering Sciences, 7 (2020) 13.
7. M. Sacco, A. Gualtieri**,** *Industry 4.0 and the Digital Twin in Subsea Engineering*, Ocean Engineering, 218 (2021) 108214.
8. COMSOL Multiphysics® v. 6.2, *Corrosion Module User's Guide*, COMSOL AB, Stockholm, Sweden, 2024.
9. EN ISO 15589-2:2014, *Petroleum, petrochemical and natural gas industries — Cathodic protection of pipeline systems — Part 2: Offshore pipelines*, International Organization for Standardization.
10. ASTM D1141-98, Standard Practice for the Preparation of Substitute Ocean Water, ASTM International, West Conshohocken, PA, 2021.
11. M.H. Sharqawy, J.H. Lienhard V, S.M. Zubair, *The thermophysical properties of seawater: A review of existing correlations and data*, Desalination and Water Treatment, 16 (2010) 354-380.
12. J. Zhang, Z. Zhang, and W. Wu, "Effects of Anode Proximity and Geometric Clustering on CP Interference in Offshore Structures," Ocean Engineering, vol. 245, p. 110482, 2022.
13. ISO 15589-2:2024, "Petroleum, petrochemical and natural gas industries — Cathodic protection of pipeline systems — Part 2: Offshore pipelines," International Organization for Standardization.
14. W. H. Hartt and N. K. Lin, "Hydrogen Induced Stress Cracking of Steels with CP in Marine Environments," Corrosion, vol. 63, no. 1, pp. 58–69, 2007.
15. A. W. Peabody, Peabody's Control of Pipeline Corrosion, 2nd Edition, NACE International, 2001
16. L. Wang, R. G. Buchheit, "Digital Twins for Corrosion: A Review of the State of the Art and Future Perspectives," Corrosion Science, vol. 189, p. 109591, 2021.
17. S. Rossi and M. Fedel, "Smart Coatings and Cathodic Protection: Towards Industry 4.0 Digital Twins," Coatings, vol. 10, no. 7, p. 642, 2020.

Photoluminescence properties of Sm^{3+}-doped ZrO_2–TiO_2–Al_2O_3 coatings

Stancho Yordanov*, Bojidar Jivov, Vladimir Petkov, Shaban Uzun, Mihaela Aleksandrova
Bulgarian Academy of Sciences, Institute of Metal Science, Equipment and Technologies with Hydro- and Aerodynamics Centre
"Acad. A. Balevski", 67 "Shipchenski prohod" Blvd., 1574 Sofia, Bulgaria
e-mail: stancho14@abv.bg

Abstract: *The emission spectrum of the ZrO_2–TiO_2–Al_2O_3–Sm_2O_3 coating was recorded at different excitation wavelengths. Under UV excitation (λ_{ex} = 354 nm), broad band with a maximum around 420–440 nm was observed and can be associated with oxygen vacancies in ZrO_2 together with Ti^{3+} centers. Weakly intense and narrower emission bands at 600 nm and 647 nm are assigned to the $^5G_{5/2} \rightarrow {}^7H_{7/2}$ and $^5G_{5/2} \rightarrow {}^7H_{9/2}$ transitions of Sm^{3+} ions. Under excitation with 404 nm the emission is dominated by defect levels in the oxide coating.*
The values of the chromaticity coordinates of the coating excited under 354 nm correspond to the pale pink color of emission (0.252, 0.272) and under 404 nm has orange color of emission (0.353, 0.370).
Keywords: *EMISSION SPECTRUM, SOL-GEL METHOD, DIP COATING, ZrO_2–TiO_2–Al_2O_3–Sm_2O_3*

1. Introduction

The use of oxide coatings is a classic technological approach for effective protection or modification of the characteristics of the working surface of various technical parts and finished products [1-4]. Coatings with increased chemical, corrosion and thermal resistance, high hardness and wear resistance, suitable optical properties, adequate biocompatibility and other performance indicators are widely used [5-11]. Various technological approaches have been developed for the deposition of functional coatings. In this aspect, a number of methods are applicable: [12-22]: physical vapor deposition (PVD), chemical vapor deposition (CVD), combustion synthesis, micro-arc oxidation, laser cladding, plasma spraying, sol-gel technique and a number of others.

Ceramic materials with increased Al_2O_3 content exhibit good wear resistance and friction, as well as stable chemical properties [23-28]. On the other hand, in some product categories, relative brittleness, inadequate thermal shock resistance, tendency to stress concentration and crack formation, as well as other operational problems are observed [29]. The development of optimized compositions based on Al_2O_3 in combination with other oxide components allows the production of coatings with appropriate phase composition, adequate microstructure and functional characteristics [25-28].

The mechanical properties and oxidation resistance of multilayer thermal barrier coatings Al_2O_3/ZrO_2 prepared by plasma-sprayed method were investigated [30]. Nanocomposite coatings Al_2O_3–ZrO_2 were prepared, which showed lower porosity and higher values for toughness and microhardness than those found for monophase coatings of Al_2O_3 or ZrO_2 [31,32]. At the same time, lower thermal conductivity was registered for Al_2O_3–ZrO_2 coatings than for Al_2O_3 samples [31].

Compared to Al_2O_3, the titanium dioxide TiO_2 is characterized by smaller brittleness and a number of favorable technological properties, therefore it is considered as a suitable oxide component applicable in the development of binary and more complex compositions. The effect of the introduction of TiO_2 to Al_2O_3-based oxide coatings on the microstructure and operational properties of the experimental samples has been analyzed [33].

The role of the composition and tribological behavior in the prepared coatings with a change in the TiO_2 content has been studied [34]. With Al_2O_3/TiO_2 coating, higher wear resistance was registered than that found with Al_2O_3 coating [35]. It has been established that the reinforcement with TiO_2 of the composite coating Al_2O_3–3%TiO_2 provides more favorable tribological properties than the reinforcement with zirconium dioxide ZrO_2 [36].

It has been proven that the Al_2O_3–40%TiO_2 coatings have a higher wear resistance than the Al_2O_3–13%TiO_2 oxide coatings. With an increase in the content of the introduced TiO_2 in the Al_2O_3–TiO_2 coatings, a decrease in porosity and the presence of cracks was found, and at the same time, an increase in tightness and the corrosion resistance [37]. At the Al_2O_3–40% TiO_2 coating, a higher microhardness was registered compared to that found at the substrate used [38].

In the ternary oxide system Al_2O_3–ZrO_2–TiO_2, a series of composite coatings and a comparative two-component sample were obtained. The effect of introducing 2 wt%, 6 wt% and 10 wt% TiO_2 to the composition of eutectic Al_2O_3-ZrO_2 (at 6:4 molar ratio) on the properties of the samples, microstructure and change in the phase composition was analyzed [29]. Composite powders (by spray granulation) were obtained from the prepared compositions, which were deposited on substrates by plasma spraying.

The presence of the crystalline phases t-ZrO_2, α-Al_2O_3, m-ZrO_2 and TiO_2 (in rutile form) was proven in the obtained composite powders. At the prepared composite coatings (Al_2O_3–ZrO_2–TiO_2) only the crystalline phases t-ZrO_2, α-Al_2O_3, γ-Al_2O_3 and amorphous phase were registered [29]. At the studied coatings, the diffraction peaks of TiO_2 were not observed, even in compositions with a content of 10 wt% TiO_2. Due to the specificity of the used technological approach and extremely high undercooling, an amorphous phase is formed in the obtained Al_2O_3-ZrO_2-TiO_2 coatings. It is assumed that a probable dissolution of TiO_2 in the amorphous phase or the formation of a solid solution together with γ-Al_2O_3 occurs during the cooling period [29].

With increasing TiO_2 content, a decrease in the porosity of the prepared Al_2O_3-ZrO_2-TiO_2 coatings was observed. At a concentration of 10 wt% TiO_2 (with Al_2O_3-ZrO_2-TiO_2 coating), a dense and uniform microstructure and higher values of adhesive strength, toughness and microhardness were found than those found for the comparative Al_2O_3-ZrO_2 coating. For an experimental sample with the composition Al_2O_3–ZrO_2–10wt%TiO_2, the adhesive strength of 25.38 MPa was registered, while for Al_2O_3–ZrO_2 coating, a value of 21.50 MPa was found [29]. It has been proven that the obtained three-component oxide coating Al_2O_3–ZrO_2–TiO_2 (with a content of 10 wt% TiO_2) has a lower friction coefficient and a lower wear rate compared to the studied two-component coating (Al_2O_3–ZrO_2). The established characteristics reduce the risk of various mechanical damage to the integrity of the coatings with a higher content of TiO_2.

At the same time, the development of innovative coatings based on modified compositions of the ZrO_2–TiO_2–Al_2O_3 system is of fundamental and applied interest.

The aim of the present work is to study the photoluminescence properties of Sm^{3+}-doped ZrO_2–TiO_2–Al_2O_3 coatings prepared in laboratory conditions. During the analysis and interpretation of the registered emission spectrum (recorded at different excitation wavelengths), experimental data on the structure and characteristics of the prepared experimental coatings were obtained.

2. Experimental Procedure

2.1. Reagents and Materials

Zirconium oxychloride octahydrate ($ZrOCl_2 \cdot 8H_2O$), samarium oxide (Sm_2O_3), alumina (Al_2O_3), titanium(IV) butoxide ($Ti(OBu)_4$), nitric acid (HNO_3), acetylacetone (AcAc), diethanolamine (DEA), ethanol (C_2H_5OH) and deionized water were used as received without further purification. Microscopic glass slides made of soda-lime glass were used as substrates.

2.2. Sol preparation and hydrolysis control

Multicomponent sols were prepared by the sol-gel method. Initially, 8.048 g $ZrOCl_2 \cdot 8H_2O$, 0.527 g Sm_2O_3 and 0.255 g Al_2O_3 were dissolved in ethanol with continuous stirring. Subsequently, 1.1 mL of titanium(IV) butoxide ($Ti(OBu)_4$) was added dropwise under vigorous stirring. Acetylacetone (AcAc) was used as a chelating agent to control the hydrolysis of the Ti(IV) particles.

After homogenization, hydrolysis of the mixed sol was initiated by adding 85 mL of ethanol, 65 mL of deionized water, 10 mL of nitric acid, and 2.5 mL of AcAc. The resulting sol was stirred for 30 min and then allowed to stand for 24 h at room temperature to ensure stabilization and completion of the sol-gel reactions.

The molar ratios of the precursors in the final solution were as follows:

- Zr : Ti = 27.3 : 1
- Zr : Sm = 43 : 1
- Zr : Al = 87 : 1
- $Ti(OBu)_4$: AcAc ≈ 1 : 1.7
- H_2O : (Zr + Ti) ≈ 16 : 1
- EtOH : (Zr + Ti) ≈ 72 : 1

2.3. Substrate cleaning

The glass substrates were ultrasonically cleaned sequentially in acetone, ethanol and deionized water, followed by air drying.

2.4. Dip coating

Before coating, the sol was filtered through a 0.45 μm PTFE membrane. Thin films were deposited on glass substrates using the dip technique at 25 °C and 40–50% relative humidity, with drawing speeds of 72.9 mm/min.

After each deposited layer, the coatings were dried at 100 °C for 10 min to remove residual solvent and promote partial gelation. Typically, 3–5 coating layers were applied to obtain films of the desired thickness.

2.5. Thermal treatment

The deposited films were thermally treated in air to obtain transparent multioxide coatings. The heating program consisted of a first stage to 300 °C at a heating rate of 1 °C/min with a holding time of 1 h, followed by additional heating to 450 °C at 2 °C/min

3. Results and Discussion

The emission spectrum of the ZrO_2–TiO_2–Al_2O_3–Sm_2O_3 coating was recorded at different excitation wavelengths. Under UV excitation (λ_{ex} = 354 nm), a broad emission band was observed in the region 370–550 nm with a maximum around 420–440 nm (fig.1).

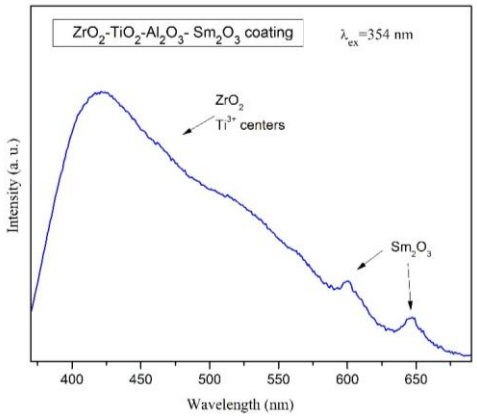


Figure 1. Emission spectrum of deposited ZrO_2 -TiO_2-Al_2O_3-Sm_2O_3 coating under 354 nm excitation.

Three kinds of different mechanisms have been proposed to explain ZrO_2 blue-green luminescence - an impurity luminescence center model, intrinsic self-trapped excitons and a structure-defect model. [P. Iacconi, D. Lapraz, R. Caruba: Phys. Status Solidi A 50, 275 (1978); M. Garc´ıa-Hipolito, R. Mart ´ ´ınez, O. Alvarez-Fregoso: J. Luminesc. 93, 9 (2001) ; V.A. Emeline, N. Serpone: Chem. Phys. Lett. 345, 105 (2001) 20 W.C. Hsieh, C.S. Su: J. Phys. D: Appl. Phys. 27, 1763 (1994); Liang J, Deng Z, Jiang X, Li F and Li Y 2002 Inorg. Chem. 41 3602]. At present, the generally accepted model is the structure-defect one, suggesting that the luminescence of ZrO_2 arises from oxygen-vacancy defects (F+ centers). Thus the observed broad band with a maximum around 420–440 nm can be associated with oxygen vacancies in ZrO_2 together with Ti^{3+} centers.

Sm^{3+} ions are characterized by narrow, sharp emission lines in the wavelength range 500 nm -750 nm, which are attributed to the characteristic intra-configuration f-transition of Sm^{3+} $^5G_{5/2} \rightarrow {}^7H_j$ where J = 5/2, 7/2, 9/2, 11/2. [W.T. Carnall, P.R. Fields, K. Rajnak J. Chem. Phys., 49 (1968), p. 4424; W.T. Carnall, G.L. Goodman, K. Rajnak, R.S. Rana J. Chem. Phys., 90 (1989), p. 3443]. Based on this, the observed weakly intense and narrower emission bands at 600 nm and 647 nm (fig1.) can be assigned to the $^5G_{5/2} \rightarrow {}^7H_{7/2}$ and $^5G_{5/2} \rightarrow {}^7H_{9/2}$ transitions of Sm^{3+} ions.

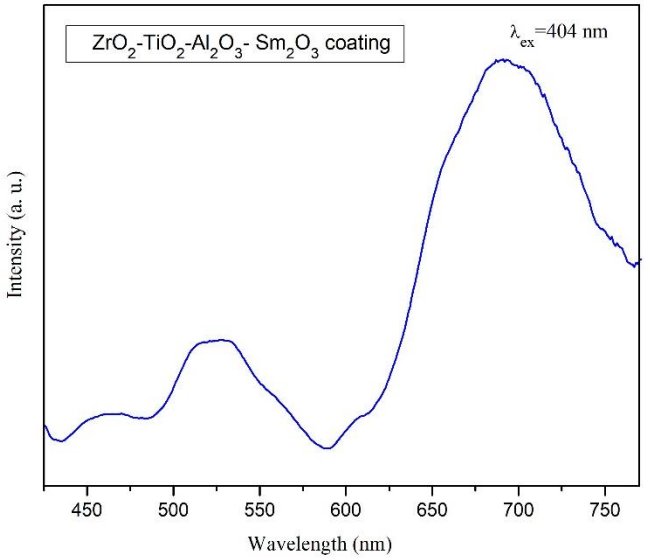


Figure 2. Emission spectrum of deposited ZrO_2 -TiO_2-Al_2O_3-Sm_2O_3 coating under 404 nm excitation.

When excited with 404 nm the spectral profile changes significantly. A broad emission in the region 500–750 nm is observed with a maximum around 680–710 nm, without clearly pronounced narrow lines characteristic of the 4f–4f transitions of Sm^{3+} . This indicates that under these conditions the emission is dominated by defect levels in the oxide coating.

It is clear that the direct luminescence of Sm^{3+} ions, which falls in the same region (680-710 nm), is strongly suppressed and does not dominate the observed emission.

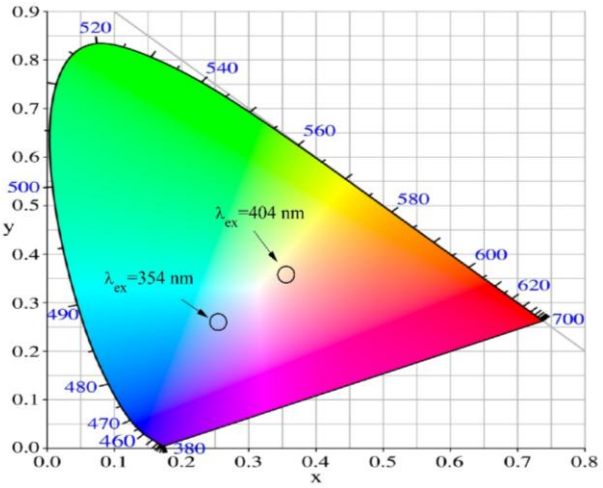


Figure 3. CIE chromaticity diagram of coatings under 354 nm and 404 wavelength of excitation.

In order to estimate the actual emitted color, the Commission International de l'Eclairage (CIE) 1931 chromaticity diagram was used [Smith, T.; Guild, J. The CIE colorimetric standards and their use. *Trans. Opt. Soc*. 1931, *33*, 73.]. The chromaticity coordinates

were calculated from the emission spectra by using color calculator software SpectraChroma (CIE coordinate calculator) [Paolini, T.B. SpectraChroma (Version 1.0.1) [Computer Software]. 2021. Available online: https://zenodo.org/records/4906590 (accessed on 7 June 2021).]. The values of the chromaticity coordinates of the coating excited under 354 nm correspond to the pale pink color of emission (0.252, 0.272) and under 404 nm has orange color of emission (0.353, 0.370).

The color purity of the synthesized samples can also be calculated via chromaticity coordinates of CIE 1931 diagram. The *following expression was used:*

$$Color\ purity = \frac{\sqrt{(x-xee)^2+(y-yee)^2}}{\sqrt{(xd-xee)^2+(yd-yee)^2}}.100\% \quad , \quad [book:$$

Schubert, E. F. (2006). Light-emitting diodes, Cambridge university press, p. 300]

where (*x*,*y*) represents the color coordinates of the synthesized glasses; (*xee, yee*) is the illuminant point of the 1931 CIE Standard Source C with color coordinates (0.3101, 0.3162); (*xd, yd*) are the chromaticity coordinates of the dominant wavelength point, which were obtained by extending the straight line between the point of (*x, y*) and the illuminant point (*xee*,*yee*) to the other side of the chromaticity diagram. Generally, it is accepted that 100 % is for pure color and 0% is for white light. The established values for the color purity of coatings excited by 354 nm wavelength is 26% and for 404 nm is 25%.

Discussion:

The lack of clearly defined linear emission peaks of the active Sm^{3+} ions, even under direct excitation around 404 nm, can be explained by competing non-radiative processes in the oxide coating, as well as by possible concentration quenching and strong interaction between Sm^{3+} ions and defect states of TiO_2/ZrO_2. The broad character of the observed emission is typical of defect-driven luminescence in amorphous or nanocrystalline oxide systems.

The obtained results show that the luminescent properties of the studied coating are determined mainly by the defective structure of the coating, creating prerequisites for further optimization of the composition and thermal treatment in order to activate the emission of rare earth ions.

4.Conclusion

Transparent Sm^{3+}-doped ZrO_2–TiO_2–Al_2O_3 coatings were successfully synthesized on glass substrates using a sol–gel dip-coating technique followed by thermal treatment. The applied synthesis approach enabled the formation of homogeneous multicomponent oxide films suitable for optical investigations.

Photoluminescence analysis revealed that the emission properties strongly depend on the excitation wavelength. Under UV excitation at 354 nm, a broad emission band centered at 420–440 nm was observed, which is mainly associated with oxygen-vacancy defects in ZrO_2 and Ti^{3+} centers. Weak emission lines at 600 nm and 647 nm correspond to the characteristic transitions of Sm^{3+} ions. When excited at 404 nm, the emission is dominated by defect-related luminescence in the oxide matrix.

Chromaticity analysis indicated pale pink emission under 354 nm excitation and orange emission under 404 nm excitation. The obtained results demonstrate that the luminescent behavior of the coatings is largely governed by defect states in the oxide structure. Such transparent luminescent coatings may be considered as promising materials for photonic applications and potentially for light management in photovoltaic devices.

5. References

1. T. A. Otitoju, P. U. Okoye, G. Chen, Y. Li, M. O. Okoye, S. Li, Advanced ceramic components: materials, fabrication, and applications, J. Industrial and Engineering Chemistry 85, 2020, pp. 34-65.

2. S. A. Kumar, B. A. Viswanath, P. Raghul, A review of preparation and characterization of sol-gel coating for corrosion mitigation, Int. J. Eng. Technol. Manag. Sci., **2** (8), 2024, pp. 11-24.

3. A. Knaislova´, D. Horkavcov´, E. Jablonska´, D. Vojtech, Sol-gel TiO_2-based coatings in 3D printed porous Ti-6Al-4V alloy structures as efficient antibacterial drug delivery systems: Thorough structural and biological characterization, Applied Surface Science Advances, 29, 2025, 100816.

4. S. Feliu Jr., F.R. García-Galvan, Corrosion and protection of metallic materials, Metals, 15, 346, 2025, pp. 1-8.

5. S. Li, J. Fu, Improvement in corrosion protection properties of TiO_2 coatings by chromium doping, Corros. Sci., 68, 2013, pp. 101-110.

6. M. K. Sahnesarayi, H. Sarpoolaky, S. Rastegari, Effect of heat treatment temperature on the performance of nano-TiO_2 coating in protecting 316L stainless steel against corrosion under UV illumination and dark conditions, Surf. Coat. Technol., 258, 2014, pp. 861-870.

7. X. Shan, L.Q. Wei, P. Liu, X.M. Zhang, W.X. Tang, P. Qian, Y. He, S.F. Ye, Influence of CoO glass-ceramic coating on the antioxidation behavior and thermal shock resistance of 200stainless steel at elevated temperture. Ceram Int., 40 (8), 2014,12327.

8. Kotlikov E. N., Lavrovskaya N. P., Tenev T. K., Milushev I. K., Aluminum oxide (Al_2O_3) optical films and their applications in the ultraviolet region of the spectrum. Journal of Optical Technology, 89, 12, 2022, DOI:10.1364/JOT.89.000752, 752-756.

9. B. C. Wyatt, S. K. Nemani, G. E. Hilmas, E. J. Opila, B. Anasori, Ultra-high temperature ceramics for extreme environments, Nat. Rev. Mat., 2023, pp. 1-17.

10. J. K. B. Balangao, Corrosion of metals: factors, types and prevention strategies. J. Chem. Health Risks, 14 (1), 2024, pp. 79-87.

11. I. P. Okokpujie, L. K. Tartibu, H. O. Musa-Basheer, Effect of coatings on mechanical, corrosion and tribological properties of industrial materials: a comprehensive review, J. Bio. Tribo Corros. 10, 2024, 2, https://doi.org/10.1007/s40735-023- 00805-1.

12. D. Barros, l. Vandenbulcke, Plasma assisted chemical vapor deposition process for depositing smooth diamond coatings on titanium alloys at moderate temperature, Diamond Relat. Mater. 9, 2000, 1862–1866,

13. Cai LF, Zhang YZ, Shi LK. Microstructure and formation mechanism of titanium matrix composites coating onTi-6Al-4 V by laser cladding. Rare Met.,26(4), 2027, 342.

14. L. Ceschini, E. Lanzoni, C. Martini, D. Prandstraller, G. Sambogna, Comparison of dry sliding friction and wear of Ti6Al4V alloy treated by plasma electrolytic oxidation and PVD coating, Wear 264 (1–2), 2008, 86–95,

15. G. Perumal, M. Geetha, R. Asokamani, N. Alagumurthi, A comparative study on the wear behaviour of Al_2O_3 and SiC coated Ti-6Al-4V alloy developed using plasma spraying technique, Trans. Ind. Inst. Met., 66, 2013, 109–115.

16. H. Li, Y.Z. Sun, J. Zhang, Effect of ZrO_2 particle on the performance of microarc-oxidation coatings on Ti6Al4V. Appl SurfSci., 342, 2015, 183.

17. Y. Wang, G. Darut, T. Poirier, J. Stella, H.L. Liao, M.P. Planche, Ultrasonic cavitation erosion of as-sprayed and laser-remeltedyttria stabilized zirconia coatings. J Eur Ceram Soc., 37(11), 2017, 3623.

18. Song J.B, Choi E, Oh SG, So J, Lee SS, Kim JT, Yun J.Y., Improved reliability of breakdown voltage measurement of yttrium oxide coatings by plasma spray. Ceram Int., 45(17), 2019, 22169.

19. Wang F, Luo GN, Huang JJ, Liu Y. Properties improvement of atmospheric plasma sprayed tungsten coating by annealing. SurfCoa Technol., 358, 2019, 276.

20. V. Ambardekar, P. P. Bandyopadhyay, S. B. Majumder, Hydrogensensing performance of atmospheric plasma sprayed tin dioxide coating. Int J Hydrogen Energ. 44(26), 2019, 14092.

21. H. D. Gao, Z. H. Wang, J. Shao, Manufacture and characteristics of Al_2O_3 composite coating on steel substrate by SHS process.Rare Met., 38(7), 2019, 704.

22. N. Kaczmarczyk, J. Szczurek, B. Babiarczuk, P. Gronowicz, M. Paszkowski, M. Kowalski, B. Borak, W. Jones, J. Detyna, J. Krzak, Thin flm quality of sol–gel SiO_2 coatings prepared on Ti6Al4V depending on their composition and titanium substrate preparation, J Mater Sci, 60, 2025, pp.13974–14004.

23. Sathish Sharma G, Sugavaneswaran M, Vijayalakshmi U, Prakash R. Influence of c-alumina coating on surface properties ofdirect metal laser sintered 316L stainless steel. Ceram Int. 2019;45(10):13456.
24. Kishida S, Ju DY, He H, Li Y. Coating of c-Al_2O_3 on thestainless steel substrate by electrophoretic deposition method.J Environ Soc Sci. 2009;21(1):S112.[14] Si TZ, Liu N, Zhang QA, You XQ. Thermal shock fatiguebehavior of TiC/Al_2O_3 composite ceramics. Rare Met. 2008;27(3):308.
25. K. P. Misra (ed), R. D. K. Misra (ed), Ceramic Science and Engineering: Basics to Recent Advancements (Elsevier Series in Advanced Ceramic Materials), Book, 1st Edition, Elsevier, 2022, 616.
26. N. Karwalo, Ceramic Engineering, Book, Discovery Publishing House, 2023, 200.
27. A. Sharma, A. Babbar, Y. Tian, B. P. Pathri, M. Gupta, R. Singh, Machining of ceramic materials: a state-of the-art review", Int. J. on Inter. Des. and Man. (IJIDeM), 17(6), 2023, pp. 2891-2911.
28. M. F. Zawrah, M. A. Taha, R. A. Youness, Advanced Ceramics: Stages of Development, In advanced ceramics., Springer Nature Switzerland, 2023.
29. Peng-Yue Gao, Yu-Duo Ma, Wen-Wei Sun, Yong Yang, Chen Zhang,Yu-Hang Cui, Yan-Wei Wang, Yan-Chun Dong, Microstructure and properties of Al_2O_3–ZrO_2–TiO_2 compositecoatings prepared by plasma spraying, Rare Met., 2021, 40(7), pp.1825–1834.
30. Limarga AM, Widjaja S, Yip TH. Mechanical properties andoxidation resistance of plasma-sprayed multilayered Al_2O_3/ZrO_2 thermal barrier coatings. Surf Coa Technol. 2005;197(1):93.
31. Ito A, You Y, Ichikawa T, Tsuda K, Goto T. Preparation ofAl_2O_3–ZrO_2 nanocomposite films by laser chemical vapourdeposition. J Eur Ceram Soc. 2014;34(1):155.
32. Chen YD, Yang Y, Chu ZH, Chen XG, Wang L, Liu Z, DongYC, Yan DR, Zhang JX, Kang ZL. Microstructure and properties of Al_2O_3–ZrO_2 composite coatings prepared by airplasma spraying. Appl Surf Sci. 2018;431, 193.
33. Toma FL, Stahr CC, Berger LM, Saaro S, Herrmann M, DeskaD, Michael G. Corrosion resistance of APS-and HVOF-sprayedcoatings in the Al_2O_3–TiO_2 system. J Therm Spray Technol.2010;19(1–2), 137.
34. Fervel V, Normand B, Coddet C. Tribological behavior ofplasma sprayed Al_2O_3-based cermet coatings. Wear. 1999; 230(1), 70.
35. Klyatskina E, Espinosa-Fernandez L, Darut G, Segovia F, Salvador MD, Montavon G, Agorges H. Sliding wear behavior of Al_2O_3–TiO_2 coatings fabricated by the suspension plasmaspraying technique. Tribol Lett. 2015;59(1):2.
36. Younes R, Bradai MA, Sadeddine A, Mouadji Y, Bilek A, Benabbas A. Effect of TiO_2 and ZrO_2 reinforcements on prop-erties of Al_2O_3 coatings fabricated by thermal flame spraying.Trans Nonferrous Met Soc China. 2016;26(5):1345.
37. Jia SK, Zou Y, Xu JY, Wang J, Yu L. Effect of TiO_2 content onproperties of Al_2O_3 thermal barrier coatings by plasma spraying.Trans Nonferrous Met Soc China. 2015;25(1), 175.
38. K. G. Girisha, K.V. Sreenivas Rao, C. Durga Prasad, Slurry erosionresistance of martenistic stainless steel with plasma sprayed Al_2O_3–40%TiO_2 coatings. Mater Today Proc., 5(2), 2018, 7388.

Modeling of Densification Kinetics during Electro-Pulse Consolidation of Titanium Powder

Olha Syzonenko, Mykola Prystash, Andrii Torpakov, Tetiana Makrukha
Institute of Pulse Processes and Technologies of NAS of Ukraine, Bohoyavlenskyi ave., 43-A, 54018, Mykolaiv, Ukraine
olgasizonenko43@gmail.com

Abstract *This study presents a theoretical investigation of the densification kinetics of titanium powder during electro-pulse consolidation. A mathematical model was developed to analyze the influence of electrical current parameters in different sintering regimes – direct current (DC), alternating current (AC), pulsed current, and their superposition – on the thermophysical processes governing sintering.*
The heating rates and the evolution of relative density were calculated for different applied pressing pressures. The results show that the superposition of currents is the most energy-efficient regime. This regime enables the material to reach a relative density above 99% within a minimal processing time. The effect is attributed to the combined action of intense Joule heating and the electroplastic effect.
KEYWORDS*: TITANIUM POWDER, ELECTRO-PULSE CONSOLIDATION, Ddensification KINETICS, JOULE HEATING, CURRENT SUPERPOSITION, SPARK PLASMA SINTERING.*

1. Introduction

The production of high-density materials from refractory metals, particularly titanium, while preserving their microstructure remains an important challenge in materials science. Conventional sintering methods require prolonged thermal exposure, which promotes grain growth and leads to degradation of physical and mechanical properties.

The use of Electric Current Assisted Sintering (ECAS) technologies is a promising approach to address these issues. These methods provide rapid powder densification due to intensive Joule heating and electroplastic effects.

The modern market offers various types of equipment for electroconsolidation. Spark plasma sintering (SPS) is the most widely used ECAS technique. It employs pulsed current (typically ~1 kHz). This approach is implemented in systems such as the Dr. Sinter SPS series (SPS Syntex Inc.) [1] and HP D systems (FCT Systeme GmbH) [2]. For studies focused on the influence of alternating current (AC), direct current (DC), and their combinations, physical simulation systems such as the Gleeble 3800 [3] are often used, as they allow flexible control of the current waveform. Some experimental setups, for example the Gefest-10 [4], enable the application of current superposition to achieve a synergistic densification effect.

Despite the availability of different equipment, direct experimental comparison of the efficiency of various current regimes (DC, AC, pulsed current, and superposition) for the same material is challenging. Differences in chamber design, thermal units, and tooling geometry in industrial systems prevent the creation of identical processing conditions required for rigorous analysis.

To address this limitation, a theoretical modeling approach to densification kinetics was adopted. This method eliminates the influence of equipment-specific design factors. Titanium powder was selected as the model material because its relatively high electrical resistivity makes it well suited for the analysis of electrothermal processes.

The aim of this study is to theoretically investigate and compare the densification kinetics of titanium powder under different current regimes and applied pressures in order to determine energy-efficient consolidation conditions.

2. Methodology

This study is based on a supervised machine learning methodology. The general scheme of the model represents a powder compact placed inside a die between two punches. To ensure the adequacy and physical consistency of the model, several key assumptions were adopted [6]:

1. The temperature field inside the sample is assumed to be spatially uniform at any given time. This assumption is justified for small specimens and high heating rates typical of the process.

2. The electrical resistance is calculated for the entire specimen volume and treated as a single equivalent resistive element.

3. Heat losses to the environment through the die and punches are neglected.

4. The densification kinetics are described using phenomenological equations. The model parameters are calibrated to qualitatively reproduce experimentally observed trends rather than to simulate micromechanical processes at the level of individual particle contacts.

Mathematical Description of the Model

The model is based on a system of coupled differential and algebraic equations that describe heat generation, thermal balance, and the kinetics of structural evolution in the powder compact.

Electrophysical Submodel and Calculation of Joule Heating

The primary energy source during the process is Joule heat generation. The instantaneous power of heat release, Q, W, is calculated according to the Joule–Lenz law [5]:

$$Q = I_{eff}^2 \cdot R(t), \tag{1}$$

where I_{eff} is the effective (root mean square, RMS) current (A), and $R(t)$ is the instantaneous electrical resistance of the sample (Ω).

An important feature of the proposed model is the inclusion of the dynamic change in the specimen height, $h_{current}(t)$, during densification. This variation is calculated according to the law of mass conservation:

$$h_{current}\,(t) = h_{initial}\,\cdot \frac{\rho_{rel,initial}}{\rho_{rel}\,(t)}. \tag{2}$$

The instantaneous electrical resistance, in turn, is a function of the specimen geometry and its effective electrical conductivity, σ_{eff}:

$$R(t) = \frac{h_{current}\,(t)}{\sigma_{eff}\,(t)\cdot A_{sample}}, \tag{3}$$

where

$$A_{sample}\, = \pi\left(\frac{d_{sample}}{2}\right)^2, \tag{4}$$

The effective electrical conductivity, σ_{eff}, of the powder compact is approximated by a linear relationship between the electrical conductivity of the fully dense material σ_{Ti} and the current relative density $\rho_{rel}(t)$.

$$\sigma_{eff}\,(t) = \sigma_{Fe}\cdot \rho_{rel}\,(t). \tag{5}$$

Evaluation of the Effective Current

A key aspect of the electrophysical submodel is the accurate calculation of the effective current, I_{eff}, for different signal types

(see Figure 1), since the RMS value determines the average power released over an oscillation period.

The model considers four main types of current namely direct current (DC), sinusoidal alternating current at 50 Hz (AC), pulsed current (~1 kHz), and a superposition of direct and pulsed current at ~50 kHz, characteristic to the Gefest-10 system.

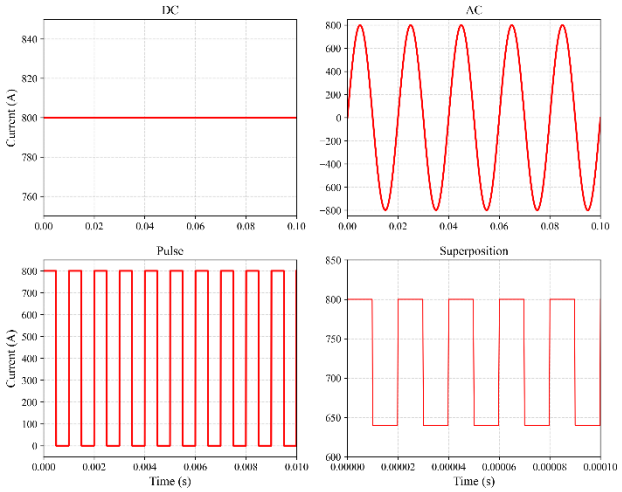


Figure 1: Considered current waveforms

The effective current, I_{eff}, for different waveform types was calculated as follows [7]:

Direct current :

$$I_{eff}^2 = I_{DC}^2. \tag{6}$$

Alternating sinusoidal current:

$$I_{eff}^2 = \left(\frac{I_{amp}}{\sqrt{2}}\right)^2 = \frac{I_{amp}^2}{2}. \tag{7}$$

Pulsed rectangular current with a duty cycle D = 0.5:

$$I_{eff}^2 = I_{amp}^2 \cdot D, \sigma_{eff}(t) = \sigma_{Fe} \cdot \rho_{rel}(t). \tag{8}$$

DC and AC superposition:

$$I_{eff}^2 = I_{DC,eff}^2 + I_{AC,eff}^2 = (0{,}8 \cdot I_{amp})^2 + \left(\frac{I_{amp}}{\sqrt{2}}\right)^2 = 0.66 \cdot I_{amp}^2). \tag{9}$$

The change in the average temperature of the sample, T, K, over time is described by the differential equation of thermal balance [8]:

$$m \cdot C_p \cdot \frac{dT}{dt} = Q_{eff}, \tag{10}$$

where m is the sample mass (kg), C_p is the specific heat capacity of the material (J/(kg·K)), T is the temperature (K), and Q_{eff} is the effective power of heat generation, W.

The averaged model does not account for the effects of increased contact resistance between particles and current concentration during the initial stages of sintering, which lead to significantly more intense heating. To compensate for this simplification, a phenomenological heating intensification factor, K_{heat}, is introduced. This factor increases the calculated Joule heating power during the heating stage ($T < T_{target}$):

$$Q_{eff} = Q \cdot K_{heat}. \tag{11}$$

In this work, the value of this factor was taken as K_{heat} = 2.5.

To adequately describe the evolution of the relative density (ρ_{rel}) and the microstructure of the sample over time, a phenomenological kinetic model based on the principle of superposition was considered. According to this principle, the overall densification rate is the sum of contributions from several simultaneously occurring mass transport mechanisms [9–10]:

Plastic deformation and creep – this mechanism dominates at relatively low temperatures and during the initial stages of densification. It is accounted for through a rate dependence on the current porosity ($1 - \rho_{rel}$)). The kinetic equation for this component is expressed as:

$$\left(\frac{d\rho_{rel}}{dt}\right)_{pl} = A_{pl} \cdot (1 - \rho_{rel}). \tag{12}$$

Here, the left-hand term represents the densification rate due to plastic mechanisms, and A_{pl} is an empirical coefficient characterizing the intensity of plastic flow and creep for the given material.

Thermally activated diffusion is the mechanism dominates at high temperatures and is responsible for the elimination of residual porosity during the intermediate and final stages of densification.

$$\left(\frac{d\rho_{rel}}{dt}\right)_{diff} = B_{diff} \cdot e^{\frac{-Q}{RT}} \cdot (1 - \rho_{rel}). \tag{13}$$

Here, the left-hand term represents the densification rate due to diffusion, B_{diff} is the pre-exponential factor, Q is the activation energy for diffusion of the material, R is the universal gas constant, and T is the absolute temperature.

The overall densification rate under standard conditions is the sum of the contributions from both mechanisms: plastic deformation/creep and thermally activated diffusion.

$$\left(\frac{d\rho_{rel}}{dt}\right)_{base} = \left(\frac{d\rho_{rel}}{dt}\right)_{pl} + \left(\frac{d\rho_{rel}}{dt}\right)_{diff} = A_{pl} \cdot (1 - \rho_{rel}) + B_{diff} \cdot e^{\frac{-Q}{RT}} \cdot (1 - \rho_{rel}). \tag{14}$$

This base densification rate is further modified by the effects of pressure and athermal current phenomena. The influence of pressure (P) is considered as a linear driving force normalized to a reference pressure, P_{ref}. Athermal effects (such as electromigration and electroplasticity) are accounted for using a dimensionless athermal activation factor, $K_{athermal,}$ which takes the following values: 1 for DC, 1.05 for AC, 1.2 for pulsed current, and 1.3 for current superposition [11].

The final equation for the densification rate used in the model is obtained by multiplying the base rate by these two factors.

$$\frac{d\rho_{rel}}{dt} = \left(\frac{d\rho_{rel}}{dt}\right)_{base} \cdot K_{athermal} \cdot \left(\frac{P}{P_{ref}}\right). \tag{15}$$

By substituting the expression for the base densification rate, the final equation is obtained, which incorporates all relevant physical effects: plastic deformation and creep, thermally activated diffusion, applied pressure, and athermal current effects.

$$\frac{d\rho_{rel}}{dt} = \left(A_{pl} \cdot (1 - \rho_{rel}) + +B_{diff} \cdot e^{\frac{-Q}{RT}} \cdot (1 - \rho_{rel})\right) \cdot K_{athermal} \cdot \left(\frac{P}{P_{ref}}\right). \tag{16}$$

The developed system of coupled differential equations is solved numerically using the explicit Euler method with a constant integration step of Δt = 0.1 s.

The following constants [12] and initial conditions were used in the calculations:

Table 1. Initial conditions of the model

Parameter	Symbol	Value	Unit
Titanium density	ρ_{Ti}	4500	kg/m³
Titanium specific heat	$C_{p,Ti}$	523	J/(kg·K)
Titanium electrical conductivity	σ_{Ti}	$2.38 \cdot 10^6$	S/m
Diffusion activation energy (Ti)	Q	$1.53 \cdot 10^5$	J/mol
Sample diameter	d_{sample}	0.01	m
Sample height	h_{sample}	0.01	m
Initial relative density	$\rho_{rel,0}$	0.6	–
Initial temperature	T_0	293.15	K
Target temperature (Ti)	T_{target}	1607.55	K
Integration step	Δt	0.1	s
Maximum simulation time	t_{max}	60	s
Plasticity coefficient	A_{pl}	$8.00 \cdot 10^{-5}$	s^{-1}
Diffusion coefficient	B_{diff}	$8.00 \cdot 10^4$	s^{-1}

For quantitative evaluation and comparison of the efficiency of different consolidation modes, a scatter plot was constructed showing "Total Energy Consumption versus Final Relative Density" [13–15].

The entire computational framework was implemented in the Python programming language using its standard scientific and engineering libraries.

3. Results and discussion

The simulations were performed by varying the current intensity at 400, 600, and 800 A, and the applied pressing pressure at 20, 35, and 50 MPa. The temperature regime was defined as reaching approximately $0.8 \cdot T_{melting} \approx 1300$ °C, followed by holding at this temperature until the maximum simulation time, t_{max}, was reached.

Based on the analysis of the obtained data, the heating rates for each consolidation regime were calculated (see Figure 2). At a current of 400 A, the heating rate was approximately 20 °C/s, regardless of the consolidation method. This is explained by insufficient power to reveal differences in thermal behavior at this energy level.

As the current increases, clear differentiation in heating efficiency is observed. At 600 A, the heating rate for samples processed with AC and pulsed current rises to about 30 °C/s, for the current superposition it reaches around 40 °C/s, while for DC it reaches approximately 60 °C/s. The most pronounced differences occur at 800 A: for AC and pulsed current, the heating rate increases to around 50 °C/s, for the current superposition to 70 °C/s, and for DC it reaches a maximum of approximately 120 °C/s.

This significant advantage of DC is attributed to the continuous generation of Joule heat, in contrast to AC or pulsed currents, where the effective power is reduced due to periodic zero crossings or pulse gaps. It is also noteworthy that the pressing pressure had little effect on the heating rate, indicating that volumetric heat generation dominates over contact resistance within the studied parameter range.

The presented densification curves for consolidation under direct current (see Figure 3) illustrate the nonlinear evolution of relative density, which can be divided into three characteristic stages:

1. An initial particle rearrangement stage with minimal density increase.

2. A stage of intensive plastic deformation and creep, where the densification rate reaches its maximum.

3. A final asymptotic stage corresponding to the closure of isolated pores.

At the maximum load (50 MPa) and a current of 800 A, the model predicts that the relative density reaches 0.99 by the 60th second of the process. In contrast, at 400 A and 20 MPa, the consolidation process is significantly prolonged.

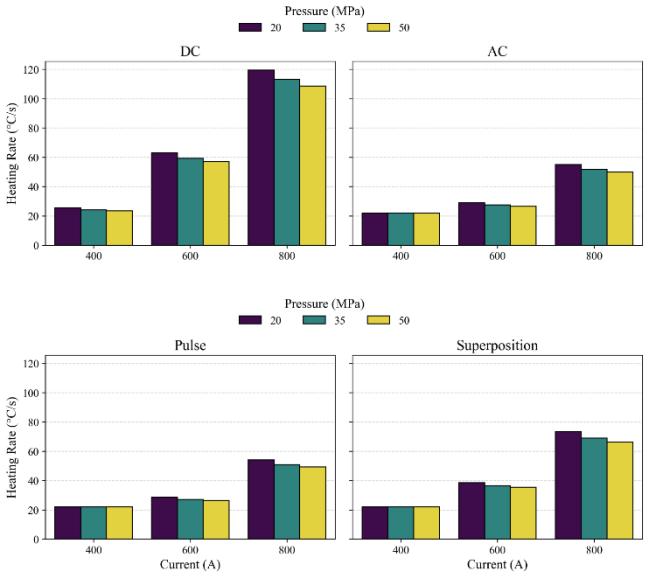


Figure 2: Comparative graphs of average heating rates

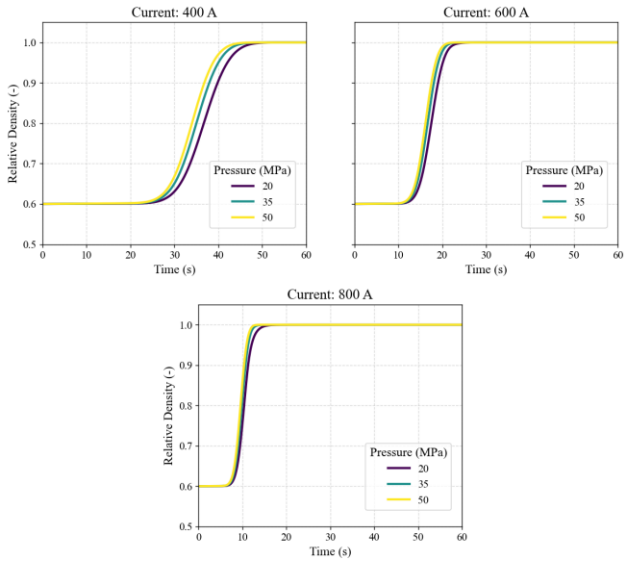


Figure 3: Evolution of the relative density of titanium powder during heating with direct current

The densification curves for alternating current (see Figure 4) show a delayed onset of intensive shrinkage compared to direct current of the same amplitude. However, due to the inclusion of the athermal activation factor, the densification rate during the active compaction stage is higher, allowing the relative density to reach 0.98–0.99 at 50 MPa. This indicates that the influence of the alternating field on the crystal lattice promotes more efficient stress relaxation.

Simulation results (see Figure 5) show that the pulsed current regime provides one of the fastest densification dynamics among the single-mode currents considered. The relative density curves exhibit a steep slope during the active sintering stage, which is

explained by the action of mechanisms such as surface oxide film removal and intensified mass transport under pulsed fields. This allows achieving a relative density of 0.99 in a shorter time than with direct current.

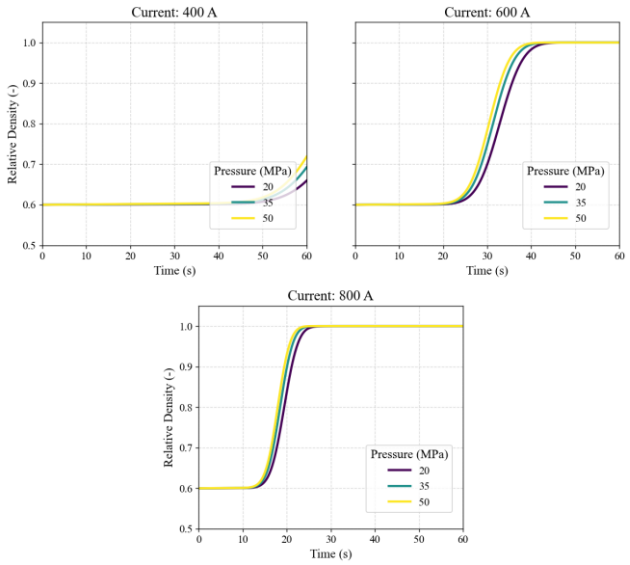


Figure 4: Evolution of the relative density of titanium powder during heating with alternating current

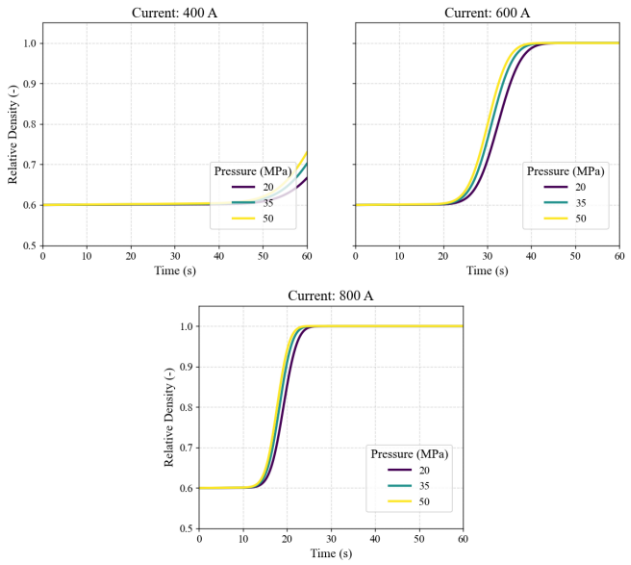


Figure 5: Evolution of the relative density of titanium powder during heating with pulsed current

The densification curves for current superposition (Figure 6) show a dynamics in which the consolidation process occurs almost immediately after reaching the threshold temperature. The high value of the athermal activation factor leads to a significant reduction of the material's yield limit (electroplastic effect), allowing the theoretical density (relative density > 0.995) to be achieved even under moderate external pressures. This makes this regime the most effective for producing high-density materials.

The derived "Total Energy Consumption – Final Relative Density" diagram (see Figure 7) clearly justifies the selection of the current superposition regime as the most promising. The points corresponding to this regime occupy the upper-left position on the graph, combining the highest achievable density (>0.995) with minimal total energy expenditure. These results indicate that high-quality densification can be achieved without increasing energy consumption.

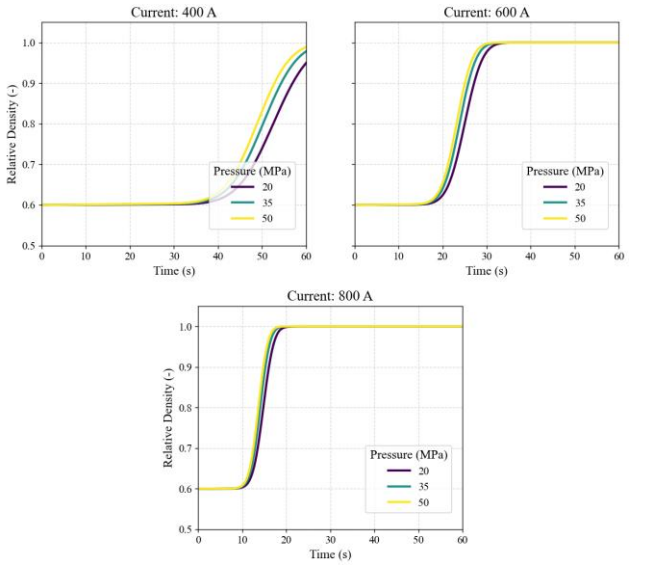


Figure 6: Evolution of the relative density of titanium powder during heating with current superposition

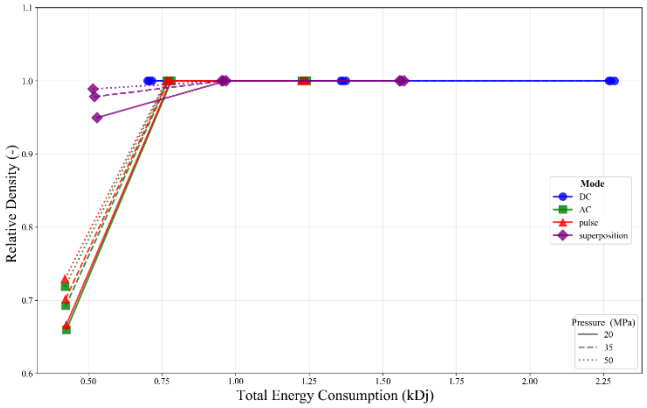


Figure 7: "Total Energy Consumption – Final Relative Density" diagram

For verification of the simulation results, titanium powder of PT-6 (TU U 14-10-026-98) (ПТ-6 ТУ У 14-10-026-98) grade with an average particle diameter of approximately 60 μm was consolidated using a superposition of direct and pulsed current at 50 kHz on the Gefest-10 system under conditions corresponding to the simulations: currents of 400, 600, and 800 A and pressing pressures of 20, 35, and 50 MPa. The temperature regime was set to reach approximately $0.8 \cdot T_{melting} \approx 1300$ °C, followed by holding at this temperature until t_{max}.

The temperature was monitored using a thermocouple on the surface of the die. Figure 8 shows the heating curve of the titanium powder, recalculated according to the die temperature using the heat exchange equations.

Figure 9 shows the actual densification curve obtained during the physical experiment. A comparative analysis with the simulated curve (see Figure 6) reveals an overall agreement in trends; however, the experimental curve exhibits a smoother initial stage, often referred to as the "incubation period."

This discrepancy can be attributed to several physical factors not fully accounted for in the model: the presence of oxide films on powder particle surfaces, which require time and energy for electrical breakdown; imperfect contacts between particles at the start of the process; and the thermal inertia of the tooling and

temperature sensors, which causes a delay in recording the onset of active densification.

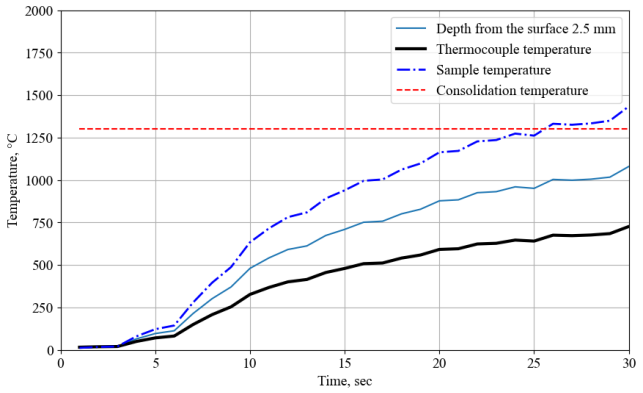


Figure 8: Heating curve of titanium powder under current superposition

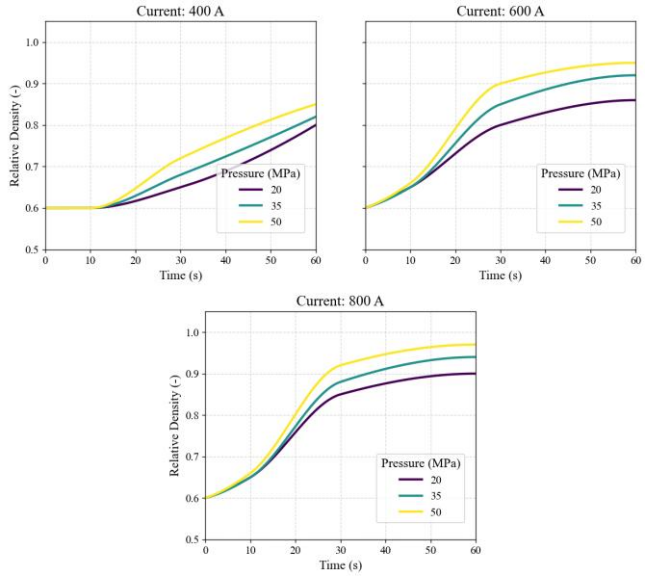


Figure 9: Experimental data of the specific density of titanium samples consolidated by current superposition versus consolidation time

4. Conclusions

1.It has been scientifically established that consolidation under direct current exhibits classical thermal kinetics, where the densification rate is linearly dependent on temperature. This regime is stable but requires a long time (over 150 s at 400 A) to achieve high density.

2.It was found that using 50 Hz alternating current introduces a cyclic loading effect, which enhances densification during the later stages of the process. However, the lower average heating rate compared to pulsed regimes limits its effectiveness at the initial stage of consolidation.

3.It has been theoretically shown that the pulsed regime (1 kHz) likely promotes effective particle surface cleaning and accelerated neck formation due to high peak current values and the presence of pauses, enabling faster achievement of high-density materials than with direct current.

4.A scientific hypothesis was proposed and justified based on simulation results regarding the synergistic effect of combining direct and alternating current components (50 kHz). This effect manifests as the highest heating rate and the activation of the electroplastic effect, allowing the theoretical density of the material to be reached in minimal time.

5.Analysis of the "energy–density" diagrams theoretically substantiates that the current superposition regime represents the technological optimum, as it uniquely combines the maximum physico-mechanical quality of the consolidated sample (relative density > 99.5%) with the lowest specific energy consumption, outperforming traditional methods.

6.Comparison of calculated and experimental data confirmed the adequacy of the developed model for predicting the final material properties. Observed deviations in the kinetics during the initial stage highlighted the influence of surface oxide films and contact resistances, which should be considered in further model refinements.

7.Based on the "Total Energy Consumption – Final Relative Density" analysis, the optimal titanium powder consolidation regime was identified: superposition of direct and alternating currents (50 kHz) with a total current of 600 A under a pressing pressure of 50 MPa. This regime achieves a relative density of 99.8% in less than 60 s, combining a high heating rate with intensified mass transport (characteristic of the AC component). Specific energy consumption is 15–20% lower compared to regimes achieving similar density purely via thermal effects, making this regime the most promising for industrial implementation.

5. References

1. Spark Plasma Sintering Systems. Dr. Sinter Lab Series : product catalog / SPS Syntex Inc. – Kawasaki, Japan, 2023. – 12 p.
2. Field Assisted Sintering Technology (FAST) / Spark Plasma Sintering (SPS) : systems specification / FCT Systeme GmbH. – Rauenstein, Germany, 2022. – 8 p.
3. Gleeble 3800 Physical Simulation System : user guide / Dynamic Systems Inc. – Poestenkill, NY, USA, 2019. – 45 p.
4. O. Syzonenko, M. Prystash, A. Zaichenko, O. Kovalenko, Materials Science. Non-Equilibrium Phase Transformations. 4(2), 41–44 (2018).
5. Halliday, D., Resnick, R., & Walker, J. (2013). Fundamentals of Physics. 10th Edition. Wiley.
6. Olevsky, E. A. (1998). Theory of sintering: from particular models to continuum theory. Materials Science and Engineering: R: Reports, 23(2), 41-100. (У статті розглядаються різні моделі для ефективних властивостей пористих тіл).
7. Nilsson, J. W., & Riedel, S. A. (2015). Electric Circuits. 10th Edition. Pearson.
8. Incropera, F. P., DeWitt, D. P., Bergman, T. L., & Lavine, A. S. (2007). Fundamentals of Heat and Mass Transfer. 6th Edition. Wiley.
9. German, R. M. (2014). Sintering: From Empirical Observations to Scientific Principles. 2nd Edition. Butterworth-Heinemann.
10. Atkins, P., & de Paula, J. (2014). Atkins' Physical Chemistry. 10th Edition. Oxford University Press.
11. Orrù, R., Licheri, R., Locci, A. M., Cincotti, A., & Cao, G. (2009). Consolidation/synthesis of materials by electric current activated/assisted sintering. Materials Science and Engineering: R: Reports, 63(4-6), 127-287.
12. ASM Handbook, Volume 2: Properties and Selection: Nonferrous Alloys and Special-Purpose Materials. (1990). ASM International.
13. Incropera, F. P., DeWitt, D. P., Bergman, T. L., & Lavine, A. S. (2007). Fundamentals of Heat and Mass Transfer. 6th Edition. Wiley.
14. Munir, Z. A., Anselmi-Tamburini, U., & Ohyanagi, M. (2006). The effect of electric field and pressure on the synthesis and consolidation of materials: A review of the spark plasma sintering method. Journal of Materials Science, 41(3), 763–777.
15. Grasso, S., Sakka, Y., & Maizza, G. (2009). Electric current activated/assisted sintering (ECAS): a review of patents 1906–2008. Science and Technology of Advanced Materials, 10(5), 053001.

Acknowledgements

Authors would like to express gratitude to the Armed Forces of Ukraine for their bravery which made this work possible even in the dark times of war.

Preparation and Optical Properties of Gelatin-SiO_2 Hybrid Coatings on Glasses for Photovoltaic Applications

Stancho Yordanov[1]*, Tatyana Ivanova[2], Shaban Uzun[1], Vladimir Petkov[1], Ina Gospodinova[1]
[1] Bulgarian Academy of Sciences, Institute of Metal Science, Equipment, and Technologies "Acad. A. Balevski" with Center for Hydro- and Aerodynamics, 67 "Shipchenski prohod" str., 1574 Sofia, Bulgaria
[2] Bulgarian Academy of Sciences, Central Laboratory of Solar Energy and New Energy Sources, Sofia, Bulgaria
e-mail: stancho14@abv.bg

Abstract: *In this study, gelatin-SiO_2 hybrid coatings were prepared on glass substrates using an acid-catalyzed sol-gel method. The deposited layers were subjected to thermal treatment at 50°C, 150°C, and 250°C to evaluate the effect of temperature on their structure and optical properties. Spectroscopic investigations in the UV-VIS-NIR range show that the hybrid coatings enhance optical transmittance and reduce reflective losses compared to uncoated glass. The best optical performance was observed for the sample thermally treated at 150 °C (GS 150), where an optimal balance between the organic (gelatin) and inorganic (SiO_2) phases was achieved, resulting in maximum transmittance and minimal light reflection. At lower treatment temperatures (50°C), the coating exhibited higher porosity but lower structural stability, whereas at higher temperatures (250°C), partial thermal degradation of the gelatin phase led to layer densification and a slight reduction in the antireflective effect. These results demonstrate that gelatin can be successfully used as a biopolymer component to control the microstructure and optical properties of sol-gel hybrid coatings. Improving optical transmittance and reducing reflective losses of glass surfaces is crucial for enhancing photovoltaic module efficiency, as it allows a greater amount of solar radiation to reach the active layer of solar cells.*

Keywords*: GELATIN-SIO_2 HYBRID, SOL-GEL METHOD, OPTICAL PROPERTIES, ANTIREFLECTIVE COATINGS*

1. Introduction

Photovoltaic (PV) systems are among the fastest-growing renewable energy sources and play a key role in the transition to sustainable energy technologies. The efficiency of photovoltaic panels depends not only on the characteristics of the semiconductor materials but also on the optical properties of the protective glass covering the active layer. Glass serves as mechanical and environmental protection but can cause optical losses due to light reflection at the air-glass interface. For standard glass, reflective losses can reach approximately 4 % per surface, reducing the amount of light reaching the photovoltaic cell and, consequently, lowering the module's energy efficiency [1, 2].

One of the most effective approaches to reduce these losses is the application of antireflective (AR) coatings on the glass surface. Such coatings are designed so that their effective refractive index lies between that of air and glass, allowing a reduction in reflection and an increase in light transmittance to the active layer of the photovoltaic cell [1]. In addition to optical performance, coatings for photovoltaic applications must have high transparency over a wide spectral range (UV-VIS-NIR), good mechanical stability, resistance to environmental conditions, and often self-cleaning properties that reduce dust and contamination accumulation on the panel surface [3].

Among the various methods for producing such functional coatings, the sol-gel technique is considered one of the most promising approaches. This low-temperature process allows the synthesis of inorganic and hybrid materials with controlled microstructure and optical properties [4,5]. The sol-gel method is compatible with industrial coating techniques for large surfaces, such as dip-coating, spin-coating, and spray-coating, making it particularly suitable for photovoltaic panel applications [6].

Silicon dioxide (SiO_2) is one of the most commonly used materials for sol-gel optical coatings due to its high transparency, chemical stability, and good adhesion to glass substrates. By controlling the porosity of the silica network, the effective refractive index of the coating can be tuned, enabling the formation of low-refractive-index layers with strong antireflective behavior [7]. Porous silica coatings with very low refractive indices ($n \approx 1.18$) have been reported, while maintaining nearly 100 % transmittance at certain wavelengths [8]. Furthermore, multilayer sol-gel silica coatings can provide broadband antireflective performance with transmittance above 98 % in the 350-1400 nm spectral range [9].

Despite these advantages, purely inorganic sol-gel silica films may exhibit limitations, such as cracking, internal stress, and limited mechanical durability during operation. One approach to overcome these issues is the development of organic-inorganic hybrid materials, where the organic component is integrated into the inorganic silica network. Such hybrid systems combine the mechanical and chemical stability of the silica phase with the flexibility and film-forming properties of the organic components [10, 11].

Biopolymers are an especially interesting class of organic additives for producing such hybrid coatings. Gelatin, obtained by partial hydrolysis of collagen, is widely used due to its biocompatibility, biodegradability, and excellent film-forming properties. The presence of functional groups such as amino (-NH_2), carboxyl (-COOH), and hydroxyl (-OH) allows interaction with hydrolyzed silicate species and participation in the formation of organic-inorganic hybrid structures [12]. Moreover, gelatin can influence the viscosity of the sol system, hydrolysis and condensation kinetics, and thin-film formation, facilitating the preparation of uniform coatings [13].

Previous studies have shown that silica-gelatin hybrid materials can form transparent coatings on glass substrates. For instance, Smitha et al. reported transparent SiO_2-gelatin coatings with a thickness of about 300 nm and optical transparency above 90 % [14]. Other studies have obtained silica-gelatin nanohybrid coatings with nearly 100 % optical transmittance, indicating that proper control of nanostructure and component dispersion can preserve high optical transparency [15].

Despite these promising results, the relationship between synthesis conditions, hybrid network structure, and optical properties of gelatin-SiO_2 coatings on glass is not yet fully understood. The optical characteristics of these materials depend on several factors, including porosity, film uniformity, particle size, and the degree of interaction between the organic and inorganic phases [16].

Therefore, the aim of this work is to prepare gelatin-SiO_2 hybrid coatings on glass substrates using the sol-gel method and to investigate their optical properties through UV-Vis spectroscopy. Particular attention is paid to the influence of synthesis parameters and thermal treatment on the transparency and antireflective performance of the coatings, with a view to their potential application in photovoltaic panels.

2. Experimental procedure

The gelatin-SiO_2 hybrid coatings were prepared via an acid-catalyzed sol-gel process using tetraethyl orthosilicate (TEOS, ≥98%), absolute ethanol, 0.1 M HCl, distilled water, and commercial gelatin, all used without further purification. Standard soda-lime glass slides were used as substrates.

The initial silica sol was prepared by mixing 19 mL TEOS (17.73 g, 0.085 mol), 30 mL ethanol (23.67 g, 0.514 mol), 2.7 mL water (2.70 g, 0.150 mol), and 0.5 mL of 0.1 M HCl. The resulting initial molar ratio of TEOS:H_2O:EtOH was 1:1.76:6.05. In a separate vessel, 2 g of gelatin was dissolved in 60 mL of distilled water at 45 °C under magnetic stirring until fully dissolved. The gelatin solution, containing an additional 60 g water (3.33 mol H_2O), was slowly added to the silica sol under continuous stirring. After addition, the total water content reached 62.7 g (3.48 mol), resulting in a final molar ratio of TEOS:H_2O:EtOH = 1:40.9:6.05 and a hydrolysis ratio R ≈ 41, characteristic of highly hydrolyzed silica systems.

For a more complete description of the composition, all components were also calculated in mass percentages. The final sol contained 59.1 wt% water, 22.3 wt% ethanol, 16.7 wt% TEOS, and 1.9 wt% gelatin. This high water fraction facilitates complete hydrolysis of TEOS and the formation of a hydroxyl-rich Si-O-Si network capable of interacting with the functional groups of gelatin. The resulting sol was stirred for 60 min and left to rest for 24 h at room temperature to stabilize the hydrolysis-condensation processes.

The glass substrates were cleaned ultrasonically in sequence with ethanol and distilled water and then dried at 100 °C. The coatings were applied via dip coating at a withdrawal speed of 72.9 mm/min under ambient conditions. After deposition, the films were allowed to dry for 2 h at 25°C and subsequently thermally treated in air at 50°C (GS 50), 150°C (GS 150), and 250°C (GS 250). These temperatures were selected to investigate the effect of partial or complete degradation of the organic phase on the optical properties and microstructure of the hybrid layers.

The optical properties of the coatings were examined using UV-VIS-NIR spectroscopy in the 300-1100 nm range in both transmittance and reflectance modes. Uncoated glass was used as a reference sample, allowing direct comparison of the effect of the hybrid layer on optical behavior.

3. Results and Discussion

The transmittance spectra of the hybrid coatings, measured with a Shimadzu UV 3600 UV-VIS-NIR spectrophotometer in the 240-1800 nm range, show a pronounced increase in optical transparency compared to uncoated glass. The spectra were recorded relative to air, with the spectrum of bare glass used as a reference. All samples exhibit higher transmittance in the 400-800 nm range, which can be attributed to the formation of a low-refractive-index porous silica layer modified by the organic gelatin phase. The highest transmittance is observed for the GS 150 sample, indicating optimal structuring of the SiO_2 network at this thermal treatment temperature. At 250°C, partial degradation of the gelatin leads to densification of the layer and a slight increase in the refractive index, reducing the antireflective effect (Figures 1, 2, 3, and 4).

Reflectance spectra, measured using an aluminum mirror as the reference standard, confirm a reduction in surface reflection for all hybrid coatings. The minimum reflectance is observed for the GS 150 sample, corresponding to the best match of the effective refractive index between air and the glass substrate. The reduced reflection indicates the presence of nanometer-scale porosity in the hybrid SiO_2 structure, induced by the organic component. At higher temperature (250°C), partial breakdown of the organic matrix results in a denser structure and, consequently, a slight increase in reflectance.

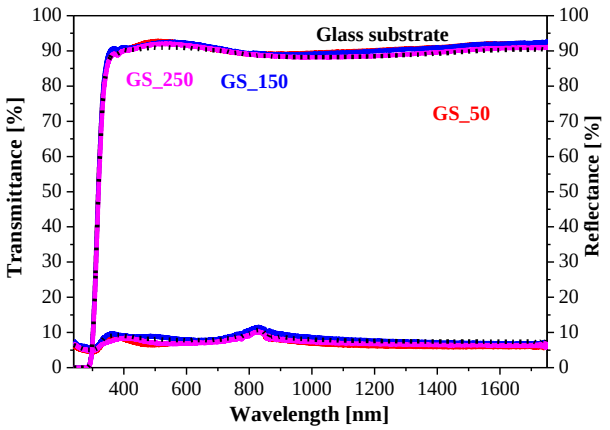


Figure 1. Transmittance and reflectance of gelatin-SiO_2 coatings after thermal treatment at 50°C, 150°C and 250°C in the region 240-1800 nm range.

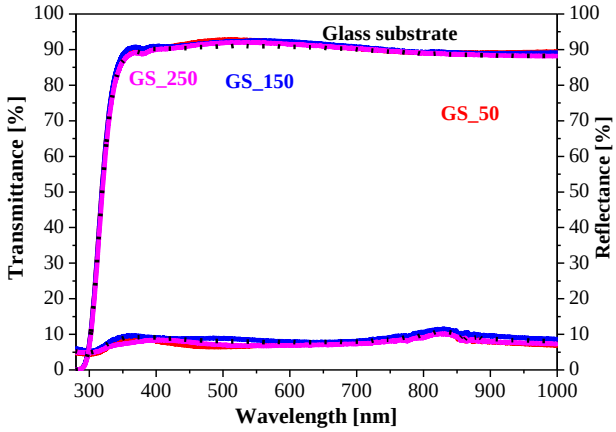


Figure 2. UV-VIS-NIR transmittance and reflectance of gelatin-SiO_2 coatings after thermal treatment at 50°C, 150°C and 250°C in the 240–1000 nm spectral range

The spectra are recorded against air, with bare glass used as reference. The GS 150 sample shows the highest transmittance due to optimal stabilization of the hybrid silica network.

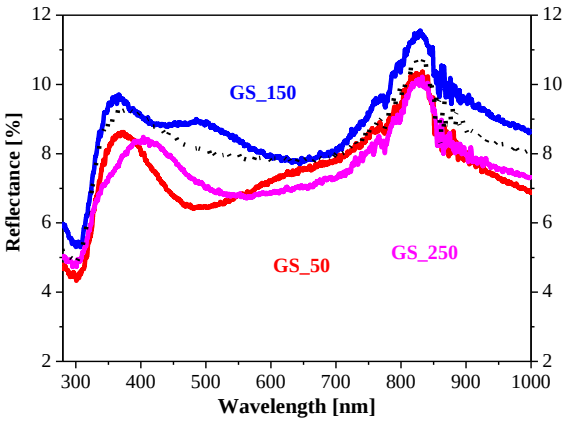


Figure 3. Reflectance in the range 2–12 % of gelatin-SiO_2 coatings after thermal treatment at 50°c, 150°c and 250°c in the region 240-1800 nm range.

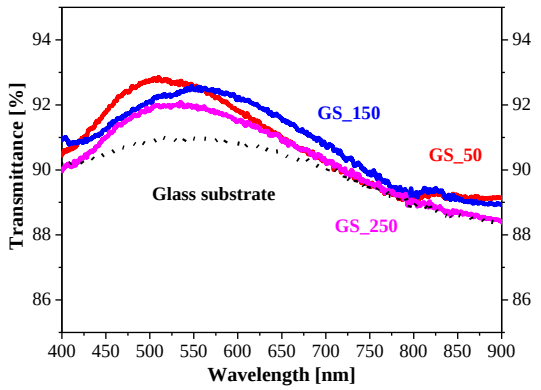


Figure 4. Transmittance in the range 86–94 % of gelatin-SiO_2 coatings after thermal treatment at 50°C, 150°C and 250°C in the region 240-1800 nm range.

Figure Summary

- GS 50: High organic phase → higher porosity, but lower structural stability.
- GS 150: Optimal balance between organic and inorganic phases → highest transmittance and lowest reflectance.
- GS 250: Partial gelatin degradation → densification of the layer, higher refractive index, reduced antireflective effect.

The results clearly demonstrate the influence of thermal treatment on the structure and optical properties of gelatin-SiO_2 hybrid coatings. At low temperature (50°C), the high organic content leads to increased porosity and lower structural stability, resulting in slightly reduced transmittance and higher reflectance. The optimal performance is observed for GS 150, where the interaction between gelatin and the SiO_2 network promotes the formation of a compact yet porous structure, which minimizes surface reflection and maximizes transmittance. This indicates that the organic phase not only facilitates the formation of a porous network but also stabilizes the hybrid structure, enhancing the optical properties.

At 250°C, partial degradation of gelatin results in densification of the layer, an increase in refractive index, and a slight rise in reflectance, confirming the role of the organic component in controlling porosity and the antireflective effect. These observations are consistent with previous studies on SiO_2-organic hybrid systems, where the balance between the organic and inorganic phases determines the optical characteristics and mechanical stability [9, 11].

Overall, the results demonstrate that by precisely controlling the thermal treatment temperature and sol composition, functional coatings with tailored optical properties can be obtained, suitable for applications such as antireflective layers on glass and potentially for photovoltaic panels.

4. Conclusion

1. Gelatin can be effectively integrated into the SiO_2 sol-gel network, providing structural adaptability and control over the porosity of the layer.
2. Gelatin-SiO_2 hybrid coatings exhibit enhanced transparency and reduced reflectance compared to uncoated glass, with optimal optical properties achieved at a thermal treatment of 150°C.
3. At lower temperature (50°C), the layer is porous but structurally less stable, whereas at higher temperature (250°C), partial gelatin degradation leads to densification and a slight reduction in the antireflective effect.
4. The results highlight the potential of gelatin-SiO_2 hybrid coatings for applications requiring transparent, antireflective, and functional glass layers, such as optical devices and photovoltaic panels.

References

1. Macleod, H. A. Thin-Film Optical Filters, CRC Press, 2010.
2. Green, M. A. Solar Cells: Operating Principles, Technology and System Applications, Prentice Hall, 1982.
3. Saravanan, S. et al. Optical investigation of sol-gel synthesized SiO_2/TiO_2 multilayers for antireflective coatings, Nanomaterials, 13 (2023) 389.
4. Brinker, C. J., Scherer, G. W. Sol-Gel Science: The Physics and Chemistry of Sol-Gel Processing, Academic Press, 1990.
5. Hench, L. L., West, J. K. The sol-gel process, Chemical Reviews, 90 (1990) 33-72.
6. Lu, S., Shao, J., Wu, F. Industrial applications of sol-gel derived coatings, Journal of Sol-Gel Science and Technology, 114 (2025) 87-97.
7. Guglielmi, M. Sol-gel coatings on metals, Journal of Sol-Gel Science and Technology, 1 (1990) 7-25.
8. Ye, L. et al. Ammonia treatment of sol-gel silica coatings to achieve a stable low refractive index, Ceramics International, 51 (2025) 25192-25197.
9. Chi, F., Zeng, Y., Liu, C. Tuning refractive indices of sol-gel silica coatings by ammonia treatment for broadband antireflection applications, Optik, 224 (2020) 165501.
10. Sanchez, C. et al. Applications of advanced hybrid organic-inorganic nanomaterials, Chemical Society Reviews, 40/2 (2011) 696-753.
11. Zvonkina, I. J., Soucek, M. D. Inorganic-organic hybrid coatings: common and new approaches, Current Opinion in Chemical Engineering, 11 (2016) 123-127.
12. Ramos, M. et al. Gelatin-based films and coatings for food packaging applications, Coatings, 6/4 (2016) 41.
13. Jitianu, A. et al. Hybrid silica-gelatin materials obtained by sol-gel method, Journal of Non-Crystalline Solids, 345-346 (2004) 596-600.
14. Smitha, S. et al. Silica-gelatin bio-hybrid and transparent nano-coatings through sol-gel technique, Materials Chemistry and Physics, 103 (2007) 318-322.
15. Smitha, S. et al. Antiwetting silica-gelatin nanohybrid coatings synthesised through an aqueous sol-gel process, Journal of Sol-Gel Science and Technology, 42 (2007) 157-163.
16. Xia, B. et al. Preparation of silica coatings with adjustable refractive indices via sol-gel method. *RSC* Advances, 8 (2018) 6091-6098.

Investigation of leak rate through a profile expanded polytetrafluoroethylene gasket

Изследване интензивността на изтичане през профилно уплътнение от експандиран политетрафлуоретилен

Евлоги Младенов
АВКО АД, гр.София, ул. Панорамен път 38А, България, quality@avko.bg
Evlogi Mladenov, AVKO JSC, 1616 Sofia, 38A Panoramen pat Str.,Bulgaria, quality@avko.bg

Abstract: This article reviews flat gaskets made of expanded polytetrafluoroethylene (ePTFE), used in industries for sealing flange joints, which prevent the mixing of working fluids and their leakage into the environment. ePTFE gaskets and solutions for improving tightness with profiled gaskets are considered. Using test equipment to measure the mass of the test gas passing through the gasket per unit time, which is one of the main operational characteristics of the gasket, a comparison of the necessary gasket stress during installation to achieve the same leakage rate. A profiled ePTFE gasket with a thickness of over 10 mm is presented. Comparative tests were conducted to determine the mass of helium gas passing through the gaskets with an integrated ring in a profiled gasket. The results of the tests conducted show an improvement in the sealing ability of the profile seal and reduction in the mass of the passing gas with the application of a lower gasket stress on the seal.

Keyword: *ePTFE(expanded polytetrafluoroethylene), Flat gasket, Leak test, Gasket stress, Leak rate*

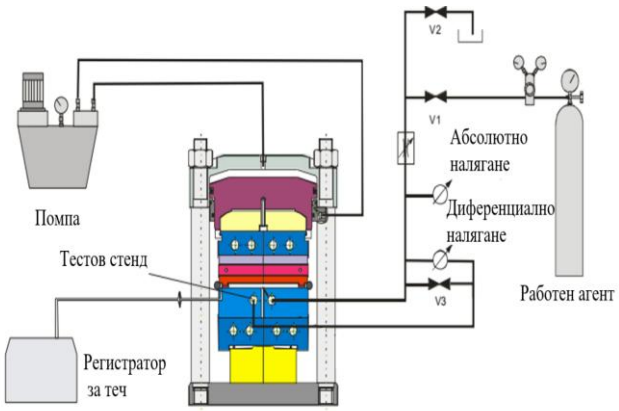
1. Въведение

Известен с добрата си химическа устойчивост и криогенен температурен диапазон, експандираният политетрафлуороетилен (еПТФЕ) се използва като уплътнителен материал в химическата, енергийната, рафинерийната, нефтената, хранително-вкусовата, водоснабдяване , фармацевтичната и други индустрии под формата на лента или плоско уплътнение. Порьозната структурата изградена от взаимосвързани възли и фибрили е определяща за намалената плътност и повишена свиваемост [1, 2]. Това обуславя способността на еПТФЕ уплътненията да компенсират несъвършенства и повреди на уплътнителните повърхности на фланците, които възникват по време на работа на оборудването. еПТФЕ уплътненията са приложими за инсталации както с масивни така и с тънки стоманени фланци дори и с крехки фланци, като пластмаса и стъкло[3], но за да се постигне уплътняване е необходимо прилагане на по-ниско контактно напрежение върху уплътнението и повишено внимание по време на монтаж. Постигане на уплътняване с намалено напрежение действащо на уплътнението и постигане на висок клас на херметичност разширява приложението на уплътненията в индустрии, където са въведени изисквания за допустими нива на изтичане в атмосферата. Изпитванията за херметичност се провеждат при стайна температура, но съществуват и тестови процедури за провеждане при повишени температури [4]. Характеристиките на уплътненията са стандартизирани, но все още има различия между Европа и Америка [5]. Съществуват еПТФЕ уплътнения с дифузионна бариера [6], с редуващи се слоеве с ниска и висока плътност [7], с локално повишена плътност [8], при изследването, на които е установено намаляване на количеството газ, преминаващ през уплътнението, когато увеличената плътност е в областта на вътрешния диаметър.

Целта на настоящото изследване е да се изследва ефектът при вграждане на еластомер извън зоната на вътрешния диаметър контактуващ с флуида в разработено профилно еПТФЕ уплътнение с дебелина над 10 mm върху интензивността на изтичане.

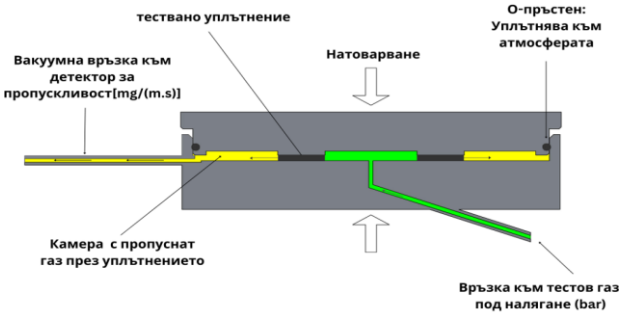
2. Методология на експеримента

За измерване на интензивността на изтичане е използвана многофункционална тестова апаратура "TEMES fl.ai1""[9], представляваща серво-хидравлична преса фиг.1 със софтуер изпълняващ алгоритъма на теста, контролиращ ефективното повърхностно напрежение на уплътнението, подаващ тестов газ под налягане и отчитащ масата на газа, преминал през уплътнението чрез хелиев масспектрометър отчитащ изтичане до 1.10^{-10} mg/(s. m), [10, 11]. Като за изпитвателен газ е използван хелий 4.6 с чистота 99,996%. Данните и резултатите се събират чрез компютър.



Фиг. 1. *Тестова апаратура "TEMES fl.ai1"[9]*

Тестовия стенд се състои от хидравлично бутало към което е закрепена горната подвижна плоча, долна неподвижна плоча, тензодатчик и датчици за преместване. Силата действаща върху уплътнителя се измерва чрез тензодатчика за натоварване монтиран в долната част на установката, а преместването/ деформацията чрез три датчика за преместване разположени през 120° един от друг, като отчитат преместването на горното бутало с точност 0,001 mm. При стартиране на теста горната тестова плоча закрепена към хидравличното бутало се придвижва, затваря камерата и уплътнението се изолира от атмосферата фиг.2.



Фиг. 2. *Херметична камера*

Уплътнението се центрира в долната неподвижна тестова плоча, фиг.3. След затваряне на камерата и осигуряване на повърхностно напрежение върху уплътнението, се подава тестов газ хелий под налягане и чрез детектор за изтичане се отчета количеството преминал газ през уплътнението.



Фиг. 3. *Тестови плочи с поставен уплътнител*

Класовете на херметичност L_N са определени в таблица 1 под формата на специфична интензивност на изтичане. При отчетено изтичане през уплътнението до 1 mg/(s.m) класа на херметичност е L_1 и намалява с понижаване на изтичането. Тестовете се провеждат съгласно стандарт БДС EN 13555 [13]. Стандартът определя характеристиките на уплътненията и предоставя процедурите за изпитване и установяване на стойностите им.

Таблица 1. *Класове на херметичност L_N .*

Клас на херметичност	L_1	L_0	$L_{0,01}$	$L_{0,001}$	$L_{0,0001}$	$L_{0,00001}$
Специфична интензивност на изтичане, mg/(s.m)	≤ 1,0	≤ 0,1	≤ 0,01	≤ 0,001	≤ 0,0001	≤ 0,00001

Специфична интензивност на изтичане се определя, като измереното количество преминал газ в mg за една секунда се раздели на средно аритметичната дължина от вътрешната и външната обиколка на запресованата/ натисната уплътняваща повърхност в метри, π /2 (D + d), където D и d са външен и вътрешен диаметър на запресованата част на уплътнителя.

Показателят $Q_{min(L)}$ представлява необходимо минимално контактно напрежение приложено на уплътнението при монтаж при стайна температура, за да се постигне желания клас на херметичност L за даденото вътрешно налягане.

Показателят $Q_{Smin(L)}$ е необходимо минимално контактно напрежение действащо на уплътнението при работни условия, т.е. след разтоварване в експлоатация при работна температура, за да се запази необходимият клас на херметичност L при даденото вътрешно налягане.

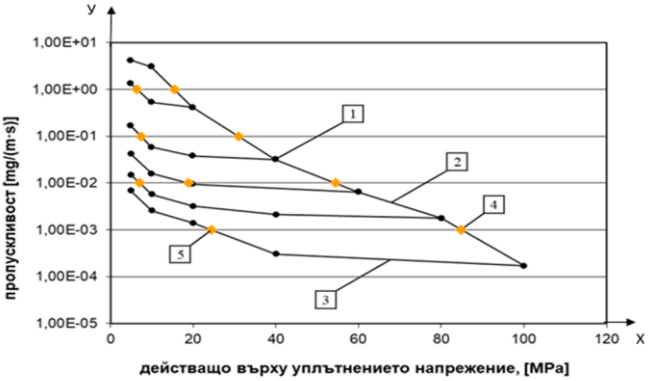
За определяне на $Q_{min(L)}$ и $Q_{S\ min(L)}$ по време на стандартизирания алгоритъм за тест, установката натоварва и разтоварва уплътнението, като се измерва специфична интензивност на изтичане при посочените в таблица 2 ефективни контактни напрежения при зададеното налягане на тестовия газ, в случая от 10 bar.

Изпитването включва натоварване с 5 MPa задържане на натоварването и измерване на специфична интензивност на изтичане, следва натоварването до 10 MPa, задържане на натоварването и измерване на специфична интензивност на изтичане, следва намаляване на натоварването до 5 MPa и отново се измерва изтичането. При следваща стъпка измерванията се извършват при 20 MPa, 10 MPa, 5 MPa и т. н., докато приключи цикълът на натоварване/разтоварване до 60 MPa.

Таблица 2. *Последователно натоварване и разтоварване на уплътнението при тест за пропускливост за определяне на показателите L_N, $Q_{min(L)}$ и $Q_{Smin(L)}$*

Натоварване до ефективно контактно напрежение, MPa	Разтоварване до ефективно контактно напрежение, MPa
5	не
10	5
20	10, 5
40	20, 10, 5
60	20, 10, 5

Методът на изпитване е показан на фиг. 4, като с 1 е означена точка на измерване при достигнато натоварване на уплътнението в MPa, 2 е линия на натоварване (повишаване на натиска върху уплътнението), 3 е линия на разтоварване (намаляване на натиска върху уплътнението), 4 е минимално контактно напрежение на уплътнението при монтаж $Q_{min(L)}$, 5 е минимално контактно напрежение на уплътнението при работни условия в експлоатация $Q_{Smin(L)}$, X е действащото напрежение върху уплътнителя в MPa, Y е пропускливостта/ изтичането в mg/(m.s).



Фиг. 4. *Схема по стандарт EN 13555 при тест за определяне на интензивността на изтичане*

3. Обект за изследване

За целите на експеримента са използвани плоски еПТФЕ уплътнения с дебелина 12 mm, плътност 0,8 g/cm^3, с външен диаметър 80 mm и вътрешен диаметър 50 mm, фиг.5 а) и разработено профилно уплътнение със същите размери с вграден пръстен в зоната на средния диаметър с конфигурация показана на фиг. 5 б)

Двата вида тествани плоски уплътнения са изрязани от еПТФЕ лист [13], като при профилното е обособен канал за вграждане на допълнителен елемент.



а) еПТФЕ уплътнение *б) Профилно еПТФЕ уплътнение*

Фиг. 5. *Изследвани уплътнения*

4. Резултати и анализ

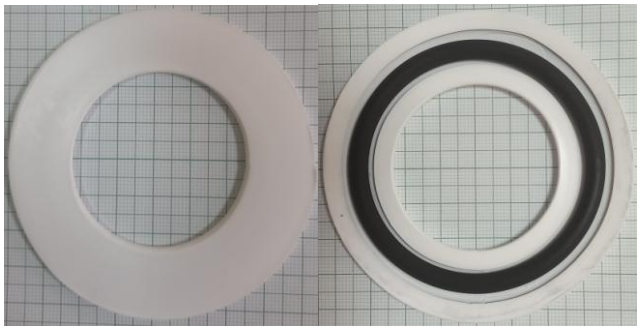
В таблица 3 са посочени стойностите от проведените тестове за определяне на изискуемо контактно напрежение върху уплътнението при монтаж $Q_{min(L)}$, за да се постигне клас на херметичност L_N при еПТФЕ уплътнение и профилно еПТФЕ с вграден пръстен в зоната на средния диаметър

Таблица 3. *Изискуемо контактно напрежение върху уплътнението при монтаж $_{Qmin(L)}$ за постигане на клас на херметичност L_N*

Клас на херметичност, L	еПТФЕ уплътнение Qmin(L), MPa	Профилно еПТФЕ уплътнение Qmin(L), MPa
1	13	5
0,1	19	7
0,01	24	10
0,001	30	13
0,0001	36	17
0,00001	47	20

Стойностите в таблица 3 показват, че за постигане на един и същ клас на херметичност, респективно интензивност на изтичане, профилното еПТФЕ уплътнение изисква прилагане на по-ниско контактно напрежение по време на монтажа в сравнение с еПТФЕ уплътнение.

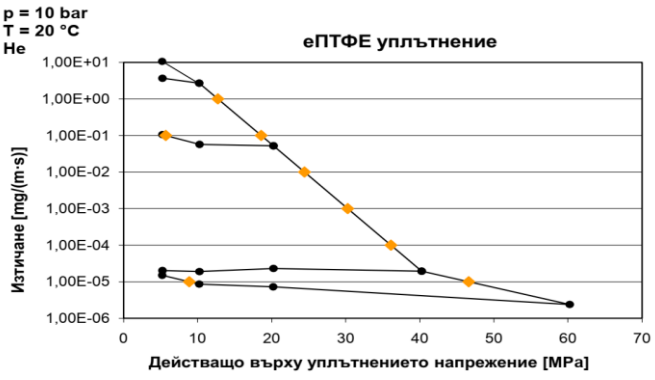
На фиг. 6 са представени двата вида уплътнения след провеждане на теста за херметичност до максимално контактно напрежение от 60 MPa.



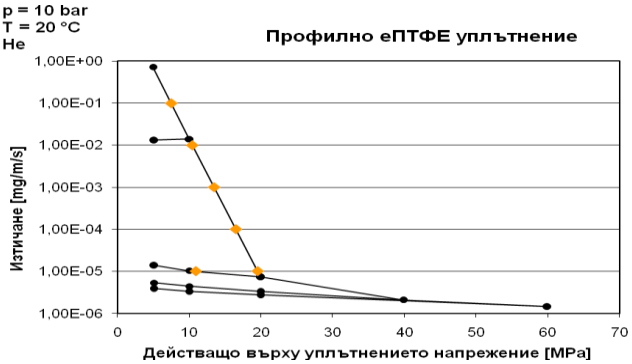
а) еПТФЕ уплътнител *б) Профилно еПТФЕ уплътнение*

***Фиг. 6**. Общ вид на уплътненията след тест*

На фиг. 7 и фиг. 8 са представени графики от проведен тест за отчитане интензивността на изтичане при еПТФЕ уплътнение и профилно еПТФЕ уплътнение.



***Фиг.7** Изтичане при еПТФЕ уплътнение*



***Фиг.8** Изтичане при профилно еПТФЕ уплътнение*

При действащо напрежение върху уплътнението 20 MPa при еПТФЕ уплътнение е установено изтичане ≤ 0,1 mg/(s.m) и е постигнат клас на херметичнос L0,1, докато при профилното еПТФЕ уплътнение е установено изтичане ≤0,00001 mg/(s.m) и е постигнат клас на херметичнос L0,00001, видно от графиките на фиг. 7 и фиг. 8.

5. Заключение

1. Установено е значително понижение на специфичната интензивност на изтичане през профилно еПТФЕ уплътнение при контактни напрежения между 10 и 30 MPa.

2. При използването на профилно еПТФЕ уплътнение с вграден еластомер се намалява контактното напрежение, необходимо за постигане на същия клас на херметичност, в сравнение с конвенционално еПТФЕ уплътнение.

3. При профилно еПТФЕ уплътнение с прилагане на контактно напрежение по време на монтаж от 20 MPa изтичането е над 1000 пъти по-малко, а при 30 MPa над 100 пъти.

4. Тестовата процедура БДС EN 13555 възприета в практиката е подходяща за изследване на интензивността на изтичане на профилно еПТФЕ уплътнение

6. Литература

1. J. Huang and L. Yuan-Haun, "Evaluation of uni-axially expanded PTFE as a gasket material for fluid sealing applications." *Materials chemistry and physics* 70.2, p.197-207 (2001).
2. C. Jones et al., Gasket-Handbook, Fluid Sealing Assosiation and European Sealing Assosiation (2017).
3. J. Czerwinski et al., A Collaborative Approach to Achieving a Gas-Tight Seal Using Expanded Polytetrafluorethylene (ePTFE) Gaskets in a Fiberglass-Reinforced Plastic (FRP) Lap-Joint Flanges. In: *Pressure Vessels and Piping Conference*. American Society of Mechanical Engineers, p. 239-246 (2012).
4. M. Staf, D. Tenkrát and T. Hlinčík, Apparatus for testing He leakage through flange gaskets at elevated pressure and temperature. *Progress in Nuclear Energy*, 139, p.103831. (2021).
5. M. Schaaf, F. Schoeckle and J. Bartonicek, "Harmonized" Gasket Testing." *ASME Pressure Vessels and Piping Conference.* Vol. 46733. pp. 189-197, (2004).
6. R. B. Minor et al., Patent US6485809, Low stress to seal gasket (2002).
7. J. W. Dolan and D. J. Mills, Patent US5879789, Rigid sheet polytetrafluoroethylene gasket (1999).

8. E. Mladenov, D. Gospodinov and R. Radev, Researc on leak rate of expanded PTFE flat gasket whit locally increased density, Proceeding of University of Ruse volume 61, book 2.1 p.14-22. (2022).
9. AMTEC, Operating instruction „TEMES fl.ai1“, (pp. 78/151). (2014).
10. M. Schaaf, F. Schöckle and J. Bartonicek, *"Gasket Characteristics in Flanged Joints* (F532)."(2003).
11. J. Bartonicek, M. Schaaf and F. Schoeckle, On the effect of temperature on tightening characteristics of gaskets. In *ASME Pressure Vessels and Piping Conference* (Vol. 19442, pp. 35-43). (2002).
12. EN13555, Flanges and their joints. *Gasket parameters and test procedures relevant to the design rules for gasketed circular flange connections.* (2021).
13. AVKO JSC, http://uim.avko.bg/english/products/expanded-ptfe-products/expanded-ptfe-sheets

Applications of DNA Complexes to Sensor Technology and Molecular Probes for Early Diagnosis of Neurodegenerative Disease

Hristina Sbirkova-Dimitrova[1*], Hristo Gerginov[1], Boris L. Shivachev [1]
1 Institute of Mineralogy and Crystallography "Acad. Ivan Kostov", Bulgarian Academy of Sciences,
Acad. G. Bonchev str., bl. 107, 1113 Sofia, Bulgaria

Structural characterization of G-rich DNA sequences in the presence of metal ions provides essential insight into quadruplex stability and ion-dependent conformational modulation. We report the crystal structure of the G-quadruplex, forming sequence GGGGTTTTGGGG in the presence of Zn^{2+}, K^{+}, and Na^{+}. It has been deposited in the RCSB Protein Data Bank under accession code **9FTA**. The structure was determined by singlecrystal X-ray diffraction at 2.49 Å resolution in the space group $P2_12_12_1$. It reveals a parallel-stranded, two-tetrad G-quadruplex stabilized by K^{+} ions within the central channel, while Na^{+} and Zn^{2+} occupy peripheral and groove-associated sites. Zn^{2+} ions engage in noncanonical coordination interactions with phosphate backbone and structured water molecules, contributing to lattice stabilization and subtle adjustments in groove dimensions (Fig. 1). The T_4 loop forms a compact, ordered motif that participates in crystal packing rather than intramolecular G4 stabilization. The presence of mixed cations produces a unique ion-mediated lattice architecture, providing structural insight into how bivalent and monovalent metals jointly modulate G-quadruplex topology. These results provide a foundation for understanding ion-specific effects on G4 structures and may guide the design of metal-responsive DNA architectures that are part of promoter sequences relevant to neurodegenerative diseases.

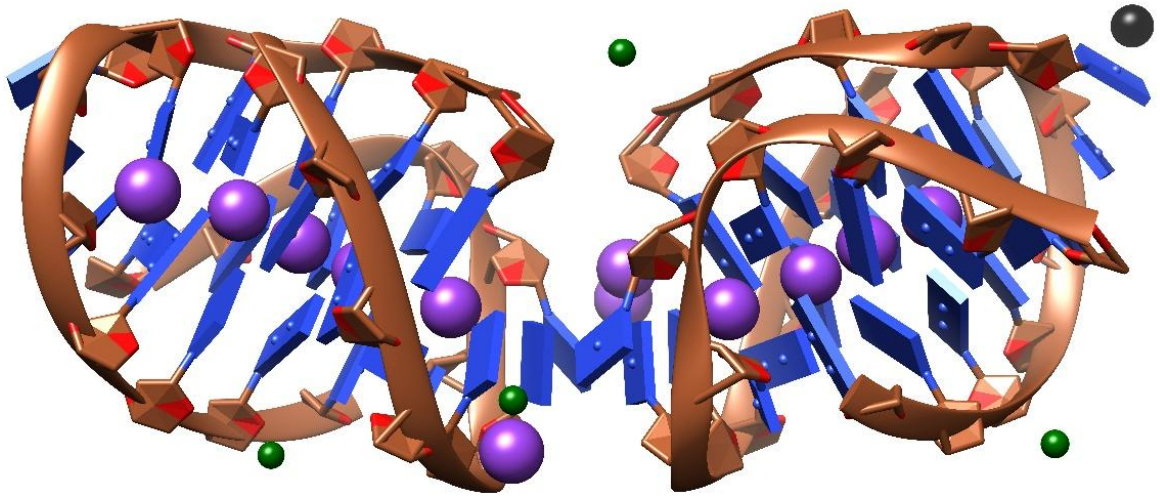


Figure 1. *View of the asymmetric unit of 9FTA, visualizing the Zn^{2+} (in green color), K^{+} (in purple color), and Na^{2+} (in black color) ions occupancy positions.*

Secondary neutron monitoring at Rozhen Observatory (MNMS-ROZH) data

H. Nichev[3,*], T. Arsov[1], Ch. Angelov[1], N. Serafimov[1], N. Tyutyundzhiev[2], M. Petrov[3]
Institute of Nuclear Energy and Nuclear Research, Bulgarian Academy of Sciences[1]
Central Laboratory of Solar Energy and New Energy Sources, Bulgarian Academy of Sciences[2]
Institut of electronics, Bulgarian Academy of Sciences[3]
e-mail nitchev@ie.bas.bg

Abstract: *Solar irradiation events monitoring and effects observation of cosmic rays at Rozhen observatory (BG) has been improved further by newly-constructed cost-effective equipment: mini-neutron monitoring(NM) station. This mini-NM installation has been built following the main requirements and traditions of ground-based NM monitors, and trying to expand the coverage of existing NM network. In this study we report comparison between two years' data and experimental results of the operation in remote area at 1750 m.a.s.l. of Rodopes mountain in Bulgaria.*

Keywords*: neutron monitoring, solar irradiation, cosmic rays*

Acknowledgment:

This research work was supported by a grant of the National Science Fund of Republic of Bulgaria under project No KP-06-N64/3, 15.12.2023 and by means of infrastructure funded by "National Road Map for Scientific Infrastructure", financially supported by the Ministry of Education and Science of Bulgaria, ACTRIS BG (Contract № D01-365/ 04.12.2023)

Development of an All-Optical Platform for Real-Time Monitoring of Hypoxia Dynamics

Stanislav Baluschev[1,2], Maria Micheva[1], Ivanka Nikolova[3], Katharina Landfester[1]
[1]Max Planck Institute for Polymer Research, Mainz, Germany
[2]Optics and Spectroscopy Department, Faculty of Physics, Sofia University "St. Kliment Ochridski", Sofia, Bulgaria
[3]Stephan Angeloff Institute of Microbiology, Bulgarian Academy of Sciences, Sofia, 1113, Bulgaria
balouche@phys.uni-sofia.bg

Abstract: *Oxygen levels in the cellular microenvironment, particularly under hypoxic conditions, play an active regulatory role in modulating cellular function, signaling pathways, and metabolic networks. A radically new concept for sensing the oxygen concentration at the extracellular liquid microenvironment was developed, based on nanoconfined upconversion optical sensors. The experimental achievements in developing technologically applicable strategies for minimally invasive monitoring of the oxygen concentration in cell microenvironment will be presented and discussed.*

Introduction

Viral infections remain a significant global health challenge, with emerging and re-emerging pathogens posing persistent threats to public health, economic stability, and societal resilience. Rapid and accurate assessment of infection status at the cellular and tissue levels is crucial for monitoring disease progression and evaluating treatment efficacy. Traditional diagnostic approaches often fail to capture the complex, dynamic interplay between viral replication, host immune responses, and microenvironmental factors such as oxygen availability.

Hypoxia - an altered oxygen balance in the local microenvironment - is increasingly recognized as a key modulator of viral pathogenesis, influencing viral replication, immune evasion, and inflammatory responses. However, direct, real-time control and monitoring of hypoxia dynamics in the intercellular space remain largely unexplored, in part due to existing at the moment technological limitations.

At this research paper this critical gap project is addresses by integrating optical control technologies with advanced microenvironmental sensing to monitor viral infection status through the modulation and observation of hypoxia. This approach is timely due to:

- The increasing frequency of viral outbreaks (e.g., SARS-CoV-2, influenza, emerging zoonotic viruses) that demand innovative diagnostic and monitoring strategies;
- Advances in optical and photonic tools that now enable precise, non-invasive control of cellular microenvironments.

Prerequisites and means for solving the problem

The study of the oxygen content of water is an important area of research because of its central role in the biochemistry of life. The ability to quantify in real time both the spatial distribution and temporal dynamics of oxygen concentration in the intercellular aquatic microenvironment is necessary for a complete understanding of the mechanisms involved in both normal physiology and disease states. Oxygen content at the cell microenvironment, especially under hypoxic conditions, plays an active and regulatory role in modulating cellular function,

signaling pathways, and metabolic networks.

There is a broad consensus [1] in the literature, that optical methods for O2-sensing are less invasive and able to provide time-resolved and 2-dimentional (2D) spatial evolution of the O2 distribution [2, 3]. Optical-sensing approaches based on phosphorescence quenching enable the direct visualization and quantification of oxygen concentrations across the intercellular aquatic phase, even in tissues [4]. The recent development of the phosphorescent oxygen sensors are summarized in comprehensive reviews [5, 6] demonstrating the importance of the studied problem for the fields of chemistry, biophysics and medicine.

Nevertheless, the process of optical oxygen sensing – either via the phosphorescence quenching methods [6, 4] or via the process of triplet-triplet annihilation upconversion, leads to the unwanted (often uncontrolled) but very effective generation of singlet oxygen [7]. The singlet oxygen oxidases efficiently intra-chain carbon double bonds [8] or terminal double bonds [9] even at physiologically relevant temperatures. Furthermore, the singlet oxygen, formed during the optical excitation, takes part in a Diels–Alder type process on a parent sensitizer molecule (in the case of TTA-UC or methods, based on phosphorescence quenching), which leads to a loss of conjugation in the π-system and to a real-time decrease of the Q-band absorption. A similar process is also involved in photo-bleaching of the fluorescent chromophores, e.g. anthracene- and perylene- derivatives, etc. [10]. The problem of unavoidably generated singlet oxygen is exacerbated when high excitation intensities (on the level of $MW \times cm^{-2}$) are used - stimulated photo-oxidation not only affects the sensing molecules (metallated macrocycles) but also the surrounding biological sample [11].

Optical sensing technologies and modalities, based on sacrificial colorimetric change of reporter molecules, immobilized in hydrogels [12, 13] are being used for determination of the oxygen content in vitro in cell cultures, exposed to external stimuli – such as medications, nutrient changes, hypoxia or infection – and also to internal alterations as gene knockout, knockdown or gene gain. Below we will describe the competitive advantages of the arising HypoVir technology compared to the current technologies used for oxygen sensing.

Solution of the examined problem

At this research paper a radically new concept for sensing the oxygen concentration at the extracellular liquid microenvironment is proposed. The process of Triplet-Triplet Annihilation Upconversion (TTA-UC) performed in nanoconfinement is used as a sensing tool.

TTA-UC takes place in a multi-chromophore system consisting of energetically optimized pairs of sensitizer and emitter molecules, well dissolved in hydrophobic matrix, Figure 1 [14]. Photon energy is absorbed (Figure 1, the dark orange arrow) in the Q-band of the sensitizer and stored in its triplet state, which is formed after the process of intersystem crossing (ISC). The excited sensitizer triplet state has three channels for relaxation: (**i**) – *via* emission of a strongly red-shifted photon, belonging to the process of residual phosphorescence (the dotted orange arrow, Figure 1, the process is marked with rPh); (**ii**) – *via* effective generation of singlet oxygen (Figure 1, the dark gray dotted arrow, the process is marked with ET, [15]); last but not least – (**iii**) via the process of triplet–triplet transfer (Figure 1, the dotted blue arrows, the process is marked with TTT). It is important to note, that both, the lifetime (τ^{rPh}) and the quantum yield ($Q.Y.^{rPh}$) of the residual phosphorescence are strongly reduced by the presence and concentration of the quenchers - either ground state oxygen molecules [16] or ground state emitter molecules [17]. The third relaxation channel is accelerated by the process of the triplet–triplet annihilation upconversion (TTA-UC), in which the excited triplet states of two emitter molecules undergo triplet–triplet annihilation (TTA), so that one emitter molecule returns to its singlet ground state and the other molecule gains the energy of both triplet states and is excited to the higher singlet state. As the singlet state emitter radiatively decays back to the ground state, a delayed fluorescence photon (the blue arrow, Figure 1, the process is denoted dF) of

higher energy than the excitation photon is emitted. Through the process of TTA-UC, both emitter molecules effectively return to the ground state and can again participate in the quenching of the excited sensitizer triplet state.

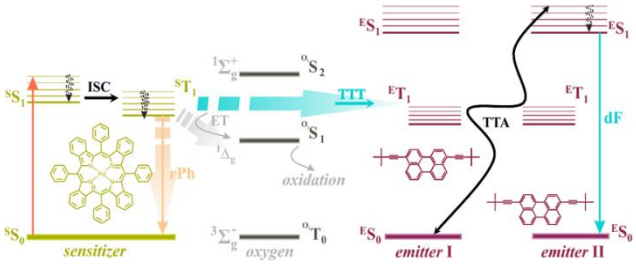


Figure 1. *Simplified energetic scheme of the triplet–triplet annihilation upconversion (TTA–UC) process in an oxygen-saturated environment.* ***Insets****: structure of meso-tetraphenyl-tetrabenzo porphyrin palladium(II) (PdTBP) sensitizer (****left****), structure of 3,10-bis(3,5-dimethoxyphenyl)perylene (BDMP) emitter (****right****).*

Results and discussion

An oxygen nanosensor **can be considered** minimally invasive **only if several** experimental criteria are simultaneously met:

(**i**) Confinement of the TTA-UC – O_2-sensing system in a hydrophobic microenvironment ensures 3D-localization of the permanently generated singlet oxygen, Figure 2**a**. The NC-core consist of a mixture of beeswax (BW, 40%wt.), squalene (SQ, 40% wt.) and rice bran oil (RBO, 20% wt.). We could not find oxygen solubility data for such complex mixture. On the one hand, the solubility of oxygen in ground state ($^{O2}T_0$) in the oil-phase of the NC-core is more than 10 times higher, than the solubility of oxygen in the surrounding water phase [18]. On the other hand, beeswax exhibits exceptionally high barrier properties against water vapor and molecular oxygen [19, 20]. We assume that not only the solubility of oxygen in the hydrophobic NC-core, but also the solubility of singlet oxygen is much lower, than the solubility of oxygen in the water microenvironment [21, 22]. Presence of large amounts of SSOS materials – SQ [23] and RBO [24], ensure effective and locally (within the NC-core) binding of the generated singlet oxygen; (**ii**) The excitation intensities required for the entire measurement process must be kept as low as possible to minimize the electromagnetic stress on the living entity, ideally below 10 W×cm^{-2}. The evolution of the living species occurred under light intensities equivalent to 1 Sun (i.e., 100 mW×cm⁻², AM 1.5). Therefore, light intensities up to 100 Suns may be considered acceptable. Often, the oxygen sensing experiments were performed at orders of magnitude higher intensities.

(**iii**) For stabilization of oil-in-water nanoconfined objects, surfactants with high HLB–value and high solubility in water are used [25]. For instance, non-ionic surfactant [26], such as Polyethylene glycol p-(1,1,3,3-tetramethylbutyl)-phenyl ether (Triton X-100, HLB = 13.4, defined following the Griffin's method), soluble in all proportions at 25 °C in water [27]. As well as ionic surfactant, for instance Sodium dodecyl sulfate (SDS, HLB = 40, defined following the Davies' method) soluble in water up to 20% wt. at 25 °C [28]. The use of highly water soluble surfactants has a major disadvantage: the molecular concentration of free surfactant in the extracellular water microenvironment is high, with a pronounced cell-toxic effect [29, 30].

Figure 2**b** shows the experimental set-up for all-optical sensing of intercellular water microenvironment. The diode laser beam pass through the spatial filter in order to reach nearly TEM_{00} transversal intensity distribution. A defocusing achromatic lens (the violet lens) placed on an electronically controlled µ-positioning stage (DL125 Delay Line Stage, *Newport Corp.*) controls the excitation spot diameter. The luminescence emission generated by the sample was collected with the same apochromatic lens, thus the excitation- and observation- spots are completely spatially overlapped. The used laser heads (TCLDM9, *Thorlabs Inc.*) allow current modulation *via* modulation input, depending on the maximal current supplied, the modulation frequency varies from 50 kHz up to 200 kHz. Therefore, the laser intensity was modulated by an arbitrary pulse generator (TGA1244, *TTi Inc.*) with caring frequency of 40 MHz. The obtained laser diode pulses have almost rectangular time-shape, with rise- and decay- slopes less than 2.5×10^{-6} s.

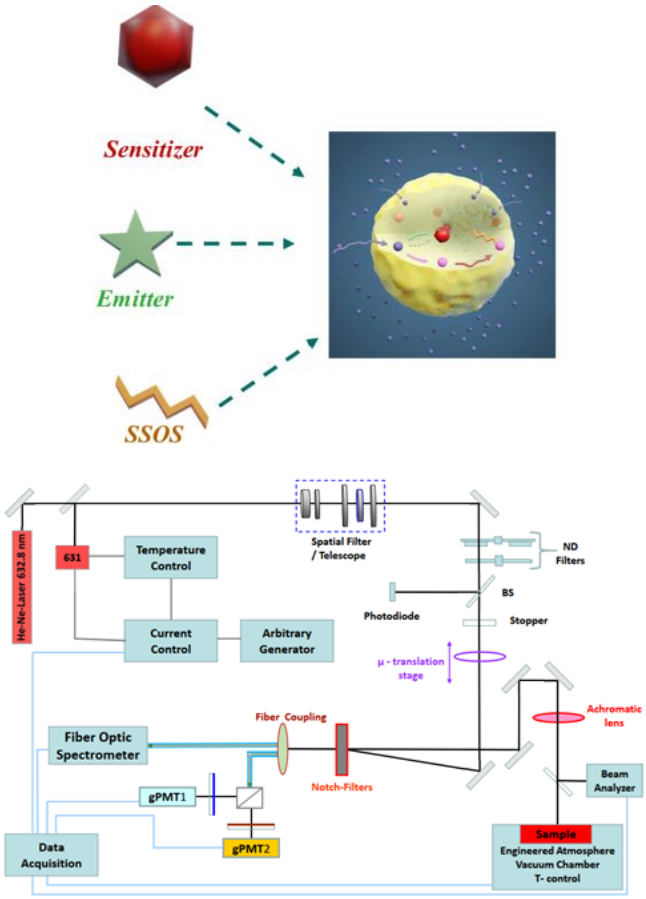


Figure 2: ***(a)*** *- Scheme of the sensing nanocapsules (NC) proposed in this project;* ***(b)*** *- Set-up for registration of the dynamical parameters of the TTA-UC in engineered atmosphere with actively controlled oxygen content, active temperature control and temperature stabilization.*

One edge-beam splitter (FF01-694/SP-25, *Semrock Inc.*) was used to spatially separate the sensitizer residual phosphorescence and delayed emitter UC-fluorescence, registered by gPMT1 and gPMT2, accordingly. Additional edge-filters, namely a short pass (SP01-633RS-25, *Semrock Inc.*) filter with cutting wavelength □□□□650 nm and long pass (HQ700LP, *Chroma GmbH*) filter with cutting wavelength □□□□700 nm, were installed in front of the registration opto-electronic devices at the delayed-fluorescence branch and phosphorescence branch, respectively. The normalized absorption spectra and normalized luminescence spectra of the sensitizer and emitter are shown in **Figure 3**.

The gPMT's are working in analogous mode with a rise- and decay-times less than 30×10^{-9} s. The gated photo-multiplier tubes are set in "Normally OFF" mode. The gating pulses should be with an amplitude of 3.5 V ÷ 5 V applied on 10 k oad, with maximal repetition rate of 10 kHz. The gPMT-operation delay is less than 0.2×10^{-6} s. Each gPMT is equipped with a wide bandwidth amplifier unit C9663 (DC up to 150MHz, Hamamatsu Photonics Inc.), where the current input signal from the photomultiplier tube is directly converted into a voltage output signal.

(**1**) Since the optical sensors are nanoconfined, and physically situated in a *close proximity* with sacrificial singlet oxygen materials, no singlet oxygen diffuses outside the sensors.
(**2**) Instead monitoring of the dependence on oxygen concentration either of phosphorescent lifetime, or delayed fluorescence lifetime of the reporter molecules, or dependence on oxygen concentration of a colorimetric changes, we identify that the observation of loss of TTA-UC-luminosity delivers *significantly higher oxygen* sensitivity, **Figure 4.**

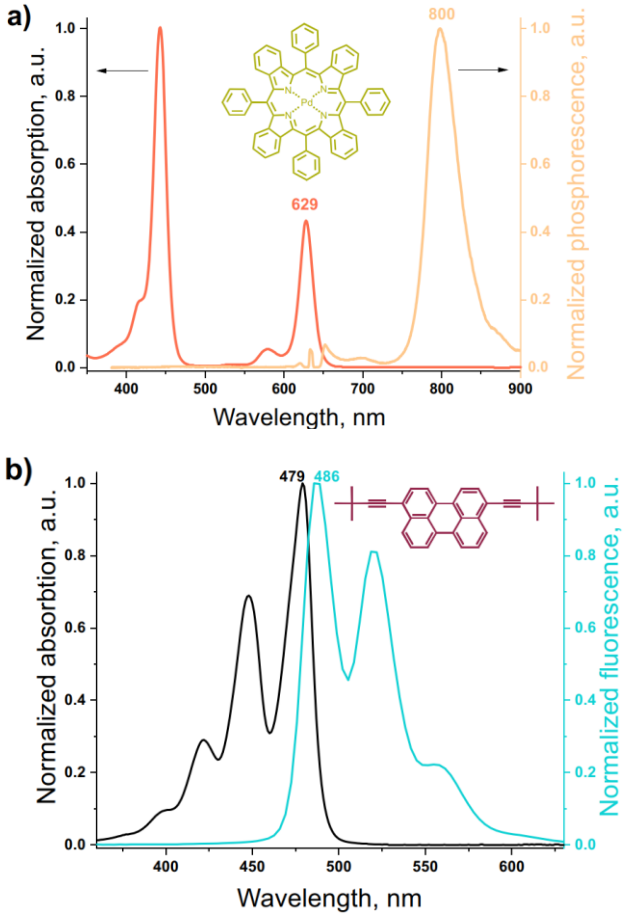


Figure 3**: (**a**) Normalized absorption spectrum (red line) and normalized luminescence spectrum (brown line, excitation wavelength λ = 635 nm) of the sensitizer molecule in toluene solution; (**b**) Normalized absorption spectrum (violet line) and normalized fluorescence spectrum (blue line, excitation wavelength λ = 459 nm) of the emitter molecule in toluene solution.* ***Insets: *structure of meso-tetraphenyl-tetrabenzo porphyrin palladium (II) (PdTBP) – sensitizer (a), structure of 3,10-bis(3,5-dimethoxyphenyl)perylene (BDMP) – emitter (b).*

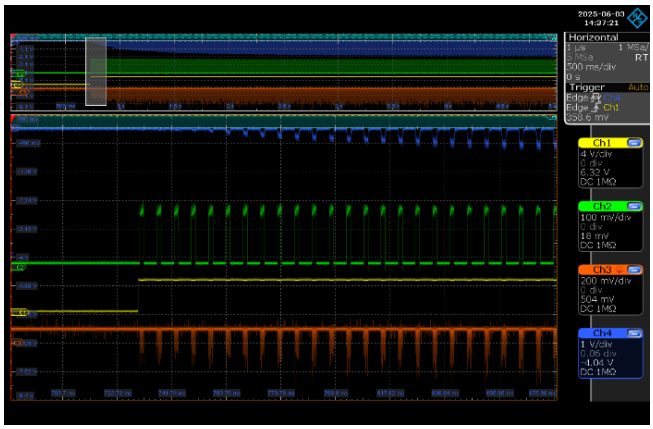


***Figure 4**: (**up**) - Time-resolved intensity of the optical signals of **dF** (the blue channel) and **rPh** (the orange channel) in oxygen saturated water macro-environment (160mm Hg); excitation pulses (the green channel); enable pulse (the yellow channel); (**down**) - The temporal magnification of the first 25 excitation pulses clearly shows the intramolecular nature of the **rPh** signal: even at the first 5 excitation pulses, there is a non-zero residual phosphorescence intensity. Conversely, the intermolecular nature of the **dF** signal explains the complete suppression of upconversion during the first 5 excitation pulses*

Conclusion

We demonstrate an original optical sensing technique for monitoring local oxygen concentration based on the observation of local quenching of nanocapsule (NC) luminescence. Rather than monitoring the oxygen dependence of either the phosphorescence lifetime or the delayed fluorescence lifetime of reporter molecules, we show that significantly higher oxygen sensitivity can be achieved by observing the local decrease in delayed fluorescence intensity. This experimental approach offers several advantages, particularly under hypoxic conditions: it directly reflects local oxygen concentration without the need for spatial or temporal averaging; it operates at low excitation intensities; and the photogenerated singlet oxygen is completely chemically bound within the sensing nano capsules, preventing diffusion into the surrounding aqueous microenvironment.

References

[1] P. R. Ogilby, “Singlet oxygen: there is indeed something new under the sun” Chem. Soc. Rev. 2010, 39, 3181–3209.
[2] X. Wang, O. S. Wolfbeis, R. J. Meier, “Luminescent probes and sensors for temperature” Chem. Soc. Rev. 2013, 42, 7834–7869.
[3] D.B. Papkovsky, R.I. Dmitriev, “Biological detection by optical oxygen sensing” Chem. Soc. Rev. 2013, 42, 8700–8732.
[4] E. Roussakis, Z. Li, A. J. Nichols, C. L. Evans, “Oxygen-Sensing Methods in Biomedicine from the Macroscale to the Microscale” Angew. Chem. Int. Ed. 2015, 54, 8340–8362.
[5] R. I. Dmitriev, D. B. Papkovsky, “Optical probes and techniques for O2 measurement in live cells and tissue” Cell Mol Life Sci. 2012, 69(12), 2025–2039.
[6] M. Quaranta, S. M. Borisov, I. Klimant, “Indicators for optical oxygen sensors” Bioanal Rev. 2012, 4, 115–157.
[7] N. Nazarova, Y. Avlasevich, K. Landfester, S. Baluschev, “All-Optical Temperature Sensing in Organogel Matrices via Annihilation Upconversion” ChemPhotoChem 2019, 3, 1020–1026.
[8] N. Shimizu, J. Ito, S. Kato, Y. Otoki, M. Goto, T. Eitsuka, T. Miyazawa, K. Nakagawa, “Oxidation of squalene by singlet oxygen and free radicals results in different compositions of squalene monohydroperoxide isomers” Sci Rep 2018, 8, 9116.
[9] F. Marsico, A. Turshatov, R. Peköz, Y. Avlasevich, M. Wagner, K. Weber, D. Donadio, K. Landfester, S. Baluschev, and F. R Wurm, “Hyperbranched Unsaturated Polyphosphates as Protective Matrix for Long-Term Photon Upconversion in Air“ J. Am. Chem. Soc. 2014, 136, 31, 11057–11064.
[10] G. Mehes, H. Nomura, Q. Zhang, T. Nakagawa, C. Adachi, “Enhanced electroluminescence efficiency in a spiro-acridine derivative through thermally activated delayed fluorescence” Angew. Chem., Int. Ed. 2012, 51, 11311–11315
[11] A. Reis, C. M. Spickett, “Chemistry of phospholipid oxidation”, Biochim Biophys Acta. 2012, 1818(10), 2374–2387.
[12] Agilent Seahorse XF Cell Mito Stress Test Report Generator (RRID:SCR_026230), can be found under http://www.agilent.com/en/product/cell-analysis/real-time-cell-metabolic-analysis/xf-analyzers
[13] Oroboros NextGen-O2k), can be found under http://www.wiki.oroboros.at/index.php/Oroboros_NextGen-O2k (accessed: 28.05.2025).
[23] Y. Li, F. Chen, Z. Gao, W. Xiang, Y. Wu, B. Hu, X. Ni, K. Nishinari, Y. Fang, “Influence of interfacial properties/structure on oxygen diffusion in oil-in-water emulsions” *Food Research International* **2023**, *170*, 112973.
[24] G. Donhowe, O. Fennema, “Water Vapor and Oxygen Permeability of Wax Films” *JAOCS* **1993**, *70(9)*, 867–873.

[25] L. Yang, A. T. Paulson, “Effects of lipids on mechanical and moisture barrier properties of edible gellan film” *Food Research International* **2000,** *33*, 571–578.
[26] S. Kim, S. Kim, W. Y. Oh, Y. Lee, J. Lee, “Evaluation of the effects of amphiphilic compounds on oxygen solubility in bulk oil” *International Journal of Food Science and Technology* **2022**, *57*, 6082–6089.
[27] M.-E. Cuvelier, P. Soto, F. Courtois, B. Broyart, C. Bonazzi, “Oxygen solubility measured in aqueous or oily media by a method using a non-invasive sensor” *Food Control* **2017**, *73*, 1466–1473.
[28] N. Shimizu, J. Ito, S. Kato, Y. Otoki, M. Goto, T. Eitsuka, T. Miyazawa, K. Nakagawa, “Oxidation of squalene by singlet oxygen and free radicals results in different compositions of squalene monohydroperoxide isomers” *Sci Rep* **2018**, *8*, 9116.
[29] K.-L. Pang, K.-Y. Chin, “The Role of Tocotrienol in Protecting Against Metabolic Diseases” *Molecules* **2019**, *24(5)*, 923.
[30] K. Landfester in *Colloid Chemistry II. Topics in Current Chemistry, Vol. 227* (Eds.: Antonietti, M.), Springer, Berlin, Heidelberg, **2003**, pp. 75–123.
[31] R. K. Sharma, G. Dey, P. Banerjee, J. P. Maity, C.-M. Lu, J. A. Siddique, S.-C. Wang, N. Chatterjee, K. Dasbc, C.-Y. Chen, “New aspects of lipopeptide-incorporated nanoparticle synthesis and recent advancements in biomedical and environmental sciences: a review” *J. Mater. Chem. B* **2023**, *11*, 10-32.
[32] Sigma Chemical, “Sigma Product Information Sheet: TRITON X-100™”, can be found under https://www.snowpure.com/docs/triton-x-100-sigma.pdf (accessed: 28.05.2025).
[33] Sigma-Aldrich, Inc., “Sodium dodecyl sulfate solution (L4522) - Product Information”, https://www.sigmaaldrich.com/deepweb/assets/sigmaaldrich/product/documents/263/218/l4522pis.pdf
[34] Â. S. Inácio, K. A. Mesquita, M. Baptista, J. Ramalho-Santos, W. L. Vaz, O. V. Vieira, “In vitro surfactant structure-toxicity relationships: implications for surfactant use in sexually transmitted infection prophylaxis and contraception” *PLoS One* **2011,** *6(5)*, e19850.

Acknowledgements:
MM, IN, SB acknowledge the Bulgarian National Science Fund, project КП-06-Н97/4 / 05.12.2025 / *HypoVir* - „Monitoring Viral Infection Status via Optical Control of Hypoxia Dynamics in the Intercellular Microenvironment“ for the financial support.

Fermented grape pomace ash – by-product of rakia (brandy) production

Aleksandar Nikolov*, Liliya Tsvetanova, Borislav Barbov, Ivan Tsanev, Yana Tzvetanova
Institute of Mineralogy and Crystallography, Bulgarian Academy of Sciences, Acad. G. Bonchev Str., bl. 107, 1113 Sofia, Bulgaria;
*drsashko@imc.bas.bg

Abstract: *This study investigates the chemical, mineralogical, and functional characteristics of fermented grape pomace ash generated after brandy production and subsequent combustion. Semi-quantitative WDXRF analysis revealed a Ca–K–P-dominated composition with high alkalinity, significant phosphorus content, and notable copper concentration. The water-soluble fraction of the ash was determined to be 17.1 wt.%, indicating a moderate content of mobile inorganic salts that may influence leaching behaviour and environmental compatibility. XRD and vibrational spectroscopy confirmed the presence of lime, calcite, silicates, sulphates, and calcium phosphate phases, including hydroxyapatite, together with a significant amorphous fraction and residual carbon. UV–Vis analysis indicated partial reduction of copper species to metallic nanoparticles, suggesting heterogeneous redox conditions during thermal treatment. The combined composition confers potential functionality in soil amendment, mineral carbonation for CO_2 sequestration, and incorporation into cementitious or alkali-activated systems, although soluble salts and copper mobility represent critical constraints, requiring application-specific environmental and performance assessment.*

Keywords*: FERMENTED, GRAPE, POMACE, ASH, CHARACTERIZATION, BY-PRODUCT*

1. Introduction

The wine and spirits industries generate substantial quantities of solid by-products, among which grape pomace represents the dominant fraction by mass. Grape pomace, consisting of skins, seeds, and varying amounts of stalks, accounts for approximately 20–30 wt.% of processed grapes and is produced continuously and seasonally in large volumes [1-3]. While numerous valorisation pathways for fresh or dried grape pomace have been explored, primarily in the food, feed, and nutraceutical sectors [4,5], the management of pomace residues following alcoholic fermentation and distillation remains comparatively underexplored. In particular, solid residues generated after brandy production are often treated as low-value waste streams, despite undergoing substantial physicochemical transformation during fermentation.

Alcoholic fermentation induces pronounced changes in grape pomace composition through the consumption of fermentable sugars, partial degradation of polysaccharides, redistribution of organic acids, and mobilization of inorganic species. Studies focusing on the chemical and nutritional composition of grape pomace consistently show that its mineral fraction is dominated by potassium, calcium, phosphorus, and magnesium, with variability arising from grape variety, processing route, and presence of stalks [1,2,5]. However, these studies primarily address unfermented or food-grade pomace, where the organic matrix remains largely intact.

Thermochemical utilization of grape pomace has been investigated mainly in the context of energy recovery. Combustion and pyrolysis studies demonstrate that grape pomace exhibits high ash content and a mineral composition prone to alkali-related challenges such as slagging, fouling, and ash deposition [6]. Mortari et al. [8] showed that water-soluble inorganic constituents, particularly potassium, significantly influence combustion behaviour and char reactivity, while Moço et al. [7] reported severe ash deposition and sintering during high-temperature combustion of pulverized grape pomace. These findings underline the strong influence of inorganic matter on the thermal behaviour of pomace-derived materials but remain focused on fuel performance, rather than on the properties or potential applications of the resulting ash.

From a resource-efficiency and circular-economy perspective, biomass ashes have attracted increasing attention as secondary raw materials in construction, agriculture, and environmental applications [8]. Depending on their oxide composition and mineralogical assemblage, ashes may exhibit alkalinity, nutrient value, or reactive phases suitable for soil amendment, stabilization processes, or incorporation into cementitious systems [9]. Given the high contents of calcium, potassium, phosphorus, and silica reported for grape pomace and its fractions [3], fermented grape pomace ash may offer functional properties extending beyond energy-related considerations. However, without systematic chemical and mineral characterization, such potential applications remain speculative.

The specific aim of this work is to characterize fermented grape pomace ash and to assess its potential applications in value-added domains. By linking elemental composition and mineralogical features to plausible functional uses, this study contributes to the broader understanding of grape pomace-derived residues within sustainable material cycles, while explicitly recognizing the influence of local feedstock variability and processing conditions.

2. Materials and methods

2.1. Materials

The grape variety used for fermentation was the black Otel from the area of Zemen, Bulgaria, vintage 2024). The grapes exhibited an initial sugar content of about 20%, determined in situ using a handheld refractometer. The grape was mechanically crushed using a manual machine. The resulting mixture of liquid, seeds, skins and stalks was used as the fermentation feedstock. An additional 15–20 wt.% sugar solution was added to the fermenting mass in order to adjust the consistency and enhance alcohol yield. Fermentation was carried out in plastic barrels at a controlled temperature of 22 °C. To ensure process homogeneity, the fermenting mass was mixed daily. After approximately three weeks, the sugar content decreased to zero, indicating completion of fermentation.

The fermented material was subsequently transferred to a 120 L traditional copper distillation unit, operated using wood as the heat source, where alcohol was extracted. The residual solid matter remaining after distillation was mechanically dewatered using a screw press and subsequently formed into briquettes with approximate dimensions of 16×8×5 cm using a manual press (Fig. 1). The briquettes were placed on an outdoor shelf under a roof and allowed to dry. The briquette was burned into wood stove (Tim Sistems, Serbia, efficiency 79%) and the obtained ash was examined.



Fig. 1. *Dried briquette produced from pressed fermented grape pomace.*

2.2. Methods

The elemental composition of the provided samples was determined using a Supermini200 spectrometer (Rigaku, Japan). Measurements were performed by wavelength-dispersive X-ray fluorescence (WDXRF) at an operating voltage of 50 kV and a current of 4.00 mA. Data processing was conducted using the ZSX software package. Samples were placed in a holder with an irradiated area of 30 mm in diameter. Before analysis, the samples were ground and pressed using a binder (Acrawax C powder) at a sample-to-binder ratio of 5:1 (w/w). A semi-quantitative method (SQX) was employed to determine elemental composition.

Powder X-ray diffraction analysis was performed on Empyrean (Malvern Panalytical, Almelo, The Netherlands) diffractometer equipped with a PIXcel3D detector and copper X-ray source (CuKa = 1.5406 Å). At 40 kV and 30 mA.

UV–Vis reflectance spectra were recorded using a Cary 4000 spectrophotometer (Agilent Technologies) equipped with an internal DRA 900 diffuse reflectance accessory (IMC-BAS). Transmittance spectra were additionally recorded using a solid sample accessory. Measurements were performed in the 200–800 nm spectral range with a spectral resolution of 1 nm. Baseline fluctuations were corrected prior to analysis. The diffuse reflectance data were converted to absorbance using the Kubelka–Munk function F(R)

Fourier-transform infrared (FTIR) spectra were collected on a Bruker Tensor 37 spectrometer in the spectral range 4000 - 400 cm^{-1} (IMC-BAS). The measurements were performed on powdered samples KBr pellet. Each spectrum represented the average of 128 scans, ensuring an enhanced signal-to-noise ratio and improved spectral resolution.

Raman measurements were carried out using an alpha300 R confocal Raman microscope (WITec) equipped with a 532 nm excitation laser (IMC-BAS). Spectra were recorded using ×10 and ×50 objectives. The spectral range covered approximately 100–3200 cm^{-1}.

The water-soluble fraction was determined by suspending oven-dried ash (80 °C) in distilled water at a solid-to-liquid ratio of 1:20 (w/v). The suspension was maintained under static conditions for 48 h with intermittent manual stirring to promote dissolution. Subsequently, the mixture was filtered, and the filtrate was collected and evaporated to dryness at 80 °C to recover the dissolved solids. The water-soluble content was calculated as the mass ratio of the recovered solid residue to the initial dry mass of the ash.

3. Results and Discussion

3.1. Water-soluble content

The water-soluble content of the fermented grape pomace ash was determined to 17.1 wt.%. This value falls within the broad range reported for biomass ashes (1–60.0 wt.%), but it is lower than the mean value summarized for various agricultural and woody biomass ashes combusted at 500 °C [10]. According to the review data, biomass ashes commonly exhibit significantly higher water-soluble fractions than the corresponding raw biomasses due to the formation of alkali chlorides, sulphates, and carbonates during combustion. The measured 17.1 wt.% therefore indicates moderate enrichment in water-soluble salts, suggesting partial development of such phases but lower overall salt accumulation compared to highly K-type or salt-tolerant biomasses described in the literature [10].

From a materials perspective, this fraction is critical because it controls alkalinity, leaching behaviour, and potential reactivity, and thus directly influences both technological performance and environmental compatibility of the ash. The solid residue was analyzed also in next section (referred as ‘washed’).

3.2. Chemical composition

The semiquantitative WDXRF analysis (Table 1) shows that the fermented grape pomace ash is predominantly composed of CaO (34.9 wt%) and K_2O (29.7 wt%), followed by significant P_2O_5 (16.3 wt%). Secondary components include MgO (5.03 wt%) and SiO_2 (5.23 wt%), while SO_3 (3.34 wt%), CuO (2.12 wt%), Al_2O_3 (1.50 wt%), and Fe_2O_3 (1.48 wt%) occur in lower concentrations. The dominance of CaO and K_2O indicates that the ash is strongly alkaline, consistent with the high mineral content typical of grape pomace residues reported in the literature (olive pomace and wine stillage studies show high ash fractions and mineral content in distillation by-products) [11]. Calcium in grape residues is largely derived from skins and seed material, where it serves as a structural component of cell walls. Upon combustion, organically bound calcium is converted primarily to CaO and CaCO3 phases, consistent with the strong alkaline character observed in other biomass ashes and their high neutralizing potential. Potassium, which is highly mobile in plant tissues, becomes relatively concentrated during fermentation and subsequent distillation of grape pomace. Although literature on XRD phases in grape pomace ash is limited, biomass ash studies generally report calcium carbonates, alkali sulphates, silicates, and other mineral phases depending on the feedstock. The presence of phosphate phases such as $Ca_5(PO_4)_3(OH)$, suggested by the P_2O_5 content, aligns with known thermal transformations of P-rich biomasses during combustion, favoring the formation of calcium phosphate minerals that are agronomically relevant. In condensed combustion residues of biomass ashes, these phosphate phases often occur alongside silicates and carbonates in ashes with high Ca and P content [12].

Table 1. *Semi-quantitative chemical composition of the Fermented Grape Pomace Ash, determined by WDXRF (in wt.%).*

Component	Fermented grape pomace ash	Fermented grape pomace ash after washing
MgO	5.03	6.37
Al_2O_3	1.50	1.57
SiO_2	5.23	6.70
P_2O_5	16.30	17.40
SO_3	3.34	0.15
Cl	0.103	0.015
K_2O	29.70	14.80
CaO	34.91	45.60
MnO	0.14	0.23
Fe_2O_3	1.48	2.81
CuO	2.12	3.50
Others	0.132	0.132

The moderate SiO_2 content and trace microelements (Cu, Zn, Mn) reflect the intrinsic mineral profile of grape biomass, which contains significant amounts of macronutrients such as K, Ca, P, and Mg in the raw pomace matrix before combustion, consistent with comprehensive characterisation studies of grape waste materials [13].

Compared with raw grape pomace and distillation stillage compositions reported in recent studies, the fermented grape pomace ash shows an enriched inorganic profile due to calcination and also the depletion of organic matter through fermentation and distillation, resulting in higher relative concentrations of ash-forming elements [11]. This trend highlights that fermented grape pomace ash is a chemically distinct material, characterised by high

alkalinity and significant Ca–K–P content, differentiating it from ashes derived from raw or minimally processed pomace.

The substantial P_2O_5 content of 16.3 wt% is particularly noteworthy. Phosphorus, initially present in both organic and inorganic forms within grape seeds and skins, becomes concentrated during combustion, leading to the formation of phosphate-bearing mineral phases. The combined presence of CaO and P_2O_5 suggest the possible formation of calcium phosphate phases, which are relevant for agronomic applications where slow phosphorus release is desired. The coexistence of MgO further supports the potential formation of mixed Ca–Mg phosphate phases or discrete MgO units. SiO_2 content is moderate compared with typical lignocellulosic biomass ashes but may derive from intrinsic plant silica and minor extrinsic contamination.

The CuO content (2.12 wt.%) is notably high for typical biomass ash and likely reflects an anthropogenic origin. A primary source is the application of Bordeaux mixture ($CuSO_4$ + $Ca(OH)_2$) in vineyards, leading to copper accumulation in grape tissues and residues [14]. An additional contribution may arise from copper distillation equipment, where acidic fermentation media can promote Cu leaching and subsequent incorporation into the solid fraction.

Overall, the oxide and mineralogical composition indicate that fermented grape pomace ash is a calcium–potassium-rich alkaline ash with considerable phosphorus content, suggesting functional relevance for agricultural (e.g., soil amendment, slow-release P source), environmental, and construction-related applications.

3.3. Mineral Composition

The principal crystalline phases identified in the fermented pomace ash were lime (CaO), calcite ($CaCO_3$), quartz (SiO_2), anorthite ($CaAl_2Si_2O_8$), arcanite (K_2SO_4), periclase (MgO), and hydroxyapatite ($Ca_5(PO_4)_3OH$) (Fig. 2). The coexistence of free lime and calcite and also potassium-calcium carbonate suggests secondary carbonation processes, either during cooling inside the kiln (reaction of CaO/K_2 O-bearing phases with CO_2 in the flue gases) or through subsequent atmospheric weathering during storage. Given the high reactivity of free CaO and alkali oxides, rapid CO_2 uptake is thermodynamically favoured under ambient conditions, especially in the presence of hygroscopic phases such as arcanite [15].

The identification of anorthite indicates interaction between Ca-rich phases and aluminosilicate components at elevated temperature, implying partial solid-state reactions within the ash matrix. Periclase likely originates from Mg-bearing organic or soil-derived inputs, while hydroxyapatite reflects the concentration of phosphorus in grape residues.

A pronounced amorphous halo is observed in the 25–35° 2θ range, indicating the presence of a substantial non-crystalline or poorly ordered phase fraction. In biomass-derived ashes, such a diffuse scattering feature is typically associated with amorphous aluminosilicate or siliceous glassy phases formed during combustion. The position of the halo suggests a silica-rich amorphous phase, potentially incorporating Ca, K, and Mg as network modifiers. The presence of amorphous phase may strongly influence the material's reactivity, particularly under alkaline activation or carbonation conditions.

3.4. Optical and Vibrational Characterization

Optical and vibrational spectroscopy were employed to refine the structural interpretation derived from XRF and XRD analyses and to clarify copper speciation, phosphate organization, and carbon structural ordering within the ash matrix. While XRF provides bulk compositional data and XRD identifies dominant crystalline phases, spectroscopic techniques enable evaluation of bonding environments, structural substitutions, and redox-related transformations.

3.4.1. UV–Vis diffuse reflectance analysis

The UV–Vis diffuse reflectance spectrum of the ash, expressed using the Kubelka-Munk function F(R), exhibits a distinct absorption band centered at approximately 566 nm (Fig. 3). This band falls within the characteristic range (~540–580) reported for localized surface plasmon resonance of metallic copper (Cu^0) nanoparticles, reflecting collective electron oscillations in zero-valent copper domains [16].

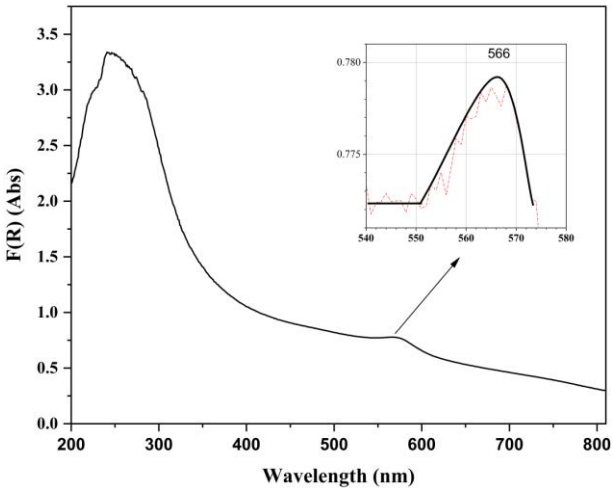


Fig. 3. *UV–Vis diffuse reflectance spectrum of copper-containing fermented grape pomace ash recorded in the 200–800 nm range and presented as the Kubelka–Munk function F(R). A surface plasmon resonance (SPR) band centred at approximately 566 nm indicates the presence of metallic copper nanoparticles.*

Considering the copper concentration exceeding 2 wt.% (expressed as CuO equivalent) established in Section 3.1, the presence of a plasmonic response indicates that a fraction of copper is present in reduced metallic form. XRD analysis suggests possible copper oxide phases; however, peak overlap prevents unambiguous phase identification. UV Vis spectroscopy therefore provides complementary information regarding copper speciation that cannot be resolved solely through bulk or crystallographic techniques.

The relatively broad character of the plasmon band suggests nanoscale dispersion and interaction with the surrounding phosphate–carbonate matrix. The occurrence of metallic copper is consistent with partial redox transformation of Cu^{2+} species during combustion. The presence of residual carbon domains, confirmed by Raman spectroscopy, supports the plausibility of localized reducing microenvironments facilitating this transformation.

The XRF analysis indicates a copper content exceeding 2 wt.% (expressed as CuO equivalent), confirming the significant presence of copper within the ash. While XRF provides bulk elemental composition, it does not differentiate between oxidation states. The detection of an LSPR band in the visible region suggests that part of the copper is present in reduced metallic form.

The formation of metallic copper nanoparticles may be attributed to partial reduction of Cu^{2+} species during combustion under locally reducing conditions created by residual carbonaceous matter. Such microenvironments are consistent with the Raman evidence of disordered carbon structures.

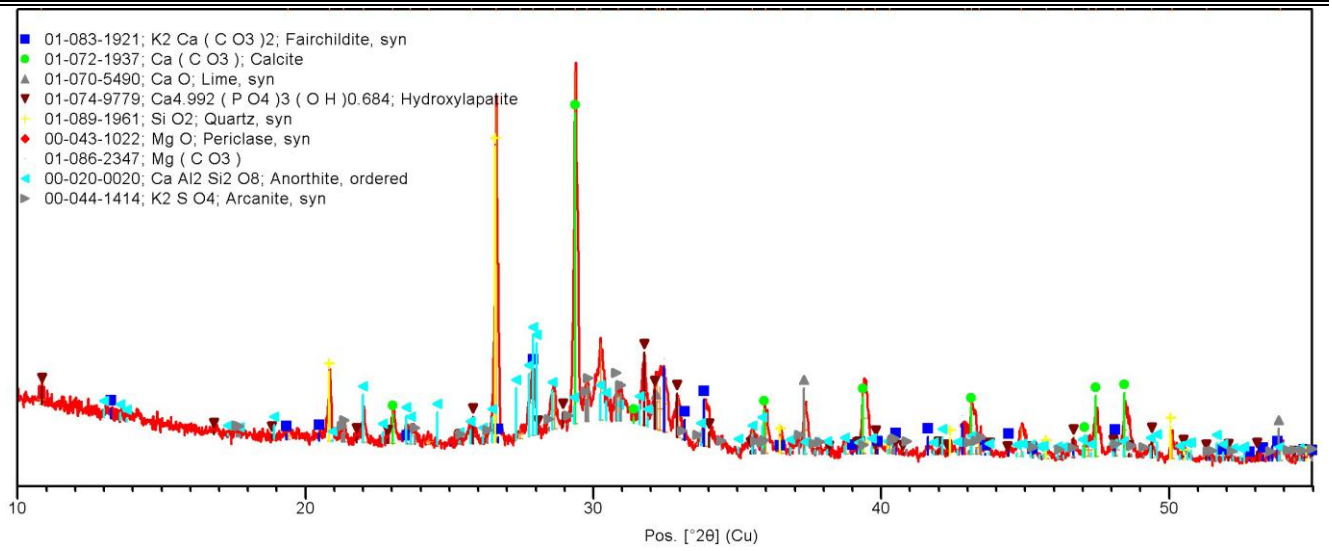


Fig. 2. *Powder XRD pattern of fermented grape pomace ash.*

3.4.2. FTIR spectroscopy

FTIR spectroscopy was employed to resolve bonding environments within the mineral matrix and to complement the structural interpretation derived from XRD and Raman analyses. The spectrum recorded in the 4000 - 400 cm^{-1} region exhibits several well-defined absorption bands indicative of a phosphate-carbonate dominated ash composition (Fig. 4).

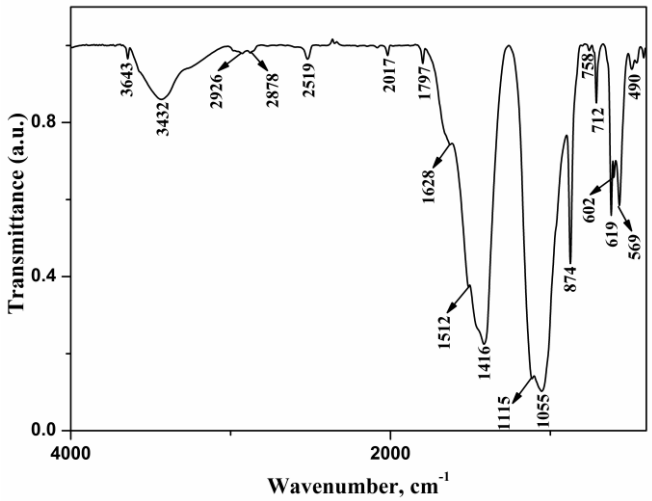


Fig. 4. *FTIR spectrum of fermented grape pomace ash Characteristic absorption bands corresponding to phosphate (PO_4^{3-}), carbonate (CO_3^{2-}), and hydroxyl groups are observed.*

A broad band centered near ~3432 cm^{-1} is attributed to O–H stretching vibrations associated with adsorbed moisture and structural hydroxyl groups, while weak features around 2926 and 2878 cm^{-1} suggest minor residual organic C–H stretching. The band at ~1628 cm^{-1} corresponds to H–O–H bending of adsorbed water [17].

The mid-infrared region is dominated by strong absorptions at ~1115 and ~1055 cm^{-1}, assigned primarily to ν3 asymmetric stretching vibrations of PO_4^{3-} groups, with possible overlap from Si–O–Si stretching, indicating coexistence of phosphate and minor silicate components [18,19]. A distinct band at ~874 cm^{-1} together with bands near ~712 and ~1416 cm^{-1} confirms the presence of carbonate groups (CO_3^{2-}), consistent with calcite formation and/or carbonate substitution within the apatite lattice [20].

Additional bands observed at ~602 and ~569 cm^{-1} correspond to ν4 bending modes of PO_4^{3-}, providing strong evidence for apatite-type calcium phosphate phases. Weak features below 500 cm^{-1} may reflect lattice vibrations of mixed Ca–O and phosphate frameworks. No clearly resolved Cu–O vibrational bands were identified, likely due to spectral overlap with phosphate modes and the relatively low or dispersed copper fraction inferred from complementary analyses.

Overall, the FTIR data corroborate a calcium phosphate-carbonate mineral framework with minor silicate contributions and hydrated surface functionalities. These findings are consistent with Raman and XRD results and support the interpretation of a partially carbonated apatite matrix hosting dispersed copper species within a thermally transformed biogenic ash.

3.4.3. Raman spectroscopy

The Raman spectrum of the mineral fraction is dominated by an intense band at 952 cm^{-1} corresponding to the ν1 symmetric stretching mode of PO_4^{3-}, which is characteristic of apatite-type calcium phosphates (Fig. 5). Additional phosphate-related vibrations are observed at 433 cm^{-1} (ν2 bending) and at 587 cm^{-1} (ν4 bending), confirming the presence of a crystalline phosphate framework [21].

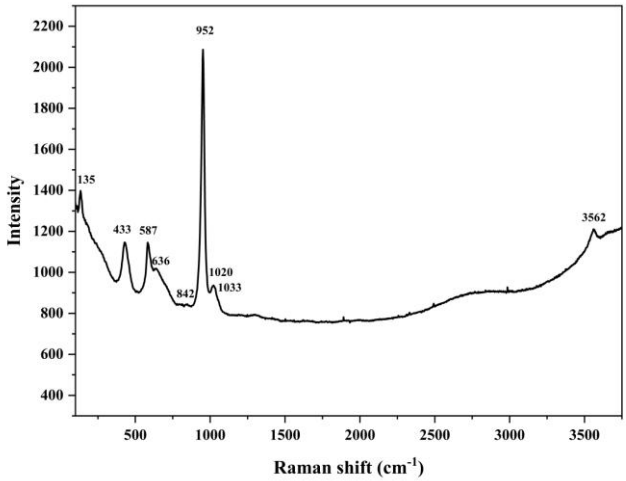


Figure 5 *Raman spectrum of the mineral fraction of fermented grape pomace ash, showing a dominant band at ~960 cm^{-1} assigned to the ν1 symmetric stretching mode of PO_4^{3-}.*

A band at 636 cm^{-1} is assigned to librational vibrations of structurally bound hydroxyl groups, while a distinct sharp peak at 3562 cm^{-1} corresponds to the ν(OH^-) stretching mode [21]. The simultaneous presence of these two hydroxyl-related Raman

features provides strong spectroscopic evidence for hydroxyapatite rather than anhydrous calcium phosphate phases.

Additional bands at 1020 and 1033 cm^{-1} are attributed to ν3 asymmetric stretching modes of PO_4^{3-}, and a feature at 842 cm^{-1} may indicate carbonate substitution within the apatite lattice [22].

Overall, the Raman data confirm that the dominant mineral phase corresponds to hydroxyl-containing, partially carbonated apatite structures, in agreement with XRD and FTIR results.

Raman spectra of carbonaceous inclusions exhibit D (~1350 cm^{-1}) and G (~1590 cm^{-1}) bands typical of disordered sp^2 carbon (Fig. 6). The estimated intensity ratio (ID/IG ≈ 0.8) indicates partially ordered but predominantly amorphous carbon, characteristic of thermally transformed lignocellulosic biomass under non-ideal combustion conditions

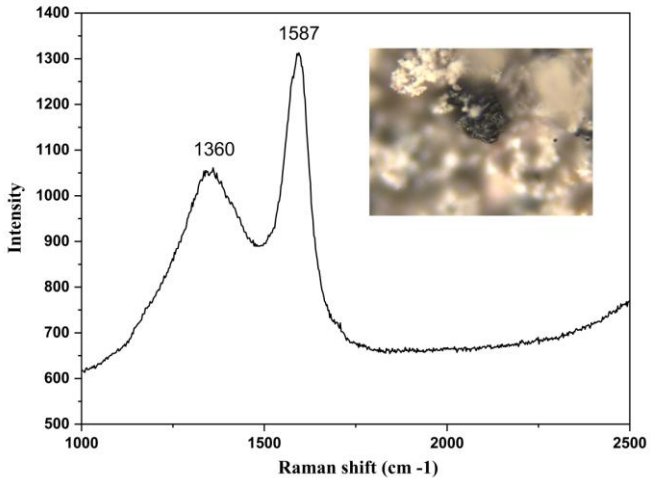


Figure 6 *Raman spectrum of a carbonaceous particle isolated from fermented grape pomace ash, exhibiting characteristic D (~1350 cm^{-1}) and G (~1590 cm^{-1}) bands typical of disordered sp^2 carbon structures.*

From a mechanistic perspective, the coexistence of disordered carbon and copper species provides a structurally consistent explanation for the partial reduction of Cu^{2+} species inferred from UV Vis analysis. Such carbon-rich microdomains may transiently act as reducing environments during thermal treatment.

Distinct Raman modes attributable exclusively to crystalline CuO were not clearly resolved, which is consistent with peak overlap in XRD and suggests fine dispersion or structural association of copper within the phosphate-carbonate matrix.

3.4.4. Structural Implications in View of Application Potential

The combined spectroscopic results refine the structural model derived from XRF and XRD analyses and provide additional insight into the physicochemical state of the material.

The ash is composed of a calcium phosphate-carbonate mineral framework incorporating dispersed copper species and residual carbon domains formed during thermal transformation. The identification of apatite-type phosphate phases with partial carbonate substitution suggests a structurally stable but potentially moderately reactive mineral matrix. The presence of disordered carbon indicates incomplete combustion and local redox heterogeneity, while UV Vis evidence of metallic Cu^0 nanoparticles confirms that partial reduction of copper species occurred during thermal processing.

From a materials perspective, this structural configuration directly influences the potential behavior of the ash under environmental or technological conditions. Phosphate bonding environments, carbonate substitution, copper speciation, and residual carbon content are expected to govern dissolution kinetics, redox interactions, nutrient release profiles, trace metal mobility, and reactivity in alkaline systems.

Accordingly, the structural features identified through optical and vibrational spectroscopy provide the physicochemical basis for evaluating the technically plausible application pathways discussed in the following section.

3.5. Potential application of fermented grape pomace ash

3.5.1. Agricultural application as fertilizer or soil amendment

The physicochemical profile of the fermented grape pomace ash, characterized by high CaO–K_2 O–P_2 O_5 contents, moderate MgO and SiO_2 fractions, a partially amorphous phase assemblage, and elevated copper concentration, enables several technically plausible application pathways. However, each route requires application-specific validation, particularly with respect to solubility, leaching behaviour, and long-term stability.

The high concentrations of potassium (29.7 wt.% K_2 O) and phosphorus (16.3 wt.% P_2 O_5), combined with Ca and Mg, position fermented grape pomace ash as a potential multi-nutrient mineral fertilizer. Potassium is predominantly present in soluble or partially soluble phases (e.g., sulphates), whereas phosphorus is largely associated with calcium phosphate phases, including hydroxyapatite. This mineralogical form suggests a relatively slow P-release profile, potentially advantageous for sustained nutrient supply and reduced leaching compared to highly soluble phosphate fertilizers. Calcium and magnesium may contribute to soil pH correction, particularly in acidic soils, due to the presence of free lime and carbonate phases. The neutralizing potential of the ash should therefore be quantified via acid–base titration and compared with conventional liming agents. A critical constraint, however, is the elevated copper content (>2 wt.% CuO equivalent). While copper is an essential micronutrient, excessive accumulation may result in phytotoxicity and soil contamination, particularly under repeated application

3.5.2. CO_2 sequestration and mineral carbonation

The high CaO content (34.9 wt.% before washing and 45.6 wt.% after washing) indicates a substantial theoretical carbonation capacity of the fermented grape pomace ash. Free lime, together with other alkaline oxides such as MgO and K_2 O, can react with atmospheric or concentrated CO_2 to form thermodynamically stable carbonate phases. The simultaneous presence of CaO and $CaCO_3$ in the analyzed material suggests that partial spontaneous carbonation has already occurred during cooling in the combustion chamber and subsequent storage under ambient conditions.

Under controlled conditions, mineral carbonation of fermented grape pomace ash could enable permanent CO_2 fixation through the conversion of reactive oxides into stable carbonates. This transformation would simultaneously stabilize free lime, reducing the risk of volumetric instability, and lower the overall alkalinity of the material, potentially decreasing the mobility of trace metals, including copper. The carbonation process may therefore function both as a carbon sequestration pathway and as a chemical stabilization strategy.

3.5.3. Use in cementitious and alkali-activated materials

The mineralogical and chemical characteristics of the fermented grape pomace ash indicate that it may be incorporated into cementitious systems either as a supplementary mineral additive at low replacement levels or as a precursor component in alkali-activated and hybrid binders. This potential derives from several intrinsic features of the material. The XRD pattern reveals a significant amorphous fraction, evidenced by the diffuse halo in the 25–35° 2θ range, which may provide pozzolanic or alkali-activation reactivity. The presence of free CaO and calcite contributes to inherent alkalinity, while moderate SiO_2 and Al_2O_3 contents offer a minimal aluminosilicate framework. After grinding, the ash exhibits

a fine particulate morphology that may support filler effects and particle packing improvement in composite systems.

In Portland cement-based matrices, fermented grape pomace ash would be expected to function as a filler and as reactive pozzolan. The elevated phosphate content, however, introduces potential interactions with early hydration processes but hydroxyapatite is relative stable in alkaline conditions. For this reason, detailed studies and setting time measurements, are necessary to quantify any modification of hydration behavior.

In alkali-activated and geopolymer systems fermented grape pomace ash may contribute additional calcium for C–A–S–H-type gel formation. The amorphous fraction could display partial dissolution under highly alkaline activation. The relatively high P content may again influence gel chemistry in Ca-rich systems, and its incorporation into the reaction products should be clarified using spectroscopic or microstructural techniques.

A significant limitation of the untreated ash is the presence of soluble sulfates and chlorides. These components may increase the risk of reinforcement corrosion, promote secondary ettringite formation under favorable conditions, and potentially affect dimensional stability and long-term durability. The washing procedure substantially reduces SO_3 , Cl, and K_2O contents, demonstrating that pre-treatment effectively lowers the concentration of soluble salts and enhances compatibility with reinforced cementitious systems.

3.5.4. UV–Vis diffuse reflectance analysis

Copper is recognized as a strategic and critical raw material within the European Union due to its central role in electrical infrastructure, renewable energy technologies, and electrification pathways. The relatively high copper concentration in fermented grape pomace ash (2.12 wt.% expressed as CuO) and 3.5wt.% in the washed ash, therefore represents a potential resource opportunity. The feasibility of selective recovery depends strongly on copper speciation. Spectroscopic evidence indicating the presence of metallic Cu^0 nanoparticles, in addition to oxidized Cu^{2+} species, suggests that at least part of the copper may be accessible through reductive or acidic dissolution routes. Hydrometallurgical processing, such as controlled acid leaching followed by electrochemical recovery or precipitation, could be considered as a valorization pathway. However, the economic viability of such an approach would depend on several interrelated factors, including the fraction of extractable copper relative to total content, the efficiency and selectivity of the leaching process in the presence of high Ca and P concentrations, the energy and reagent demand, and the overall scale of ash generation.

An alternative strategy is direct functional utilization of the copper-bearing ash without prior extraction. Copper species, including both Cu^0 nanoparticles and Cu^{2+} ions, are widely recognized for their bactericidal and fungicidal properties [23]. In this context, fermented grape pomace ash could serve as an antimicrobial additive in mineral matrices. One practical application may involve incorporation into lime-based formulations for winter treatment of fruit tree's trunks, where copper-based compounds are traditionally employed. In addition, the ash could be explored as a functional component in antimicrobial mineral coatings or as a filler in cementitious composites designed for hygienic or high-contact surfaces.

4. Conclusions

Fermented grape pomace ash derived from brandy production represents a chemically complex Ca–K–P-rich biomass ash characterized by pronounced alkalinity, elevated phosphorus content, and a notable concentration of copper. A water-soluble fraction of 17.1 wt.% indicates the presence of mobile salts (mostly arcanite), which govern leaching behaviour and define both functional reactivity and environmental risk.

Accordingly, this material should be regarded not as a waste residue but as a multifunctional secondary raw resource, with prospective applications in soil amendment, mineral CO_2 sequestration, and incorporation into cementitious or alkali-activated binder systems, subject to appropriate environmental and performance validation.

Acknowledgements: This work has been carried out in the framework of the National Science Program "Critical and strategic raw materials for a green transition and sustainable development", approved by the Resolution of the Council of Ministers № 508/18.07.2024 and funded by the Ministry of Education and Science (MES) of Bulgaria. We would like to express our gratitude for the technical support to programme "Research, Innovation and Digitalisation for Smart Transformation" 2021–2027, funded by the European Union, Project BG16RFPR002-1.014-0007 "Center for Competence PERIMED-2".

5. References:

1. Miranda, M.; Arranz, J.; Román, S.; Rojas, S.; Montero, I.; López, M.; Cruz, J. Characterization of grape pomace and pyrenean oak pellets. *Fuel processing technology* **2011**, *92*, 278-283.
2. Pereira, P.; Palma, C.; Ferreira-Pêgo, C.; Amaral, O.; Amaral, A.; Rijo, P.; Gregório, J.; Palma, L.; Nicolai, M. Grape pomace: A potential ingredient for the human diet. *Foods* **2020**, *9*, 1772.
3. Pop, I.; Pascariu, S.M.; Simeanu, D.; Radu-Rusu, C.; Albu, A. Determination of the chemical composition of the grape pomace of different varieties of grapes. *Scientific Papers-Animal Science Series: Lucraritiinifice-Seria Zootehnie* **2015**, *63*, 76-80.
4. Valiente, C.; Arrigoni, E.; Esteban, R.; Amado, R. Grape pomace as a potential food fiber. *Journal of Food Science* **1995**, *60*, 818-820.
5. Mohamed Ahmed, I.A.; Özcan, M.M.; Al Juhaimi, F.; Babiker, E.F.E.; Ghafoor, K.; Banjanin, T.; Osman, M.A.; Gassem, M.A.; Alqah, H.A. Chemical composition, bioactive compounds, mineral contents, and fatty acid composition of pomace powder of different grape varieties. *Journal of Food Processing and Preservation* **2020**, *44*, e14539.
6. Mortari, D.; Perondi, D.; Rossi, G.; Bonato, J.; Godinho, M.; Pereira, F. The influence of water-soluble inorganic matter on combustion of grape pomace and its chars produced by slow and fast pyrolysis. *Fuel* **2021**, *284*, 118880.
7. Moço, A.; Costa, M.; Casaca, C. Ash deposit formation during the combustion of pulverized grape pomace in a drop tube furnace. *Energy conversion and management* **2018**, *169*, 383-389.
8. Vassilev, S.V.; Baxter, D.; Vassileva, C.G. An overview of the behaviour of biomass during combustion: Part I. Phase-mineral transformations of organic and inorganic matter. *Fuel* **2013**, *112*, 391-449.
9. Nikolov, A.; Kostov, V.; Petrova, N.; Tsvetanova, L.; Vassilev, S.V.; Titorenkova, R. Sunflower Shells Biomass Fly Ash as Alternative Alkali Activator for One-Part Cement Based on Ladle Slag. *Ceramics* **2025**, *8*, 79.
10. Vassilev, S.V.; Vassileva, C.G. Water-soluble fractions of biomass and biomass ash and their significance for biofuel application. *Energy & Fuels* **2019**, *33*, 2763-2777.
11. Oliveira, M.; Teixeira, B.M.; Toste, R.; Borges, A.D. Transforming wine by-products into energy: Evaluating grape pomace and distillation stillage for biomass pellet production. *Applied Sciences* **2024**, *14*, 7313.
12. Kalembkiewicz, J.; Galas, D.; Sitarz-Palczak, E. The physicochemical properties and composition of biomass ash and evaluating directions of its applications. *Polish Journal of Environmental Studies* **2018**, *27*, 2593-2603.
13. Machado, A.R.; Voss, G.B.; Machado, M.; Paiva, J.A.; Nunes, J.; Pintado, M. Chemical characterization of the cultivar 'Vinhão'(Vitis vinifera L.) grape pomace towards its circular valorisation and its health benefits. *Measurement: Food* **2024**, *15*, 100175.

14. Wang, J.; Ma, T.; Wei, M.; Lan, T.; Bao, S.; Zhao, Q.; Fang, Y.; Sun, X. Copper in grape and wine industry: Source, presence, impacts on production and human health, and removal methods. *Comprehensive Reviews in Food Science and Food Safety* **2023**, *22*, 1794-1816.
15. Nikolov, A.; Kostov-Kytin, V.; Tarassov, M.; Tsvetanova, L.; Lazarova, H.; Tasheva, T. Products of carbonation of cement kiln dust. *Review of the Bulgarian Geological Society* **2024**, *85*, 163-166.
16. Kandikonda, R.; Murugadoss, G.; Venkatesh, N.; Subbaraj, S.S.V.; Palani, D.; Thota, S.; Rajaboina, R.K.; Divi, H.; Dhayalan, M.; Phanumartwiwath, A. Redox-driven synthesis of stable copper nanoparticles via metal displacement and their application in organic dye degradation. *Materials Advances* **2025**, *6*, 9575-9589.
17. Rehman, I.; Bonfield, W. Characterization of hydroxyapatite and carbonated apatite by photo acoustic FTIR spectroscopy. *Journal of materials science: materials in Medicine* **1997**, *8*, 1-4.
18. Grunenwald, A.; Keyser, C.; Sautereau, A.-M.; Crubézy, E.; Ludes, B.; Drouet, C. Revisiting carbonate quantification in apatite (bio) minerals: a validated FTIR methodology. *Journal of archaeological science* **2014**, *49*, 134-141.
19. Apfelbaum, F.; Diab, H.; Mayer, I.; Featherstone, J. An FTIR study of carbonate in synthetic apatites. *Journal of inorganic biochemistry* **1992**, *45*, 277-282.
20. Stoch, A.; Jastrzębski, W.; Brożek, A.; Trybalska, B.; Cichocińska, M.; Szarawara, E. FTIR monitoring of the growth of the carbonate containing apatite layers from simulated and natural body fluids. *Journal of Molecular Structure* **1999**, *511*, 287-294.
21. Baldassarre, F.; Altomare, A.; Mesto, E.; Lacalamita, M.; Dida, B.; Mele, A.; Bauer, E.M.; Puzone, M.; Tempesta, E.; Capelli, D. Structural characterization of low-Sr-doped hydroxyapatite obtained by solid-state synthesis. *Crystals* **2023**, *13*, 117.
22. Penel, G.; Leroy, G.; Rey, C.; Bres, E. MicroRaman spectral study of the PO4 and CO3 vibrational modes in synthetic and biological apatites. *Calcified tissue international* **1998**, *63*, 475-481.
23. Nikolov, A.; Dobreva, L.; Danova, S.; Miteva-Staleva, J.; Krumova, E.; Rashev, V.; Vilhelmova-Ilieva, N. Natural and modified zeolite clinoptilolite with antimicrobial properties: A review. *Acta Microbiologica Bulgarica* **2023**, *39*, 147-161.

Influence of femtosecond laser processing parameters on the surface morphology of titanium alloy

Ljerka Slokar Benić[1*], Hrvoje Skenderović[2], Franjo Kozina[1], Matej Barać[1]
University of Zagreb Faculty of Metallurgy, Aleja narodnih heroja 3, 44000 Sisak, Croatia[1]
Institute of Physics, Bijenička cesta 46, 10000 Zagreb, Croatia[2]
slokar@simet.unizg.hr

Abstract: *Titanium alloys are essential in biomedicine due to their high specific strength and biocompatibility, with surface properties directly influencing the successful osseointegration of implants. In this study, surface texturing of an experimental titanium alloy was performed using an ultrafast femtosecond laser with varying pulse energies. Roughness and topography were analysed using optical profilometry and confocal laser scanning microscopy, while microhardness was measured by the Vickers method. The results show that a pulse energy of 2.1 μJ, with a wavelength of 1030 nm, pulse duration of 190 fs, and repetition rate of 1 MHz, constitutes the optimal laser process parameters for achieving the desired surface properties in engineering and biomedical applications.*
Keywords*: TITANIUM ALLOY, FEMTOSECOND LASER, ROUGHNESS, MICROHARDNESS*

1. Introduction

Due to their biocompatibility and excellent mechanical and corrosion properties, titanium alloys play a significant role in modern engineering and biomedical applications, particularly in the production of orthopaedic and dental implants. Additionally, surface properties are crucial for successful interaction with biological tissue and the long-term functionality of implants. The femtosecond laser offers great potential for biomedical applications because it provides high precision, flexibility, and broad applicability. Femtosecond laser ablation is notable among techniques for modifying the texture and roughness of implant surfaces to improve osseointegration. This method is increasingly used due to its precise control over surface topography, high efficiency, and low material consumption. Numerous studies confirm that specially patterned roughness can improve tensile properties and help prevent bacterial colonization [1]–[5].

This work aims to analyse the surface morphology, specifically surface roughness and microhardness, of an experimental titanium alloy to determine the femtosecond laser process parameters required to achieve favourable surface properties for biomedical applications.

2. Materials and Methods

An experimental titanium alloy with the chemical composition Ti-10Nb-10Cr was produced by melting in an electric arc furnace under an argon atmosphere in a copper mould, which was rapidly cooled with water. Casting was performed by a pressure process in a vacuum furnace to form a plate measuring 32 mm × 10 mm × 1 mm. The cast plate was metallographically prepared by grinding and polishing. For surface texturing of the samples in this work, a PHAROS-type Yb femtosecond laser (Light Conversion, Vilnius, Lithuania) was used. The optical system is shown schematically in Figure 1.

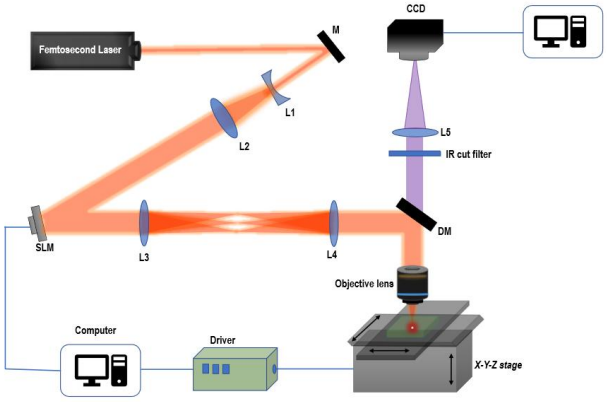


Fig. 1 *Schema of optical system.*

A femtosecond laser system emits ultrashort pulses at a central wavelength of 1030 nm with a tunable pulse repetition rate, ranging from single pulses to 1 MHz. The 190 fs pulse duration enables very high peak pulse power, allowing nonlinear interaction with the material and precise ablation with minimal thermal impact. Experiments were conducted at various pulse energies (Table 1) to investigate their effects on the morphology and topography of the titanium alloy surface. The pulse energy was the primary parameter controlling the laser-material interaction, while the pulse frequency determined the average power and heat accumulation.

Table 1: *Parameters of the femtosecond laser used in the experiment.*

Sample	1	2	3	4	5
Pulse energy [μJ]	0.7	1.5	2.1	2.6	3.0

The roughness of the femtosecond laser-textured surface was measured using a 3D optical profilometer, Filmetrics ProFilm 3D (KLA Corporation, Milpitas, CA, USA). This optical profilometer is a measuring system for non-contact determination of surface topography with high spatial resolution. The device is based on white light interferometry and enables precise measurement of surface irregularities, height differences, and shapes over a wide range of dimensions. The system provides a three-dimensional display of the surface in natural colours, with each pixel optimally focused throughout the entire measurement range.

Confocal laser scanning microscopy was used to characterise the surfaces of samples textured with a femtosecond laser. For this purpose, an Olympus LEXT OLS5100 confocal laser scanning microscope was used with the Olympus OLS5100 Data acquisition application and Olympus OLS5100 analysis application software packages.

The microhardness of the titanium alloy before and after texturing with a femtosecond laser was measured by the Vickers method (HV) using a Leica VHMT hardness tester (Leica Microsystems, Wetzlaru, Germany). Measurements were carried out with a force of 9.80 N (HV1), and the indenter's dwell time was 10 seconds. The microscope magnification used to measure the diagonals of the impression was 500×.

3. Results and Discussion

In Figure 2, surfaces of titanium alloy textured with a femtosecond laser are shown, photographed with a digital camera through a magnifying glass. Dark squares measuring 1 mm × 1 mm are visible.

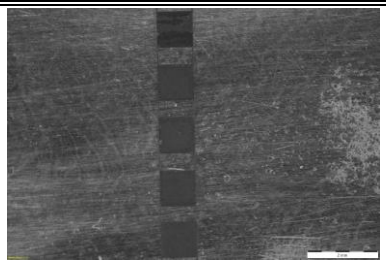


Fig. 2 *Femtosecond laser-textured titanium alloy surfaces.*

The surface roughness of the titanium alloy after texturing with a femtosecond laser at different pulse energies was measured using an optical profilometer.

First, the surface roughness of the titanium alloy that was not laser-textured was measured. Its surface roughness value is S_a = 0.18 µm, indicating a relatively smooth, unchanged surface. The topography of the surface that was not treated with the laser is shown in Figure 3.

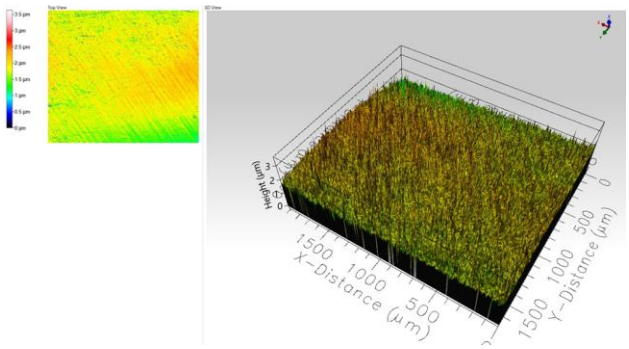


Fig. 3 *Topography of titanium alloy before fs texturing.*

Figure 3 shows the three-dimensional topography of the titanium alloy surface, obtained using a 3D optical profilometer. The measurement covers an area of approximately 1500 × 1500 µm, with the surface height distribution displayed in the nanometre range using a colourimetric scale. The results indicate a relatively smooth and homogeneous surface with small height variations. Slight irregularities, primarily resulting from previous mechanical processing such as grinding and polishing, are predominant. The low roughness value (S_a = 0.18 µm) indicates limited topographic complexity, which may be unfavourable for biological integration, as such a surface provides fewer sites for cell and protein adhesion.

Measurements of surface roughness were also carried out at five different pulse energies: 0.7 µJ, 1.5 µJ, 2.1 µJ, 2.6 µJ, and 3.0 µJ. The mean arithmetic roughness values, Sa, are shown in Table 2.

The results in Table 2 clearly show that roughness increases with higher laser pulse energy. At the lowest energy (0.7 µJ), the sample surface was relatively smooth, with a S_a value of 0.23 µm, indicating minimal material removal and slight texturing. Increasing the pulse energy to 1.5 µJ and 2.1 µJ led to a gradual rise in the S_a value to 0.32 µm and 0.37 µm, respectively, as a result of more intense material removal and the formation of deeper microstructures on the surface.

Table 2: *Surface roughness of titanium alloy textured with a femtosecond laser.*

E (µJ)	S_a (µm)
0.7	0.23
1.5	0.32
2.1	0.37
2.6	0.56
3.0	0.86

A more significant increase in roughness is observed at energies of 2.6 µJ and 3.0 µJ, with S_a values reaching 0.56 µm and 0.86 µm. This trend can be explained by the higher local laser energy density, which leads to more intense melting and ablation of the material, resulting in the formation of more pronounced micro-nanostructures. Such an exponential increase in roughness at higher energies indicates that the surface is transitioning from a phase of mild microtexture to one of significant microporosity.

Comparison with the untreated surface clearly shows that femtosecond laser texturing can precisely increase the roughness of titanium alloy, and its intensity can be controlled from minimal modifications to pronounced microstructures by simply adjusting the pulse energy. Such control of surface morphology is particularly relevant in applications where it is important to optimise adhesion to coatings or improve osseointegration of medical implants.

These results are consistent with the literature, which shows that increasing the pulse energy of a femtosecond laser directly affects the depth and sharpness of surface microstructures, while too low energies do not produce significant morphological changes. For applications requiring controlled roughness, such as improving adhesion to coatings or osseointegration in medical implants, it is possible to optimise the pulse energy to achieve the desired Sa value without excessive material ablation. The generally accepted roughness classification for implants is as follows: < 0.5 µm = smooth; 0.5–1.0 µm = minimally rough; 1.0–2.0 µm = moderately rough; > 2.0 µm = highly rough. According to the measured roughness values in this experiment, the surfaces are considered smooth or minimally rough. Authors state that moderately rough surfaces (approximately 1–2 µm S_a) significantly improve osseointegration and biological response compared to smooth surfaces [6], [7].

The dependence of the surface roughness of the titanium alloy on the applied pulse energies is shown graphically in Figure 4.

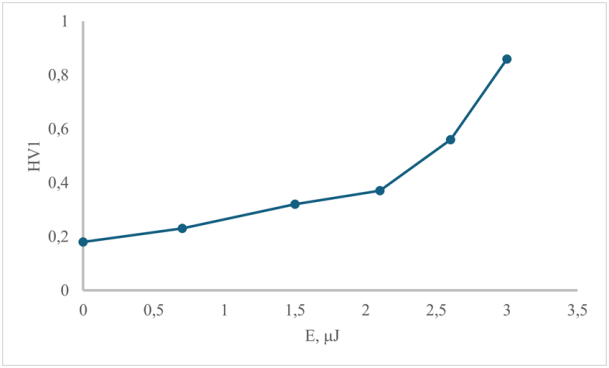


Fig.4 *Dependence of surface roughness of textured titanium alloy on femtosecond laser pulse energy.*

Experimental data confirm that the roughness of the titanium alloy surface increases as the pulse energy of the femtosecond laser increases, with the largest increase observed between 2.6 µJ and 3.0 µJ. These results indicate that the surface morphology and functional properties of titanium surfaces can be controlled by precisely adjusting the laser parameters.

A three-dimensional representation of the morphology of fs-textured surfaces obtained by a 3D profilometer is shown in Figure 5. Figure 5a shows the three-dimensional topography of the surface of a titanium alloy textured with a fs laser at a pulse energy of 0.7 µJ. The topography analysis indicates that the laser treatment modified the surface morphology compared to the initial state. The resulting surface exhibits a pronounced microrelief structure with noticeable elevations and depressions, visible in both 2D and 3D views. The height differences on the surface reach several micrometres, indicating effective interaction of the laser beam with the material at the selected pulse energy. The inhomogeneous colour distribution (green–yellow–red) reflects local variations in ablation depth and redistribution of molten material. The texture appears to spread relatively evenly over the entire analysed area,

without large macroscopic defects such as cracks or areas of excessive thermal damage.

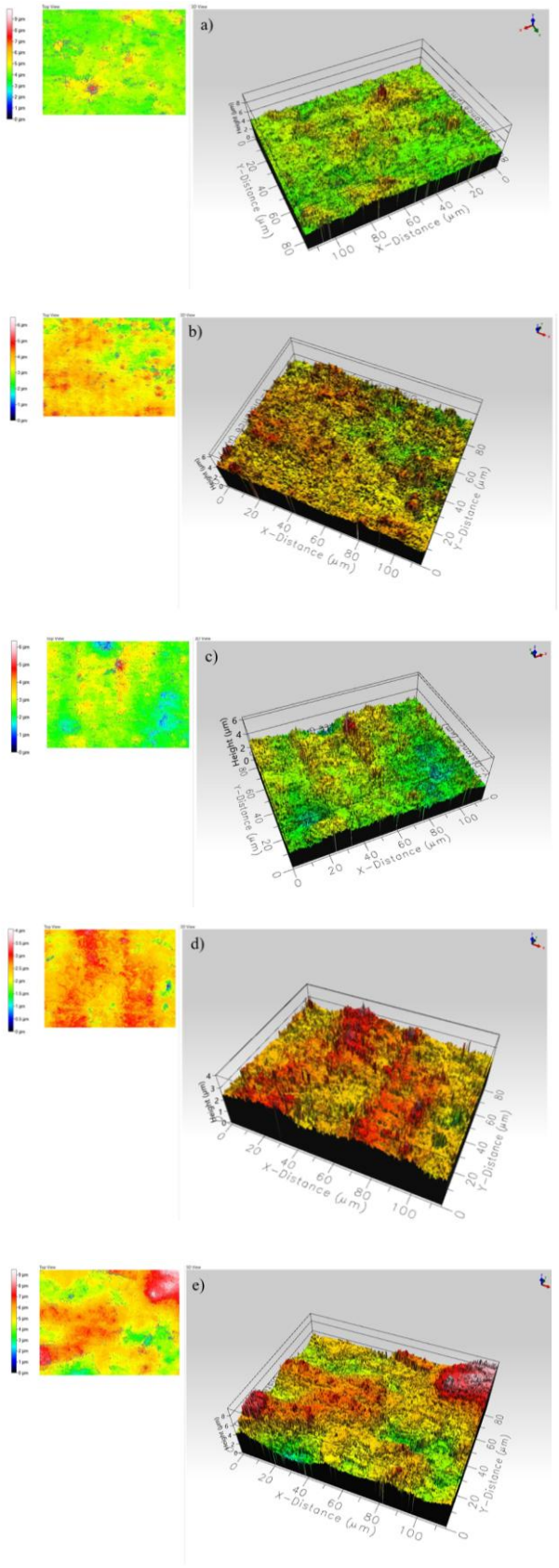


Fig.5 *Titanium alloy surfaces textured with various pulse energies: a) 0.7 µJ; b) 1.5 µJ; c) 2.1 µJ; d) 2.6 µJ; e) 3.0 µJ.*

At a pulse energy of 1.5 µJ, the microrelief structure develops further compared to lower energies (Figure 5b). 2D and 3D analyses show more pronounced and clearly defined elevations and depressions, as well as greater height differences, indicating a more intense interaction between the laser radiation and the material and more effective ablation. The more contrasting colour distribution in the 3D view confirms greater local variations in depth, with no signs of uncontrolled thermal damage. The surface remains homogeneous, without cracks or major defects, confirming the stability and repeatability of the processing. Increased roughness (S_a = 0.32 µm) indicates a transition towards a more pronounced microstructured surface, suitable for improved adhesion and proliferation of osteoblastic cells, while maintaining mechanical stability.

By increasing the pulse energy to 2.1 µJ, the microrelief becomes more pronounced, with greater surface roughness (Figure 5c). The 3D topography reveals a more complex morphology with micro- and sub-micrometre features and larger height differences compared to lower energies. A more uneven distribution of colours indicates more pronounced local variations in ablation intensity, probably due to nonlinear interactions of the femtosecond pulses with the material. Despite this, the absence of macroscopic defects and heat-affected zones confirms that the process remains predominantly ablative, without significant melting of the surrounding material.

At an energy of 2.6 µJ, there is a sudden increase in roughness and more pronounced morphological changes (Figure 5d). The 3D topography reveals deep depressions and sharp ridges, indicating strong ablation and a larger volume of material removed per pulse. Marked contrasts in the colour distribution suggest locally intensive ablation and possible redeposition of material. Although macroscopic defects are mostly absent, signs of weaker process control are evident. Increased roughness (S_a = 0.56 µm) can be functionally beneficial, but in biomedical applications it may cause stress concentrations, greater corrosion propensity, and an unfavourable biological response.

The highest applied energy, 3.0 µJ, resulted in an extremely rough and strongly modified topography (Figure 5e). Two-dimensional and three-dimensional images reveal deep crater structures, irregular shapes, and large height differences, indicating the dominance of strong ablation and non-linear processes. The highly inhomogeneous colour distribution suggests significant differences in ablation depth and possible melting and resolidification of the material. Such morphology can impair mechanical stability and promote the retention of impurities or bacteria. Although high roughness (S_a = 0.86 µm) increases the specific surface area, it is considered less favourable in biomedical applications due to potentially adverse long-term biological and corrosion behaviour.

Figure 6 shows the topography of the surface of a titanium alloy previously textured by a femtosecond laser, obtained using a confocal laser scanning microscope at a magnification of 500×. The image is presented as a height map, where different colours represent relative differences in surface height. Blue and green areas correspond to lower regions of the surface, while yellow and red tones indicate raised structures. A pronounced heterogeneity of the relief is visible, with clearly observed depressions and elevations, which is characteristic of laser processing on ultrashort time scales. The texture displays oriented irregularities that can be associated with the laser beam path and local energy distribution during femtosecond ablation. The presence of fine microstructures indicates dominant nonlinear laser–material interactions, with a minimal heat-affected zone, which is one of the key advantages of femtosecond laser texturing.

By analysing confocal images of titanium alloy surfaces processed with pulsed energy ranging from 0.7 µJ to 3.0 µJ, a clear and systematic trend in the evolution of the surface morphology of the titanium alloy is observed (Figure 6a-6e). At the lowest pulse energy tested, 0.7 µJ, the initial formation of laser-induced periodic surface structures (LIPSS) appears on the titanium alloy surface. These structures manifest as weakly expressed, predominantly vertically oriented lines covering the analysed area.

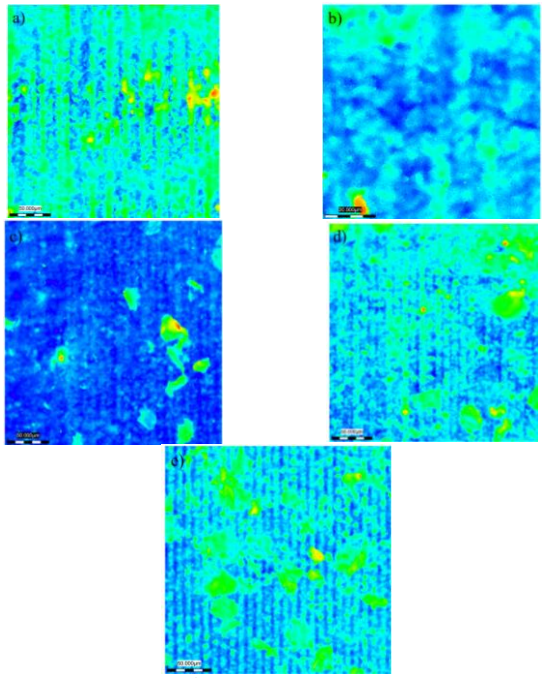


Fig. 6 *Titanium alloy surfaces textured with various pulse energies: a) 0.7 μJ; b) 1.5 μJ; c) 2.1 μJ; d) 2.6 μJ; e) 3.0 μJ.*

The appearance of LIPSS indicates that the applied pulse energy is slightly above the ablation threshold for the titanium alloy used, where nonlinear optical effects and surface electromagnetic interference dominate. In this regime (0.7 μJ), the morphology is relatively uniform with a small amplitude of height deviations, confirming the precision of texturing with minimal thermal influence. With an increase in pulse energy to 1.5 μJ, the periodic line structures become less well defined, and the relief becomes more diffuse. This state suggests a transitional area between dominantly optically driven LIPSS formation and thermally assisted structuring, where, along with pure ablation, local surface melting also begins to occur. At higher energy levels (≥ 2.1 μJ), there is a clear change in the processing regime, where deeper micro-channels and accumulations of deposited material (debris) are observed instead of LIPSS. Although at the highest energy of 3.0 μJ properly oriented vertical channels can still be seen in the background, the presence of large fragments created by explosive ablation disrupts the functional regularity and purity of the underlying periodic texture. Thus, as the energy increases, there is a gradual development and deepening of LIPSS structures, which at lower energies are regular and shallow, while at higher energies they become wider, deeper, and less homogeneous. In parallel, a significant increase in surface roughness is noted, clearly visible through the expansion of the colour range on the height maps of the confocal microscope. At the same time, increased pulse energy leads to a greater amount of secondary deposited material, marking the transition from the precise laser texturing regime to the coarse ablation regime. This transition is key for process optimisation, as it defines a trade-off between the regularity of the structure and the degree of thermal damage to the surface.

The HV1 microhardness measurement results for all samples are shown in Table 3. The reference sample without laser treatment (E = 0 μJ) exhibited a microhardness of 392 HV1. After femtosecond laser texturing, changes in surface hardness were observed, depending on the applied pulse energy. At a pulse energy of 0.7 μJ, microhardness decreased to 339 HV1, which can be attributed to initial softening of the surface layer due to local thermal effects and microstructural changes without significant hardening. Increasing the pulse energy to 1.5 μJ resulted in a significant rise in microhardness to 464 HV1, while the maximum value of 526 HV1 was achieved at 2.1 μJ. This increase suggests a more effective influence of femtosecond lasering, likely related to microstructure refinement, increased dislocation density, and possible formation of compressive residual stresses in the surface layer. Further increasing the pulse energy to 2.6 μJ and 3.0 μJ led to a decrease in microhardness, to 356 HV1 and 365 HV1, respectively. This trend can be attributed to excessive laser energy, which causes stronger ablation, local overheating, or partial relaxation of residual stresses, thereby reducing the surface hardening effect.

Table 3: *Microhardness of all samples of the experimental titanium alloy*.

E (μJ)	HV1
0.7	392
1.5	339
2.1	464
2.6	526
3.0	356

Overall, the results of microhardness measurements indicate an optimal range of femtosecond laser pulse energy (approximately 1.5–2.1 μJ) in which surface microhardness increases compared to the untreated sample. Outside this range, the effect of laser treatment on surface hardness is reduced, emphasising the importance of proper selection of process parameters.

4. Conclusion

In this study, the surface of an experimental titanium alloy with the chemical composition Ti-10Cr-10Nb was textured using a femtosecond laser at different pulse energies. Results clearly show that the laser pulse energy has a decisive influence on the surface topography, roughness, and microhardness of the material. The results confirm that by varying the pulse energy, the surface characteristics can be controlled in a targeted manner, but there is also a significant compromise between the topographic and mechanical properties.

Based on all the results obtained, it can be concluded that a pulse energy of 2.1 μJ at a laser beam wavelength of 1030 nm, a pulse duration of 190 fs, and a repetition rate of 1 MHz represents the optimal value of the process parameters. Such a surface simultaneously ensures mechanical stability and a microrelief suitable for biological adhesion, which is especially important in applications such as biomedical implants.

5. References

1. S. Shaikh, S. Kedia, D. Singh, M. Subramanian, S. Sinha, J. Laser Appl. **31**, 2, 1–22 (2019)
2. A. M. Beltrán et al., Materials **15**, 2969 (2022)
3. S. M. Eun et al., J. Funct. Biomater. **14**,10 (2023)
4. K. Zhou et al., Micromachines **15**, 152 (2024)
5. H. Sun, J. Li, et al., Coatings **12**, 10 (2022)
6. A. Wennerberg, T. Albrektsson, Clin. Oral Implants Res. **20**, 4, 172–184 (2009)
7. N.P. Lang, S. Jepsen, Clin. Oral Impl. Res. **20**, 4, 228–231 (2009)

Acknowledgments

The investigation was carried out as part of the Institutional Research Project the "Synthesis and characterization of biomedical materials (SIKABIM)" financed by the EU – Next Generation EU. The views and opinions expressed are those of the author and do not necessarily reflect the official positions of the European Union or the European Commission. Neither the European Union nor the European Commission can be held responsible for them. The research was conducted as part of the scientific applied project "Fabrication of bioelectronic elements using fs laser", financed by the EU – Next Generation EU. The views and opinions expressed are those of the author and do not necessarily reflect the official positions of the European Union or the European Commission. Neither the European Union nor the European Commission can be held responsible for them.the scientific research infrastructure projects: Center for Foundry – SIMET (code: KK.01.1.1.02.0020) and VIRTULAB – Integrated Laboratory for Primary and Secondary Raw Materials (code: KK.01.1.1.02.0022), funded by the European Regional Development Fund, Operational Programme Competitiveness and Cohesion 2014–2020.

Effect of non-metallic inclusions on the grain structure of low-carbon steels under severe plastic deformation

Svetlana Gubenko
[1]Iron and Steel Institute of National Academy of Science of Ukraine,
[2]Ukrainian State University of Science and Technologies: Prydniprovska State Academy of Civil Engineering and Architecture; Aerospace Institute. Dnepr, Ukraine
sigubenko@gmail.com

Abstract. *The features of localization of severe plastic deformation in a steel matrix near non-metallic inclusions are studied. In the steel matrix, near inclusions and at the inclusion-matrix interphase boundaries, the nature of the stressed and deformed states changes, the strain increment is determined by the rotation angle of the inclusion during its movement in the plastic region. Processes of local structural transformations near non-metallic inclusions in steels exposing to intensive plastic deformation were investigated. The influence of non-metallic inclusions on the local refinement of the steel microstructure is an important effect during severe plastic deformation, which makes it possible to obtain additional nanostructural strengthening near the inclusions during the general refinement of grains to a submicrocrystalline state. It was shown the influence of non-metallic inclusions on mechanical properties of these steels.*
KEYWORDS: *SEVERE PLASTIC DEFORMATION, LOW-CARBON STEELS, NON-METALLIC INCLUSIONS, THE GRAIN STRUCTURE, SUBMICROCRYSTALLINE STATE, NANOSTRUCTURAL STRENGTHENING.*

1.Introduction

Severe plastic deformation SPD is one of the promising methods for obtaining the Ultrafine-Grained structure of metallic materials, which makes it possible to obtain a high-strength state, as well as unique functional properties of these materials without changing the chemical composition [1 - 9]. Currently, many Ultrafine-Grained Materials are obtained by this method, in particular, non-ferrous metals and their alloys, steels have been studied to a lesser extent, in addition, the role of non-metallic inclusions in the formation of the Ultrafine-Grained structure has not been studied in the study of steels. **The goal** of this work was to study the local processes of plastic structure formation occurring in low-carbon steels near non-metallic inclusions during severe plastic deformation by the method of equal-channel angular pressing.

2. Materials and Procedures.

Samples of steels 08Al, 08Cr18Ni10T, 09Mn2Si, having dimensions of ø20x80 mm, were subjected to plastic deformation by the ECAP method in four passes (one pass with a channel intersection angle of 90° and three passes with an angle of 120°), which corresponded to a true deformation of 3.2. Structural analysis was performed using an Olympus PME 3 optical microscope, as well as JEM 100CX and JXA-50F electron microscopes; the nanohardness of the steel matrix near and far from inclusions was measured on a Nano Indenter II setup at a load of 10 mN. Tensile tests of the samples of 08Al steel 08Al after severe plastic deformation were carried out.

3. Results and discussion.

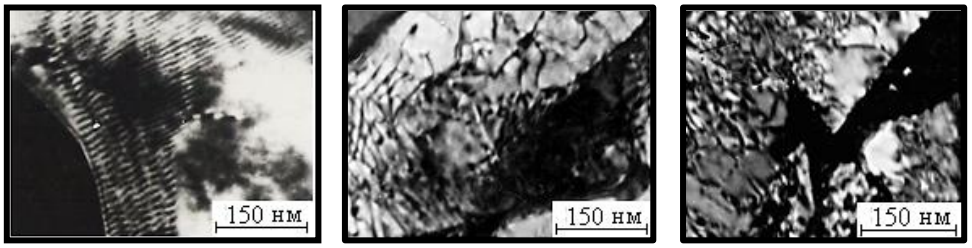
During severe plastic deformation SPD changes occurred in steels associated with the formation of oriented structural elements measuring 80…260 nm and separated by high-angle boundaries (Fig. 1, a - c), as evidenced by the presence of individual point reflections in the annular electron diffraction pattern. Such structural elements are characterized by the presence of dispersed curved mesobands of deformation, twins, elongated subgrains, and, in the case of 08Cr18Ni10T steel, also martensite plates [10]. With an increase in the number of passes, fragmentation of the mesobands of deformation occurred, leading to significant of grain refining. In addition, individual equiaxed grains appeared, caused by the growth of subboundary misorientations in the developed cellular structure, which is associated with the development of cold dynamic recrystallization. The obtained structures are characterized by an increase in the dislocation density to $(3.2...5.6)\cdot10^{12}$ cm^{-2}, which is three orders of magnitude higher compared to the initial state, as well as an increase in nanohardness with an increase in the number of passes from 2.5 to 4.2 kN/mm^2 for the different steels.

The effects that arise during structural changes in steels occur at the mesoscopic level and are associated with the transition from continuous plastic flow to localized flow in microshear bands during SPD. Such processes require repeated loading with changes in the direction of deformation, leading to the continuous evolution of the dislocation substructure, the transition to localization in shear bands and rotational localization, the introduction of high-angle boundaries, and the formation of junction disclinations. These processes lead to generate powerful internal stresses and facilitate the collective nature of the accommodative motion of dislocations, as well as fragmentation and rotation of fragments, which creates the conditions for refining the steel microstructure to the level of the substructure's cell size. The described general picture of grain refinement during SPD does not take into account the influence of non-metallic inclusions.

The synergetic methodology of physical mesomechanics requires determining the nature of possible stress concentrators, which are always present in a loaded solid, as well as the mechanisms of nonequilibrium structural transformations in localized zones of stress concentrators [11]. Such stress concentrators include non-metallic inclusions, as well as inclusion-matrix interphase boundaries separating two deforming phases with different elastic moduli. This contributes to the loss of shear stability and the emergence of various localized processes of structural and phase transformations in the steel matrix near the non-metallic inclusions and at the boundaries themselves during SPD. At the inclusion-matrix interface, oscillations of local stresses occur under loading, which can significantly exceed the average applied stresses. Obviously, it is necessary to consider the possible relaxation processes of these local stresses, which will improve the mechanical properties and reduce the risk of failure of steels subjected to equal channel angular extrusion.



a b c



d e f

Fig. 1. *Structure of steels 08Cr18Ni10Ti (a, e, g), 09Mn2Si (b, c), 08Al (d), deformed by equal channel angular extrusion.*

Inclusion particles under equal channel angular extrusion conditions disrupt the homogeneity of deformation and facilitate its localization. The strain increment is determined by the inclusion's rotation angle as it moves through the plastic zone. Near the non-metallic inclusion, various spatial deformation patterns are realized by changing the position of the shear planes, the nature of which obviously depends on the inclusion's degree of plasticity. The presence of non-metallic inclusions should have a significant impact on the development of multiple shear deformation, used in fractional deformation along fixed planes with shear in mutually opposite directions, combined with uniform stress and strain states, as well as on the ultimate ductility of steels.

During SPD, plastic deformation gradients in the steel matrix lead to plastic rotation of non-metallic inclusions, which act as barriers to dislocation movement. Localized deformation zones (Fig. 1, d) form near the inclusions. These zones contain inhibited curved fragmented shear bands, broken subboundaries, microtwins, and vortex formations caused by rotational localization and the formation of discrete misorientations (Fig. 1, e). The cell sizes of the substructure are approximately 2…3 times smaller than those far from the non-metallic inclusions. Furthermore, several foci of rotational localization can be observed near a single inclusion (Fig. 1, f). Plastic deformation gradients in the steel matrix lead to plastic rotation of inclusions, which act as barriers to dislocation movement.

A defective layer, representing a complex dislocation-disclination system, develops near non-metallic inclusions, where accommodative collective motion of dislocations and dangling dislocation boundaries occurs. Since the density of point defects is always elevated near inclusions, it is in these zones of localized deformation that diffusion accommodation within the system of dislocations and junction disclinations is most likely, which is the factor governing the limit of deformation-induced grain refinement in the steel matrix near inclusions. On average, nanograins sizes near inclusions are 2…3 times smaller than those farther away.

The nanohardness values of the steel matrix near non-metallic inclusions depended on the type of steel, but in all cases they exceeded similar values far from the inclusions by 20...35% (Table 1). Near plastic inclusions of sulfides and silicates, the nanohardness values are lower than near non-deformable oxides and carbonitrides of titanium, which is associated with a certain deformation relaxation of stresses in the plastic inclusion-matrix system [10 - 12]. In cases of localized dynamic cold recrystallization near inclusions, the nanohardness of the steel matrix decreased by approximately 10%. With developed deformations, most of the deformation energy is converted into heat due to the dissipation of mechanical energy, which can lead to heating of the metal to the recrystallization onset temperature. The probability of such heating increases with significant differences in the arrangement and vibrations of atoms located near non-metallic inclusions and at the inclusion-matrix boundaries, compared to atoms located within the grains. Cold recrystallization near inclusions occurs under conditions of a high concentration of defects in the crystalline structure, which do not have time to rearrange themselves to such a level as to ensure significant weakening of these areas. Recovery and recrystallization near inclusions can be significantly suppressed by limiting dislocation mobility by impurities present in these matrix zones in increased quantities.

Table 1. *Nanohardness of the steel matrix near non-metallic inclusions and far from them (in brackets) after SPD in four passes (kN/mm^2)*

08Cr18Ni10Ti, TiCN	4,97 (3,8)
08Al, $MnO{\cdot}Al_2O_3$	4.49 (3,4)
08Al, (Fe,Mn)S	3,92 (3,4)
09Mn2Si, SiO_2	5,38 (4.2)
09Mn2Si, $MnO{\cdot}SiO_2$	4,93 (4.2)

In steel 08Cr18Ni10Ti, rims of martensite phase were observed near non-metallic inclusions. This is associated with the redistribution of nonequilibrium defect flows during SPD, leading to concentration stratification of austenite and the formation of areas enriched in either nickel or iron and chromium. Electron microscopic studies allowed us to determine the basic reflections of fcc and bcc lattices with the presence of $\{111\}_{fcc}$ and $\{211\}_{bcc}$ deformation textures. Martensite grains have sizes of approximately 10…30 nm. Apparently, in localized areas of the austenite matrix near the non-metallic inclusions, a mechanism of concentration redistribution is realized, facilitating a local loss of nickel concentration, which leads to the formation of deformation-induced martensite. Far from the inclusions, the sizes of martensite grains reach 50…80 nm.

The relationship between the diffusion coefficients and the thermodynamic parameters in this steel during SPD should be taken into account. The diffusion coefficients of iron and chromium are approximately equal, while nickel has the maximum diffusion mobility. The appearance of nonequilibrium vacancies and the movement of impurity atoms toward non-metallic inclusions during SPD leads to the formation of nonequilibrium segregations near the inclusions and at the inclusion-matrix boundaries, which disturb the thermodynamic state of the steel, as well as to the action of the inverse Kirkendal effect in the presence of inclusions and inclusion-matrix boundaries serving as sources and sinks of vacancies [10 - 12]. Iron and chromium atoms in this steel are "slow" impurities and, in the case of a vacancy sink directed toward the inclusions, will be localized in the sink areas, while the more mobile nickel atoms move toward the vacancy flow from the inclusions (inverse Kirkendal effect). A decrease in nickel concentration in localized matrix volumes near non-metallic inclusions leads to a transition of the lattice areas bordering the inclusions to the bcc phase - martensite. Thus, the presence of martensite grains near non-metallic inclusions indicates their participation in the transport of nonequilibrium vacancy flows during SPD, which can lead to concentration redistribution in localized areas of the steel's base components, which have different mobility.

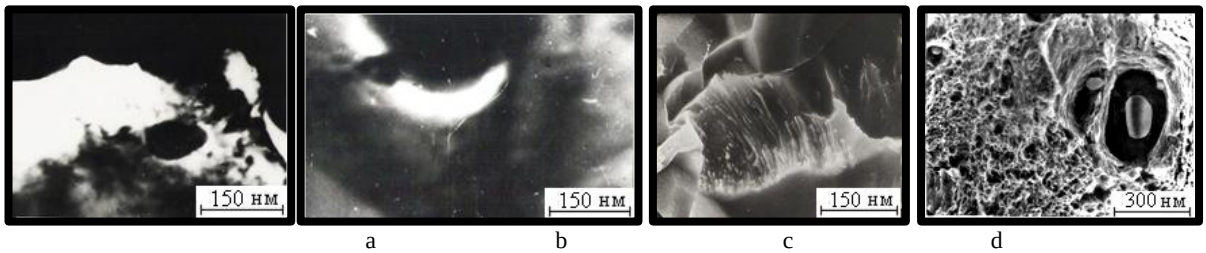
The inverse Kirkendal effect in steel with non-metallic inclusions acting as localized sources and sinks for vacancies results in a spatial scale on the order of several grain sizes. This

mechanism is associated with the activation of rotational deformation modes near the inclusions, which was observed in all the steels studied, as well as the activation of slip along the inclusion-matrix boundaries. During SPD, the density of excess interphase defects (introduced dislocations and nonequilibrium vacancies) at the inclusion-matrix boundaries also increases, leading to an increase in the free volume of these boundaries and an increase in their diffusion permeability [4, 10-12]. Apparently, the presence of several rotational localization areas near the non-metallic inclusions contributes to the fact that deformation microvortices "sweep" lattice defects into the inclusion-matrix boundaries.

As the misorientation of inclusion-matrix boundaries increases during SPD, the flux of lattice dislocations entering them exceeds the flux of dislocations emitted by the boundaries. Deformation energy, previously dissipated within the grain bulk and propagated to an increase in internal energy and the formation of nonequilibrium point, linear, and surface defects, is localized at such interphase boundaries. The increase in distortions and stresses at nonequilibrium inclusion-matrix boundaries leads to a relaxational rearrangement of their structure and delocalization of dislocation cores within these boundaries. This results in cold slip along the inclusion-matrix boundaries, which can be accompanied by the generation of point defects within the grain. Accommodation of rotational displacements near inclusions is also a cause of cold slip along inclusion-matrix boundaries. It seems obvious that after SPD, inclusion-matrix interphase boundaries possess increased boundary energy, which ensures high diffusion rates within these boundaries.

Viscous microcracks and cavities associated with delamination or viscous decohesion of inclusion-matrix interphase boundaries were observed near inclusions in areas of localized deformation of the steel matrix. A study of the microcracks revealed that the type of nonmetallic inclusion influences on the mechanism of their formation. Viscous microcracks were observed near silicate and titanium carbonitride inclusions (Fig. 2, a), while corundum and spinel inclusions typically formed cavities due to viscous decohesion of inclusion-matrix boundaries (Fig. 2, b). Clearly, under SPD conditions, the original structure of inclusion-matrix interphase boundaries retains its influence on their cohesive strength and the mechanism of microfracture formation [12]. It should be noted that SPD did not produce brittle microcracks in the steel matrix near inclusions, which is due to the high level of ductility under these conditions. The structure of the cavity surfaces indicates active plastic processes accompanying their formation and growth (Fig. 2, c).

Characteristic features of the tensile stress-strain curves of the specimens after SPD include the absence of the area of uniform elongation and also the onset of localized deformation with neck development immediately after reaching the yield point, which is close to the elastic limit and ultimate tensile strength, indicating a high-strength condition of the steel (Table 2). The elliptical cross-section of the neck in the specimens indicates significant anisotropy of steel deformed by simple shear. An increase in the content of non-metallic inclusions led to a significant reduction in both strength and ductility properties (Table 2). The fracture micromechanism in steel deformed by equal channel angular extrusion is predominantly dimpled (Fig. 2, d). However, fractures have a complex topography due to the formation of inhomogeneous deformation structures during SPD, as well as the presence of non-metallic inclusions. Large dimples are associated with non-metallic inclusions. Furthermore, areas resembling ductile intergranular fracture are found near the inclusions. This is due to the sharp localization of deformation in the steel matrix, as well as the development of cold slip along the inclusion-matrix boundaries. Therefore, the problem of non-metallic inclusions is also relevant for steels subjected to SPD.



a b c d

Fig. 2. *Microcracks near inclusions that arose during the SPD process in steels 08Cr18Ni10Ti (a), 08Al (b, c) and fracture structure of 08Al steel, deformed by equal channel angular extrusion.*

Table 2. *Mechanical properties of steel 08Al with different non-metallic inclusion contents deformed by equal channel angular extrusion.*

melt number	$\sigma_{0,2}$	$\sigma_в$	δ	ψ
	MPa		%	
1	654	643	12	32
2	533	521	7	24

4. Conclusions.

During SPD of steels subjected to equal channel angular extrusion, nonmetallic inclusions cause a number of effects: refinement of the nanograin structure, localized cold recrystallization and cold sliping along inclusion-matrix boundaries, as well as concentration redistribution in the matrix and martensite formation. Inclusions affect the mechanical properties of steels subjected to equal channel angular extrusion.

In the steels under study, structure formation during severe plastic deformation is associated with the formation of oriented structural elements that have dimensions of 100…260 nm and are separated by high-angle boundaries, which are characterized by the presence of dispersed curved mesobands of deformation, and in steel 08Kh18N10T also martensitic plates. With an increase in the number of passes, fragmentation of the mesobands of deformation occurred, which led to a significant fragmentation of the grains. Near the inclusions, the grain sizes are significantly smaller than far from them and are 75…100 nm.

The nanohardness values of the steel matrix near the inclusions were 25…40% higher than the similar values far from the inclusions. Near plastic inclusions of sulfides and silicates, the values of nanohardness are lower than near non-deformable oxides and titanium carbonitrides, which is associated with a certain deformation relaxation of stresses in the plastic inclusion-matrix system. In cases of localization of dynamic cold recrystallization near inclusions, the nanohardness of the steel matrix decreased by about 10%.

The influence of non-metallic inclusions on the local refinement of the steel microstructure is an important effect during severe plastic deformation, which makes it possible to obtain additional nanostructural strengthening near the inclusions during the general refinement of grains to a submicrocrystalline state.

5. Literature.

1. Segal V.M., Reznikov V.I., Kopylov V.I. et al., Processes of Metal Structure Formation upon Plastic Deformation. Minsk, Navuka i Tekhnika (1994) 232 p.
2. Segal V.M. Equal channel angular extrusion: from macromechanics to structure formation // Mater. Sci. Eng. A. 1999. Vol. 271. P. 322–333.
3.Ostanina T.V., Shveykin A.I., Trusov P.V. The grain structure refinement of metals and alloys under severe plastic deformation:experimental data and analysis of mechanisms. PNRPU Mechanics Bulletin, 2020, no. 2, pp. 85-111. DOI:10.15593/perm.mech/2020.2.08
4.Валиев Р.З., Александров И.В. Наноструктурные материалы, полученные интенсивной пластической деформацией. М., Логос, 2000, 272с.
5.Zehetbauer M.J., Valiev R.Z.. Nanomaterials by Severe Plastic Deformation. Proceedings of the Conference “Nanomaterials by Severe Plastic Deformation – NanoSPD-2”, Wiley-VCH, December 9-13, Vienna, Austria, 2002. 389 p.
6.Valiev R.Z., Zhilyaev A.P., Langdon T.G. Bulk Nanostructured Materials: Fundamentals and Applications. John Wiley & Sons, Inc., 2014. 456 p.
7. Nanomaterials: synthesis, properites and applications. Eds Edelstein A.S., Cammarata K.C.. Bristol: J.N. Arrowsmith Ltd., 1998. 461 p.
8.Nanoparticles and nanostructured films / Ed. Fendler.: Wiley-VCH, 1998. 468 p.
9.Vasylyev M.A., Voloshko S.M., Mordyuk B.M. Surface severe deformation of the carbon steels. Microstructure and properties”. LAP LAMBERT Academic Publishing, 2021. 110 p.
10.Gubenko S.I. Non-metallic inclusions and ductility of steels. The physical basis of the ductility of steels. - Saarbrücken: LAP LAMBERT. Palmarium academic publishing, 2016. - 549 p.
11.Панин В.Е. Физическая мезомеханика материалов. Механика твердого тела, 1999, №5, с. 88-108.
12.Gubenko S.I., Oshkadepov S.P. Non-metallic inclusions in steel. – Kiev: Naukova dumka, 2016. - 528 p.

Comparative Analysis of Natural Ruby and Synthetic Corundum Ceramics by UV–Vis and Raman Spectroscopy

Ivan Tsanev[*1], Tsvetan Dimitrov[2], Liliya Tsvetanova[1], Rositsa Titorenkova[1,3]
Institute of Mineralogy and Crystallography, Bulgarian Academy of Sciences, Acad. G. Bonchev Str., bl. 107, 1113 Sofia, Bulgaria[1]
University of Ruse "Angel Kanchev", Razgrad Branch 7200, Bulgaria[2]
PERIMED, Central District, Vasil Aprilov Blvd. 15A, 4002 Plovdiv, Bulgaria[3]
*ivan_tsanev@imc.bas.bg

Abstract: *This study presents a comparative spectroscopic investigation of natural Cr^{3+}-bearing ruby and multiphase Al_2O_3-based ceramics derived from industrial waste. The natural corundum shows characteristic Cr^{3+} crystal-field absorption bands at ~405 and ~550 nm and sharp R-line emission near 693 nm, confirming a structurally ordered α-Al_2O_3 lattice. In contrast, the waste-derived ceramics exhibit charge-transfer-dominated absorption associated mainly with V^{5+} and Fe^{3+} under oxidizing firing conditions. Strong UV absorption (220–300 nm) and the absence of vanadium crystal-field transitions indicate predominant V^{5+} stabilization, consistent with chemical and phase analysis. The ceramics display high lightness ($L^* \approx 93$) and a yellow hue ($b^* = 10–23$) governed by ligand-to-metal charge-transfer processes. The results demonstrate the effectiveness of combined UV–Vis and Raman spectroscopy for distinguishing crystal-field and charge-transfer mechanisms and for resolving dopant-related colour formation in alumina systems.*

Keywords*: α-Al_2O_3; WASTE-DERIVED CERAMICS; VANADIUM OXIDATION STATE; CRYSTAL-FIELD TRANSITIONS; CHARGE-TRANSFER ABSORPTION; UV–VIS SPECTROSCOPY; RAMAN SPECTROSCOPY*

1. Introduction

Corundum (α-Al_2O_3) is a structurally robust and chemically stable oxide occurring both as a natural mineral and as an industrial ceramic material. Its exceptional mechanical strength, thermal resistance and chemical inertness make it essential for refractory, structural and optical applications. In its gem-quality form, ruby represents chromium-doped corundum, where Cr^{3+} substitutes for Al^{3+} in octahedral coordination, producing the characteristic red colour through spin-allowed d–d transitions and sharp R_1–R_2 luminescence lines near 693–694 nm. The crystal-field behaviour of Cr^{3+} in corundum has been extensively described within the framework of crystal-field theory and electronic spectroscopy [1–4].

In addition to chromium, minor transition metal ions such as Fe, Ti and V may significantly influence the optical absorption behaviour and hue of corundum. Vanadium is particularly important due to its multiple oxidation states (V^{3+}, V^{4+}, V^{5+}), each associated with distinct electronic and charge-transfer transitions. In natural systems, V^{3+} may contribute to absorption in the UV-blue region, whereas V^{4+} and especially V^{5+} are commonly linked to broad $O^{2-} \rightarrow V$ charge-transfer bands that modify colour saturation and absorption edge characteristics [5–7,10].

Natural Cr^{3+}-bearing corundum from the village of Mishevsko (Eastern Rhodopes, Bulgaria) was recently characterized using UV–Vis, Raman and photoluminescence spectroscopy [1]. The study revealed well-resolved Cr^{3+} absorption bands at ~405 and ~550 nm, sharp R_1–R_2 emission lines, and additional absorption features in the UV-blue region attributed to minor V and Ti admixtures. These results define a structurally ordered α-Al_2O_3 reference system in which chromium is the principal chromophore and vanadium acts as a secondary modifier of the optical response.

In contrast, Al_2O_3-based ceramics derived from industrial waste represent chemically complex multicomponent systems containing vanadium, iron, alkali elements and silica-rich phases. During high-temperature processing in an oxidizing atmosphere, vanadium is predominantly stabilized as V^{5+}, favouring intense ligand-to-metal charge-transfer transitions in the UV region. Moreover, the coexistence of multiple crystalline polymorphs of Al_2O_3 (α- and κ-phases), together with cristobalite (SiO_2) and residual amorphous material, results in heterogeneous optical behaviour governed by both crystal-field and charge-transfer mechanisms.

Consequently, colour formation in such engineered ceramics cannot be interpreted solely within the classical crystal-field framework typical of ruby, but must also consider oxidation-state equilibria, phase interactions and defect chemistry.

UV–Vis diffuse reflectance spectroscopy provides information on electronic transitions and oxidation states of transition metal ions, whereas Raman spectroscopy offers a structural fingerprint of α-Al_2O_3 and related ceramic phases, as well as luminescent signatures of Cr^{3+} and other dopants [3,8]. The combination of these techniques enables differentiation between Cr^{3+}-controlled crystal-field coloration and vanadium- or iron-dominated charge-transfer absorption in complex Al_2O_3-based systems.

The present study presents a comparative spectroscopic investigation of a natural Cr^{3+}-bearing ruby [1] and synthetic Al_2O_3-based multiphase ceramics derived from industrial waste containing a wide range of impurities, including vanadium and iron. The objective is to correlate dopant chemistry and oxidation state with UV–Vis absorption behaviour, Raman structural features and Cr^{3+} luminescence characteristics, as well as CIELAB colour coordinates. By comparing a structurally ordered natural α-Al_2O_3 reference with chemically complex waste-derived ceramics, the study highlights the capability of combined UV–Vis and Raman spectroscopy to distinguish crystal-field and charge-transfer mechanisms, detect oxidation-state variations, and resolve subtle differences in dopant environment and lattice structure.

2. Materials and Methods

2.1 Samples

Ruby: Natural corundum containing Cr^{3+} and traces V^{3+}/V^{4+} and other transition metal ions (after Ref. [1]).



Figure. 1 *Vanadium-bearing natural ruby crystals from the Eastern Rhodopes (Bulgaria). The colour variations reflect minor vanadium incorporation in Cr^{3+}-doped α-Al_2O_3, where vanadium acts as a secondary chromophore modifying the UV-blue absorption region.*

Synthetic ceramic: The spent catalyst with a complex chemical and phase composition is mixed with chemically pure reagents (Al_2O_3) for the production of multiphase ceramics by one-step solid-phase sintering method. The mixture was homogenized and sintered in a laboratory muffle furnace with a heating rate 500°C/h in air with isothermal retention of 2 h at the final temperatures of 1200°C and 1300°C.

2.2 Analytical methods

Phase composition was analysed using a Bruker D8 Advance and Empyrean (Malvern Panalytical) powder X-ray diffractometers with Cu Kα radiation operating at 40 kV and 30 mA, in the range 10 - 80 °2θ. Pulse height distribution (PHD) optimization procedures have been applied in order to reduce the fluorescence-induced background and peak-to-background ratio.

Wavelength Dispersive X-ray Fluorescence Spectroscopy (WDXRF) was used to determine the chemical composition using Supermini 200 (Rigaku, Japan) spectrometer operating at 50 kV and 4.00 mA. The powder samples were pressed to obtain a tablet. The weight ratio of the amount of sample to the amount of glue (Acrawax C powder) was 5:1. A semi-quantitative method (SQX) was used to determine the elemental composition.

Diffuse reflectance spectra were recorded using a Cary 4000 (Agilent) UV-Vis spectrophotometer equipped with an internal DRA 900 integrating sphere accessory. Measurements were performed in the 200–800 nm spectral range with a spectral resolution of 1 nm. The reflectance data were baseline-corrected and transformed using the Kubelka-Munk function F(R) to obtain absorption-related spectra suitable for comparison with the natural corundum reference. UV–Vis transmittance spectra of the natural ruby samples were collected in the same spectral range using a solid-sample transmission accessory.

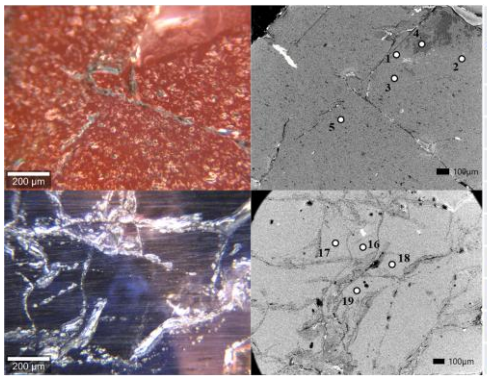
Raman spectra and photoluminescence (PL) measurements were performed using a WiTec alpha300 R confocal Raman microscope with a 532 nm laser and ×50 objective, producing a laser spot of ~1 μm. Each PL spectrum was recorded with an acquisition time of 0.05 s and averaged over 20 accumulations.

The colour of the ceramics was measured using a Lovibond Tintometer RT 100 and presented in the CIELAB colour space.

3. Results and Discussion

3.1. Phase composition of the studied samples

Rubies samples consist α-Al₂O₃ with trace Ti, V, Cr and Fe [1].



Point	Elements ,wt %			
	Ti	V	Cr	Fe
1	0.28	0.12	0.14	<0.05
2	0.25	0.25	0.21	0.26
3	0.13	<0.05	0.26	<0.05
4	0.05	<0.05	0.16	<0.05
5	0.17	0.20	0.14	<0.05
16	<0.05	<0.05	<0.05	<0.05
17	0.05	<0.05	<0.05	<0.05
18	0.05	<0.05	0.07	0.18
19	0.23	<0.05	<0.05	0.17

Figure 2. *X-ray diffraction pattern of the natural ruby (after Ref. [1]) confirming single-phase α-Al₂O₃ with trace substitution of transition metal ions (Cr, V, Ti, Fe) in the corundum lattice.*

Synthetic ceramics were obtained from industrial waste with the following composition: SiO_2 (55.7 wt %), SO_3 (22.8 wt %), K_2O (11.95 wt %), V_2O_5 (4.36 wt %), Al_2O_3 (2.32 wt %), Na_2O (1,47 wt %), Fe_2O_3 (0.81 wt%), CaO (0.36 wt %), Cs_2O (0.13 wt %), As_2O_3 (0.1 wt %), P_2O_5 (0.05 wt %) and others (0.14 wt %) and addition of Al_2O_3 in an amount necessary to obtain a 1.5 molar ratio of Al_2O_3/SiO_2. 100g waste+140 g Al_2O_3 The mixture was homogenized and sintered in a laboratory muffle furnace with a heating rate of 200°C/h in an air atmosphere with an isothermal retention of 2 h at final temperatures of 1200°C and 1300°C.

The phase composition of the resulting ceramic sintered at 1100°C, 1200°C, and 1300°C determined based on the X-ray diffraction patterns (Figure 3), is presented in Table 1.

Table1. *Quantitative phase composition (wt.%) of ceramics sintered at different temperatures, determined from XRD data.*

Sample	α -Al_2O_3	κ -Al_2O_3	cristobalite	amorphous
1100°C	55%	21%	24%	28%
1200°C	56%	30%	14%	23%
1300°C	43%	42%	16%	26%

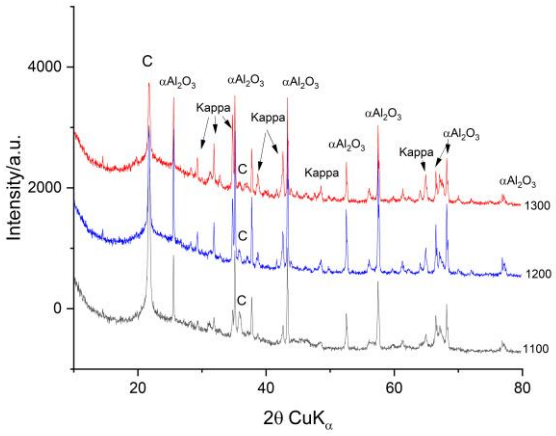


Figure 3. *X-ray diffraction patterns of waste-derived ceramics sintered at 1100°C, 1200°C and 1300°C. Indexed reflections of α-Al₂O₃, κ-Al₂O₃ and cristobalite illustrate temperature-dependent phase evolution under oxidizing firing conditions.*

3.2. Chemical composition (XRF data)

The chemical composition of the ceramic sintered at 1100°C, 1200°C, and 1300°C expressed as weight percent oxides, is present in Table 2.

Table 2. *Chemical composition of the sintered ceramics.*

Oxides, wt%	1100°C	1200°C	1300°C
Na_2O	0.83	1.06	1.03
Al_2O_3	46.2	41.6	40.5
SiO_2	41.4	44.4	45.6
P_2O_5	0.022	0.02	-
SO_3	0.25	0.25	0.06
Cl	0.01	-	-
K_2O	6.41	7.35	7.6
CaO	0.18	0.18	0.21
TiO_2	0.08	0.12	-
V_2O_5	3.70	4.13	4.1
Fe_2O_3	0.85	0.90	0.93
CuO	0.021	0.02	0.03
As_2O_3	0.073	0.05	0.03
MoO_3	-	0.02	0.02

3.3. Optical absorption spectra

Natural ruby: The UV-Vis spectrum of the natural ruby exhibits well-resolved spin-allowed d–d transitions of Cr^{3+} centred at ~550 nm, together with higher-energy bands near 405 nm (Fig. 4). Weak absorption features in the 400 and 600 nm region indicate minor contributions from V^{3+}/V^{4+}, while an increase in absorption below 320 nm is attributed to ligand-to-metal charge-transfer transitions involving trace V^{5+}. The sharp R-line emission at ~693 nm confirms the presence of structurally ordered Cr^{3+} in the α-Al₂O₃ lattice [1,4,9].

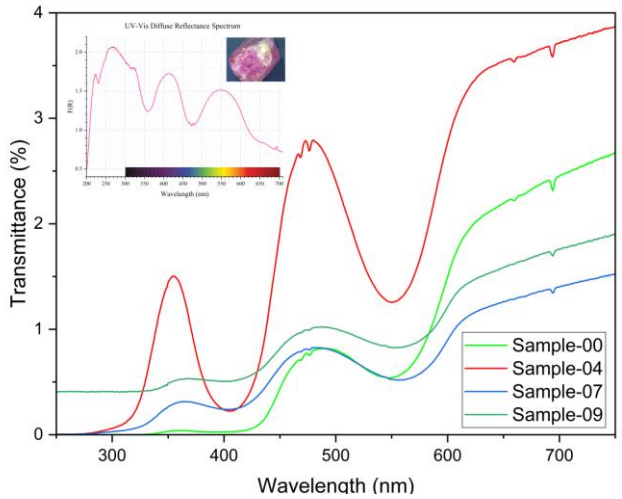


Figure 4. *UV-Vis transmittance spectra of vanadium-bearing natural ruby samples showing characteristic Cr^{3+} crystal-field absorption bands at ~405 and ~550 nm together with enhanced UV-blue attenuation (below ~320–400 nm) attributed to V^{3+}/V^{4+} crystal-field transitions and $O^{2-} \rightarrow V^{5+}$ charge-transfer processes. The spectra demonstrate the role of vanadium as a secondary chromophore modifying the absorption edge [5–7,9].*

Synthetic corundum ceramic: In contrast, the synthetic ceramics exhibit strong and broad absorption in the 220–300 nm range, characteristic of $O^{2-} \rightarrow V^{5+}$ charge-transfer transitions (Fig.5). Crystal-field d–d transitions of vanadium are largely suppressed, indicating that vanadium is predominantly stabilized in its highest oxidation state under oxidizing firing conditions. A weak band near ~700 nm may suggest minor V^{4+} species associated with oxygen-deficient sites.

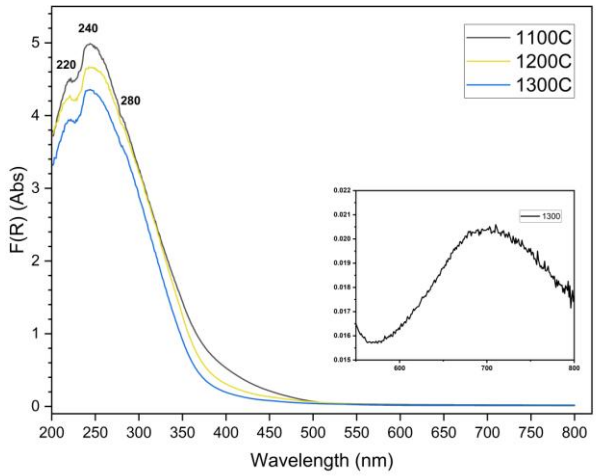


Figure 5. *UV–Vis diffuse reflectance spectra of waste-derived alumina ceramics showing dominant $O^{2-} \rightarrow V^{5+}$ charge-transfer absorption in the 220–300 nm region and broad visible absorption associated with Fe^{3+} species, confirming charge-transfer-controlled colour formation [5–7].*

The visible region is dominated by broad overlapping absorption features attributed to Fe^{3+} and vanadium-related charge-transfer processes. The absence of distinct Cr^{3+} -type transitions confirms a fundamentally different chromophore mechanism compared to natural ruby.

When Al_2O_3 reacts with vanadium-containing species in air atmosphere, the formation of $AlVO_4$ is thermodynamically favoured, further supporting stabilization of V^{5+}. This interpretation is consistent with XRF data showing significant V_2O_5 content and with the observed yellow colour coordinates.

3.4 Raman Spectroscopy

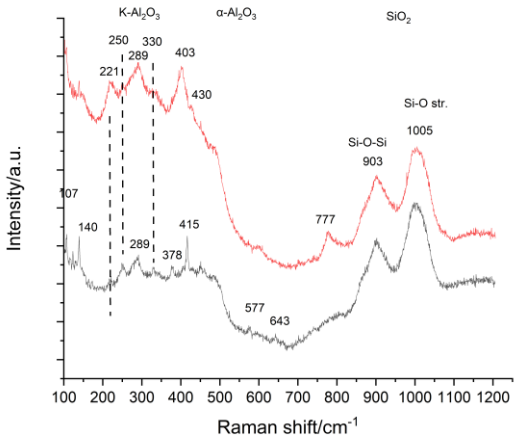


Figure 6. *Raman spectra of waste-derived ceramics illustrating vibrational modes of α-Al_2O_3, κ-Al_2O_3, cristobalite and amorphous silica, confirming the multiphase structure of the sintered system.*

The natural ruby crystallizes in the trigonal α-Al_2O_3 structure (space group R $\bar{3}$c), where Cr^{3+} substitutes for Al^{3+} in octahedral coordination without symmetry modification. Group theoretical analysis predicts seven Raman-active modes, and experimentally well-defined bands at 378, 415, 430, 577 and 643 cm^{-1} confirm a structurally ordered corundum lattice [3,4].

In contrast, the Raman spectra of the synthetic ceramics reveal multiphase composition. The presence of κ-Al_2O_3 (orthorhombic polymorph) introduces additional vibrational modes due to its lower symmetry and multiple non-equivalent Al sites, producing bands near ~250, 300 and 500 cm^{-1}. Cristobalite contributes intense peaks at ~500 and 770 cm^{-1}, while the amorphous phase is characterized by broad bands in the 900–1100 cm^{-1} region (Fig.6) [8].

Under 532 nm excitation, luminescence lines associated with Cr^{3+} electronic transitions are also observed, indicating trace chromium incorporation despite the absence of ruby-type colouration (Fig. 7) [1,4,9].

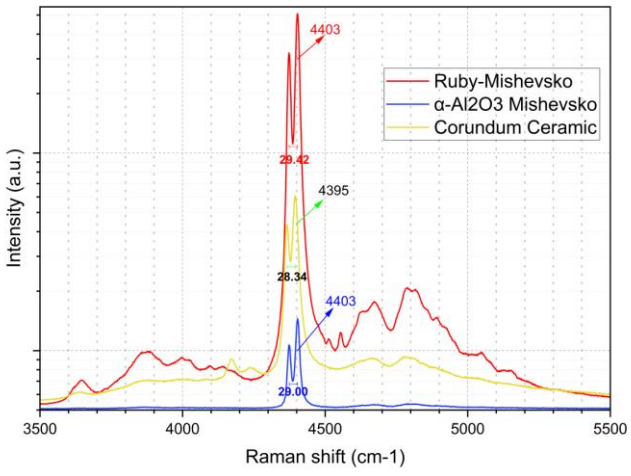


Figure 7. *Raman spectra of natural ruby and synthetic ceramic under 532 nm excitation showing Cr^{3+} R_1 and R_2 luminescence lines. The R_1 peak is positioned at 4403 cm^{-1} Raman shift for natural ruby and 4395 cm^{-1} Raman shift for the synthetic ceramic, indicating lattice strain and structural differences.*

The R_2-R_1 separation equals 29.00 cm^{-1} for weakly luminescent natural corundum, 29.42 cm^{-1} for strongly luminescent natural corundum (≈30× higher intensity), and 28.34 cm^{-1} for the ceramic.

Variations in peak position and splitting reflect differences in crystal-field strength, dopant environment and structural order between the natural α-Al_2O_3 reference and the multiphase waste-derived ceramic.

3.5. Colour

The optical neutrality of pure Al_2O_3 implies that colour in both systems originates exclusively from transition metal ions.

In ruby, the red colour arises from spin-allowed d–d transitions of Cr^{3+} in octahedral coordination, which selectively absorb blue and green light, resulting in red transmission and characteristic emission near 696 nm [2–4].

In the synthetic ceramics, however, the colour is yellow despite the presence of Cr^{3+} luminescence. CIELAB measurements show high lightness (L* ≈ 92–93), negligible red-green contribution (a* ≈ -1), and pronounced yellow component (b* = 10–23) [12].

Table 3. *CIELAB colour coordinates (L*, a*, b*) of waste-derived ceramics.*

Composition	T, °C	Colour	L*	a*	b*
Ceramics: α -Al_2O_3, κ-Al_2O_3, cristobalite, amorphous	1100		92.2	-1.0	23.4
	1200		93.1	-1.0	15.0
	1300		93.2	-1.1	10.5

The high lightness is explained by the dominance of colourless high-band-gap phases (α-Al_2O_3, κ-Al_2O_3, cristobalite and amorphous silica) which efficiently scatter light. The yellow hue originates primarily from ligand-to-metal charge-transfer absorption of V^{5+} and Fe^{3+} in the blue spectral region. The absence of positive a* values confirms that Fe^{3+} does not induce significant red coloration under the studied conditions [5-7,10,12].

4. Conclusion

This comparative study demonstrates that colour formation in alumina systems is governed by fundamentally different electronic mechanisms in natural and waste-derived materials.

In natural ruby, colour is controlled by Cr^{3+} crystal-field transitions within a structurally ordered α-Al_2O_3 lattice [2–4]. In contrast, the engineered multiphase ceramics exhibit charge-transfer-dominated absorption, primarily associated with V^{5+} and Fe^{3+} stabilized under oxidizing firing conditions [5–7,10].

The shift of the Cr^{3+} R_1 line (4403 → 4395 cm^{-1}) and variations in R-line splitting (29.42–28.34 cm^{-1}) confirm structural and crystal-field differences between natural and synthetic systems [1,4,9].

Vanadium oxidation-state stabilization emerges as a key technological parameter controlling optical response in alumina ceramics derived from secondary raw materials. The combined use of UV–Vis and Raman spectroscopy provides a reliable diagnostic tool for oxidation-state monitoring, phase verification and targeted colour engineering under sustainable processing conditions [3,8,11].

Industrial Relevance Statement

Control of vanadium oxidation state and phase composition enables predictable colour tuning in waste-derived alumina ceramics, supporting sustainable valorisation of industrial residues into functional ceramic materials.

Acknowledgements:

The financial support of this work by the Bulgarian Ministry of Education and Science, National Research Fund under the contract number KP-06-H87/14 - 2024 is gratefully acknowledged.

This work also has been carried out in the framework of the National Science Program "Critical and strategic raw materials for a green transition and sustainable development", approved by the Resolution of the Council of Ministers № 508/18.07.2024 and funded by the Ministry of Education and Science (MES) of Bulgaria.

We would like to express our gratitude for the analytical support to programme “Research, Innovation and Digitalisation for Smart Transformation” 2021–2027, funded by the European Union, Project BG16RFPR002-1.014-0007 “Center for Competence PERIMED-2”.

References

1. I. Tsanev et al., Rev. Bulg. Geol. Soc. **86(2)**, 54–58 (2025)
2. R.G. Burns, *Mineralogical Applications of Crystal Field Theory*, Cambridge University Press, Cambridge (1993)
3. D.S. McClure, *J. Chem. Phys.* **36**, 2757–2779 (1962)
4. S.P.S. Porto, R.S. Krishnan, J. Chem. Phys. **47**, 1009–1012 (1967)
5. B.J. Reddy, L.R. Moorthy, Pramana J. Phys. **19**, 449–454 (1982)
6. H.H. Tippins, Phys. Rev. B **1**, 126–135 (1970)
7. J. Ferguson, P.E. Fielding, Chem. Phys. Lett. **10**, 262–265 (1971)
8. E.V. Dubinsky et al., Gems Gemol. **56**, 2–28 (2020)
9. D. Bersani, P.P. Lottici, Anal. Bioanal. Chem. **397**, 2631–2646 (2010)
10. E. Fritsch, G.R. Rossman, *Gems Gemol.* **24**, 3–15 (1988)
11. P. Kubelka, F. Munk, *Z. Tech. Phys.* **12**, 593–601 (1931)
12. ISO/CIE 11664-4:2019, *Colorimetry – Part 4: CIE 1976 L*a*b* colour space* (International Organization for Standardization, Geneva, 2019)

Observed Damage Patterns and Material Strength Deficiencies in URM Dwellings After the 2019 Albania Earthquake

Marjo Hysenlliu
Department of Mechanics of Structures, Polytechnic University of Tirana, Albania
mhysenlliu@gmail.com

Abstract: *This paper investigates the link between earthquake damage and material strength deficiencies in four unreinforced masonry (URM) dwellings in Kruja, Albania, which all reached Damage State 4 (DS-4) during the Mw 6.4 earthquake of 26 November 2019. Post-earthquake field inspections showed similar failure patterns in all buildings, including diagonal shear cracking, corner separation and local out-of-plane instability, pointing to limited shear capacity and weak masonry bonding.*
To clarify the causes of this behaviour, laboratory tests were carried out on brick units, mortar samples and masonry prisms taken from the damaged buildings. The test results indicate that both mortar and masonry compressive strengths are significantly lower than the values commonly assumed in Eurocode 6 for structural assessment. This strength deficit explains the brittle response and the rapid stiffness degradation observed during the earthquake.
The combined use of field observations and laboratory data confirms the key role of construction quality in the seismic vulnerability of older URM dwellings and underlines the importance of material-based assessment approaches for similar residential buildings.
Keywords*: earthquake damage, unreinforced masonry, material strength deficiencies, laboratory tests, field investigation*

1. Introduction

Unreinforced masonry (URM) buildings represent a large portion of the residential stock in Albania, particularly in towns such as Kruja, where most dwellings were constructed with limited engineering supervision and without modern seismic provisions. The Mw6.4 earthquake of 26 November 2019 exposed the structural vulnerability of these houses, many of which suffered extensive cracking, loss of stiffness, and partial wall detachment. Although several studies have linked URM damage to poor structural configuration and inadequate detailing, the influence of material quality—especially mortar, brick strength, and overall masonry capacity—has received comparatively less attention.

In older URM construction, material degradation and low mortar strength can critically reduce both shear resistance and wall integrity, making buildings highly susceptible to brittle failures during strong shaking. Understanding this connection is essential not only for explaining the observed damage but also for improving future assessment and retrofit practices.

This study combines two complementary sources of evidence:
• field observations from four heavily damaged URM dwellings in Kruja, and
• laboratory tests on mortar, brick and masonry samples extracted from these buildings.

The laboratory results are compared with the minimum performance expectations of Eurocode 6, allowing a direct evaluation of how material deficiencies contributed to the DS-4 damage documented on site. By linking observed damage patterns with measured material strengths, the paper highlights the central role of construction quality in the seismic behaviour of older URM dwellings and provides practical insights for their evaluation and strengthening.

2. Study case and field investigation

The study focuses on four unreinforced masonry (URM) dwellings located in the city of Kruja, all of which were classified as Damage State 4 (DS-4) following the Mw6.4 earthquake of 26 November 2019. Although the houses differ in layout and construction period, they share the same traditional URM typology commonly found in Albania: clay brick masonry walls, lime–cement mortar of varying quality, timber or mixed floor systems, and shallow foundations without seismic reinforcement.

Despite their differences, the four dwellings exhibited remarkably similar seismic behaviour, making them suitable for a comparative assessment of damage patterns and material strength. A brief overview of each building is provided below.
• Building 1 - A two-storey URM dwelling with relatively regular plan geometry. Damage was concentrated in ground-floor walls, where diagonal cracking and corner separation were widely observed.



Fig. 1 *Building façade photos (right), plan view (left).*

• Building 2 - This house includes several large openings and slender wall segments. Shear cracking and wall–slab separation were prominent, and several panels showed signs of partial out-of-plane deformation.



Fig. 2 *Building façade photos (right), plan view (left).*

• Building 3 - A URM structure with poor mortar quality confirmed during inspection. Extensive diagonal cracks and crushing around window openings indicated limited material cohesion and weak tensile resistance.

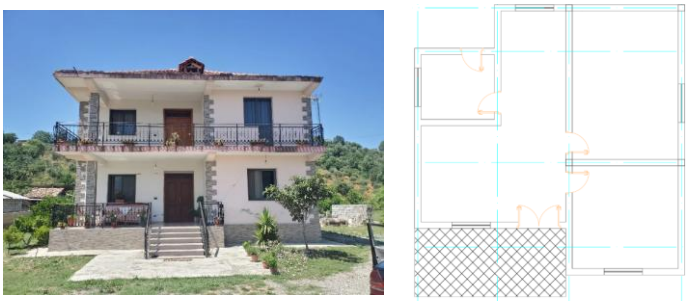


Fig. 3 *Building façade photos (right), plan view (left).*

• Building 4 - The most heavily damaged among the four, featuring widespread shear cracking, vertical splitting at corners, and permanent lateral displacement of upper façade walls.

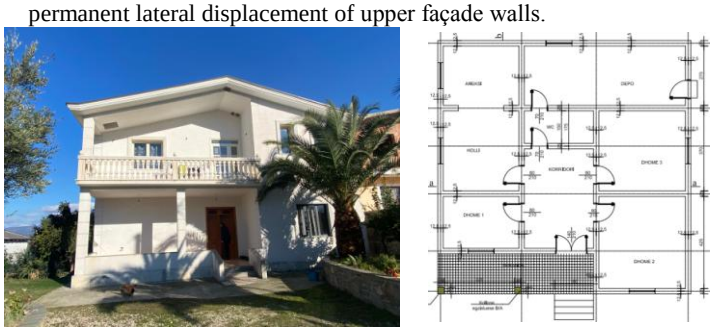


Fig. 4 *Building façade photos (right), plan view (left).*

Together, these four dwellings represent a typical sample of older URM construction in Kruja and provide a reliable basis for examining how material deficiencies influence seismic damage.

3. Observed damage patterns

Post-earthquake field inspections carried out on the four unreinforced masonry (URM) dwellings revealed a consistent set of damage mechanisms, despite differences in geometry, construction period and layout. The similarity of the observed damage indicates that the seismic response was largely governed by the inherent weakness of the masonry materials rather than by geometric irregularities alone.

The most common damage mechanism was diagonal shear cracking in masonry piers, particularly at ground-floor level. Cracks typically followed X-shaped patterns and extended through the full height of the walls, reflecting the low shear capacity of the masonry. This behaviour is characteristic of URM buildings with weak mortar and poor brick–mortar bonding, conditions later confirmed by laboratory testing.

Vertical cracking and separation at wall intersections were also frequently observed. These cracks indicate a loss of box behaviour and insufficient connection between perpendicular walls, a typical deficiency in older masonry construction where proper interlocking and transverse bonding are often absent. As a result, corners became highly vulnerable during seismic loading.



Fig. 5 *Building 4 damage around openings.*

Several façade walls showed signs of out-of-plane deformation, including cracking, rotation and local bulging, particularly at upper-storey levels. Weak mortar joints and degraded brick units reduced the tensile capacity required to maintain wall stability under out-of-plane seismic forces. In some cases, these deformations were accompanied by permanent lateral displacements.

Damage was also concentrated around door and window openings, where cracks radiated from lintel corners and localized crushing was observed above openings. These effects reflect the limited compressive strength of the masonry, which restricts its ability to redistribute stress concentrations around structural discontinuities.

In all four dwellings, horizontal cracking and separation were observed at the wall–slab interface. Timber floors or weak concrete slabs provided limited diaphragm action, allowing relative movement between walls and slabs. The poor bonding capacity of the masonry further exacerbated this separation.



Fig. 6 *Building 2 slab degradation and separation from walls.*

Overall, the damage patterns consistently point to material weakness as a primary cause of the poor seismic performance. Low mortar strength, variable brick quality and inadequate bonding led to brittle failure mechanisms, rapid stiffness degradation and extensive damage. These observations are quantitatively supported by the laboratory test results presented in the following chapter.

4. Laboratory tests and material strength results

To better understand the causes of the extensive DS-4 damage observed in the four URM dwellings, laboratory tests were performed on masonry units, mortar samples and composite masonry prisms extracted from the buildings during the post-earthquake evaluation phase. These tests provide a direct measure of the mechanical properties governing the in-plane and out-of-plane behaviour of the walls, and allow a quantitative comparison with the minimum strength values typically assumed by EC-6.

The tests conducted included:

- Mortar compression tests (f_m),
- Brick (unit) compression tests (f_b),
- Masonry prism compression tests (f_k),
- Shear strength tests on bed joints (f_{vk}), where samples were available.

Although the results vary slightly between buildings, the general trend is consistent: all samples exhibit significantly lower strength than modern standards, and in several cases below even the minimum assumed values for older masonry.



Fig. 7 *Testing sample extracting Building 2.*

Summary of Measured Strengths

The following table presents representative ranges from the laboratory tests (using typical values obtained from the four buildings).

Table 1: *Summary of laboratory material test results*

Material property	Measured Range	Typical EC6 Reference Values
Mortar compressive strength	1–2 MPa	3.0 – 5.0 MPa (for basic masonry)
Brick compressive strength	5–7.5 MPa	7.5–15 MPa (common fired brick)
Masonry compressive strength	2–3 MPa	≥ 5 MPa (for structural walls)
Initial shear strength	0.03–0.08 MPa	0.15 – 0.30 MPa

Interpretation of laboratory results

The results clearly show:

• Mortar is significantly weaker than expected for load-bearing walls, with values often less than half of the typical EC6 reference.
• Brick units exhibit large variability, with some samples showing considerable degradation, likely due to age, moisture exposure and inconsistent firing quality.
• Composite masonry strength (fk) is well below the lower limit typically associated with reliable in-plane performance.
• Shear strength (fvk) is critically low, explaining the dominance of diagonal cracking and sliding mechanisms observed in the buildings.

Overall, the material tests confirm that the masonry has insufficient cohesion, low compressive resistance, and inadequate shear capacity, all of which strongly contributed to the brittle damage patterns documented on site.

Link to field observations

The laboratory results provide a quantitative foundation for several damage mechanisms discussed in Chapter 3:
• Low mortar strength → shear cracking and poor joint bonding
• Weak bricks → crushing near openings and compressive failure
• Low shear resistance → rapid stiffness loss and DS-4 behaviour
• Weak bonding → corner separation and out-of-plane tendencies

This direct correspondence is explored further when the measured strengths are compared with Eurocode 6 benchmarks in the next chapter.

5. Comparison with EC-6 requirements

Eurocode 6 (EN 1996-1-1) establishes minimum mechanical properties for masonry materials to ensure adequate performance under vertical and lateral loads. Although these limits are not intended to represent high-quality masonry, they define baseline values below which a structural wall is expected to exhibit poor strength, limited ductility and brittle failure modes.

When the laboratory results obtained from the four URM dwellings are compared with the Eurocode reference ranges, a clear gap emerges between expected and actual material performance.

Mortar strength deficiency

Eurocode 6 generally assumes mortar compressive strength values in the range of 3–5 MPa for traditional masonry.
In contrast, the tested mortar samples measured only 1.0–2.0 MPa, meaning:
• mortar strength is 50–70% below typical EC6 assumptions,
• shear transfer between bricks is severely reduced,
• joint cohesion is insufficient to prevent diagonal cracking.

This large discrepancy explains the pervasive shear cracking and widespread joint degradation observed in all four buildings.

Brick and Masonry Strength Comparison

Tested brick strengths ranged between 5 and 7.5 MPa, significantly lower than the 7.5–15 MPa range commonly associated with fired clay bricks in Eurocode guidance.

Similarly, masonry prism strengths (2.0–3 MPa) fall well short of the ≥5.0 MPa value generally considered acceptable for structural walls. The implications are clear:
• masonry walls had limited compressive reserve,
• crushing around openings and pier ends was expected,
• global stiffness was inherently low.

These weaknesses match the brittle in-plane behaviour and rapid damage progression recorded during field inspections.

Shear Strength and Sliding Resistance

Eurocode 6 prescribes initial shear strengths (v_0) of approximately 0.15–0.30 MPa, depending on mortar class.

Measured values from the Kruja buildings were only 0.03–0.08 MPa, indicating:
• extremely poor sliding resistance,
• high susceptibility to diagonal shear failure,
• inability of the masonry to redistribute forces once cracking initiated.

This numerical contrast is directly reflected in the observed X-shaped cracks and panel distortions throughout all buildings.

Implications for Seismic Performance

When considered together, the measured strengths—particularly the mortar and shear values—fall well below Eurocode expectations for even minimal structural performance. As a result:
• the walls entered nonlinear behaviour at very low drift levels,
• stiffness degradation occurred almost immediately,
• failure mechanisms became brittle and uncontrolled,
• buildings reached DS-4 with relatively moderate displacements.

In other words, the Eurocode comparison confirms that these URM dwellings did not possess the material capacity required to withstand the seismic demands imposed by the 2019 earthquake.

This relationship between material deficiencies and damage severity is discussed further in the following chapter.

6. Discussion: Link between material weakness and observed damage

The combination of field evidence and laboratory test results provides a coherent explanation for the severe damage sustained by the four URM dwellings during the 2019 earthquake. Although geometric irregularities and inadequate diaphragms contributed to the buildings' vulnerability, the dominant factor influencing their seismic performance was the poor quality of the masonry materials.

The mortar samples exhibited compressive strengths far below the values typically assumed for structural masonry. Weak mortar reduces bed-joint cohesion, limits the ability of wall piers to transfer shear, and accelerates the transition from elastic to cracked behaviour. This is entirely consistent with the widespread diagonal shear cracking documented in all four buildings, especially at ground-floor piers where seismic demand is highest.

The variability and degradation of the brick units further weakened the structural system. In several cases, brick strength was low enough to cause localized crushing around openings and vertical splitting at pier ends. Such behaviour aligns closely with the damage patterns observed at lintels, corners and wall edges, where compressive stress concentrations are typically highest.

Masonry prism tests confirmed that the composite behaviour of brick and mortar was insufficient to provide the stiffness and compressive capacity expected for load-bearing walls. As a result, once cracking initiated, the walls experienced rapid stiffness loss and could not redistribute seismic forces effectively. This explains why the dwellings deteriorated quickly during shaking and why damage propagated through multiple interconnected panels.

The very low shear strength values measured in the laboratory also match the failure mechanisms observed in the field. Sliding cracks along bed joints, stepped shear cracks across piers, and interface separation at wall junctions are all symptoms of insufficient shear resistance. These patterns were present in every building included in the study.

When compared with Eurocode 6 reference values, the deficiencies in material strength are substantial. Mortar and masonry strengths were often less than half of the minimum values recommended for structural walls, and shear strength was in some cases only one quarter of typical EC6 assumptions. This large discrepancy implies that the buildings had limited reserve capacity even before the earthquake, making brittle and extensive damage almost unavoidable under strong ground motion.

Overall, the discussion highlights that material weakness was not simply a contributing factor but a defining characteristic of the seismic behaviour of these URM dwellings. The correlation between laboratory-measured strengths and field-observed damage provides strong evidence that improving the material quality of existing masonry buildings—or strengthening them to compensate for these deficiencies—is essential for reducing their seismic risk..

7. Conclusions

This study combined field observations and laboratory material testing to investigate the reasons behind the severe DS-4 damage sustained by four unreinforced masonry (URM) dwellings in Kruja during the 2019 Albania earthquake. Although geometric irregularities and inadequate diaphragms played a role, the results show that material deficiencies were the primary driver of the brittle seismic behaviour. Mortar compressive strengths were typically less than half of the values assumed by Eurocode 6, brick units showed significant variability and degradation, and masonry prisms exhibited low compression and shear capacity. These weaknesses directly correspond to the observed damage patterns, including widespread diagonal cracking, corner separation, sliding along bed joints and localized crushing around openings.

In summary:

- Measured mortar, brick and masonry strengths were well below Eurocode 6 reference values, explaining the limited in-plane and out-of-plane resistance.
- Observed field damage matched the expected failure modes for low-strength masonry, particularly brittle shear cracking and rapid stiffness degradation.
- Material quality was the dominant factor influencing seismic performance, overriding many secondary geometric or detailing inconsistencies.
- Strength assessment and retrofit strategies for older URM buildings must explicitly account for material degradation, as analytical models alone may overestimate capacity if Eurocode default values are used.

The strong correlation between laboratory results and field damage highlights the need for material-based evaluation approaches for existing URM buildings in Albania and similar seismic regions.

Conflict of interests

The author would like to confirm that there is no conflict of interests associated with this publication and there is no financial fund for this work that can affect the research outcomes.

8. References

1. Academy of Sciences of Albania. KTP-N.2-89: Technical Conditions for the Design of Anti-Seismic Constructions. Tirana, Albania, 1989.
2. Eurocode 0. EN 1990:2002/A1:2005 – Basis of Structural Design. CEN, Brussels, 2005.
3. Eurocode 1. EN 1991-1-1:2002 – Actions on Structures. CEN, Brussels, 2002.
4. Eurocode 6. EN 1996-1-1:2005 – Design of Masonry Structures. General Rules for Reinforced and Unreinforced Masonry. CEN, Brussels, 2005.
5. Eurocode 8. EN 1998-1:2004 – Design of Structures for Earthquake Resistance. Part 1: General Rules, Seismic Actions and Rules for Buildings. CEN, Brussels, 2004.
6. NATO Science for Peace Project 983054. Harmonization of Seismic Hazard Maps for the Western Balkan Countries. ORFEUS & Institut d'Estudis Catalans, 2007–2010.
7. IGJEUM (Institute of Geosciences, Energy, Water and Environment). The Earthquake in Durrës on November 26, 2019. Tirana, Albania, 2020.
8. INGV (Istituto Nazionale di Geofisica e Vulcanologia). Characteristics of the Adriatic Sea Earthquake of 26 November 2019. Rome, Italy, 2019.
9. Brzev S., Astroza M. "Confined and Unreinforced Masonry: Behaviour and Construction Practices." Earthquake Spectra, 2018.
10. Lourenço P.B. "Computations on Historic Masonry Structures." Progress in Structural Engineering and Materials, 2002.
11. Tomaževič M. Earthquake-Resistant Design of Masonry Buildings. Imperial College Press, 1999.
12. Hysenlliu, M., Deneko, E., Bidaj, A., Bilgin, H. Seismic Strengthening Design and Post-Intervention Capacity Evaluation of a Low-Rise Masonry Building. *Journal of Integrated Engineering and Applied Sciences*. 2025; 3(2); 249-256.

Structure and properties of AlB_{12}-Al detonation coatings on Steel 45

Aleksandr Umanskyi[1], Valery Muratov[1], Vladimir Sheludko[1*], Konstantin Haltsov[1], Aleksey Bondarenko[1], Tatiana Mosina[1], Vyacheslav Syrovatka[1], Irina Martsenyuk[1], Victor Varchenko[1], Valery Kremenitsky[2], Anatolii Minitskyi[3], Aleksey Kushchev[1]
[1] Frantsevich Institute for Problems of Materials Science, NAS of Ukraine, 3 Omelyana Pritsaka (Krzhyzhanovsky) Str., 03142 Kyiv, Ukraine
[2]Technical Center, NAS of Ukraine, 13 Pokrovskaya Str., 04070 Kyiv, Ukraine
[3]National Technical University of Ukraine "Igor Sikorsky Kyiv Polytechnic Institute", 37 Beresteysky Ave., 03056 Kyiv, Ukraine
v.sheludko@ipms.kyiv.ua

Abstract: *The work is dedicated to the study of the properties of detonation coatings AlB_{12}-30 wt.% Al (AB70) applied to Steel 45 using the DNEPR-5M installation. The coatings have the following characteristics: thickness h ~ 170-200 μm, $H_μ$ = 27-29 GPa, HV = 4.35 GPa. Changes in the tribological characteristics of the composite depending on the friction mode are analyzed. The AB70 coating is found to have stable tribological characteristics: f = 0.21-0.38, wear rate I = 3.3-8.6 μm/km. Samples with coatings exceed uncoated Steel 45 in wear resistance. Changes in the surface structure after friction depending on the sliding speed and load are shown. Two wear mechanisms – oxidative and adhesive-abrasive – are established. A conclusion was drawn regarding the possibility of using the AlB_{12}-Al system to apply detonation coatings.*

KEYWORDS*: ALB_{12}-AL, DETONATION COATINGS, MICROSTRUCTURE, HARDNESS, X-RAY DIFFRACTION, SEM, TRIBOLOGICAL CHARACTERISTICS*

1. Introduction

The properties of the working surfaces of parts and structural elements of machines and constructions are determining factors in their operational reliability and service life [1]. Increasing the service life of machine parts can be achieved by applying coatings on their surfaces protecting them from corrosion and erosion, wear, high-temperature action of aggressive environments, etc. [2-4].

In this regard, detonation spraying (D-spraying) has become widespread. This method is based on the principle of heating the sprayed material (usually a powder) followed by its acceleration and transfer to the sprayed part using the detonation products of gas-oxygen fuel (propane-butane or acetylene-oxygen mixtures are commonly used) [5]. Due to the high velocity of the sprayed particles (600-1000 m/s), D-coatings have minimal porosity (~1%) and significant adhesive strength (40-200 MPa) of the coating to the part, depending on the sprayed material. Moreover, heating of the sprayed product is insignificant (up to ~250°C), which helps prevent volumetric changes in the part. In addition, D-spraying is a very economical, but not very productive method (compared, for example, to high-velocity thermal spraying). As a rule, it is economical for spraying surfaces no more than a few square centimeters in area.

Detonation spraying allows to apply a wide range of materials: metals and alloys, oxides, their mixtures, hard metal-ceramic alloys based on tungsten carbides, chromium, titanium, mixtures of carbides with metals, as well as borides [1, 5, 6-10].

Among the latter, aluminum dodecaboride AlB_{12} is of interest. The method of its synthesis from Al and BN developed at the Frantsevich Institute for Problems of Materials Science of NAS of Ukraine, turn to be more rational and cost-effective than direct synthesis from Al and B [11]. AlB_{12} has a low density (~2.52 g/cm^3), and the particularity of its crystalline structure (icosahedral boron framework) determines its high hardness (22-24 GPa), and infusibility (2070 ^{o}C) [12].

However, the low crack resistance of aluminum dodecaboride significantly limits the scope of its application [12]; therefore, it is advisable to use AlB_{12} in combination with ductile bonded metal. It is promising to use aluminum, which is characterized by high plasticity, low density (2.7 g/cm^3) and low melting point (660 °C). Al was found to wet AlB_{12} well with the formation of contact angles $\Theta \approx 20$ deg, and there are no secondary phases in the interaction zone at the Al-AlB_{12} interface [12]. In particular, the composite material AlB_{12}-50 wt.% Al was used in the deposition of electric spark coatings on titanium (VT1-0) and aluminum (D1) alloys, as well as on Steel 45 [13-15].

The aim of the work is to investigate the possibility of using the composite powder material "aluminum dodecaboride AlB_{12}-Al" to obtain D-coatings on Steel 45, and to investigate the structure and properties of these coatings.

2. Experimental

Powder materials used in this study were high-purity Al (99.8 %) and AlB_{12} produced by CVD method due to reaction of hexagonal boron nitride and aluminum: $12BN + 13Al \rightarrow AlB_{12} + 12AlN$ [16]. The average size of AlB_{12} powder particles was 150÷200 nm. The AlB_{12}-Al composite powder was produced by conglomerating the starting components in an organic binder (zapon) followed by sieving to obtain a particle size in the range of -63…+20 μm. The resulting composition was AlB_{12}-30 wt.% Al, hereinafter referred to as AB70.

D-coatings were applied to a 1×1 cm Steel 45 (GOST 1050-88) substrate using a DNEPR-5M installation in the following mode: spraying distance L = 170 mm, combustible mixture: acetylene C_2H_2/oxygen O_2 = 20/30 g, frequency f = 4 Hz, spraying time t = 10 s.

The microhardness of the D-coatings was measured using a PMT-3 microhardness tester at a load of P = 0.5 N. The Vickers hardness HV was measured using a FALCON500 stationary hardness tester (INNOVATEST, the Netherlands) at a load of P = 1.96 N.

Tribological studies of the D-coatings were conducted on an M-22M friction machine in accordance with GOST 26614-85 under the following conditions: P = 2, 4, and 6 MPa, V = 2 and 4 m/s, friction path S = 2 km. Hardened Steel 45 (HRC 45-50) was used as the counterbody.

X-ray diffraction analysis of the D-coatings surface was performed on a Rigaku Ultima-IV diffractometer (Rigaku Corp., Tokyo, Japan) using $CuK_α$-filtered radiation (λ = 1.54051 Å).

The structure of the D-coatings was studied using a JEOL JSM-6490 LV SEM equipped with an INKA Energy 350XT energy-dispersive spectrometer (Oxford Instruments plc.) and a REM-106I SEM (JSC "SELMI", Sumy, Ukraine).

3. Results and discussion

The general view and microstructure of the AB70 D-coating cross-section are shown in Fig. 1. The average thickness is 170-200 μm, and the microhardness is $H_μ$ = 27-29 GPa. However, there are also sections with $H_μ$ = 7-9 GPa and 0.9-2.8 GPa. The Vickers hardness, measured perpendicular and parallel to the coating thickness, averages HV = 4.35 GPa.

The surface of the AB70 composite is uniform. AlB_{12} particles, 2.9-3.4 μm in size, are evenly distributed within the Al_2O_3 matrix. On the one hand, these particles adhere more tightly to the counterbody surface, increasing the tribocontact area, on the other hand they also promoting more intense oxidation with the formation of oxide layers. The periodic destruction of these layers reduces the strength of the microvolumes in the surface layer of the tribocontact, promoting oxidative wear.

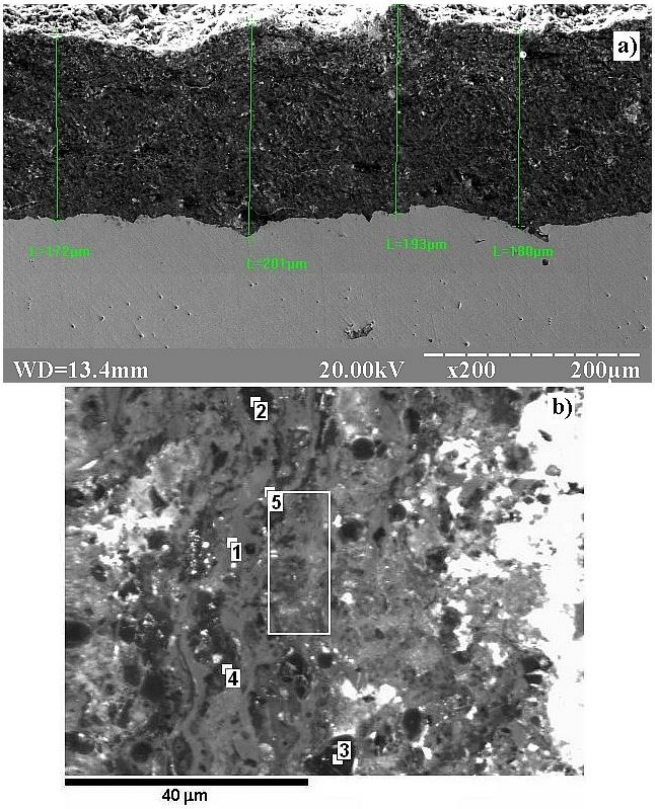


Fig. 1. *Microstructure of the cross-section of the D-coating AB70 with the results of local elemental analysis: a – general view; b – cross-section*

The results of the local elemental analysis of the AB70 D-coating and its phase composition are presented in Table 1 and Fig. 2. The data in Table 1 indicate that the composite contains regions with increased Al (~57 wt.%) and oxygen (~43 wt.%) contents. Boron is part of AlB_{12}, and oxygen and aluminum form secondary structures (mainly oxides) during friction.

Table 1. *Results of local elemental analysis of AB70 D-coating (Fig. 1)*

Spectrum	Element, wt.%				Total
	B	O	Al	C	
AB70 D-coating					
1		43.16	50.69	6.15	100
2	83.09		16.91		
3	81.87	0.61	17.52		
4	68.99	10.77	20.24		
5		32.89	57.11	8.67	

Elemental analysis confirms the presence of elements in the coating corresponding to the main phases (Al, Al_2O_3, AlB_{12}, Fig. 2).

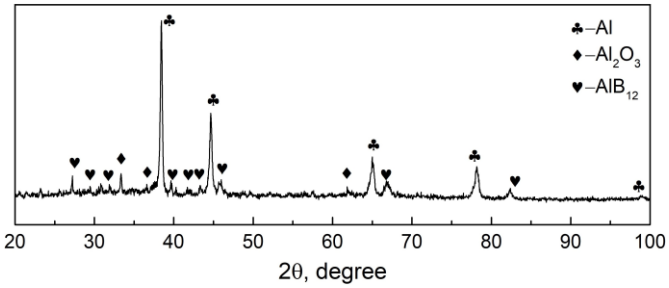


Fig. 2. *Diffraction pattern of AB70 D-coating on Steel 45*

Fig. 3 shows the results of tribological tests of AB70 samples in dry friction mode. These data indicate that with increasing load and sliding speed, the friction coefficient decreases and wear intensity increases. Compared to uncoated Steel 45, the AB70 composition exhibits significantly improved wear resistance. With increasing load to 6 MPa, the wear of uncoated Steel 45 becomes catastrophic.

Fig. 4a shows the surface of the AB70 coating after friction on Steel 45 (P = 2 MPa, V = 4 m/s). A characteristic feature is the presence of dark areas consisting of AlB_{12} aggregates penetrated by light particles (ranging in size from 3 to 6.2 µm). The light areas are represented by elongated conglomerates or individual grains. A characteristic feature is the presence of zones with a high oxygen content (up to 51.73 wt.%) and iron (up to 77.23 wt.%), which indicates the formation of Al and Fe oxides during friction (Table 2). Hard AlB_{12} fragments act as an abrasive on the counterbody surface, crushing and cutting off protrusions, facilitating the transfer of iron from the counterbody. Thus, areas with iron inclusions appear on the surface. Heating the surface (T ~ 230 °C) during friction promotes the oxidation of Al and Fe, forming solid oxides that also contribute to abrasive wear. Thus, in this case, two conjugated wear mechanisms are present – oxidative and adhesive-abrasive.

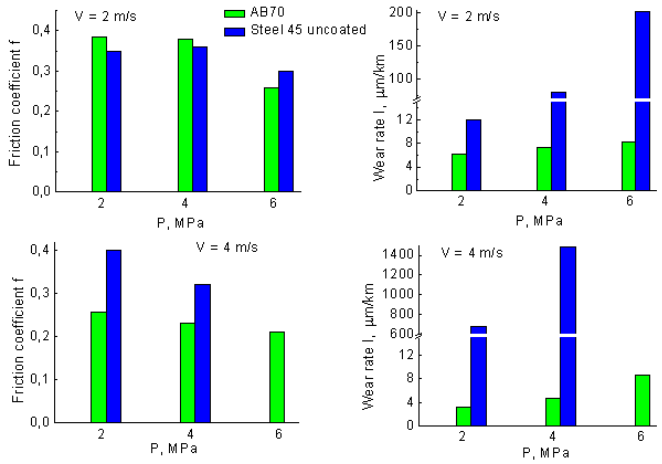


Fig. 3. *Tribological characteristics of AB70 D-coating on Steel 45 and Steel 45 without coating under different loads and sliding speeds*

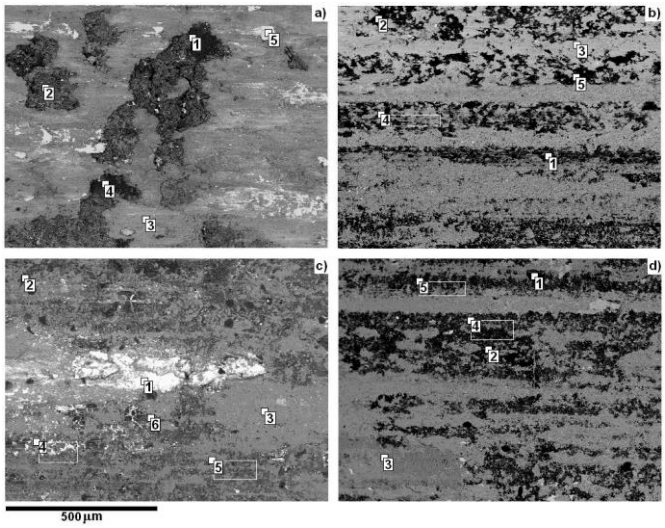


Fig. 4. *Surface of the D-coating AB70 under friction on Steel 45 (V = 4 m/s): a – P = 2 MPa; b – P = 4 MPa; c – P = 6 MPa and d – surface of the AB70 coating under friction on steel ShKh15 (P = 6 MPa, V = 6 m/s) with the results of local elemental analysis*

As the load increases to P = 4 MPa at the same sliding speed, ordering of the relief occurs and alternating layers form (Fig. 4b). Layers with dark AlB_{12} inclusions (62 to 100 µm in size) alternate with light layers 212 to 225 µm in width. Local microanalysis data (Table 2) indicate that this mode results in the formation of larger AlB_{12} grains, distributed within the layers and between them as fine particles, covering the entire surface. As a result, the AlB_{12} particles exhibit a more intense abrasive effect, promoting the formation of iron in the contact zone, followed by the formation of complex $Al_xFe_yO_z$ oxides.

Table 2. *Results of local elemental analysis of the friction surface of the AB70 D-coating (Fig. 4)*

Spectrum	Element, wt.%									Total
	B	O	Al	C	Cr	Fe	Si	Mn	Ni	
Fig. 4a										
1	82.67	1.36	15.97							100.00
2		46.06	52.05	0.43	1.11	0.35				
3		51.73	20.93			27.34				
4	82.77	10.45	16.78							
5		21.09	0.93			77.23	0.75			
Fig. 4b										
1	81.49	1.89	16.62							100.00
2	81.72	0.73	17.01			0.54				
3		37.18	10.46			52.36				
4		40.01	28.67			31.32				
5	44.30	26.07	23.98			5.64				
Fig. 4c										
1		22.53	0.46			76.19		0.82		100.00
2	43.90	26.36	25.56			4.18				
3		44.21	18.72	4.44		32.63				
4		30.76	28.55	4.56	1.05	32.47			2.61	
5		45.04	37.35		1.22	16.39				
6	82.02	1.53	16.45							
Fig. 4d										
1	81.07	1.53	15.06						2.34	100.00
2	81.90	1.03	17.07							
3		43.88	15.56	3.79		36.77				
4		41.67	42.70			15.63				
5		40.43	46.07			13.50				

The system we consider as a frictional contact is dissipative and meets the criteria of self-organization (system openness, nonlinear processes of deformation and wear, formation of secondary structures, etc.). During friction, incoming energy is dissipated into other forms of energy, particularly heat, and accumulated by secondary structures, resulting in self-organization of the system. Furthermore, the principle of structural dissipation of accumulated energy into structural elements in the form of elastic energy is realized within them [17].

Like most structural materials, the composite under study is statistically nonuniform, which determines the nonlinearity of the deformation and wear processes during frictional interaction [18]. The authors [19, 20] note the role of secondary contact structures in the boundary layers of the metal during friction and wear. Such secondary structures can be oxide films in the boundary layers or a supersaturated oxygen solution in plastically deformed surface volumes of the metal, defects and damage of structures in the contact volumes, etc. [21]. During friction, as a result of the interaction of particles of the original disordered system, the deformation contact adapts to changing conditions (temperature, sliding speed, and load). The most important result of such adaptation is the self-organization (ordering) of the system, as a result of which the energy, force, tribomechanical parameters of friction and wear are reduced. These are friction coefficient, temperature, mass wear of the sample and wear intensity [19].

In our system, with a further increase in load to P = 6 MPa, the surface morphology changes (Fig. 4c). The striped relief structure is transformed into a uniform surface with light gray and darker areas. The continuous AlB_{12} network includes individual dodecaboride grains ranging in size from 12.5 to 25 μm. Note the high iron content at different points, ranging from 4.18 to 79.19 wt.% (Table 2). As a result of surface seizure followed by tear-out, a large elongated conglomerate consisting mainly of iron oxide FeO is formed. A more uniform contact surface aids in reducing the friction coefficient to f = 0.21 and the abrasive effect of the resulting oxides increases the wear intensity (Fig. 3).

Any macroscopic system consists of a large number of microscopic states (e.g., volume, temperature, pressure, etc.), characterized by entropy. The evolution of a tribological system consists in achieving a state with entropy lower than its initial value [22]. For example, if the system is heated from temperature T_1 to T_2, the change in entropy ΔS is expressed by the following expression [23]:

$$\Delta S_{1\to 2} = S_2 - S_1 = \int\limits_{1\to 2} \frac{dQ}{T}, \quad (1)$$

where $\frac{dQ}{T}$ – the reduced amount of heat imparted to the system during its transition from state 1 to state 2. Taking into account $dQ = mcdT$, where *m* is the mass of the sample, *c* is its specific heat capacity, formula (1) will take the form (T_1 = 298 K):

$$\Delta S = mc \ln\left(\frac{T_2}{T_1}\right) \quad (2)$$

The data in Fig. 3 indicate that the AB70 sample is characterized by minimal values of tribotechnical characteristics compared to uncoated Steel 45, which is one of the external manifestations of self-organization [19]. At a load of P = 6 MPa and a sliding speed of V = 4 m/s, the result of self-organization of the system is not only a change (ordering) of the surface microgeometry (Fig. 4b, c), but also a decrease in the tribotechnical characteristics. Therefore, it was of interest to compare the change in entropy during friction of a sample with and without a coating. The calculation was carried out using formula (2) and the results are presented in Table 3. Analysis of the change in ΔS indicates that at V = 4 m/s and P = 2 and 4 MPa, the change in entropy during friction of the AB70 composite is 137 and 114 times less than during friction under the same conditions of uncoated Steel 45, which confirms the assumption of self-organization of the system during friction.

Table 3. *Results of entropy calculation ΔS*

Friction mode	Sample temperature T_2, K		Entropy ΔS, J/K	
	AB70-coated Steel 45	Uncoated Steel 45	AB70-coated Steel 45	Uncoated Steel 45
P = 2 MPa V = 4 m/s	500	471	0.00338	0.4654
P = 4 MPa V = 4 m/s	610	496	0.00462	0.5283

Analyzing the data in Fig. 4, one can note the following sequence of changes in the tribocontact relief and wear mechanisms depending on the friction mode.

The friction process at P = 2 MPa and V = 4 m/s is characterized by two conjugated wear mechanism: oxidative and adhesive-abrasive. As the load increases to 4 MPa at the same speed, the microgeometry of the relief changes toward ordering (self-organization). Layers with larger grains of hard AlB_{12} can move over layers with fine particles, reducing the friction coefficient. The composite structure contains zones with increased oxygen and iron content due to the formation of oxides through the oxidative wear mechanism. The presence of AlB_{12} aggregates does not exclude the possibility of abrasive wear, which results in the formation of iron in the contact zone.

With increasing load to 6 MPa, a continuous, uniform relief is formed with dispersed AlB_{12} grains with increased oxygen, aluminum, and iron content, as well as particles of the oxide layer (Table 2), indicating an oxidative wear mechanism. In this case, the influence of temperature, which contributes to oxidative wear, cannot be excluded, since in this mode the temperature in the tribocontact zone is ~360 °C.

It is of interest to compare the obtained data with the results of friction in contact with a harder counterbody. Fig. 4d shows the surface of the AB70 coating during friction on ShKh15 ball bearing steel, the hardness of which (HRC61-63) exceeds the hardness of Steel 45 counterbody. The tests were carried out under more severe conditions (P = 6 MPa, V = 6 m/s). The AB70 coating remained resistant to this mode. At friction on a harder counterbody, a less ordered surface structure is formed with wider bands, which mainly contain aluminum, oxygen, and iron. The iron content is lower (from 13.5 to 36.77 wt.%, Table 2), since the harder counterbody is less susceptible to the abrasive action of AlB_{12} and complex oxides. Increasing the hardness of the counterbody makes difficult plastic deformation and micro-cutting of the friction surface. At that, the friction coefficient f = 0.24, the mass wear of the sample increased slightly to 2.8 mg/km, while that of the counterbody decreased to 0.18 mg/km. The wear rate of the friction pair is I = 8.2 μm/km. Increasing the temperature in the contact zone to T = 432 °C promotes intensification of oxidation processes with the formation of complex oxides $Al_xFe_yO_z$ and the transition to oxidative wear mode.

4. Conclusions

For the first time, using D-spraying, a coating of the AlB_{12}-Al system with different contents of boride and aluminum components was obtained (AlB_{12}-30 wt.% Al (AB70)), and some of its properties such as thickness h = 170-200 μm, microhardness H_μ = 27-29 GPa, Vickers hardness HV = 4.35 GPa were determined. The AlB_{12}-Al system can be used to produce D-coatings on steels.

Tribological tests of the coatings were conducted at sliding speeds V = 2, 4, and 6 m/s and loads P = 2, 4, and 6 MPa. The AB70 composition has the following characteristics: f = 0.21-0.38, I = 3.3-8.6 μm/km.

The structure of the surface layer changes depending on the sliding speed: the alternating strip relief at V = 4 m/s is transformed into a uniform surface at V = 6 m/s, which indicates the processes of ordering (self-organization) of structures in the contact zone with a decrease in the entropy value.

Based on the results of local microanalysis, the formation of iron and aluminum oxides in the friction zone was established. This indicates an oxidative wear mechanism, and the appearance of iron in the contact zone confirms adhesive-abrasive wear as a result of the impact of solid AlB_{12} particles and oxides on the surface of the counterbody.

By replacing the counterbody material with harder hardened ShKh15 steel, the coating proved resistant to severe friction conditions: f = 0.24, I = 8.2 μm/km. The counterbody's mass wear rate was decreased by approximately 35 times (to 1.8 mg/km).

5. References

1. P.A. Vityaz', A.F. Il'ushchenko, A.I. Shevtsov, *Fundamentals of Applying of Wear-, Corrosion-resistant and Heat-shielding Coatings* (Bel. Nauka, Minsk, 2006) [in Russian]
2. Virupakshappa Lakkannavar, K.B. Yogesha, C. Durga Prasad et al., Results Surf. Interfaces, **16**, 100250 (2024)
3. H. Bai, L. Zhong, L. Kang et al., J. Alloys Compd., **882**, 160645 (2021)
4. T. Hoornaert, Z.K. Hua, and J.H. Zhang, Proc. of CIST2008 & ITS-IFToMM2008, Beijing, China, 24-27 September 2008.– PP. 774–779
5. A. Hasui, *Spray-Coating Technique*. [Russian Translation] (Mashinostroenie, Moscow, 1975)
6. J. Keränen, T. Stenberg, T. Mäntylä et al., Surf. Coat. Technol., **82**(1-2), 29 (1996)
7. Gao Yang, Hei Zu-kun, Xu Xiaolei, and Xin Gang, J. Therm. Spray Technol., **10**(3), 456 (2001)
8. H. P. Lv, J. Wang, Y. G. Yan et al., Mater. Sci. Technol., **26**(8), 950 (2010)
9. Lakhwinder Singh, Vikas Chawla, J.S. Grewal, J. Miner. Mater. Charact. Eng., **11**(3), 243 (2012)
10. V.P. Konoval, O.P. Umanskyi, O.A. Bondarenko et al., Powder Metall. Met. Ceram., **59**(5-6), 308 (2020)
11. O.O. Vasiliev, V.B. Muratov, T.I. Duda, Phys. Chem. Solid St., **18**(3), 358 (2017)
12. P.S. Kisly, V.A. Neronov, T.A. Prikhna et al., *Aluminum Borides* (Nauk. Dumka, Kiev, 1990) [in Russian]
13. A.P. Umanskyi, M.S. Storozhenko, V.E. Sheludko et al., Funct. Mater., **28**(4), 694 (2021)
14. A.P. Umanskyi, M.S. Storozhenko, V.E. Sheludko et al., Metallophys. Adv. Technol., **43**(11), 1443 (2021)
15. A.P. Umanskyi, A.I. Dukhota, V.E. Sheludko et al., Funct. Mater., **29**(4), 514 (2022)
16. UA Patent 107193 (2016)
17. S.V. Fedorov, E. Assenova, J. of Science and Education of North-West Russia, **3**, 1 (2017) [in Russian]
18. A.G. Kuzmenko, Problems of Tribology, **3**, 106 (2012) [in Russian]
19. D.M. Baranovskiy, Eastern-European J. of Enterprise Technologies, **3/8(39)**, 28 (2009) [in Ukrainian]
20. O.A. Mikosianchyk, R.G. Mnatsakanov, V.I. Kalinichenko et al., Problems of Tribology, **3**, 6 (2016) [in Russian]
21. M.I. Denysenko, O.V. Zazimko, V.F. Labunets et al., Problems of Friction and Wear, **4(69)**, 38 (2015) [in Russian]
22. V.V. Aulin, *Physical fundamentals of processes and states of self-organization in tribotechnical systems* (KOD, Kirovograd, 2014) [in Ukrainian]
23. D.V. Sivukhin, *General Course of Physics*. In 5 vols. V. II. *Thermodynamics and Molecular Physics* (FIZMATLIT, Moscow, 2005) [in Russian]